IN-SITU TIME RESOLVED X-RAY DIFFRACTION STUDY OF MICROSTRUCTURAL EVOLUTION DURING LOW PRESSURE CARBURIZATION OF STEELS

Vom Fachbereich Produktionstechnik

Der

UNIVERSITÄT BREMEN

zur Erlangung des Grades
Doktor-Ingenieur
genehmigte

Dissertation

von

M. Sc. Ogün Baris Tapar

Gutachter: Prof. Dr.-Ing. habil. Rainer Fechte-Heinen
Prof. Dr.-Ing. Karen Pantleon (Technical University of Denmark)

Tag der mündlichen Prüfung:07.11.2024

Danksagung

Die vorliegende Arbeit entstand während meiner Tätigkeit am Leibniz-Institut für Werkstofforientierte Technologien - IWT in Bremen im Rahmen von DFG-geförderten Projekten.
Ich möchte mich zuerst bei Prof. Dr.-Ing. habil. Rainer Fechte-Heinen für die Betreuung der Arbeit und deren Begutachtung bedanken. Die immer freundliche und konstruktive Zusammenarbeit sowie die intensive Durchsicht meiner Arbeit haben maßgeblich zu ihrem Gelingen beigetragen. Weiterhin möchte ich Prof. Dr.-Ing. Karen Pantleon für ihr engagiertes Interesse an meiner Arbeit und die Übernahme des Zweitgutachtens herzlich meinen Dank aussprechen.
Prof. Dr. Bernd Mayer möchte ich für die Übernahme des Prüfungsvorsitzes sowie für die angenehme Atmosphäre und den reibungslosen Ablauf des Kolloquiums danken. Ebenso bin ich Prof. Dr.-Ing. habil. Franz Hoffmann und Niklas Sopke für die Mitwirkung im Prüfungsausschuss zu Dank verpflichtet.
Besonderer Dank gilt meinem Abteilungsleiter Dr.-Ing. Jeremy Epp, der mich durch die freundschaftliche Zusammenarbeit und konstruktiven Diskussionen sowie die Durchsicht meiner Arbeit sehr unterstützt hat. Außerdem möchte ich mich bei all meinen Kollegen der Abteilung Physikalische Analytik, und insbesondere bei Alexander Kohl, für die Unterstützung beim Bau der im Projekt verwendeten Versuchskammer herzlich bedanken.
Zusätzlich möchte ich unseren Projektpartnern Dr.-Ing. Jens Gibmeier, M.Sc. Michael G. Zürn, Marcel Miatke, Rafael Hofsäß und M.Sc. Sebastian Ohneseit vom Karlsruher Institut für Technologie (KIT) für ihren wertvollen Beitrag zu den Versuchsanlagen und den Messungen meinen Dank aussprechen.
Außerdem möchte ich dem DESY-Personal, insbesondere Dr. Norbert Schell und Ursula Tietze, meinen Dank für die Bereitstellung der erforderlichen Materialien, die Unterstützung bei der Nutzung der Beamline und sowie die vielfältige Hilfe während der Synchrotronmessungen aussprechen. Darüber hinaus bin ich der DESY-Sicherheitsabteilung für ihre Unterstützung im Bereich der Prozesssicherheit besonders dankbar.
Nicht zuletzt möchte ich den Mitarbeiterinnen und Mitarbeitern aus der Härterei, Werkstatt und metallografische Analytik für die Unterstützung bei der Durchführung der Aufgaben im Rahmen der Arbeit danken.
Schließlich bedanke ich mich ganz herzlich bei meiner Familie und besonders bei meiner Frau für ihre geduldige und liebevolle Unterstützung während der Ausarbeitung meiner Dissertation.

Table of Content

Nomenclature

Symbol	Description
2θ	2-theta, Bragg angle between the incident and diffracted X-ray beams
C_2H_2	Acetylene
Q	Activation energy
M_c	Amount of carbon absorbed in sample
θ	Angle of the diffraction
at. %	Atomic percent
$e^{\frac{-Q}{kT}}$	Boltzmann factor
A_{cm}	Boundary line in Iron-Cementite phase for γ / γ + cementite region
B(2θ)	Broadening function
C_4H_{10}	Butane
$I_{n(c)}$	Calculated peak intensity
x_C^r	Carbon content in atomic percent
x_C	Carbon content in mass percent
M_c^A	Carbon dissolved in austenite
J_c	Carbon Flux
CO	Carbon monoxide
C_P	Carbon potential of atmosphere
C_C^S	Carbon potential of sample surface
β	Carbon transfer coefficient / mass transfer coefficient
Fe_3C / θ	Cementite
χ	Chi, rotation angle in the plane normal to that containing omega and 2θ
d_c/d_x	Concentration gradient in Fick's laws of diffusion
D	Diffusion coefficient
D_c	Diffusion coefficient of carbon
D_c^γ	Diffusion coefficient of carbon in austenite
D_c^θ	Diffusion coefficient of carbon in cementite
$E^{\{hkl\}}$	Elastic modulus dependent on {hkl}
C_{ij}	Elastic stiffness coefficient
F_m	Energy barrier required for diffusional jump of the atom
C_g	Equilibrium carbon content

K	Equilibrium constant
final	Equilibrium Temperature
T_q	Final temperature reached during quenching
J_D	Flux Density
D_0	Frequency factor
R	Gas constant
J(2θ)	Geometrical instrument function
ΔG	Gibbs free energy
G_A	Gibbs free energy of austenite
G_M	Gibbs free energy of martensite
H_2	Hydrogen molecule
K(2θ)	Instrument profile shape
$\mathcal{E}$	Kinetic energy of electrons
a_A	Lattice constant a in tetragonal lattice
c_A	Lattice constant c in tetragonal lattice
d	Lattice spacing
$d_{\Phi\Psi}$	Lattice spacing for every tilt angle calculated by Bragg's law
η	Lorentzian mixing ratio
A_{C1}	Lower Critical Temperature
M_f	Martensite finish temperature
M_s	Martensite start temperature
Ma. %	Mass percent
I_{max}	Maximum intensity of the peak after background subtraction
σ_m	Mean hydrostatic stress
CH_4	Methane
µm	Micrometer
σ_Φ	Normal stresses
$I_{n(o)}$	Observed peak intensity
ω	Omega, angle between the incident X-ray beam and the sample surface
p	partial pressures of the corresponding gases
I_{int}	Peak area after background subtraction
A	Peak Height
x_0	Peak position
$(\sigma_x)^\xi$	Phase specific stresses in x direction

Φ	Phi, angle of rotation of the sample about its surface normal
$\nu^{\{hkl\}}$	Poisson's ratio dependent on {hkl}
I(2θ)	Profile function
C_3H_8	Propane
β	Proportionality factor
Ψ	Psi, angles through which the sample is rotated
$\otimes$	Representation of convolution operation
σ^I	Residual stresses of the first kind
σ^{II}	Residual stresses of the second kind
σ^{III}	Residual stresses of the third kind
HRC	Rockwell hardness
τ_Φ	Shear stresses
ε_{ij}	Strain tensor
$\varepsilon_{\Phi\Psi}$	Strain tensor for every tilt angle
d_0	Stress-free lattice spacing
σ_{ij}	Stress tensor
T	Temperature
ΔT	Undercooling or change in temperature
A_{C3}	Upper Critial Temperature
V_m	Volume of martensite
λ	Wavelength
W(2θ)	Wavelength profile function
w_n	Weighting factor
ZrN	Zirconium nitride

Abbreviation	Description
XRD^2	2D X-ray Diffraction
BMs	Bending magnets
BCC	Body Centered Cubic
BCT	Body-centered Tetragonal
CHD	Case hardening depth
CCT	Continuous Cooling Transformation
DESY	Deutsches Elektronen-Synchrotron
DICTRA	Diffusion Module of the software Thermo-Calc for making diffusion simulations
EBSD	Electron back scattered diffraction
EMPA	Electron micro probe analysis
ESRF	European Synchrotron Radiation Facility
FCC	Face Centered Cubic
FDM	Finite-difference methods
FWHM / HWHM	Full width at half maximum / Half width at half maximum
FPA	Fundamental parameter approach
GDOES	Glow discharge optical emission spectrometry
IDs	Insertion devices
IB	Integral breadth
KIT	Karlsruhe Institute of Technology
IAM-WK	KIT, Institute for Applied Materials – Materials Science and Engineering
KM	Koistinen and Marburger (KM) model
LINAC	Linear accelerator
LPC	Low Pressure Carburizing
PVII	Pearson VII fitting function
PVD	Physical vapor deposition
PSD	Position sensitive detector
PXRD	Powder X-ray diffraction
pV	Pseudo-Voigt fitting function
RF	Radio frequency
RA	Retained austenite
SEM	Scanning electron microscope
S-OES	Spark plasma optical emission spectroscopy
TCHZ	Thompson-Cox-Hasting pseudo-Voigt fitting function
TTA	Time Temperature Austenitisation
TTT	Time Temperature Transformation
TEM	Transmission Electron Microscope
V	Voigt fitting function
XRD	X-ray Diffraction
CTE	Thermal expansion coefficient
PSD	Position sensitive detector

Zusammenfassung

Die Niederdruckaufkohlung ist ein thermochemisches Einsatzhärtungsverfahren, bei dem die Werkstoffoberfläche durch Erhöhung des Kohlenstoffgehalts verfestigt wird. Es wird in einem Vakuumofen unter Verwendung von Kohlenwasserstoffgasen bei sehr niedrigem Druck und erhöhten Temperaturen durchgeführt, um eine harte, verschleißfeste Oberfläche in Verbindung mit einem zähen Kern zu erhalten. Der Prozess wird im Allgemeinen in zwei Schritte unterteilt, die als Boost und Diffusion bezeichnet werden. Im Boost-Schritt wird Kohlenwasserstoffgas bei hoher Temperatur und niedrigem Druck in den Ofen eingeleitet, wodurch der Kohlenstoff von der Stahloberfläche absorbiert wird. Im folgenden Diffusionsschritt wird die Probe bei hoher Temperatur im Vakuum gehalten, damit der Kohlenstoff in die Tiefe des Werkstoffs diffundieren kann.

Obwohl die Niederdruckaufkohlung in der Industrie etabliert ist, fehlt es noch an detaillierten Mechanismen der Gefügeentwicklung und an grundlegendem Verständnis. Insbesondere sind die detaillierten Kenntnisse über die Kinetik der lokalen Kohlenstoffanreicherung, die zu einer sukzessiven Karbidbildung und -auflösung während der verschiedenen Prozessschritte führen könnte, noch unvollständig. Ziel dieser Dissertation ist es daher, den aktuellen Stand des Wissens und des Verständnisses über das Niederdruckaufkohlen zu erweitern.

Um dieses Ziel zu erreichen, wurden während des gesamten Niederdruck-Aufkohlungsprozesses in-situ-Synchrotron-Röntgenexperimente an der Hochenergie-Synchrotron-Beamline P07-EH3 von PETRA III am Deutschen Elektronen-Synchrotron (DESY) in Hamburg durchgeführt. Eine spezielle Kammer und ein Prozesskontrollsystem wurden entwickelt, um industriell relevante Experimente während kontinuierlicher Röntgenbeugungsmessungen durchführen zu können.

Während der gesamten Experimente wurden insgesamt etwa 150.000 einzelne 2D-Beugungsbilder aufgenommen. Die 2D-Bilder wurden mithilfe der leistungsfähigen PyFAI-Software der European Synchrotron Radiation Facility (ESRF) integriert und nach der Rietveld-Methode ausgewertet. Dabei kam eine automatische Auswertung mit selbst entwickelten Auswertemakros zum Einsatz, die in die kommerziell erhältliche Software TOPAS von Bruker und MATLAB integriert wurden. Daraus wurden zeit- und temperaturabhängige Informationen über vorhandene Phasen, Phasenanteile und Gitterkonstanten gewonnen. Der Kenntnisstand über mikrostrukturelle Veränderungen und die Entstehung von Spannungen während aller Behandlungsschritte konnte erheblich verbessert werden.

Darüber hinaus wurden die Gefügeveränderungen während der Aufkohlungsversuche, die mit verschiedenen Prozessparametern durchgeführt wurden, untersucht und diskutiert. Bei diesen Parametern handelt es sich um die Prozesstemperatur, die Acetylenmenge und die Anzahl der Boost-Diffusionszyklen.

Des Weiteren wurden die Ergebnisse der Änderung des Spannungszustandes während der verschiedenen Schritte der Aufkohlungsversuche aufgezeigt und diskutiert.

Schließlich wurden die experimentellen Daten und die durch die bestehende Simulation vorhergesagten Daten verglichen. Aufgrund neuer Erkenntnisse wurden die Berechnungen der Simulation verbessert, indem die neuen Parameter angewendet wurden. Für diesen Vergleich wurde eine spezielle Simulation gewählt, da sie viele Phänomene berücksichtigt, die während der Niederdruckaufkohlung auftreten, wie z. B. Karbidbildung und -auflösung, und somit präzise Ergebnisse für industriell relevante Prozessparameter vorhersagt.

Die Sättigungsgrenze des Austenits wurde innerhalb von Sekunden nach dem Aufheizen erreicht, weil der Kohlenstoff sehr schnell aus der Atmosphäre in die Probe aufgenommen wurde. Dieser schnelle Anstieg wurde unabhängig von den Prozessparametern beobachtet. Die Kohlenstoffatome sammelten sich an der Oberfläche an und es kam zu einer raschen Ausscheidung von Karbiden. Daher wurde die Kohlenstoffdiffusion aus der Atmosphäre an die Oberfläche verlangsamt. Unterstützende Experimente im Reflexionsmodus zu den Hauptexperimenten im Transmissionsmodus ergaben, dass der im Austenit gelöste Kohlenstoffgehalt nach 20 Sekunden Boost-Schritten den Spitzenwert erreicht und dann aufgrund der Diffusion von Kohlenstoff abnimmt, obwohl in der Atmosphäre noch Acetylen vorhanden war. Dies wurde als starker Beweis für die Verlangsamung der Kohlenstoffaufnahme durch die Karbidschicht, hauptsächlich Zementit, gewertet, die sich auf der Oberfläche des Materials gebildet hatte. Diese Karbidschicht wurde auch durch Zementit-Peaks in der Röntgenbeugung während der Boost-Schritte und sowie durch metallographische Analysen von Proben bestätigt, die unmittelbar nach der Boost-Schritte abgeschreckt wurden.

Die Karbide, die sich in den ersten Sekunden der Boost-Schritte an der Oberfläche des Materials bildeten, begannen sich in den folgenden Diffusionsschritten aufzulösen. Die Bildungs- und Auflösungskinetik der Karbide hing stark von der Menge der Karbide und dem Grundkohlenstoffgehalt in der austenitischen Matrix ab. Mit zunehmender Anzahl der Boost-Aufladeschritte nahm auch die Stabilität des Zementits zu. So blieb die Menge des im ersten Verstärkungsschritt Boost gebildeten Zementits konstant, während der im zweiten und dritten Verstärkungsschritt gebildete Zementit sogar bis zum Ende der ersten Minute der folgenden Diffusionsschritte weiter anstieg.

In den ersten Minuten aller Diffusionsschritte blieb der im Austenit gelöste Kohlenstoffgehalt nahezu unverändert. Diese Stabilität des Kohlenstoffgehalts wurde bereits am Ende der Boost-Schritte erreicht. Während dieses Zeitraums wurde beobachtet, dass der Zementitgehalt beim zweiten und dritten Boost-Schritt weiter anstieg, obwohl kein weiteres Kohlenstoffspendergas in die Kammer eingeführt wurde.

Während des Abschreckens hatte der früh gebildete Martensit ein niedrigeres c/a-Verhältnis als der später gebildete. Dieser Unterschied wurde auf die frühe Phasenumwandlung von Austenitkörnern mit geringerem Kohlenstoffgehalt zurückgeführt. Andererseits wurden auch sofortige self-tempering, zweiter Art Eigenspannungen zwischen Austenit und Martensit und eine Umverteilung/Ordnung des Kohlenstoffs erwartet, was zu einer geringeren Tetragonalität führt.

Um die Auswirkungen der Temperatur zu untersuchen, wurden zwei Versuche mit denselben Prozessparametern bei 960 °C und 920 °C durchgeführt. Eine höhere Temperatur führte zu einer höheren Kohlenstoffabsorption während des Boost-Schrittes. Die Auswirkung der hohen Temperatur war in den frühen Stadien des Prozesses dominanter und nahm in jedem folgenden Schritt ab.

Um die Auswirkung der Acetylenmenge auf die Prozessschritte zu untersuchen, wurden zwei Experimente mit unterschiedlichen Acetylenflussraten und unterschiedlicher Dauer der Boost-Schritte durchgeführt. Die Dauer der Boost-Schritte wurde um das Zweifache und die Acetylen-Durchflussmenge um das Achtfache erhöht. In der ersten Minute der Boost-Schritte wurden deutliche Unterschiede im Kohlenstoffgehalt, der im Austenit gelöst war, beobachtet. Das Experiment mit der höheren Durchflussrate hatte einen höheren Kohlenstoffgehalt. Nach der ersten Minute blieb der Kohlenstoffgehalt bei der Probe mit der höheren Acetylen-Durchflussrate jedoch fast konstant, während bei der anderen Probe ein geringer Anstieg zu beobachten war, was darauf hindeutet, dass die Kohlenstoffzufuhr zur Oberfläche dieser Probe noch immer langsam erfolgt. Am Ende der Erhöhungsschritte für zwei Proben lagen die endgültigen Kohlenstoffgehalte an der Oberfläche trotz sehr unterschiedlicher Durchflussraten und -dauern sehr nahe beieinander. Quantitative Karbidanalysen wurden auch für den zweiten Boost-Schritt der Probe mit der höheren Acetylenmenge durchgeführt. Die Zunahme des Zementitgehalts war ähnlich der Zunahme des im Austenit gelösten Kohlenstoffs. In der Anfangsphase nahm der Zementitgehalt stark zu, dann verlangsamte sich die Zunahme und nach etwa 100 Sekunden war die Zementitmenge konstant. Es wurde festgestellt, dass Karbide je nach Prozessparameter einen erheblichen Beitrag zum endgültigen Kohlenstoffgehalt leisten, der bei den Berechnungen berücksichtigt werden sollte.

Um die Auswirkungen der Boost- und Diffusionszyklen zu untersuchen, wurden Versuche mit 3 und 4 Zyklen durchgeführt. Die Probe mit der höheren Anzahl an Boost-Diffusionszyklen hatte einen niedrigeren Oberflächenkohlenstoffgehalt, aber eine höhere Kohlenstoffeindringtiefe, da auch die Diffusionsdauer höher war. Bei dieser Probe wurde auch die Bildung von Zementit während der Boost-Schritte anhand der Röntgenbeugungspeaks beobachtet.

Die Entwicklung sowohl der abweichenden als auch der mittleren Spannung in eine Richtung wurde bei jedem Schritt der Niederdruckaufkohlung-Behandlung beobachtet. Wie erwartet, gab es vor den Boost-Schritten keine Eigenspannungen bei hohen Temperaturen. Das Hauptaugenmerk fiel auf die Eigenspannungen während des Abschreckens, infolgedessen drei Proben mit unterschiedlichen Kohlenstofftiefenprofilen wurden mit derselben Abschreckrate untersucht. In der Anfangsphase des Abschreckens traten bis etwa 420 °C thermische Spannungen in Zugrichtung auf. Über etwa 420 °C nahmen die Zugspannungen aufgrund der martensitisch-bainitischen Umwandlung des Kerns zu. Bei Erreichen der martensitischen Umwandlungstemperatur der Oberfläche begannen die Zugspannungen zu sinken und änderten dann irgendwann ihre Richtung in Richtung Druck. Bei den meisten Proben war die Druckeigenspannung im Restaustenit am Ende des Abschreckens umgekehrt proportional zum Kohlenstoffgehalt der Probe. Zusätzlich wurden bei allen Proben

höhere Druckspannungen im zuerst gebildeten Martensit erzeugt, die im weiteren Verlauf der martensitischen Umwandlung abgebaut wurden.

Im letzten Teil der Arbeit wurden die Ergebnisse aus den Versuchen mit den Ergebnissen der von Steinbacher und Hunkel entwickelten Simulation verglichen. Es wurden neue Randbedingungen vorgeschlagen, um genauere Vorhersagen zu treffen. In-situ-Untersuchungen zeigten, dass einer der Hauptunterschiede zwischen dem berechneten Gradienten des Kohlenstoffgehalts und der Simulation durch die Variation der Temperatur verursacht wird, da diese sowohl die Diffusionsgeschwindigkeit des Kohlenstoffs im Material als auch die Karbidbildungs- und -auflösungskinetik beeinflusst. Daher wurden Proben mit unterschiedlichen Prozesstemperaturen und auch unterschiedlichen Härtetemperaturen untersucht und die berechneten Kohlenstoffprofile mit den Simulationswerten verglichen. Darüber hinaus wurden auch Prozesspläne mit unterschiedlichen Boost-Schrittdauern untersucht. Es zeigte sich, dass kürzere Boost-Schritte von weniger als einer Minute zu einer Unterschätzung des Kohlenstoffgehalts in der Simulation geführt haben. Als Grund hierfür wird angenommen, dass die Hauptkohlenstoffaufnahme aus der Atmosphäre in der Probe in den ersten Sekunden der Boost-Schritte abgeschlossen ist. Das Simulationsprogramm geht jedoch von einer gleichmäßig verteilten Kohlenstoffaufnahme über die gesamte Boost-Schrittdauer aus, was zu einer Unterschätzung führt. Wird die Dauer des Boost-Schritts verlängert, wird der Kohlenstoffgehalt überschätzt. Dieses Phänomen wird auf die Bildung von Karbiden an der Oberfläche zurückgeführt, die die Kohlenstoffaufnahme verlangsamen. Das Simulationsprogramm berücksichtigt zwar die Karbidbildung jedoch nicht vollständig deren negative Auswirkungen auf die Acetylenzersetzung, wodurch es wiederum zu einer Überberechnung des Kohlenstoffgradienten kommt.

1 Introduction

Heat treatment is a process of heating materials in a defined atmosphere during a defined time to produce a predictable change in the structure of a material. It can affect the mechanical, physical or metallurgical properties of most metals and alloys; especially ferrous alloys, such as steels, which undergo pronounced changes in properties [1].

For specific applications, heat treatments focus on particularly to the case of the material. Carburization case hardening processes are currently among the widely used surface hardening treatments [2]. It generates a high-strength surface layer along with a tough core, which in particular enhances the wear and fatigue properties of the component [3]. Moreover, compressive residual stresses generated in the case layer contribute to an improvement of the fatigue strength. Low pressure carburizing (LPC), among other carburizing techniques, has an increasing industrial importance in today's manufacturing because of its high carbon activity which enables blind holes and wide surfaces to be uniformly carburized, and elimination of surface oxidation. Moreover, it is more efficient due to less consumption of process gases and shorter process time.

LPC is a recipe-controlled thermochemical treatment that is generally composed of several boost and diffusion steps. Compared to gas carburizing, which is an equilibrium process, low pressure carburizing is a non-equilibrium process that uses a carburizing atmosphere of pure hydrocarbons with a very high carbon transition. During the process, components are heated to a defined carburizing temperature under vacuum that leads to the dissolution of initially present carbides. Afterwards, a carbon donor gas is introduced into the furnace in a controlled pressure range (1 to 30 mbar). In this step, dissociation, adsorption and diffusion of the carbon atoms present in the atmosphere take place, leading to an increased carbon content in the case of the workpiece. This enrichment stage of the surface by carbon is called the boost step. Afterwards, the furnace chamber is evacuated from the remaining gases to let the carbon diffuse towards the core of the workpiece. Thus, the carbon content close to the surface decreases and the carburizing depth increases due to the existing carbon at the surface diffusing towards the core. This step is called the diffusion step. This sequence of boost and diffusion steps can be repeated several times until the desired carbon profile is achieved. The process-related parameters such as temperature, the number and duration of boost/diffusion steps, carburizing gas flow rate and pressure can be varied to achieve the desired case profile. Different types of process strategies can be found in industrial applications [4]. When the desired carbon profile is reached, samples are generally quenched with high-pressure inert gas such as helium or nitrogen or in oil, to achieve the desired martensitic microstructure and hardness gradient toward the core. Several hydrocarbon gases can be used as a carbon donor gas such as propane, methane or acetylene. However, LPC using acetylene is particularly economical and environmentally friendly [5,6]; also more effective since acetylene directly participates in the carburizing reactions rather than pyrolyzing other carburizing gases [7].

Although LPC is established in the industry, it still lacks detailed information on the mechanisms of microstructural evolution. Especially, detailed knowledge about local carbon enrichment, which could lead to successive carbide formation and dissolution during different process steps, is still incomplete. This shortage of information exhibits the necessity of a better understanding of the process.

Currently, there are several practical approaches for the optimization of process parameters and the understanding of the process kinetics [7–11], but common methods are often limited to the characterization of the initial and final stages or interruption of the process by cooling. This causes a change in the properties of materials and a loss of information. For this reason, it is great interest to find a description of the carburizing kinetics that applies generally to all stages of the process. This investigation is only possible by getting real-time insights into the process of the LPC combined with a spatially resolved analysis. In situ X-ray diffraction methods, particularly synchrotron X-ray diffraction approaches, are excellently suitable for obtaining information about microstructural evolution [12–14] and redistribution of interstitials [15]. Moreover, structure evolutions during other thermochemical surface treatments such as ion nitriding could also be observed successfully by in situ synchrotron diffraction techniques [16]. An investigation regarding LPC in this manner, as far as the author's knowledge, has never been done previously. Therefore, the primary goal of this thesis is to extend the current state of knowledge and understanding of the LPC on the base of in-situ X-ray diffraction experiments. In this manner, time-resolved qualitative and quantitative information related to microstructures, present phases and interstitials can be gathered during the entire process.

This thesis describes the developed heat treatment chamber and control system designed for in situ X-ray diffraction analyses in both transmission and reflection mode. Furthermore, the thesis aims to provide insights into the kinetics of the low pressure carburizing treatment. In order to reach this objective, in-situ X-ray diffraction experiments were performed during the LPC including subsequent quenching at the Deutsches Elektronen-Synchrotron (DESY) in Hamburg, Germany. The microstructural evolution was precisely tracked with high spatial and time resolution throughout the treatment. In addition to microstructural evolution, stress generation was also investigated. To validate the observations made at high temperature, supplementary metallographic investigations were performed after the treatment.

The investigated material in this thesis was AISI 5120 (20MnCr5), a carburizing steel grade widely used for the manufacturing of gears. This steel was prepared in desired dimensions, and diffusion barrier coating was applied to the side surfaces to eliminate unwanted carbon intake. Prior to any investigations in the newly developed chamber, it had to be demonstrated that the chamber is capable of reproducing industrial low pressure carburizing. Consequently, the present thesis begins with the demonstration of the reliability of the chamber by comparing two samples carburized in an industrial furnace and the in-situ chamber with different material characterization techniques. In

addition, it has also been demonstrated that treatments conducted in in-situ chamber are repeatable and yields consistent results.

Subsequently, the data analyses procedure was documented by demonstrating the microstructural evolution of two samples during the entire LPC treatment. The influence of process parameters on low pressure carburizing was then investigated, focusing on three chosen parameters: temperature, acetylene amount, and the number of boost-diffusion cycles. The results of these experiments were afterwards compared to observe the effect of each parameter.

The subsequent section demonstrates the evolution of stresses in each step of the LPC, with particular emphasis on the quenching step, where the primary stress generation is observed. The investigation extends to three different samples with distinct carbon content depth profiles during the quenching step, while for other steps of the low-pressure carburizing process, stress evolution is presented for a single sample.

In the final investigation, the acquired data were compared with existing simulations, highlighting differences that could serve as potential openings for improvement.

Throughout these investigations, data obtained from the synchrotron experiments were integrated into 2D-diffraction frames, with special attention given to the combination of temperature and diffraction data. Full diffraction ring fittings were conducted for phase and microstructure analysis, while partial azimuthal integration of single peaks was performed for stress analyses. From these analyses, changes in phase contents and lattice parameters, as well as the generation of stresses, were extracted for different stages of the LPC process. Complementary methods, including metallographic investigations, scanning electron microscope analyses, and micro-hardness measurements, were employed to support these investigations.

2 State of the Art

2.1 Iron Carbon Equilibrium Phase Diagram

The Iron–carbon phase diagram is given in Figure 2-1. At ambient temperature, α-ferrite, characterized by a body centered cubic (BCC) structure, represents the thermodynamically stable form of the iron. Upon heating, α-ferrite undergoes a phase transition at 912 °C to a face-centered cubic (FCC) γ-iron, commonly named as austenite. Austenite remains stable up to 1394 °C, where it further transforms into another variant of the BCC phase, named δ-ferrite, eventually reaching its melting point at 1538 °C. These transformations are graphically illustrated along the left vertical axis of the phase diagram. The composition axis extends to 6.70 mass % C, which is the theoretical maximum solubility of carbon in iron in the form of cementite (Fe_3C), an intermediary compound of iron carbide. Beyond this, graphite starts to form [17].

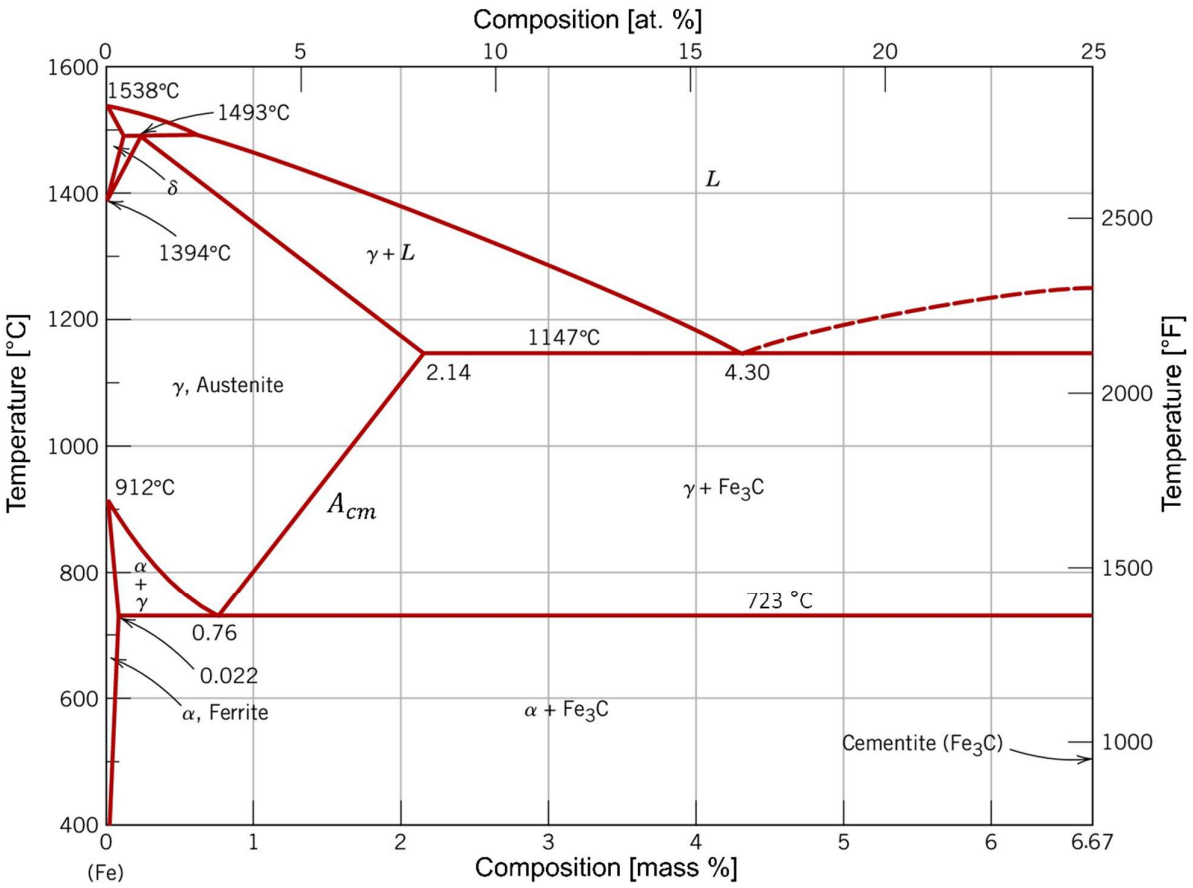

Figure 2-1: Iron-cementite metastable phase diagram [17]

In practice, steels are defined by a carbon content below 2.14 mass % C. Carbon functions as an interstitial alloying element in iron, establishing a solid solution with both α- and δ-ferrites, as well as austenite. The solubility of BCC α-ferrite is notably constrained; with a maximum solubility of

0.022 mass % at 727 °C. This limited solubility caused by the arrangement of interstitial sites in the crystal structure of the BCC lattice. Each BCC lattice contains two iron atoms, six octahedral sites, and twelve tetrahedral sites. The maximal radius of an atom which could fit within these interstitial sites without distortion of the lattice is limited to 0.036 nm. As the radius of a carbon atom is about 0.074 nm at ambient temperature, substantial lattice distortions are needed to accommodate the presence of carbon [18,19]. Figure 2-2 shows the unit cell of BCC and FCC with interstitial sites.

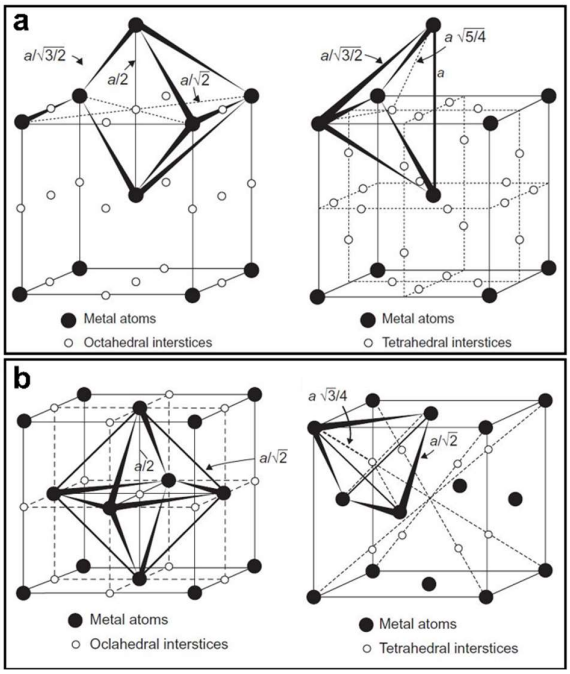

Figure 2-2: Unit cell crystallographic structure of BCC (a) and FCC (b) with. Octahedral and tetrahedral interstitial sites [20].

The presence of even a relatively low concentration of carbon in the lattice significantly influences the mechanical properties, microstructure and transformation behavior of ferrite.

Austenite, with only carbon as an alloying element, is not stable below 723 °C. The maximum solubility of carbon is 2.14 mass % which occurs at 1147 °C. This higher solubility of austenite compared to ferrite is due to the larger FCC interstitial positions. There are a total of four octahedral and eight tetrahedral sites and carbon occupies at octahedral sites. The maximal radius of an atom which could fit within these interstitial sites without distortion of the lattice is limited to 0.053 nm [18,19]. Therefore, transformations involving austenite are very significant for steel hardening. A Supersaturated solid solution of carbon in iron is formed by rapid quenching from the austenite region to room temperature [21]. The δ-ferrite has no practical importance for the scope of this thesis, so it will not be discussed further.

Cementite (Fe_3C) forms when α-ferrite or γ-austenite exceeds their solubility. It is a chemically defined structure with the formula Fe_3C. This means that cementite contains 75 at. % iron and 25 at. % carbon. With the molar mass of iron (M_{Fe}=55.845 g.mol^{-1}) and that of carbon (M_C=12.01 g.mol^{-1}) the mass content of carbon in cementite is 6.67 ma. % which corresponds to the value given

in Figure 2-1. Cementite is mechanically very hard and brittle; it exhibits great hardness (the Vickers hardness ranges from 750-1580 depending on temperature and alloying elements) [22]. The strength of some steels is greatly enhanced by its presence, depending on its amount and distribution. Cementite has an orthorhombic lattice structure with a large lattice parameter of a = 0.50915 nm, b = 0.67446 nm and c = 0.45276 nm, explaining its hardness [19,22].

2.2 Structural Transformation in Steel

Technical heat treatment processes of heating (austenite formation) and cooling (austenite transformation) can be explained in special non-equilibrium diagrams under simplified conditions of theoretically infinite slow heating and cooling rates. However, in practical conditions characterized by finite heating and cooling rates, the transformation temperatures undergo variations. Hence, time-temperature-austenitization (TTA) diagrams are employed to illustrate the kinetics of austenite formation. The kinetics of the transformation of supercooled austenite are further described using time-temperature transformation (TTT) diagrams and continuous cooling transformation (CCT) diagrams [23].

When steel is cooled slowly from the austenite state, it transforms to ferrite and cementite. In most cases, depending on the carbon content, a portion of these two phases creates a lamellar structure at room temperature known as pearlite. Ferritic and pearlitic transformation caused by slow cooling is not practically important for the case of carburizing, therefore it will not be discussed further. Conversely, during rapid cooling from the austenitic state, structures such as bainite and/or martensite are formed, representing the desired final structure for carburized parts.

2.2.1 Phase Transformation During Heating

In the majority of cases, the heat treatment of steels initiates with the heating process into the austenitic field, including carburizing. Consequently, the austenitization step holds critical importance as it profoundly influences the properties of the final product.

2.2.1.1 Austenite Formation

Properties of austenite such as grain size and homogeneity of alloying elements have significant influence on transformation behavior, microstructure, and mechanical properties of the final product [19,24,25].

Austenitization starts with heating from ferritic state. Ferrite/carbides with lamellar or spherical interfaces are preferable austenite nucleation points and the mechanism of nucleation is heterogeneous [26,27]. Figure 2-3 shows the 2D phase field simulation of nucleation of austenite near spherical and lamellar cementite. In the top figure, austenite nucleates near one of the spherical cementite particles and grows towards the second cementite particle via ferrite grain boundary. In the bottom image, nucleation of austenite occurs at the boundary of the ferrite colony.

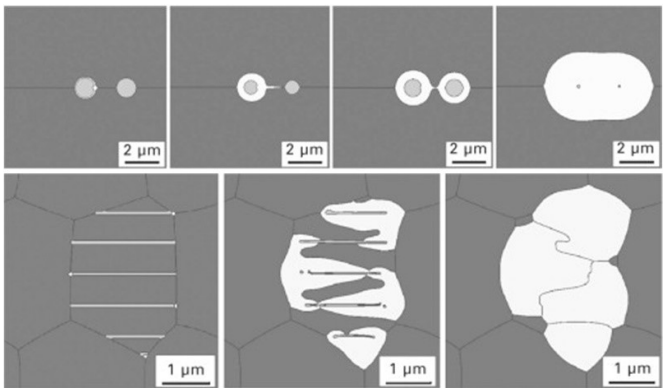

Figure 2-3: 2D phase field simulation of austenite nucleation and growth near globular cementite (top) and lamellar cementite (bottom) located at a ferrite grain boundary. White phase is austenite, dark grey phase is ferrite and light grey is cementite. [28,29].

Although there are some special cases, especially for higher carbon levels, where not all carbides can be dissolved, the aim of all hardening processes including carburizing is to form a solid solution in order to adjust the supercooled state. This is accomplished by austenitization and choosing suitable cooling condition.

Austenite formation depends on temperature and time, which can be obtained from TTA diagrams. They describe changes in grain size, homogenization of austenite crystals and dissolution of carbides [23]. An example of TTA diagram and a description of the transformation can be found in appendix section 10.1.1.

2.2.2 Phase Transformation Upon Cooling

Two main transformations upon cooling are bainitic and martensitic transformations. The degrees of each transformation can be illustrated by continuous cooling transformation (CCT) diagrams as a function of time for consistently decreasing temperature, as desired for most hardening operations including carburizing. Details of the CCT diagram can be found in appendix section 10.1.2.

Among these two, martensitic transformation holds particular importance in the hardening of steels, including its crucial role in carburizing processes, as it presents a hard, wear-resistant, and fatigue-resistant structure. Consequently, in this thesis, bainitic transformation will be explained briefly, while martensitic transformation will be discussed in detail.

2.2.2.1 Bainite Transformation

An intermediate cooling rate during cooling has the potential to form a certain amount of bainite. Bainite is a dual-component microstructure comprising fine aggregates of ferrite plates and cementite particles. The specific microstructure of bainite depends on the transformation temperature. While the formation temperature of bainite is influenced by alloying elements, and there is no inherent limit to the bainite start temperature, it is commonly observed that bainite formed between approximately 550 °C to 400 °C is termed upper bainite. In contrast, bainite formed between 400 °C to 250 °C is referred to as lower bainite [21,30].

In upper bainite, carbon-rich components, such as cementite, martensite, and/or retained austenite, align between the laths of the ferrite in which carbon is rejected during the growth. In lower bainite, carbides precipitate within the ferrite plates. Both types of bainite can appear in the microstructure simultaneously. It is very difficult to differentiate these two microstructures because of their very fine structure. Thus, transmission electron microscopy (TEM) is usually applied to differentiate upper bainite and martensite [30,31]. Figure 2-4 presents the TEM micrographs of two structures.

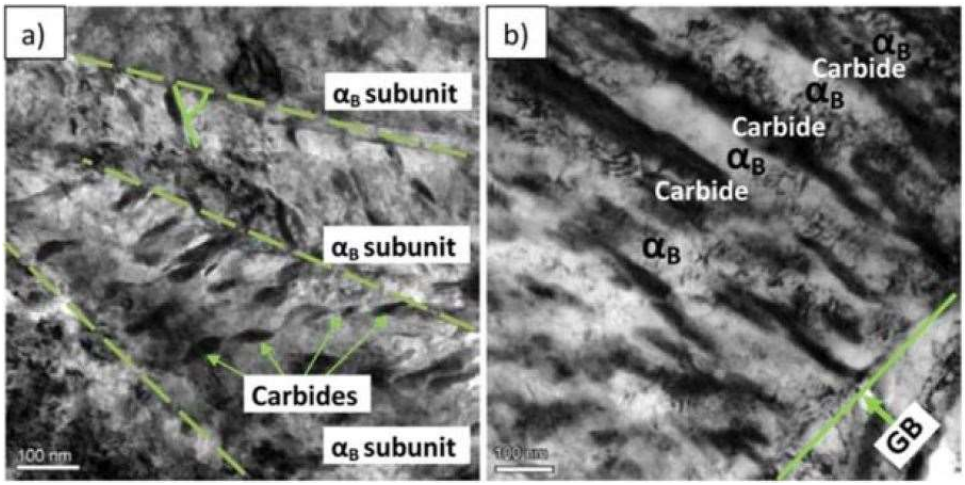

Figure 2-4: TEM micrographs of 100Cr6 steel (a) lower bainite, (b) upper bainite; α_B: bainitic ferrite, θ: cementite and GB: grain boundary [30]

2.2.2.2 Martensite Transformation

The martensite transformation takes place during quenching of the high-temperature austenitic phase. It is a non-equilibrium phase that results from a displacive transformation of austenite; wherein diffusional movement of atoms is either not involved or occurs very minimally [17,25]. The transformation causes a volume expansion accompanied by a large shear. This volume expansion depends on alloying elements, mainly carbon, and varies from 1.9 % to 3.1 % [32]. The consequential volume expansion can generate high residual stresses in the final component, a topic that will be further explored in subsequent sections.

Martensite has a body centered tetragonal (BCT) lattice formed by polymorphic transformation from FCC austenite. This transformation is called “Bain model” [33]. More detailed information about crystal structure of martensite and kinetics of martensitic transformation can be found in appendix section.10.2.

2.2.3 Retained Austenite

Austenite or γ-iron is a high-temperature, face centered cubic (FCC) structured phase having a lattice parameter of 0.3573 nm for pure iron at room temperature. Addition of alloying elements, particularly interstitials like carbon; and changes in temperature affect the austenite lattice parameter. One of the models that describe this relation is the model developed by Onink from

neutron diffraction experiments [34]. According to the model lattice parameter of austenite is formulated as

$$a_\gamma = (0.363067 + 0.000783x_C^r) \cdot [1 + (24.92 - 0.51x_C^r) \cdot 10^{-6} \cdot (T - 1000)] \qquad \textit{Eq. 2-1}$$

Where x_C^r is at. % carbon and *T* is the temperature in K. This model is used to determine the carbon content in steel at high temperature. A more detailed discussion of its application and implications will be presented in section 5.1 and 5.2.

With higher carbon contents and the presence of other alloying elements, the M_s and M_f temperatures tend to decrease. This can lead to an incomplete martensitic transformation, resulting in the presence of metastable austenite, so called *retained austenite.*

The retained austenite is likely to lower the hardness and tensile strength of component [35]. Under conditions of elevated mechanical strain/stress or a continued decrease in temperature relative to its quenching temperature, retained austenite has the potential to transform into martensite [36]. This transformation-induced volume change may be significant enough to initiate material cracking [37].

Conversely, empirical evidence suggests that retained austenite can enhance fatigue resistance in specific applications. In the context of carburized steels, an observed correlation indicates that increasing retained austenite fractions may enhance bending fatigue [38]. Increasing the austenite content is also associated with improved impact strength, attributed to the higher toughness of the austenitic phase [37].

Furthermore, the transformation of retained austenite to martensite during deformation introduces a mechanism known as transformation-induced toughening, potentially enhancing fatigue resistance through crack blunting and increased plane strain fracture toughness [39].

In summary, the influence of retained austenite on the material's properties depends on factors such as the amount, morphology, distribution, and application. Literature indicates that the presence of retained austenite can have both positive and negative effects.

2.3 Diffusion in Solids

2.3.1 Basic Diffusion Laws

Transportation of individual atoms in materials via random migration steps is called diffusion. While liquids and gases have a diffusion rate in the range of millimeters or even centimeters per second, transport in solid materials is rather slow [40].

According to the classical observations of Fick, a concentration gradient acts as a driving force for diffusion and causes a flux of particles to move along it. Thus, this gradient becomes smaller in time and, finally, is eliminated. The diffusion flux density J_D [cm^{-2}/s] is defined as the number of particles that pass through a unit area in a unit of time and it is proportional to the concentration gradient [41]. Fick's first law can be written as follows for 1 and 3 dimensions;

1D $$J_D = -D\frac{d_c}{d_x}$$ *Eq. 2-2*

3D $$J_D = -D\nabla_c \text{ where } \nabla_c \text{ is } (\frac{\delta_c}{\delta_x}, \frac{\delta_c}{\delta_y}, \frac{\delta_c}{\delta_z})$$ *Eq. 2-3*

The minus sign indicates the flux to be transported from the higher to the lower concentration, i.e. opposite to the concentration gradient [41]. Here, *c* represents the concentration, as d_c/d_x denotes the concentration gradient. The constant *D* is the diffusion coefficient with units of cm^2/s or m^2/s and depends on the temperature and alloy concentration. It described by means of an Arrhenius equation;

$$D = D_0 e^{-\frac{Q}{RT}}$$ *Eq. 2-4*

with Q = activation energy ($\frac{J}{mol}$), R = gas constant ($8.314\frac{J}{mol \cdot K}$) *T* = absolute temperature (K), and D_0 = frequency factor ($\frac{m^2}{s}$).

In industrial practices such as low pressure carburizing, the concentration gradient changes with time. To deal with this situation, planes A and B of unit area are considered which are separated by a small distance dx. Also the increase rate of the concentration of atoms (d_c/d_t) in the space between the two planes were taken because of the difference between the flux into and out of the volume element. The flux across one plane is J_x and across the other J_x+dJ_x, so the difference being dJ_x. During time d_t, this flux difference leads to a deficiency of the number of vacancies within the volume element by $dJ_x\, d_t$, and this equals $-d_c d_x$. Therefore, this gives the second law of Fick [42];

1D $$\frac{\delta_c}{\delta_t} = D\frac{\delta^2 c}{\delta x^2}$$ *Eq. 2-5*

3D $$\frac{\delta_c}{\delta_t} = D(\frac{\delta^2 c}{\delta x^2}, \frac{\delta^2 c}{\delta y^2}, \frac{\delta^2 c}{\delta z^2})$$ *Eq. 2-6*

Fick's second law of diffusion states that the compositional change rate is proportional to the rate change of concentration gradient rather than to the concentration gradient itself. This is the reason why, it often takes very long time to reach uniform composition via diffusion. As equilibrium is approached and composition gradients flatten out, $\delta^2 c/\delta x^2$ goes to zero, and hence δ_c/δ_t goes to zero. Thus, although the composition gradient may be large at the start of a diffusion process, it is very small towards the end of the process [42].

2.3.2 Diffusion in Iron

The kinetics of diffusion in iron can be described based on the existing phases and the diffusing element. In this section, fundamental concepts on this topic will be presented, with a specific focus on carbon diffusion in austenite and cementite. This emphasis is made due to their high relevance in the context of low-pressure carburizing.

Figure 2-5 shows the atomic model of diffusion. The thermally activated jump of atoms constitutes the mechanism of diffusion in solids. Two main categories of atoms are identified: interstitial and substitutional. Substitutional atoms, such as chromium, nickel, and manganese, have similar diameters to iron; while interstitial atoms, like carbon, nitrogen, and hydrogen, have smaller diameters than iron.

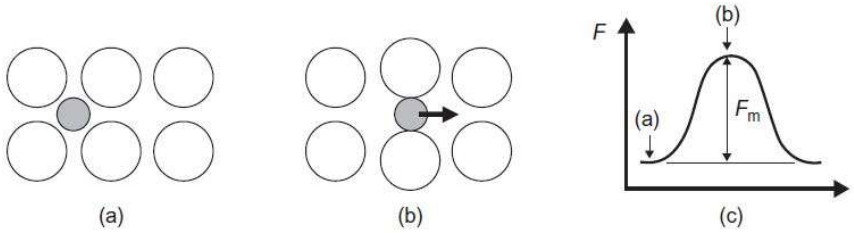

Figure 2-5: Atomic model of diffusion [42]

The jump motion of substitutional atoms is more difficult as the neighboring lattice point of a foreign atom is usually occupied [41]. In the case of interstitial atoms, such as carbon in steel during low-pressure carburizing, it is easier to visualize that a foreign atom can move to a next neighbor interstitial site through sufficient thermal activation.

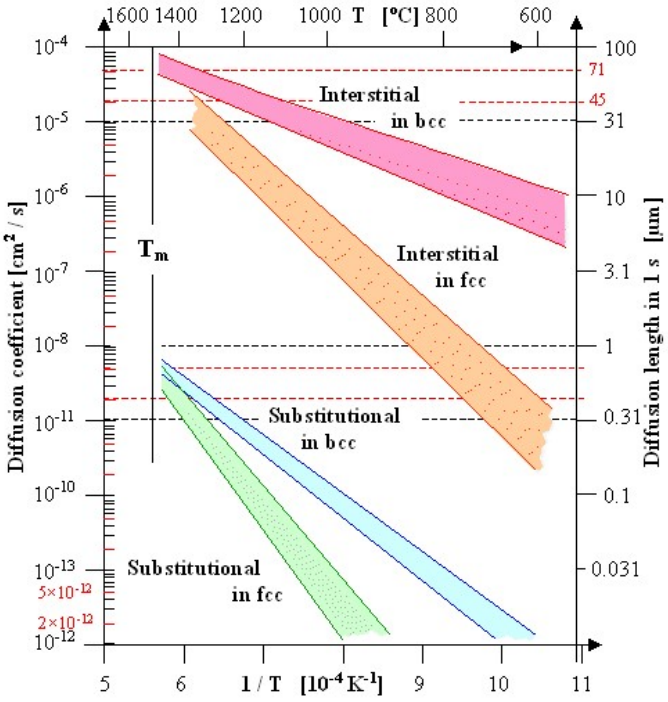

Figure 2-6: Diffusion coefficient of interstitially and substitutionally dissolved elements in BCC and FCC iron [43].

If the energy barrier required for diffusional jump of the atom (F_m) is exceeded, there is a probability of the atom changing the position. Figure 2-6 shows the diffusion coefficient of interstitially and substitutionally dissolved elements in BCC and FCC iron. It is apparent that the interstitial atoms can diffuse several orders of magnitude faster than the substitutional atoms because of their low activation energy. The diffusion rate in BCC lattice is significantly higher than that in FCC lattice at the same temperature because of the higher frequency factor. The high frequency factor can be explained by the higher number of the octahedral interstices over interstitial sites and lower pack density in BCC lattice [30].

As Figure 2-7 shows, diffusion coefficient increases as activation energy decreases if carbon content in austenite increases at constant temperature. Several factors contribute to this phenomenon. Free energy gradients, rather than concentration gradients, are the driving force of diffusion; thus, there is a thermodynamic factor related to the way in which the activity of carbon depends on concentration. However, this does not explain the whole phenomenon since carbon atoms repel each other in close proximity, introducing an additional factor promoting diffusion along the concentration gradient. Additionally, the atoms cause a concentration-dependent dilatation of the lattice. As a result, the diffusion coefficient is often expressed empirically with unit of m^2/s as [21,44]

$$D_c^{\gamma} = 4.53 \cdot 10^7 \left[1 + y_c(1 - y_c)\frac{8339.9}{T}\right] \cdot exp\left\{-\left(\frac{1}{T} - 2.221 \cdot 10^{-4}\right)(17767 - 26436y_c)\right\} \quad \textit{Eq. 2-7}$$

where y_c is the ratio of carbon atoms to all other atoms in the material.

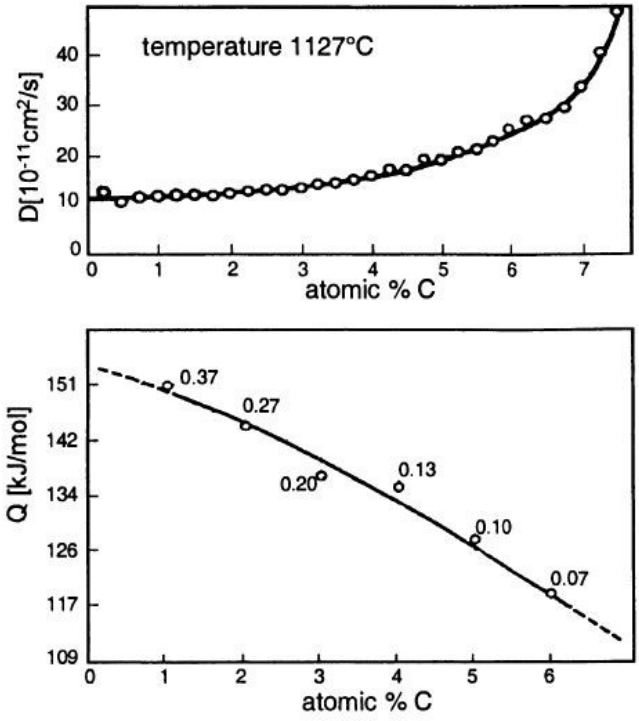

Figure 2-7: Composition dependence of activation energy and of the diffusion coefficient as a function of C in austenite [45].

In order to predict the distribution of carbon content over the depth of the material accurately for carburizing, an exact determination of the diffusion coefficient is necessary. There are more rigorous approaches to define the mechanism of diffusion of carbon in austenite, which defines the activation energy for diffusion as about 150 kJ/mol at a low carbon concentration [21,46,47]. One of the approaches that is used in the simulation program for the LPC developed by Steinbacher [48] is the model of Smith [49] and Wells [45] as described by Leyens et al. [50,51]. Diffusion coefficient of carbon in austenite in this approach can be described as

$$D = D_0 \cdot e^{\left[\left(\frac{4300}{T} - 2.63\right) \cdot c^{1.5}\right]} \left[\frac{cm^2}{s}\right]$$

$$D_0 = e^{-\left[\frac{18900}{T} + 0.38\right]} \left[\frac{cm^2}{s}\right]$$

Eq. 2-8

$$D = 0.68 \cdot e^{\left[\left(-\frac{18900}{T}\right) + \left(\frac{4300}{T} - 2.63\right) \cdot c^{1.5}\right]} \left[\frac{cm^2}{s}\right]$$

Eq. 2-9

The provided equations are derived from experiments conducted on plain Armco iron, which is nearly pure iron. Consequently, additional corrections were implemented on the diffusion coefficients to account for the impact of alloying elements. The influence of alloying elements on the diffusion of carbon has been extensively discussed in the literature [52,53]. The influence of certain alloying elements typical in case-hardening steel on carbon diffusion is shown in Figure 2-8.

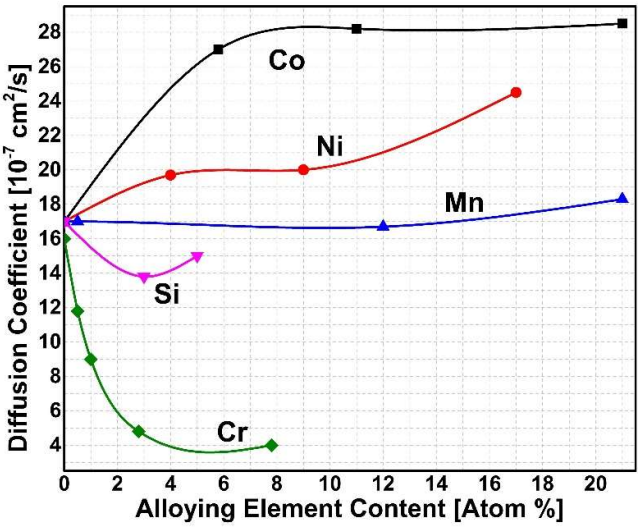

Figure 2-8: Effect of alloying elements on the diffusion coefficient of C in austenite [48].

The steel used to gather this data was carbon steel having 0.4 ma. % carbon and temperature was 1200 °C. As mentioned earlier in Eq. 2-4, the diffusion coefficient is highly sensitive to temperature. Since diffusion involves the thermally activated movement of atoms, the temperature dependence

is inherent and straightforward. Thermally activated processes always exhibit a temperature dependent Boltzmann factor $e^{\frac{-Q}{kT}}$ [41].

Figure 2-9 shows experimental results depicting the diffusion of carbon and nitrogen in iron as a function of temperature [40,54–56]. Carbon diffusion in cementite is a crucial consideration for low-pressure carburizing. In the boost step of the process, the very high carbon activity can lead to rapid reaching of the solubility limit in austenite, causing cementite to form at the material's surface. Accurately predicting carbon intake necessitates a dependable description of carbon diffusion in cementite.

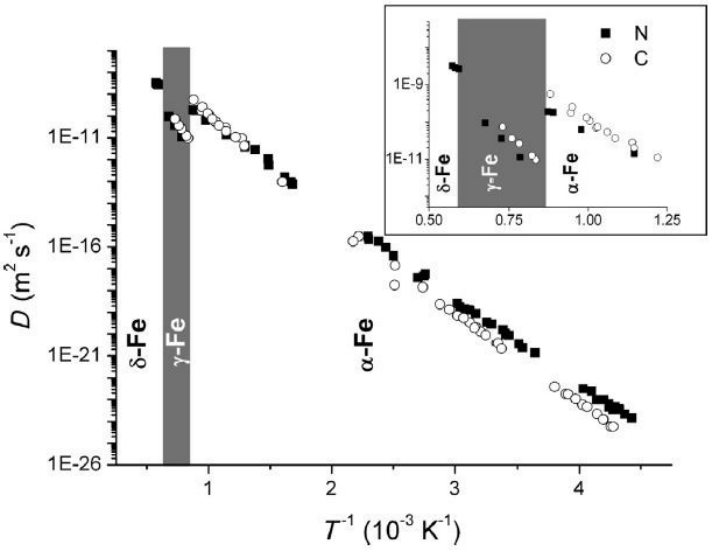

Figure 2-9: Effect of temperature on the diffusion coefficient of carbon and nitrogen [40,54–56].

A diffusion of free carbon occurs also at interstitial sites for cementite [57,58]. The diffusion coefficient is calculated according to the following equation [48,57].

$$D = 0.018 \cdot exp\left(-\frac{172800}{RT}\right) \; in \frac{cm^2}{s} \qquad \textit{Eq. 2-10}$$

A comparison of the diffusion coefficient for carbon in cementite and in austenite is shown in Figure 2-10 based on carburizing experiments in pure iron. Diffusion is accelerated in both phases with increasing temperature. It can also be seen that the diffusion coefficient of carbon in austenite is approximately 3 orders of magnitude higher than that of carbon in cementite.

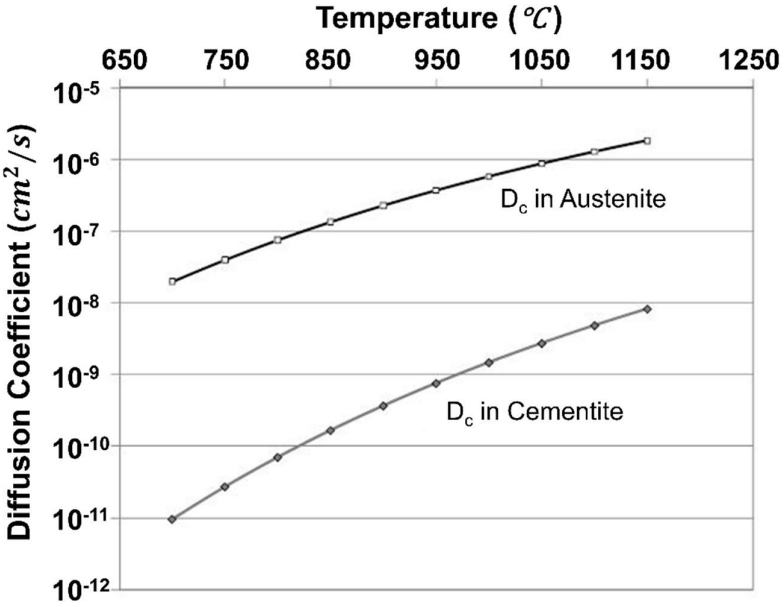

Figure 2-10: Representation of the diffusion coefficient of carbon in iron cementite and austenite [48]

2.4 Carburizing in Gas Atmosphere

Gaseous carburizing is a thermochemical process that is conducted in a special atmosphere inside the carburizing furnace and increases the carbon content of the surface region of materials via diffusion [2]. The gas atmosphere inside the furnace is generated by mixing of hydrocarbon gases and an oxidizing gas. Most widely used hydrocarbon gases in the process are natural gas (containing mostly methane (CH_4)), propane (C_3H_8) or butane (C_4H_{10}); and oxidizing gases are air, O_2, H_2O and CO_2 [59,60]. Combination of different gases creates a different carbon monoxide content in the furnace atmosphere at a given temperature. The assumption is that the carburizing is taking place as a direct result of the CO content in the atmosphere [59]. Therefore, CO content should be controlled in order to achieve uniform carburizing conditions [2].

Generally for gas carburizing, there is an excess of carbon. Therefore, the furnace atmosphere must be controlled in order to eliminate soot formation at the furnace walls. The pre-request for this control is the determination of the carbon potential of the atmosphere which is defined as the amount of carbon that sample will reach when chemical equilibrium is maintained with the surrounding gases. It depends on the alloy concentration, furnace temperature, and the CO content of the carburizing atmosphere. Depending on the oxidation gases used, knowledge of dew point of water vapor or partial pressure of carbon dioxide or partial pressure of oxygen is also required to determine the carbon potential since these three atmosphere constituents are by-products of carburizing reactions [2]. Since the main focus of this thesis is low pressure carburizing, details of the ambient pressure gas carburizing reactions and carbon potential are not further described here (see appendix section 10.4 for more details).

When the carbon flux reaches the steel surface, carbon content in solution increases and carbon diffuses through the steel sample according to Fick's laws. These laws were explained in section

2.3.1. Based on Fick's law, the depth of the carbon diffusion, CD, can be calculated using the approximated formula presented by Wünning [61].

$$CD = \frac{0.79 \cdot \sqrt{(D \cdot t)}}{0.24 + \frac{c_L - c_C}{c_S - c_C}} - 0.7 \cdot \frac{D}{\beta} \quad \textit{in cm} \qquad \textit{Eq. 2-11}$$

where t is the carburizing time in second, c_L is the carbon limit in the depth CD in ma. %, c_C is the core carbon content in ma. %, c_S is the surface carbon content in ma. %, D the diffusion coefficient in cm^2/s, and β is the carbon transfer coefficient in cm/s.

One of the most important side effects of gas carburizing is the occurrence of oxidation. Internal oxidation and the associated metallurgical problems cannot be completely avoided during industrial carburizing [62]. Alloying elements with a higher affinity with oxygen, such as titanium, silicon, manganese and chromium, form oxides in the surface layer. These oxides grow during the process, leading to a decrease in alloy content in austenite. Surface oxidation strongly reduces the strength and hardenability of the component, as the critical cooling rate for quenching is no longer achieved [60,63]. However, the lower diffusion rate of oxygen in steel and the interaction of oxygen atoms with alloying elements at the surface prevent oxygen from penetrating too deeply into the steel. Therefore, Oxide layer detected in commercial case-hardening steels are typically less than 25 µm [63].

2.5 Low Pressure Carburizing

In this section, modern low pressure carburizing and process parameters will be explained. Brief information on the early development of the process can be found in appendix section 10.3.

2.5.1 Modern Low Pressure Carburizing

The LPC processes in current applications start with evacuating the furnace until approximately pressure of $5 \cdot 10^{-2}$ mbar or lower. The furnace is then filled with protective gas, mostly nitrogen, and heated to the process temperature. The protective gas is used to enhance the efficiency of heating through convection rather than a vacuum. Before reaching the process temperature, the protective gas is evacuated from the furnace, and the final stages of heating are conducted under vacuum conditions. The process is generally conducted at 850 °C–1050 °C [2].

When the process temperature is reached, hydrocarbon gas is introduced into the furnace with several nozzles. This step is called the boost step. The reason for using several nozzles is to evenly distribute the process gases in the entire furnace as fast as possible. Samples are strategically placed in the furnace to ensure they are positioned in the middle of the directed gas flow between the vacuum pump and nozzles. The inlet pressure of the hydrocarbon gas, which refers to the pressure of the gas directed to the chamber with nozzles (not the pressure inside the chamber), is adjustable and depends on the load and furnace volume. It is, for example, generally 1.5-2 bar for

acetylene. Amounts of process gases are controlled with mass flow controllers and mass flow controllers can be regulated based on target pressure by process control unit [48].

The description of the gas flow is very difficult due to the complexity in the structure and lack of precise numerical data. There are several simulation trials in the literature to address this issue. For example, Yada and Watanabe proposed an approach to simulate both gas flow and fluid solid interaction by using computational fluid dynamics software Ansys Fluent 13 [7]. They utilized the Poiseuille flow solution to investigate the velocity profile of the gas flow and found a good agreement between calculated data and theory. Also, Buchholz et al. worked on the simulation of acetylene gas pyrolysis by using Detchem and Fluent software, and they also found a good agreement with experimental results [64].

The duration of the boost step is generally a few minutes depending on the surface area of the component. After that, the gas supply is interrupted and the remaining gas molecules are pumped out to initiate the diffusion step. The vacuum line is generally built as a single outlet to maintain uniform gas flow in one direction [48]. The duration of the diffusion step is generally at least ten times that of the boost step but it is highly dependent on the load, the number of boost steps and the required carburizing depth. These boost and diffusion cycles are repeated as many times as needed. When the required carbon content is reached, the temperature is often reduced from the process temperature to the hardening preparation temperature which helps to reduce distortion caused by quenching [2]. This hardening preparation temperature is adjusted based on the carbon content and gradient to maintain the austenitic state and avoid any transformation before quenching, typically in the range of 830 °C – 880 °C. As a final step, the sample is quenched with high pressure gas or in oil bath [65,66]. Figure 2-11 shows a schematic representation of the LPC with three boost-diffusion cycles.

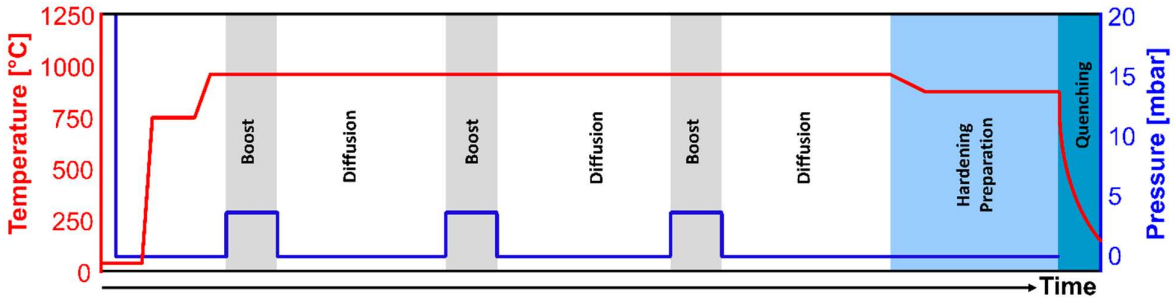

Figure 2-11: Schematic representation of the LPC with 3 boost-diffusion cycles

Compared with oil quenching, gas quenching is increasingly demanded due to its ecological and economic advantages. Non-reactive gases are used as a quench media, leaving no residue on the parts, which results in cost savings for cleaning [67]. Gas quenching also offers the advantage of lower distortion in the parts. Additionally, the gas velocity can be adjusted using nozzles to meet specific requirements [68,69]. However, it is worth noting that gas quenching may not be suitable for large components due to slower cooling rates.

In gas carburizing, carbon potential control can be carried out by an oxygen sensor placed in the furnace. Additionally, in-situ diffusion calculations can be employed to calculate the actual state during heat treatment. However, low-pressure carburizing is conducted under non-equilibrium conditions, which makes carbon potential control not possible with the techniques commonly used. Therefore, the duration and repetition of the boost and diffusion cycles in LPC are typically determined beforehand based on previously conducted trial and error experiments with known carbon profiles or by using diffusion calculations. This approach requires high-quality input variables. [48]. Altena proposed a method to regulate the carburizing potential of the LPC process. According to this approach, hydrogen sensor can be used to determine the hydrogen content of the exhaust gas, providing insights into gas conversion [70]. However, it was found that the technology is more useful for process monitoring than for effectively controlling the carburizing process. Therefore, carbon mass flow density (m_c) is the most important parameter in LPC. It is defined as the quantity of carbon introduced into the material per unit of surface and time ($\frac{g\cdot}{m^2 h}$). This parameter allows a direct comparison with gas carburization [65].

2.5.2 Development of the Microstructure During Low Pressure Carburizing

During low-pressure carburizing, the surface of the sample undergoes carbon enrichment. The diffusing carbon provided by the carburizing medium results in a gradual increase in the austenite lattice parameter. At the end of the process, during quenching, the martensitic transformation can lead to different amounts of retained austenite, depending on the surface carbon content and cooling rate. The cooling conditions of the process significantly impact the final mechanical properties of the material, with fatigue properties being particularly influenced under different conditions [71]. A higher case carbon content, caused by excessively long carburizing, increases carbide formation in the surface layer, ultimately negatively affecting the mechanical properties of the material [72].

During low-pressure carburizing, another phenomenon known as manganese effusion occurs. The low pressure within the process chamber causes the vapor pressure of manganese to be exceeded at typical carburizing temperatures (930°C – 1000 °C), leading to the depletion of manganese from the surface layer of the component. This results in a reduction in hardenability within the surface layer of the components [3]. The austenitizing temperature is also a crucial process parameter for the self-adjusting surface layer. Large austenite grains can lead to the formation of coarser martensite needles, degrading the mechanical properties of the component [73]. Therefore, especially in long-lasting processes where a greater carburizing depth is required, the occurrence of coarse-grained martensite can be a problem. This issue can be eliminated by single hardening. This process will be explained in detail at section 2.5.3.2.

2.5.3 Process Parameters of Low Pressure Carburizing

2.5.3.1 Process Gases

In current industrial application, acetylene (C_2H_2) and propane (C_3H_8) are the most common and advantageous gases for the LPC [74].

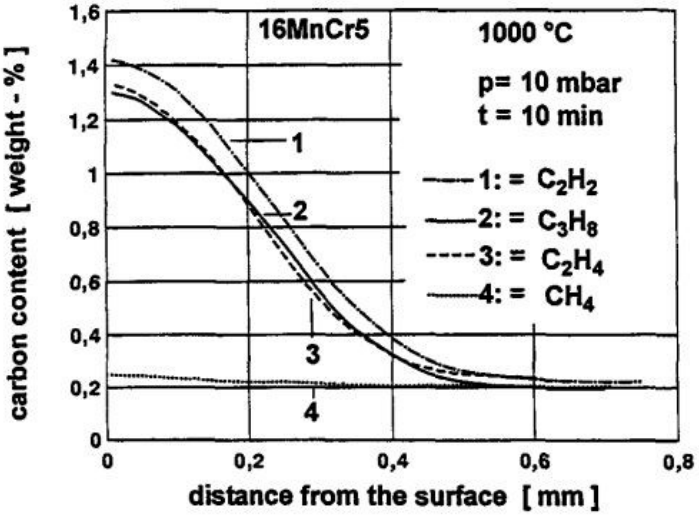

Figure 2-12: Carbon profiles of 16MnCr5 steels after the LPC by different gases [75].

There are several studies about comparison of efficiency of both gases. For example, Gräfen and Edenhofer compared the effect of different process gases on the carbon profiles of 16MnCr5 steel [75]. The carburizing temperature and pressure were 1000 °C and 10 mbar, respectively, and the process involved a single 10-minute boost step. Figure 2-12 shows the result.

According to the results, samples carburized with acetylene achieve a higher surface carbon content and carburizing depth compared to those treated with other gases. The study concluded that the carbon transfer rate of acetylene is approximately 20% higher than that of propane.

Experiments conducted in a thermo-balance by Steinbacher demonstrated differences in the mass increase of samples carburized with propane or acetylene, as shown in Figure 2-13 [48].

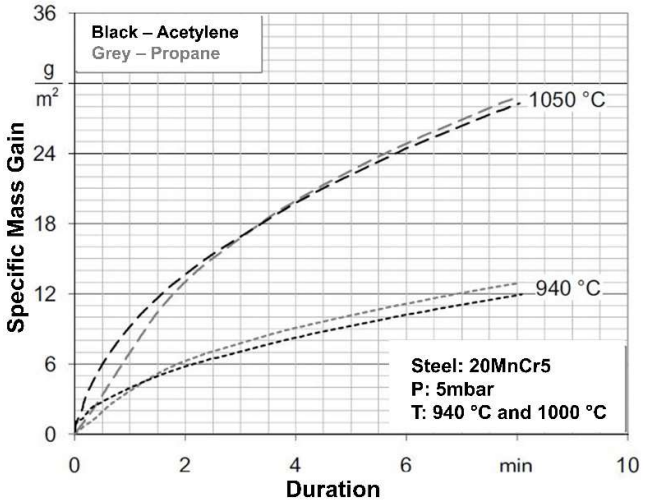

Figure 2-13: Specific mass gain of 20MnCr5 carburized with acetylene and propane at different temperatures [48].

The results are very close to each other. However, it is noticeable that in the early stages, the mass increase of the sample carburized with acetylene is higher than that of the sample carburized with propane. For longer carburizing times, the mass gain of the sample carburized with propane surpasses that of acetylene. According to Steinbacher, the pyrolysis of propane in the low-pressure atmosphere, which is more complex compared to acetylene, results in a delayed carbon uptake in the initial step.

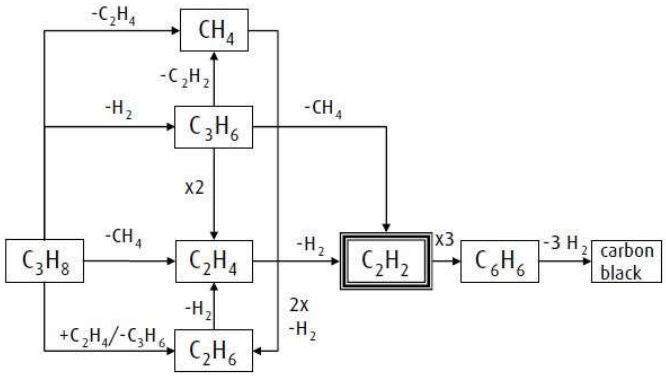

Figure 2-14: Pyrolysis of propane [48,76]

Figure 2-14 illustrates the reaction network of homogeneous propane pyrolysis during low-pressure carburizing, as derived from experimental data obtained through investigations conducted in a semi-industrial test reactor by Graf et al [76].

As depicted in the figure, the breakdown of propane occurs through various reaction components, with the proportion of acetylene generated in the pyrolysis remaining below 20%. Consequently, only a fraction of the carbon supplied in the form of propane is accessible for the carburizing process [76].

The decomposition reaction of acetylene is given in Eq. 2-12, and unlike propane, it does not undergo decomposition into different hydrocarbon gases. It is worth noting that the actual acetylene

decomposition process is considerably complicated and varies depending on the temperature range. For more in-depth information on the pyrolysis of both acetylene and propane, readers are directed to the PhD thesis by Gräfen [77] and the article by Khan et al.[78]

$$C_2H_2 = 2C + H_2 \qquad \textit{Eq. 2-12}$$

Longer boost times in low pressure carburizing can cause carbide formation at the surface and excessive carbide formation is generally detrimental for mechanical properties. Therefore, in current applications, carburizing pulses (boost steps) in the minute range are usually preferred, within which the carbon availability of acetylene outweighs that of propane [60], making it the more advantageous choice in most industrially relevant applications. Additionally, acetylene decomposition into carbon and hydrogen is a catalytic reaction, necessitating the presence of an iron catalyst for the breakdown. Conversely, propane is thermally decomposable, initiating the decomposition reaction directly upon introduction into the hot zone of the vacuum furnace. This eliminates the carbon's ability to react with the steel surface and creates undesirable hydrocarbon contamination [79,80]. Furthermore, it is very unlikely, due to low pressure, that acetylene molecules and their partly dissociated by-products combine to form long chain hydrocarbons [81]. Moreover, acetylene has a higher average carbon flux than propane. A Schematic representation of acetylene decomposition can be seen in Figure 2-15.

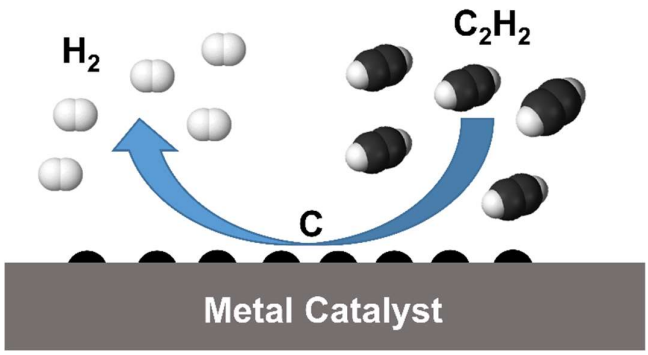

Figure 2-15: Pyrolysis of acetylene

Along with the proper selection of the process gas, the quantity and flow rate of the gas play crucial roles in achieving the desired material properties. Rokicki and Dychton conducted a study on the impact of the acetylene flow rate [82]. Their findings indicated that excessive acetylene usage in the carburizing atmosphere of the furnace restricts the diffusion process of carbon into the material, leading to carbide formation on the surface. Conversely, insufficient acetylene amounts result in a diminished carburizing effect. They found a 250 l/h flow rate as an optimum value for the best results for the carburized surface area that they used. It's important to note that this optimal value will vary based on factors such as furnace volume, sample complexity, and carburized surface area. Moreover, Wolowiec-Korecka et al. suggested that constantly reducing flow rates depending on the individual boost step can significantly reduce the consumption of carbon donor gas. They gradually

reduced the usage of acetylene in the boost step and found out that gas consumption was 46% lower than the usage of constant flow rate [83].

2.5.3.2 Temperature and Pressure

The LPC processes are typically carried out within the temperature range of 920 °C to 980 °C. In certain applications, particularly when a greater carburizing depth is required, temperatures may be elevated to exceed 1000 °C. The choice of higher process temperatures results in a significant reduction in process time, contributing to cost reductions. However, this approach introduces some undesirable metallurgical problems, including grain growth in conventional case-hardening grades. The utilization of more advanced steel grades, featuring classical micro alloying elements like titanium and niobium, as well as less commonly used micro alloying elements such as aluminum, can effectively mitigate grain growth, allowing these steels to surpass temperature limits.[84,85].
In cases where the steel does not belong to advanced grades, a suitable approach involves slow cooling to room temperature after carburizing, followed by rapid reheating to the austenitizing temperature and subsequent quenching. During this reheating phase, coarse-grained martensite transforms into fine-grained austenite through re-austenitization, resulting in a fine-grain martensite structure at the end of the process. This particular process is referred to as single hardening. Additionally, low-temperature carburizing is a feasible option in certain situations. For stainless steels containing chromium, it is essential to eliminate carbide formation to preserve corrosion resistance. Therefore, the carburizing of these steels is carried out under the A_{cm} temperature.
Low-pressure carburizing is typically carried out within the pressure range of 2-10 mbar. Variations within this range do not exert a significant impact on the process. However, pressures exceeding 25 mbar can result in increased molecular reactions, leading to soot formation [86]. In industrial applications, pressures are generally maintained below 25 mbar to avoid issues related to soot formation. For complex geometries, the use of lower pressure and a dynamic exchange of gas proves advantageous in reaching less accessible areas, such as blind holes.

2.5.3.3 Quenching Parameters

Quenching is a critical step in the LPC process to achieve the desired hardness and structure while minimizing unwanted distortion. As mentioned before, gas quenching is the preferred quenching technique due to its abilitly to create lower distortion in the parts and the cleanness of the process. Figure 2-16 shows the comparison of cooling rates of various quenching techniques.

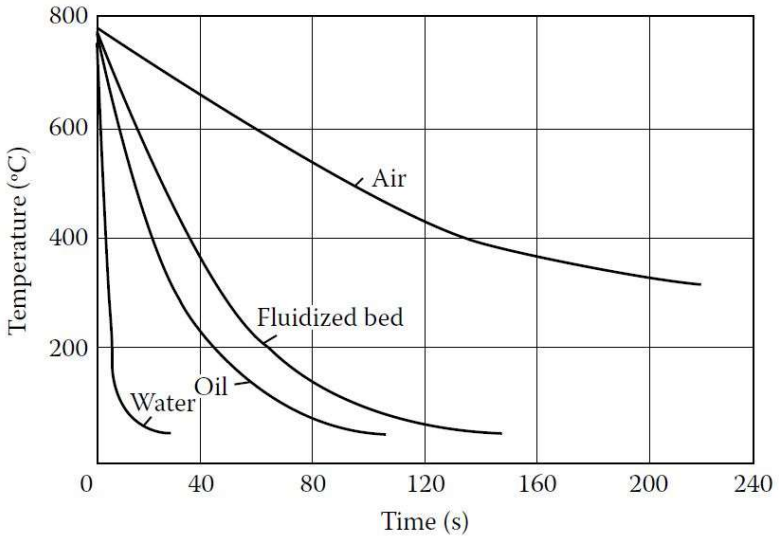

Figure 2-16: Comparison of cooling curves for 16 mm diameter steel bars cooled in various quenching media. [87].

Inert gases are used as a quench media and most widely used ones are argon, nitrogen, helium, and hydrogen [88]. Their heat transfer coefficients are given below in the Table 2-1.

Table 2-1: Heat Transfer Coefficient Variation with Respect to Parallel and Perpendicular Gas Flow and Gas Selection[a] [87].

Gas	**Perpendicular Flow Impingement**		**Parallel Flow Impingement**	
	h_{gas} (W/m^2K)	h_{gas}/h_{argon} x 100 (%)	h_{gas} (W/m^2K)	h_{gas}/h_{argon} x 100 (%)
Argon	85	100	58	100
Nitrogen	127	149	85	147
Helium	215	253	88	152
Hydrogen	284	334	118	203

[a] Heat transfer conditions: V_g = 10 m/s; P_g = 4 bars; T_g = 100 °C; T_m = 700 °C; d = 0.1 m; l =0.2 m

Argon exhibits the least efficiency as a quenching medium compared to others. It is typically preferred when the sample surface reacts with other gases. Nitrogen is widely used for quenching, although its cooling rate may be insufficient to fully harden certain steels and components with certain dimensions. Helium serves as a viable alternative to nitrogen, but its usage is limited due to its high cost. Hydrogen is both effective and cost-efficient; however, safety concerns often restrict its common use. Figure 2-17 shows the effect of cooling curves of the mentioned gases for 25 mm diameter slugs.

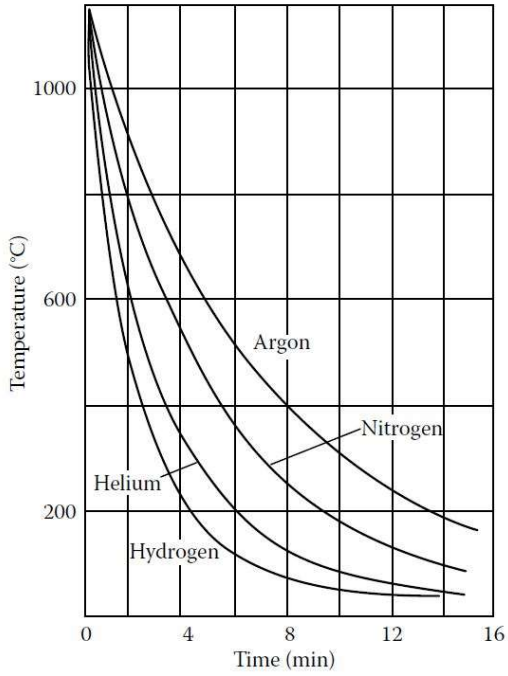

Figure 2-17: cooling curves of 25 mm diameter slugs in different gases [87].

While thermal and physical properties of a quenching gas, such as density, thermal conductivity, and specific heat, contribute to the cooling rate during quenching, it is essential to note that these properties are dependent on the type of gas used. As a result, factors like pressure and flow rate take precedence in the context of process control. [87]. Higher cooling rates can be achieved with higher gas pressure, this relationship can be described with formula proposed by Stratton as [87,89,90];

$$\text{Cooling rate in K/s} = k \cdot P^{0.466} \qquad \text{Eq. 2-13}$$

where k is a constant depending on a gas. Figure 2-18 represent this relationship.

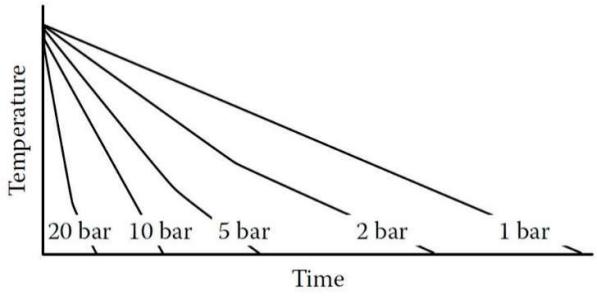

Figure 2-18: Schematic illustration of the effect of increasing pressure on cooling curve behavior [87].

Increasing the flow rate has similar effect with pressure on the cooling rate of the component. The important parameter linked with flow rate is a uniform flow and greater flow rate does not always provide a uniform flow. Quench uniformity can be reasonably enhanced by reversing the flow direction which minimizes the distortion [87,91].

2.6 Simulations/Modeling of Carburizing

2.6.1 Approaches and Challenges

An early attempt to model the carburization process was made by Goldstein and Moren [92], which relies on the Fick's 2nd law. Models based on this approach are still used for the simulation of gas carburizing [93–96]. Fick's 2nd law, being a parabolic partial differential equation [97], lacks an analytical solution unless constant diffusion coefficients and surface carbon concentration are assumed. Therefore, certain models [98,99] use constant diffusion coefficients of carbon in austenite based on empirical equations, which are available in the literature [45,54,100–102]. These models assume that the surface carbon concentration is constant and equal to the carbon potential of the furnace.

Since the carburizing atmosphere contains CO and H_2 in the gas carburizing, the treatment proceeds under the conditions closely approaching to the thermodynamic equilibrium [103]. However, in industrial applications, the surface carbon content does not reach equilibrium with the atmosphere but instead is controlled by reductive chemical reactions at the steel surface. To address this problem, several models [104,105] use mass balance as a boundary condition. This approach describes the carbon flux at the steel surface, deviating from the equilibrium assumption. The carbon flux, representing the mass of carbon atoms passing through a unit area of the material, can be formulated as

$$J_C^S = \beta(C_P - C_C^S(t)) \qquad \textit{Eq. 2-14}$$

Where C_P and C_C^S are carbon potential of the atmosphere and surface carbon content in ma. %, respectively. β is mass transfer coefficient which is the measure of the carbon absorbed by the steel surface and describes the rate of mass transfer throughout the process. Despite variations in the mass transfer coefficient throughout the process due to changes in the atmosphere and steel surface, many models utilize a constant, experimentally determined mass transfer coefficient. One well-known model using this principle for multicomponent systems was developed by Andersson and Ågren [106], and has been implemented into the commercially available software DICTRA [107] which is also frequently used for modelling of carburizing processes [108,109].

As mentioned before, due to the absence of an analytical solution for Fick's 2nd law, some models suggest a numerical solutions [110].

2.6.2 Modeling of Low Pressure Carburizing

Simulations of low pressure carburizing can be separated into three parts [111];

1. Transport of carbon from the atmosphere to the steel surface.
2. Reductive chemical reactions at the surface.

3. Diffusion of the carbon atoms accumulated at the surface along the concentration gradient toward the bulk of the steel.

The third part, the diffusion of atoms within a solid body, can be modeled using the same principles of diffusion calculations as those used for atmospheric gas carburizing. In this case, the solid body is represented by a steel specimen, particularly the austenite phase, and the diffusing atom is carbon.

As mentioned in section 2.3, the LPC model used in this thesis was developed by Steinbacher and Hunkel and brings new approaches to the problems described above. The model will be explained briefly in the following subsections. Detailed information can be found in the PhD thesis of Steinbacher [48].

2.6.2.1 Solving Fick's Second Law

As mentioned earlier in this section, analytical solution to Fick's second law is not available for low pressure carburizing. Consequently, the model uses a discretization Fick's second law by means of explicit finite-difference method (FDM).

Second law

$$\frac{\Delta c}{\Delta t} = -\frac{\Delta J}{\Delta x} \qquad \textit{Eq. 2-15}$$

First law

$$J = -D_c \frac{\Delta c}{\Delta x} \qquad \textit{Eq. 2-16}$$

where

$$\Delta J = J_{i-\frac{1}{2}} - J_{i+\frac{1}{2}} \qquad \Delta c = c_i - c_{i+1}$$

$$\Delta t = t_i - t_{i+1} \qquad \Delta x = x_i - x_{i+1}$$

The method of discretization is shown schematically in Figure 2-19. To ensure favorable adjustment of the time step size to the resolution of the network, the simulation model uses Neumann's stability analysis formulated as [112].

$$\Delta t = \frac{1}{2}\frac{(\Delta x)^2}{D} \qquad \textit{Eq. 2-17}$$

The model adopts a minimum resolution (Δx) of 10 µm and maximum process temperature of 1050 °C. When the chosen resolution value and diffusion coefficient of carbon in austenite at 1050°C, as reported by Leyens [50], are substituted into the equation, the required maximum time step becomes 1.75 seconds. Therefore, the model uses 0.05 seconds to ensure favorable resolution and feasible calculation time.

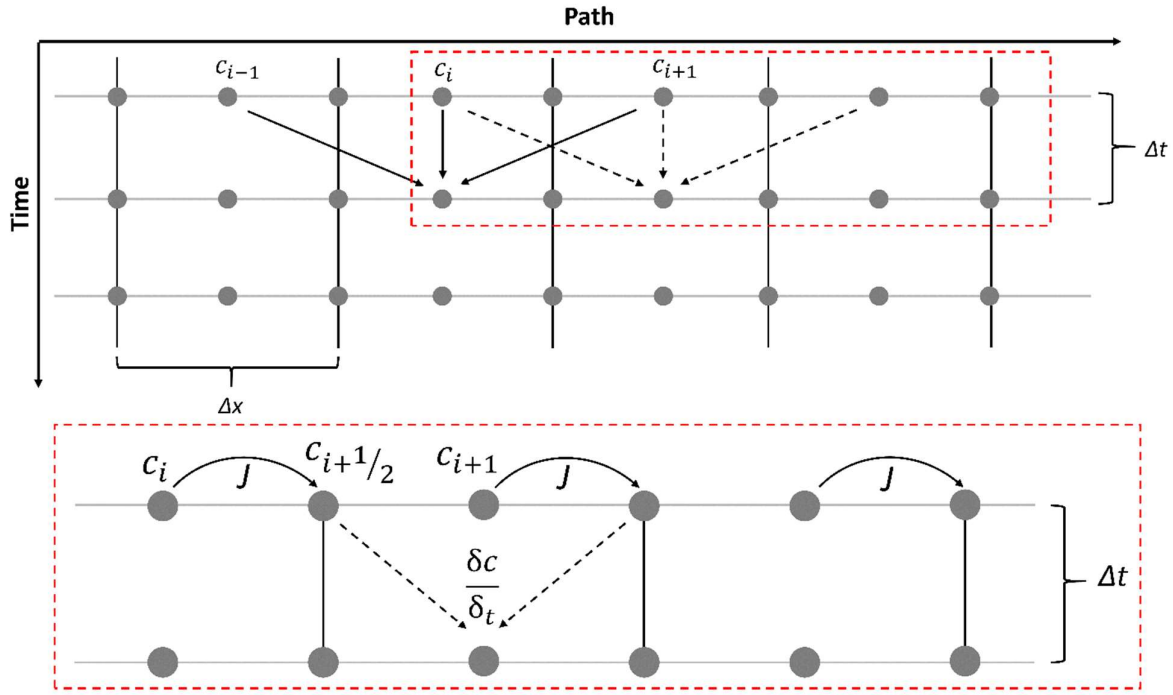

Figure 2-19: Schematic representation of the path and time discretization with variables of diffusion coefficient for the explicit finite difference method. Area with red-dashed rectangle is enlarged at the bottom.

2.6.2.2 *Carbon Absorption at the Surface*

In order to include the surface related effects, such as a solubility limit that differs from the base material, in the calculations, the first element at the surface is substituted into five sub-elements and the time step size is reduced to one tenth of the basic time step size. This substitution is illustrated in Figure 2-20.

In the model, the first element (shown in dashed line in Figure 2-20 and representing the surface) is filled with a constant carbon mass flow specific to acetylene.

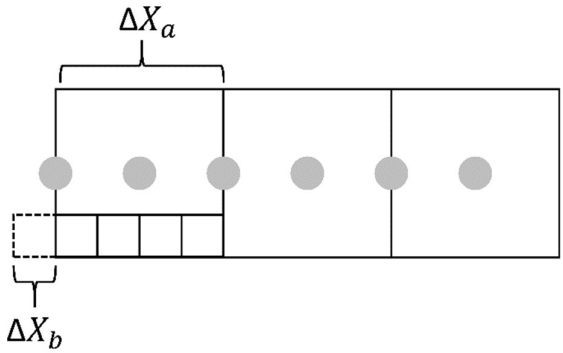

Figure 2-20: Substitution of the surface into five elements.

The diffusion in the first time step is calculated in the refined matrix with the specified time step. The maximum solubility of the first element is limited to the formation of 100 % iron carbide and thus 6.67 ma. % carbon. Subsequent transport within the matrix takes place according to diffusion laws. For this further diffusion, a diffusion coefficient as a function of carbon content is used, and the effect

of other alloying elements is neglected since they are assumed to have homogeneous distribution. This relation of carbon content and diffusion coefficient is described by Neumann and Person [113] At the beginning of the calculation, the finer elements are first filled with the basic carbon content of the first element of the matrix. The transfer of the carbon content between the two matrixes at each time step is carried out by transferring the carbon concentration of the first element to all elements with the exception of the first element.

The maximum solubility limit of the remaining elements in the material is determined by calculating temperature and alloys composition dependent A_{cm} carbide line (see Figure 2-1 for A_{cm} line).

2.6.2.3 Solubility Limit of Austenite

Solubility limit of austenite in the model depends on temperature and alloy composition. Two solubility limit calculations are defined in the model: the beginning of the carbide region and the maximum carbon solubility of austenite.

The cementite region is calculated by using the iron-cementite diagram presented by Chipman [114]. A second degree polynomial fitting function of temperature is used to approximate the A_{cm} line of the diagram and determine the cementite boundary in terms of carbon percentage dissolved in austenite, beyond which cementite starts to form. The effect of alloying elements on the final results of the fitting is determined by an alloy factor addition from the research of Neumann [51].

As an initial trial of using A_{cm} line also for solubility limit of austenite led to very low surface carbon content, the maximum solubility of austenite is calculated with the addition of temperature-related excess solubility limit. Additionally, the effect of alloying elements on this supersaturation of austenite is also integrated into the model by using finding of experiments conducted by Steinbacher. The alloying elements taken into account are Si, Cr, Mn, Mo and Ni.

2.6.2.4 Carbide Formation and Dissolution

In the model, carbides start to form when the solubility limit of austenite surpassed. This process is regulated by the calculation of the carbide formation potential at each time step, which is the difference between the solubility limit of austenite and the matrix carbon content. The carbon mass flow that contributes to the formation of carbides is then calculated by using carbide formation potential. The model is adapted a time delay above the saturation limit of austenite for carbide formation, meaning that carbides do not form immediately. Formed carbides are stored into the initial element (dashed square in Figure 2-20) but they don't provide diffusible carbon.

When carbon dissolved in austenite drops below the maximum solubility of carbon in austenite, carbides start to dissolve. The dissolution process follows similar steps and starts with the carbide potential calculation. There is also a time delay factor for dissolution of carbides along with a temperature factor.

2.6.3 Summary of Modeling and Motivation

Numerous initial parameters and equations were defined and briefly explained in the previous subsections that contribute to accurate modelling. Thus, it is evident that the accurate modeling of the LPC process requires the precise determination of these parameters. Along with individual parameters, establishing their relation with influencing factors such as temperature and alloy composition is also crucial for accurate modelling, considering that some of these parameters may vary during the process.

For instance, the formation of carbides at the surface during the boost step may slow down diffusion and alter the diffusion constants. Attempts to precisely model low-pressure carburizing have faced challenges due to the non-equilibrium nature of the process and the lack of reliable data. While there are certain models providing accurate results, many depend on empirically determined boundary conditions, as described above. These empirical determinations may yield inaccurate results for non-standard process parameters. Therefore, this thesis also aims to give some base data from different steps of the low pressure carburizing process to contribute to the accurate determination of modeling parameters and modification equations.

2.7 X-ray Diffraction

X-ray diffraction (XRD) is a powerful technique for the crystalline materials characterization. It provides information on phases, structures, texture, internal stresses and other structural parameters, such as crystal defects and average crystallite size. The principle of the method is to target the material with an X-rays beam and to detect the diffracted signal from atomic planes. The geometrical condition of the diffraction can be described by using Bragg's Law [115];

$$n\lambda = 2d\sin\theta \qquad \textit{Eq. 2-18}$$

Where n is the order of diffraction, λ is the wavelength of the incident beam in nm, d is the lattice spacing in nm and θ is the angle of the diffracted beam in degree. Figure 2-21 shows conditions of diffraction described by Bragg's law.

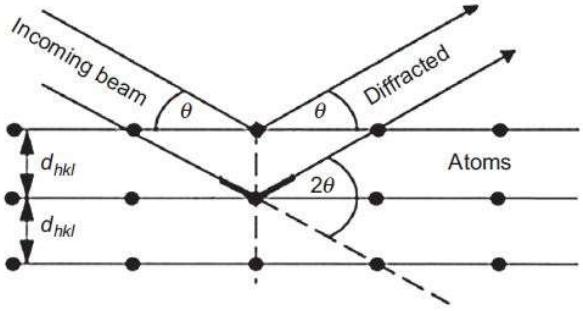

Figure 2-21: Geometrical condition the diffraction [116,117].

The X-ray beam is diffracted from each lattice plane of each crystalline phase in a way that satisfies Bragg's law. In polycrystalline materials with small grains, diffraction cones occur, creating so-called Debye rings as shown in Figure 2-22. The rings or portions of rings can be detected by different types of detectors and analyzed by suitable software [116].

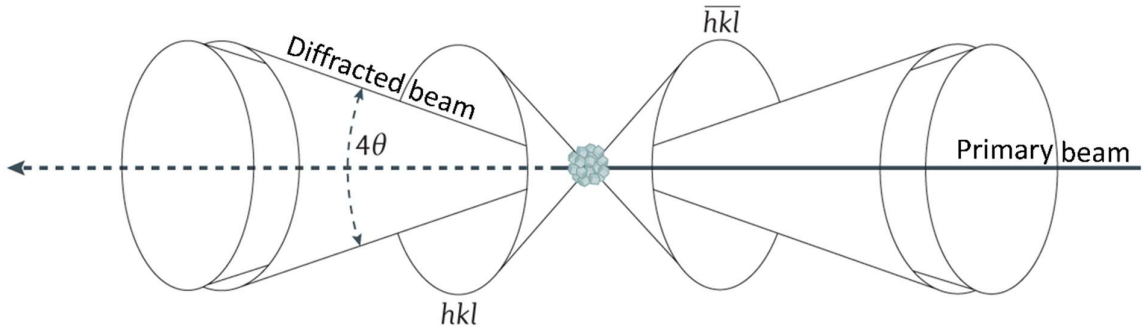

Figure 2-22: Diffraction cones in polycrystalline materials [118].

Materials and/or measurement devices always have imperfections; therefore the intensity distribution of the obtained signal is affected by different factors. These factors are, for example, instrumental contributions such as broadening depending on X-ray source, optics, detectors, etc.; homogeneity of the material; crystal defects such as dislocations, twins, etc.; crystallite size of the material and lastly microstrains [116]. Instrumental contributions can be determined by recording a data of reference sample without own signal broadening.

X-ray diffraction data are mostly extracted as an intensity distribution over 2θ angle. Depending on the wavelength of the X-ray source, the 2θ angle range changes. The most common X-ray sources are Cr, Cu, Mo, Mn and Iron. The choice of the correct X-ray source is important for the quality of the measurement. For example, the use of Cu-radiation in alloys containing iron, chromium, or titanium can cause fluorescent background intensities which greatly reduce the peak quality [119].

A representative image of X-ray diffractograms of a single peak can be seen in Figure 2-23.

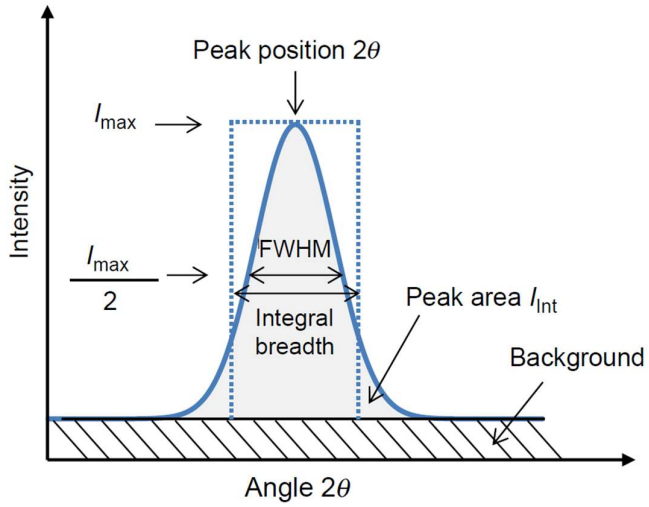

Figure 2-23: Diffraction peak with significant terms [116].

I_{max} represents the maximum peak intensity and I_{int} is the peak area after background subtraction. The Full width at half maximum (FWHM) or integral breadth (IB) serves as a characterization of peak width. As the name suggest, FWHM is the peak width at half of the maximum intensity and IB is the width of a rectangle of the same maximum and integrated intensity [116].

XRD is a non-destructive technique, which makes it suitable for in-situ studies. Time-resolved determination of the changes in each parameter provides various insights into specific material properties. For example, information about macroscopic or homogeneous microscopic strain in the material and the amount of interstitials can be gathered by using peak position. Information about crystallite size and lattice defects can be determined by peak broadening/peak asymmetry analyses. The quantitative amounts of phases and texture information can be obtained by using peak intensity. Changes in the given terms might be because of single cause or combination of the different causes. Consequently, the X-ray diffraction pattern is the fingerprint of the microstructural and atomic condition of the investigated material.

Phases present in a material can be accurately identified with X-ray diffraction analyses. Although there are several ways for qualitative and quantitative phase analyses, only Rietveld method will be discussed in further section 2.7.2 as it is the method used in this thesis.

2.7.1 Synchrotron X-ray Diffraction

Synchrotron radiation is a type of electromagnetic radiation which is emitted when charged particles, such as electrons, are forced to make a fast change of trajectory while traveling in a circular path by a magnetic field [120]. Synchrotron X-ray diffraction is a very powerful tool in materials investigation due to the tunable energy of the radiation up to high energy ranges and the very high brilliance of the beam. Synchrotron investigations in this thesis were conducted at Desy PETRA III. As an example, machine parameters are given in the Table 2-2.

Table 2-2: General Parameters of PETRA III [121]

Electron energy[1]	6.0 GeV	**Electron Beam Current**	100 mA
Circumference	2304 m	**Electron Beam Charge**	769 nC
RF	499,564 MHZ	**Number of electrons**	4,8 10^12
Revolution Time	7.685 µsec	**Emittance Ratio**	1 %
Revolution Frequency	130,1 kHz	**Horizontal Emittance**	-1.2 nmrad

Synchrotron sources offer a broad spectrum ranging from low energies of a few keV up to several hundreds of keV. The beam can be adjusted to the desired wavelength for the intended experiment using crystal monochromators or multilayer mirrors. This is one of the main advantages of synchrotron over laboratory X-ray devices. As a result, 2D detectors with exceptionally high counting

[1] Kinetic energy of electrons are one of the characteristic parameters of storage rings. It is 6 GeV in the storage ring at the DESY PETRA III. This should not be confused with the energy of the photons produced by deflecting these electrons in a magnetic field, i.e. the synchrotron radiation, which is several orders of magnitude smaller (See appendix section 10.5 for details)

rates can be employed, enabling rapid data collection. This capability is particularly valuable for in-situ analyses [120]. The high energy of the radiation provides the possibility to receive several diffraction peaks in a very small angular range without detector movement. Moreover, the high brightness along with high energy, creates a high penetration ability, which makes the synchrotron beam especially suitable for diffraction of materials in special environments or with a high thickness, up to several cm. A schematic representation of synchrotron and detailed explanation of the main components can be find in appendix section 10.5.

2.7.2 Quantitative Phase Analysis with Rietveld Refinement

Quantitative phase analysis means the determination of amount of each phases in multi-phase samples. Recorded X-ray diffraction data reflect particular characteristics of each phase, which enable to analyze several properties. If the material is not strongly textured, the intensities of the peaks of specific phases are proportional to their amount.

2.7.2.1 The Rietveld Method: General Description

Phase analyses with Rietveld refinement method uses least square approximation, which is obtaining a single equation by minimizing the sum of the data points from the plotted curve. The method can be formulated as [19,122];

$$S=\sum_n w_n \left|I_{n(o)} - I_{n(c)}\right|^2 \qquad \textit{Eq. 2-19}$$

where indices n represent each calculation position; $I_{n(o)}$ and $I_{n(c)}$ are observed and calculated intensities at each 2θ; w_n is a weighting factor based on the experimental error margins. It is considered to be proportional to the $\sqrt{\mathrm{I_{n(o)}}}$ following Poisson counting statistics [116,122]
The calculation of $\mathrm{I_{n(c)}}$ at each position n is a function of the diffraction signal of all present phases, instrumental contribution, backgrounds, etc. For precise determinations, various factors depending on each analyzed phase must be considered. Some of these factors include temperature and occupation factor, the position of all atoms in the elementary lattice, the space group of the lattice, lattice parameters, and phase contents [116,117]. Additionally, to separate the contribution of the instrument and sample, several instrumental parameters are taken into account. These include 2θ shifts (instrument error), instrumental profile, profile asymmetry, background, wavelength (emission profile), sample positioning error, and absorption [116,117].

2.7.2.2 Diffraction Line Profiles in the Rietveld Method

Rietveld method was originally designed as a method of refining crystal structure data obtained by neutron powder diffraction with low resolution by Hugo M. Rietveld in 1967 [123,124]. In that time, Gaussian peak profile function was appropriate to describe this low resolution data. However, over the years, when there is a need of extension of the model, new profile functions and analyze

approaches are introduced. In the scope of this thesis, the most important one is fundamental parameters approach, which will be discussed further. Detailed information about chronological introduction of models and related literature can be found in appendix section 10.6.

2.7.2.3 The Fundamental Parameter Approach (FPA)

FPA is a line profile fitting method that uses physically based models to generate line profile shapes [125]. In this way, the observed diffraction peaks are modelled by the convolution of various functions that represent the instrument profile shape K(2θ), the geometrical instrument function J(2θ), the wavelength profile W(2θ) and the broadening function B(2θ), as given in [116,125–127].

$$K(2\theta) = W(2\theta) \otimes J(2\theta) \qquad \text{Eq. 2-20}$$

$$I(2\theta) = K(2\theta) \otimes B(2\theta) \qquad \text{Eq. 2-21}$$

where ⊗ represents the convolution operation [125]. The first step is the synthetization of instrument profile shape *K(2θ)* by convoluting the geometrical instrument function *J(2θ)* together with the wavelength profile *W(2θ)* at the Bragg angle 2θ of the peak, where the function *J(2θ)* is also a convolution of the various instrument aberration functions associated with the diffractometer. The second step is similarly the synthetization of profile function *I(2θ)* by convoluting the broadening function *B(2θ)* with the instrument profile function *K(2θ)* as shown in Figure 2-24 [125]

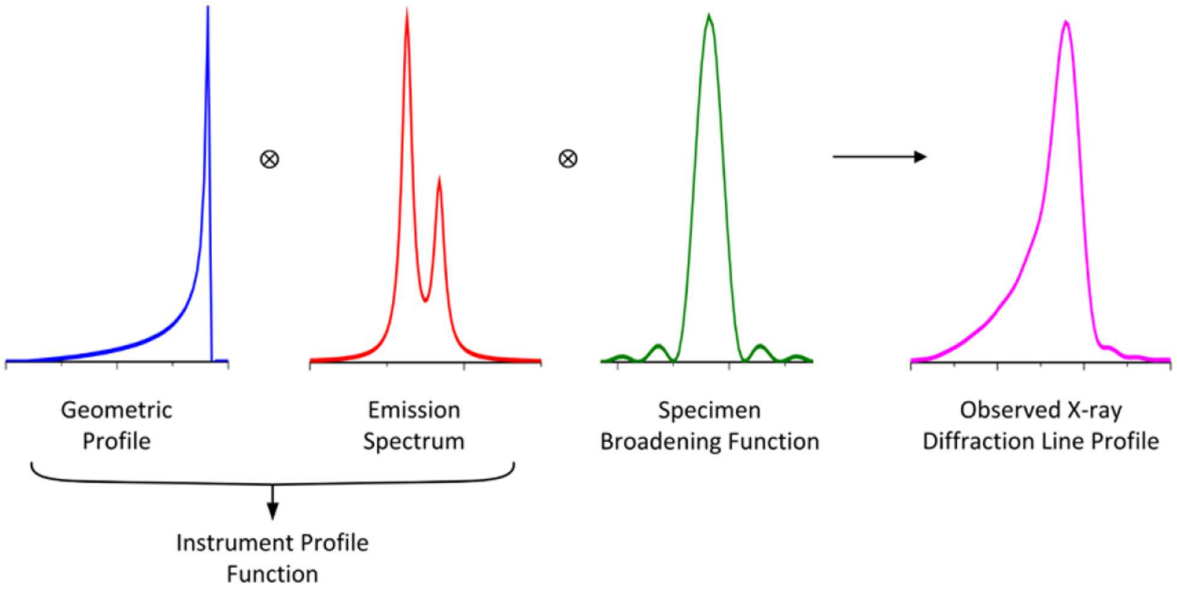

Figure 2-24: Generation of a line profile via convolutions in the FPA [125]

If instrumental functions are calculated and extracted correctly, the contribution of sample properties to the diffraction pattern can be analyzed [116,128]. As an alternative, a standard sample without sample broadening such as SRM660a (LaB_6) can also be measured and used to determine the instrumental function.

2.7.3 Residual Stress Analyses by X-ray Diffraction

Residual stresses play a crucial role in the service life and performance of engineering components, making them a regular topic in research. The XRD technique is one of the most used methods to characterize residual stresses.

2.7.3.1 Definition and Determination of Residual Stress

Residual stresses are mechanical stresses which remain in a material in the absence of any external mechanical loading and under a homogeneous and temporal stable temperature field [116]. They are balanced within the component.

Residual stresses can be categorized into three types based on their scope of action [116,129]. Residual stresses of the first kind (σ^I) are the volume averages of the position-dependent residual stresses that are acting on a representative microstructure within the considered bulk. These represent the macroscopic material balancing over the entire work piece and are also called *macro residual stresses* [116,129]. Residual stresses of the second kind (σ^{II}) are stresses balancing at the scale of grains. They are also called *homogeneous micro stresses* [116,129].Residual stresses of the third kind (σ^{III}) are local variations at a submicroscopic scale, for example due to dislocations or other lattice defects. They are also called *inhomogeneous microstresses* [116,129]. An illustration of the scope of action of the three kinds of residual stresses is given in Figure 2-25.

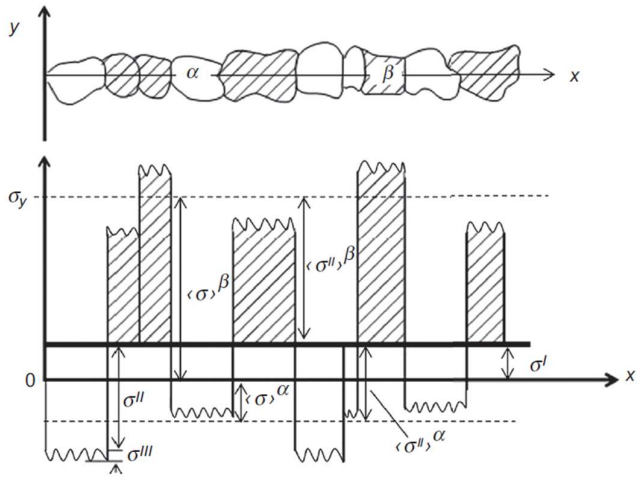

Figure 2-25: Three kinds of residual stresses distributed over several grains material having phases of α and β [116].

Since stress is an extrinsic property, it cannot be measured directly. All stress determination methods rely on measurement of some intrinsic property, such as strain, and following calculation of the associated stresses. The primary principle for determining residual stress using X-ray diffraction involves measuring a strain in the crystal lattice and subsequently calculating the stresses responsible for this strain using relevant equations and material constants [119].

This strain can be obtained by measuring the lattice d-spacing from the diffraction peak position change in the crystallites using Bragg's law. The stress measurement methods by X-ray diffraction can be divided in two as the conventional $\sin^2\psi$ method and the 2D method (XRD^2).

2.7.3.2 Conventional Method ($\sin^2\psi$)

Strains in the material volume are expressed as the components of a 2nd order strain tensor, depending on the sample rotation and material state as shown in Figure 2-26 and Eq. 2-22.

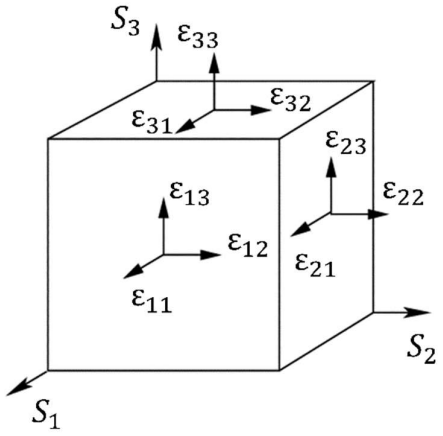

Figure 2-26: Strain tensor components on volume element [130]

$$\varepsilon_{ij} = \begin{bmatrix} \varepsilon_{11} & \varepsilon_{12} & \varepsilon_{13} \\ \varepsilon_{21} & \varepsilon_{22} & \varepsilon_{23} \\ \varepsilon_{31} & \varepsilon_{32} & \varepsilon_{33} \end{bmatrix} \qquad \textit{Eq. 2-22}$$

When two indices are identical, this strain is called normal strain which is created by a force acting perpendicular to the corresponding surface. When two indices are different, this strain is called shear strain which is created by a dislocation parallel to the considered surface.

A stress tensor can be expressed as the sum of two other stress tensors: a mean hydrostatic stress tensor, sometimes also called mean normal stress tensor or volumetric stress tensor, and a deviatoric stress tensor as shown in Eq. 2-23 [120].

$$\sigma_{ij} = \begin{bmatrix} \sigma_{11} & \sigma_{12} & \sigma_{13} \\ \sigma_{21} & \sigma_{22} & \sigma_{23} \\ \sigma_{31} & \sigma_{32} & \sigma_{33} \end{bmatrix} = \begin{bmatrix} \sigma_m & 0 & 0 \\ 0 & \sigma_m & 0 \\ 0 & 0 & \sigma_m \end{bmatrix} + \begin{bmatrix} \sigma_{11}^d & \sigma_{12}^d & \sigma_{13}^d \\ \sigma_{12}^d & \sigma_{22}^d & \sigma_{23}^d \\ \sigma_{13}^d & \sigma_{23}^d & \sigma_{33}^d \end{bmatrix} \qquad \textit{Eq. 2-23}$$

Where σ_m is the mean hydrostatic stress given by

$$\sigma_m = \frac{\sigma_{11} + \sigma_{22} + \sigma_{33}}{3} \qquad \textit{Eq. 2-24}$$

And σ_{ij}^d is the stress deviation tensor. Hydrostatic tensor tends to change the volume of the crystal body and the stress deviator tensor tends to change the shape of the crystal [120].

In the conventional method for polycrystalline materials, typically point detectors or line detectors are used and the stress or stress tensor is calculated from diffraction peak 2θ shifts of a specific lattice plane family with different sample orientations. Figure 2-27 shows angles and rotations for stress measurement in conventional laboratory X-ray diffractometers. Three main tilting axes can be distinguished as Ω (OMEGA), χ (CHI) and Φ (PHI). Axes are generally represented with Greek uppercase letters while tilting/rotation angles with Greek lowercase letters. Tilting around χ-axis is indicated by the angle χ (chi), which is the angle between the normal of the sample surface and the normal of the diffracting plane series. Phi (Φ), giving the angle φ, is the angle of rotation of the sample about its surface normal. Omega (ω), changed by the rotation around Ω-axis, is the angle between the incident X-ray beam and the sample surface. 2-theta (2θ) angle is the diffraction angle between the incident and diffracted X-ray beams, and finally Psi (ψ) is the angles through which the sample is rotated [131,132].

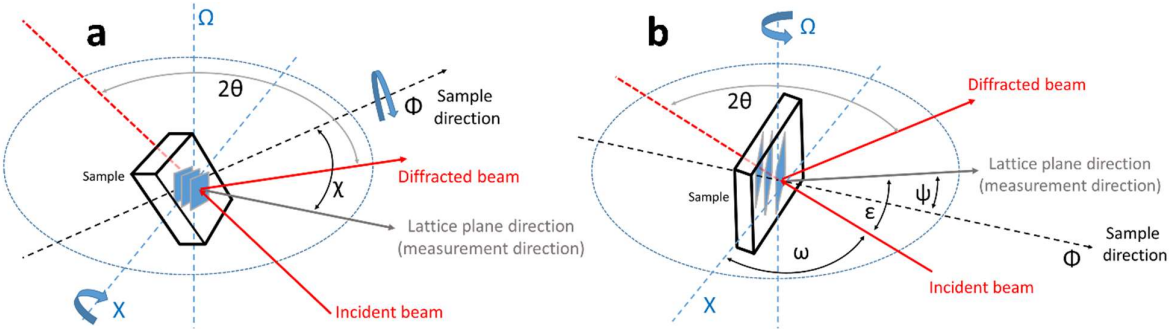

Figure 2-27: General scheme, tilting axes and relevant angles of rotations for measurement. (a) $\chi \neq 0$, (b) $\chi = 0$ [132]

The measurements can be taken in either Omega (ω) or Chi (χ) mode, depending on the equipment available. A short description and a graphic explanation of both method can be found in appendix section 10.7.

In general, $\sin^2\psi$ method is used with conventional laboratory diffractometer alignment. This method involves conducting multiple X-ray measurements with different tilt angles within a suitable 2θ range for the targeted peak. After that, peak positions for each measurements are determined by using peak shape functions such as Gaussian, Pearson VII or Pseudo-Voight; or peak positioning methods such as parabola method or center of gravity method which all are integrated to residual stress determination software.

By using the 2θ position of the measured peak and Bragg's law (Eq. 2-18), d-spacing for every tilt angle can be found.

$$\varepsilon_\psi = \frac{d_{\Phi\Psi} - d_0}{d_0} \qquad \textit{Eq. 2-25}$$

Eq. 2-25 gives the strain for each tilt angle by the using stress-free lattice spacing (d_0) and the lattice spacing for every tilt angle calculated by Bragg's law ($\mathrm{d}_{\Phi\Psi}$).

Calculation of the strain in a desired direction can be done by determining the strain tensor in the sample coordinates. The fundamental equation governing the relationship between the measured normal strain and the strain tensor expressed in the sample coordinates is given by [120,133]

$$\varepsilon_{\Phi\Psi} = \varepsilon_{11}cos^2\Phi sin^2\Psi + \varepsilon_{12}sin2\Phi sin^2\Psi + \varepsilon_{22}sin^2\Phi sin^2\Psi + \varepsilon_{13}cos\Phi sin2\Psi + \varepsilon_{23}sin\Phi sin2\Psi + \varepsilon_{33}cos^2\Psi \quad \textit{Eq. 2-26}$$

Every strain tensor component has corresponding stress tensor component which can be determined by Hooke's law as given in Eq. 2-27.

$$\sigma_{ij} = C_{ijkl}\varepsilon_{kl} \quad \textit{Eq. 2-27}$$

where C_{ij} are elastic stiffness coefficients. It is practical and reasonable to assume isotropic elastic behavior and a homogeneous structure on a macroscopic scale for most of the polycrystalline materials without texture or with weak texture [120]. In these cases, the stress–strain relationship can be simplified and Hooke's law can be rewritten as

$$\varepsilon_{ij}^{\{hkl\}} = \frac{1 + v^{\{hk\}}}{E^{\{hkl\}}} \cdot \sigma_{ij} - \frac{v^{\{hk\}}}{E^{\{hkl\}}} \cdot \delta_{ij} \cdot Spur\boldsymbol{\sigma} \quad \textit{Eq. 2-28}$$

where $\mathrm{E}^{\{\mathrm{hkl}\}}$ and $\mathrm{v}^{\{\mathrm{hkl}\}}$ are hkl dependent material constants called the elastic modulus in MPa and Poisson's ratio, respectively. δ_{ij} is the Kronecker delta, 1 for normal stresses and 0 for shear stresses. $Spur\boldsymbol{\sigma}$ represents the sum of all normal stresses and $\{hkl\}$ indicates the lattice plane dependence of the material constants.

It is important to consider that even if the investigated polycrystalline material is isotropic regarding its macroscopic elastic properties, at the scale of the crystal structure, the elastic properties of every crystallite are not isotropic due to crystal anisotropy. Therefore, the elastic properties are lattice plane dependent [116]. Tables containing relevant X-ray elastic constants can be found in the literature [133,134]. The formulation of X-ray elastic constants are introduced in the next page.

Stress and strain relationships of isotropic materials can be written as Eq. 2-29**.**

$$\varepsilon_{11} = \frac{1}{E}[\sigma_{11} - v(\sigma_{22} + \sigma_{33})]$$

$$\varepsilon_{22} = \frac{1}{E}[\sigma_{22} - v(\sigma_{33} + \sigma_{11})] \quad \textit{Eq. 2-29}$$

$$\varepsilon_{33} = \frac{1}{E}[\sigma_{33} - v(\sigma_{11} + \sigma_{22})]$$

$$\varepsilon_{12} = \frac{1+v}{E}\sigma_{12},\ \varepsilon_{23} = \frac{1+v}{E}\sigma_{23},\ \varepsilon_{31} = \frac{1+v}{E}\sigma_{31}$$

When these strain values are substituted to related places in Eq. 2-26**,** fundamental equation can be re-written as

$$\varepsilon_{\Phi\Psi} = -\frac{v}{E}(\sigma_{11}+\sigma_{22}+\sigma_{33}) + \frac{1+v}{E}(\sigma_{11}cos^2\Phi + \sigma_{12}sin2\Phi + \sigma_{22}sin^2\Phi)sin^2\Psi + \frac{1+v}{E}(\sigma_{13}cos\Phi + \sigma_{23}sin\Phi)sin2\Psi + \frac{1+v}{E}(\sigma_{33}cos^2\Psi) \qquad \textit{Eq. 2-30}$$

Due to the limited penetration of X-rays, the normal stress at the sample surface can often be assumed as zero (σ_{33} = 0). This is called a plane stress state. It should be kept in mind that, although this assumption is particularly true for Cr radiation, when a multiphase material with a repeatedly distributed phase is measured, 2nd kind residual stresses in the present phases can be nonzero with opposite signs [19,135]. This is the case when the second phase is distributed up to the depth which is smaller than the depth of X-ray penetration. Then, equation can be simplified further, assuming a plane stress state by replacing term as

$$\sigma_\Phi = \sigma_{11}cos^2\Phi + \sigma_{12}sin2\Phi + \sigma_{22}sin^2\Phi$$

$$\tau_\Phi = \sigma_{13}cos\Phi + \sigma_{23}sin\Phi$$

$$\frac{1}{2}S_2 = \frac{1+v}{E} \qquad \textit{Eq. 2-31}$$

$$S_1 = -\frac{v}{E}$$

Where σ_Φ and τ_Φ are normal and shear stresses respectively. If plane stress is assumed, (i.e. (σ_{33} = 0). Then, Eq. 2-30 simplifies to

$$\varepsilon_{\Phi\Psi} = S_1(\sigma_{11}+\sigma_{22}) + \frac{1}{2}S_2(\sigma_\Phi)sin^2\Psi + \frac{1}{2}S_2(\tau_\Phi)sin2\Psi \qquad \textit{Eq. 2-32}$$

The stress state given in Eq. 2-32 is referred to as biaxial with shear. For only biaxial stress state, where σ_{13} = σ_{23} = 0, equation becomes

$$\varepsilon_{\Phi\Psi} = S_1(\sigma_{11}+\sigma_{22}) + \frac{1}{2}S_2(\sigma_\Phi)sin^2\psi \qquad \textit{Eq. 2-33}$$

It can be noticed from this simplest form of the equation that the measured strain is a linear function of $sin^2\Psi$. If the first derivative with respect to $sin^2\Psi$ is taken, obtained equation can be given as

$$\frac{\partial\varepsilon_{\Phi\Psi}}{\partial sin^2\Psi} = \frac{1}{2}S_2(\sigma_\Phi) = m \qquad \textit{Eq. 2-34}$$

where *m* is the slope of the measured strain in the $\sigma_{\Phi\Psi}$ - $sin^2\Psi$ plot. This means that σ_Φ can be calculated from the slope and the elastic constant by collecting diffraction profiles of the {hkl} peak at several Ψ-tilt angles. The normal stress components of σ_{11} and σ_{22} can be determined by measurements at $\Phi = 0°$ and at $\Phi = 90°$ = 0 respectively. Further details of the $sin^2\Psi$ can be found in [120] or [133].

2.7.3.3 Two-dimensional X-ray Diffraction Method (XRD²)

Two-dimensional X-ray diffraction (XRD²) systems utilize area detectors capable of capturing a large portion of the diffraction rings in a single measurement. This significantly reduces the measurement time compared to conventional laboratory X-ray devices with point or line detectors [120].
Diffraction rings measured by an area detector are normally fully circular in a stress-free state but stress can alter size and shape of the rings depending on its nature. This stress can be determined by using the fundamental relationship between the distortion of diffraction rings and stress. Figure 2-28 shows a schematic representation of a sample measured in transmission mode with high energy by the XRD² method.

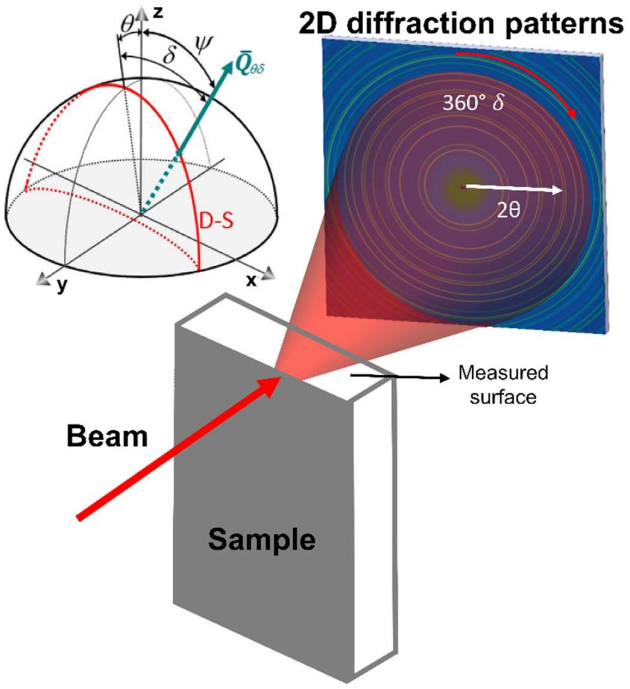

Figure 2-28: Schematic representation of the sample measured with XRD² in transmission mode. Debye-Scherrer ring (D-S) and a representative orientation of the diffraction vector ($Q_{\theta\delta}$) can be seen in stereographic projection, whose orientation in the sample coordinate system x, y and z is defined by angles δ , θ and Ψ.[136].

The principle is similar to the conventional method but the equation should be adapted to the measurement system. The process starts with the determination of {hkl} specific lattice spacing for different intervals of the full diffraction rings. Figure 2-29 shows the interval, in another saying “cake”, analyses from full (360°) diffraction rings at azimuthal angles of 0°, 90°, 180° and 270° and corresponding {211} martensite peaks for these angles. It is evident that peak positions are different

for perpendicular cakes, indicating the distortion of the rings induced by deviatoric strains or stresses.

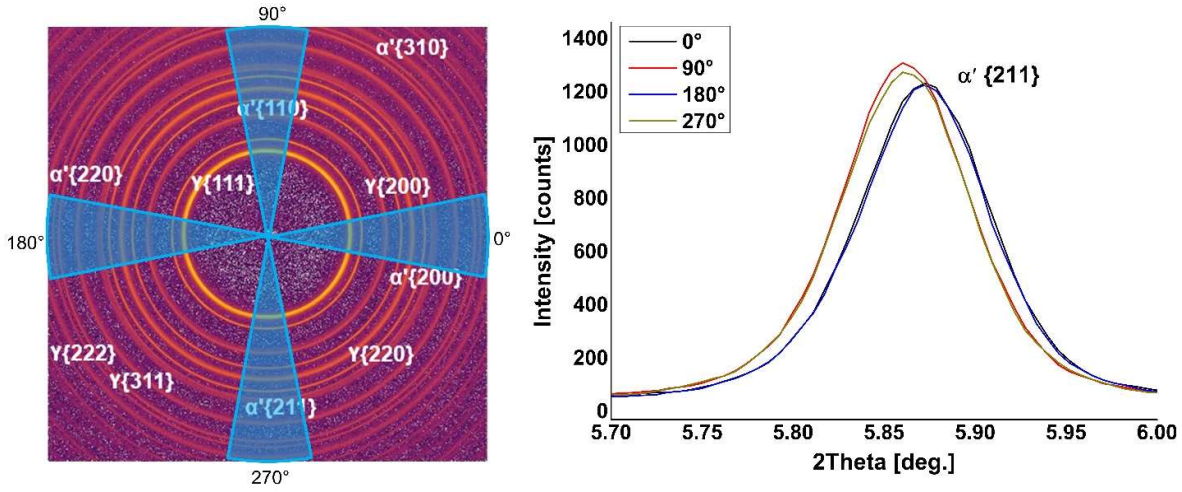

Figure 2-29: Integration of 5° cakes from full diffraction ring and corresponding {211} martensite peak at azimuthal angles of 0°, 90°, 180° and 270° for residual stress determination.

When peak positions are found for every cake, strain values can also be determined as described before in Eq. 2-25. Additionally, strain in the desired direction can be calculated similar to the conventional method by using the fundamental equation given in Eq. 2-26. However, the orientation of the diffraction vector depends on Phi (Φ) and Psi (Ψ) angles in the fundamental equation used in the conventional method but for synchrotron radiation in transmission mode these angles should be replaced with θ and δ due to the different geometrical condition (See Figure 2-28).

Eq. 2-35 shows the fundamental equation where x is the direction on the measured surface perpendicular to the beam, y is the beam direction and z is the normal direction to the measured surface perpendicular to the beam (See Figure 2-28)

$$\varepsilon_{\Phi\Psi} = \varepsilon_{xx}(sin^2\theta sin^2\Psi) + \varepsilon_{xy}(sin2\theta sin^2\Psi) + \varepsilon_{xz}(sin\theta sin2\Psi) + \varepsilon_{yy}(cos^2\theta sin^2\Psi) + \varepsilon_{yz}(cos\theta sin2\Psi) + \varepsilon_{zz}(cos^2\Psi) \qquad \textit{Eq. 2-35}$$

This equation has Ψ tilt angle which needs to be converted into an azimuthal angle since measurements in synchrotron are generally made without tilting at a fixed geometry in transmission mode. For these, two main dependencies will be used.

1. $cos\Psi = cos\theta \cdot cos\delta$ [136–138]

2. $sin^2\Psi = tan^2\theta = sin\delta$ [136]

If all angles are replaced with suitable dependencies then fundamental equation can be re-written as

$$\varepsilon_{\theta\delta} = \varepsilon_{xx}(cos^2\theta sin^2\delta) - \varepsilon_{xy}(sin2\theta sin\delta) + \varepsilon_{xz}(cos^2\theta sin2\delta) + \varepsilon_{yy}(sin^2\theta) - \varepsilon_{yz}(sin2\theta cos\delta) + \varepsilon_{zz}(cos^2\theta cos^2\delta) \quad \textit{Eq. 2-36}$$

This equation have sin(θ) and sin(2θ) terms which takes very small values for high energy synchrotron beam due to small diffraction angles below 10°; therefore, they are mostly inaccessible and can generally be neglected making the ε_{yy}, ε_{xy} and ε_{yz} components unaccessible. Then the equation can be further simplified as

$$\varepsilon_{\theta\delta} = \varepsilon_{xx}(cos^2\theta sin^2\delta) + \varepsilon_{xz}(cos^2\theta sin2\delta) + \varepsilon_{zz}(cos^2\theta cos^2\delta) \quad \textit{Eq. 2-37}$$

Similar to the conventional method, when strain values in Eq. 2-29 are introduced, fundamental equation for synchrotron transmission geometry can be re-written as

$$\varepsilon_{\theta\delta} = -\frac{v}{E}(\sigma_{xx} + \sigma_{zz}) + \frac{1+v}{E}(\sigma_{xx}cos^2\theta sin^2\delta + \sigma_{zz}cos^2\theta cos^2\delta) - \frac{1+v}{E}\sigma_{xz}cos\delta sin2\theta \quad \textit{Eq. 2-38}$$

The size of the cakes depends on the quality of the diffracting signal. They should be as small as possible to determine directional stresses more precisely. On the other hand, they should be large enough to give a good peak quality for fitting. Splitting the diffraction ring into more cakes has the advantage of providing more input to the equations and a more precise determination of stress positions. However, more cakes mean cakes with a narrow azimuthal angle, which might affect the peak quality.

As mentioned earlier in this section, the position of the peak can be determined using different peak shape functions or methods [139]. For synchrotron data, the peak position of each cake can be determined by profile fitting. One of the highly preferred profile fitting functions is the Pseudo Voigt function. The probability distribution of the Voigt profile can be obtained by the convolution of the Gaussian and the Lorentzian function meaning that it contains the half width half maximum (HWHM) of both the Gaussian and the Lorentzian contribution [140]. The Pseudo Voigt function is a simple approximation for the Voigt profile function which is a linear combination of Gaussian and Lorentzian functions with the same full width at half-maximum (FWHM) instead of convolution of both functions [141]. A general representation of Pseudo Voigt function, and Lorentzian and Gaussian functions along with detailed mathematical background can be found in the literature [120,141].

2.7.4 Residual Stress Generation During Heat Treatment

2.7.4.1 Thermal Stresses

Thermal stresses are a subset of residual stresses generated during heat treatment due to the thermal expansion or contraction of a homogeneous material. A one of the example is the generation of 1st-kind residual stresses resulting from inhomogeneous cooling conditions. When single phase samples are subjected to rapid quenching from elevated temperatures, the surface undergoes faster

cooling than the core, creating a temperature gradients. This non-uniform cooling leads to a thermal contraction, thereby generating thermal stresses within the material [19,142].

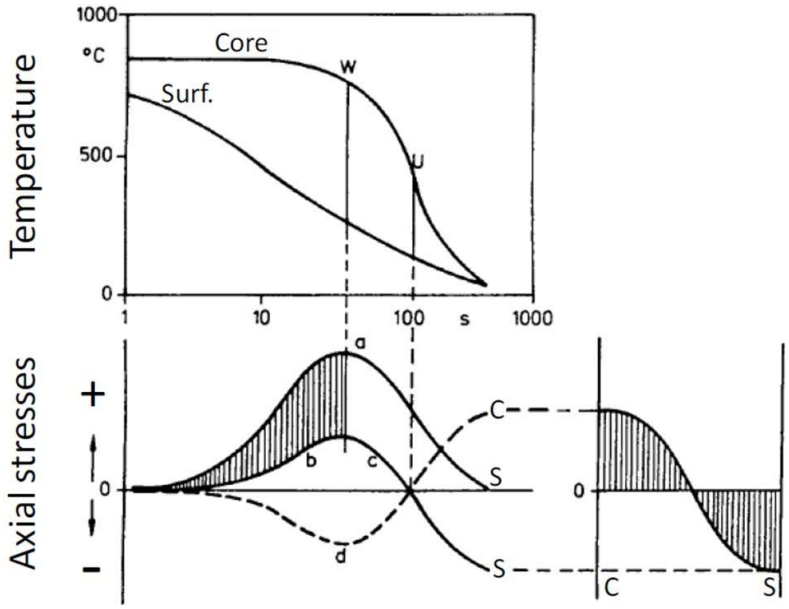

Figure 2-30: generation of thermal stresses during quenching of a monophasic cylindrical metallic sample involving no phase transformation [19,143]

Figure 2-30 shows the development of thermal stresses during the quenching. Notably, the surface temperature experiences a more rapid decrease than the core temperature, resulting in a larger specific volume for the core compared to the surface. This variation in specific volume prevents volume contraction at the surface that leads to tensile thermal stresses at the surface and compressive stresses in the core. If the yield stresses are never reached, residual stresses at the end of the cooling would be zero, since inhomogeneous strain as a source of stresses would be fully removed. In cases where the yield stress (curve b) is lower than the theoretical elastic stress (curve a), plastic deformation occurs, as indicated by the dashed area. At point “W”, where the temperature gradient is maximum, the stresses at the core and at the surface begin to change direction; and at the point “U” they change sign. At room temperature, compressive residual stresses remain at the surface while tensile residual stresses are present in the core [19,87,144].

Additionally, thermal effects contribute to the generation of 2nd kind residual stresses. For the case of quenching of a multiphase polycrystalline material, grains of the phase having a larger thermal expansion coefficient undergo more shrinkage compared to grains of the phase having a smaller thermal expansion coefficient. Consequently, compression stresses develop in the grains with a smaller thermal expansion coefficient, while tensile stresses occur in the grains with the larger coefficient. It is important to note that this represents a simplified two-dimensional description of the impact of thermal expansion at the grain scale. A more detailed description of the phenomenon can be found in the study of Sherby et al. related to a model proposed to explain the formation and crystal structure of martensite in quenched Fe-C systems [145].

2.7.4.2 *Transformation Stresses*

Transformation stresses are generated due to the changes of different the specific volume of phases during phase transformation [142]. In practical applications, mainly for the quenching processes, most steels exhibit a combination of transformation and thermal stresses. The most common examples is the transformation of austenite to martensite in steel during quenching.

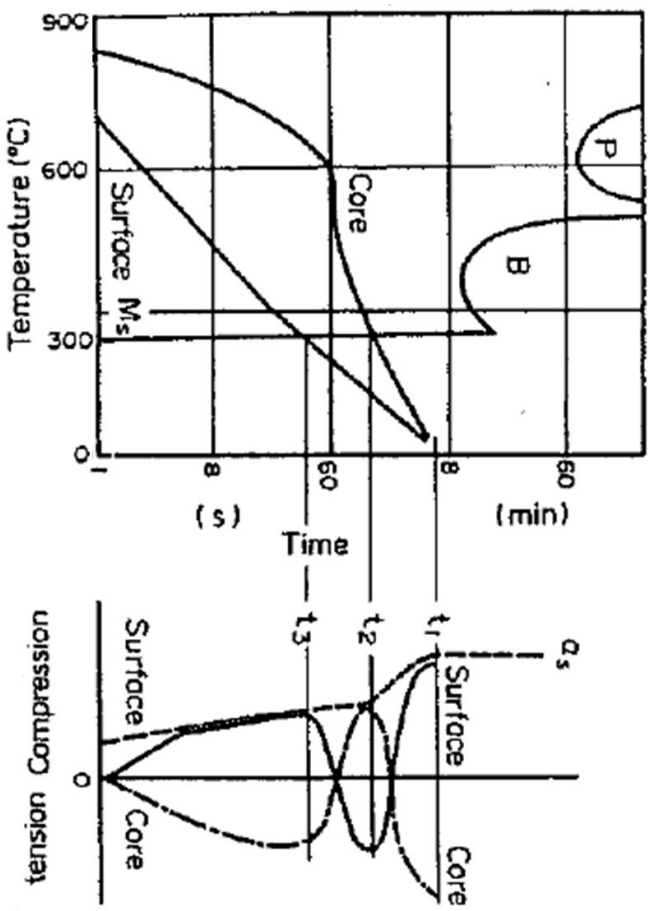

Figure 2-31: Formation of residual stresses during transformation of austenite to martensite [144]*. After 60 seconds, the time unit is minute.*

In Figure 2-31, the effect of the austenite to martensite transformation in steels on the generation of stresses is demonstrated. During cooling without any transformation, tensile thermal stresses are generated at the surface, compensated by compressive thermal stresses at the core. After around 50 seconds ($t_{3)}$, where surface temperature falls below the martensite start temperature (M_s), surface starts to transform. This transformation causes an expansion of the surface that counteracts the thermal stresses. The volume increase from austenite to martensite induces high compressive stresses at the surface which leads to a sign change of the stresses. Another stress reversal is caused by the core transformation at the time t_2, the core transformation time [87,144]. After cooling, transformation induced tensile stresses at the surface dominate over thermally induced compressive stresses, which is different than the case presented in Figure 2-30.

2.7.4.3 Generation of the Stresses in Carburized Parts

The introduction of compressive residual stresses at the surface is one of the major benefits of the carburizing, which is caused by the interaction of the case and core during cooling. As mentioned in the previous sections, during cooling of carburized parts, thermal shrinkage strains causing a contraction of the part also occur. Additionally, high-temperature processing of steels involves transformations from austenite to ferrite, pearlite, bainite or in many cases due to rapid quenching, martensite, leading to transformation stresses.

The main important point during quenching of carburized parts is the initiation time and place of the transformation. Increasing the carbon content at the surface decreases the martensite start temperature significantly, which delays the surface transformation. However, heat is extracted from the surface during the entire quenching, maintaining the core at a high temperature compared to the surface. This delays the core transformation. Therefore, knowledge of TTT and CCT diagrams at each respective surface distances is crucial to determine residual stress generation [146].

If the surface transforms earlier than the core, the formation of residual stress will be similar to the case in Figure 2-31. Figure 2-32 shows the development of residuals stress along with the CCT diagram when the transformation of the core precedes the surface transformation.

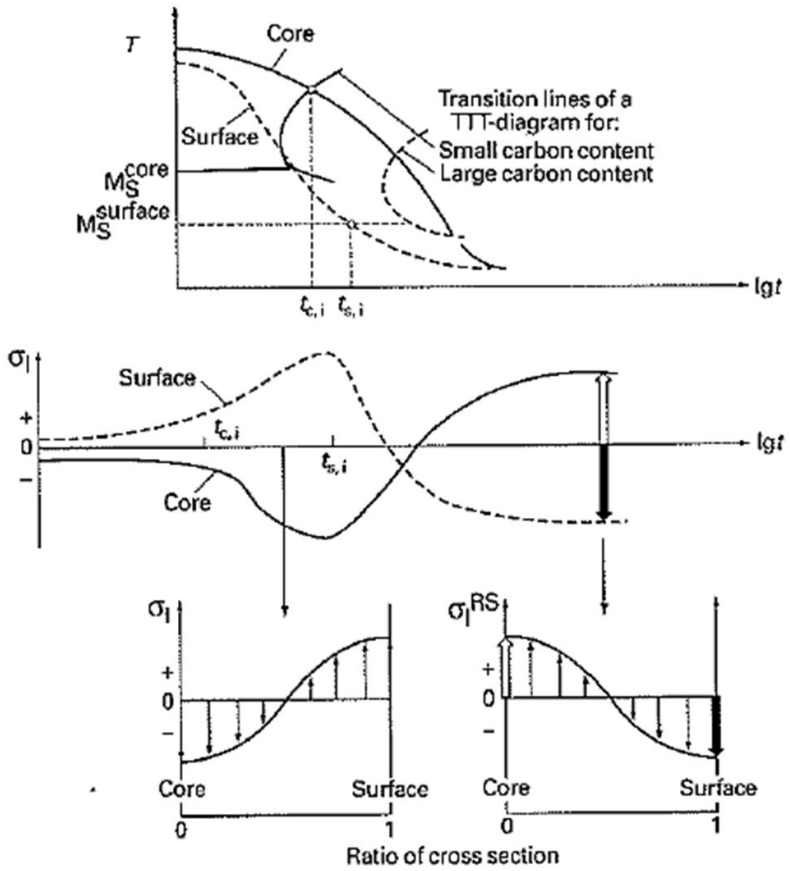

Figure 2-32: Transformation temperatures and stresses of the core and surface when core transforms earlier than the surface [146,147]. *Bottom two graph shows the stress distribution from core to surface at given points.*

At the time $t_{c,i}$ the bainite transformation of the core begins while the core is under the compressive thermal stresses, which are compensated by tensile stresses at the surface. During further cooling, the transformation proceeds from the core to the surface, and at time, $t_{s,i}$, the surface, having higher carbon content, transforms to martensite. However, the area between the core and the surface is relatively cool and rigid which causes a restriction against the expansion of the surface. Consequently, at the end of cooling, compressive stresses are generated at the surface while the core is under tensile residual stresses [146,147].

2.7.5 Previous Studies Related to In-Situ X-ray Diffraction during Heat Treatments

For the direct in-situ investigation of phase transformation in steels by X-ray diffraction under laboratory conditions, Epp et al. [148,149] developed a variety of methods. A special 0.8 liter experimental furnace was developed for heat treatments. The carbide dissolution in the bearing steel 100Cr6 was investigated in situ at different austenitizing temperatures by means of diffractometry. X-ray diffraction measurements were made by using Cr radiation and data were collected with a two-dimensional multiwire proportional counter detector. The analysis of the diffraction patterns was performed with the Rietveld software TOPAS from Bruker-AXS and background was manually subtracted with the software EVA in order to obtain good fittings with TOPAS. By using a rotary anode generator and 2D detector, it was possible to detect Fe_3C below 1% by mass during austenitizing.

Additionally, during thermochemical processes, particularly in gas and plasma nitriding, X-ray diffraction techniques have been developed and applied to laboratory diffractometers [150,151]. These experiments utilized the Bragg–Brentano geometry (θ–$2\,\theta$) XRD diffractometer with a scintillation counter detector and chromium radiation.

In [14,19,152,153], in-situ investigations during the austenitization and quenching of the steels 100Cr6 and 20MnCr5 were carried out by means of synchrotron X-rays, without prior carburization. Epp et al. conducted experiments at the European Synchrotron Radiation Facility (ESRF) in Grenoble, France, on beam line ID11. Heat treatments were conducted using commercial heating device (ETMT, Instron, Pfungstadt, Germany) using resistive heating. Throughout the entire heat treatment process, diffraction frames were recorded in transmission mode using the FRELON (ESRF, Grenoble, France) camera with an exposition time of 0.4 seconds for each frame during quenching. The beam energy was set at 71 keV, and the primary beam size was 100 µm high and 300 µm width. The recorded frames were integrated using dedicated software, and subsequent diffraction patterns were analyzed through Rietveld refinement using the TOPAS software. The kinetics of the martensitic transformation could be described. In both steels, massive plastic deformation of the austenite was observed during the transformation. The state of phase stress during the quenching of different austenitizing temperatures was monitored in a time-resolved manner by means of in-situ X-ray diffraction. The development of hydrostatic stresses (residual) in austenite could be tracked in time, and experimentally demonstrated for the first time. It was thus

confirmed that very high hydrostatic residual compressive stresses can develop in the retained austenite. Precise analysis of lattice constants also enabled accurate determination of the dissolved carbon content. It was shown that self-tempering effects and carbon accumulation of austenite occur during quenching, presenting difficulties in accurately determining hydrostatic stresses [19,153].

Additionally, Villa et al. conducted two in-situ synchrotron radiation experiments with 100Cr6 steel samples austenitized at very high temperatures to dissolve all carbon in austenite [154,155]. In these experiments, tempering and cryogenic treatments down to 77 K were performedat quenched state which contains both martensite and retained austenite. In-situ synchrotron angular XRD was performed at the MagS station (HZB-BESSY II) in Bragg–Brentano geometry. Heat treatments were carried out in a dilatometry setup to record the process related volume changes. The wavelength of the radiation was 0.1 nm, focused on a 1 mm spot. The quantification of the measured phases was performed by fitting Lorentzian functions to the recorded line profiles. Integrated intensities of γ {200}, γ {220} and γ {311} for austenite; α' {200}/{002} and α' {211}/{112} for martensite were considered. The effect of thermal strain due to differences in thermal expansion coefficients of austenite and martensite led to the creation of tensile stresses when no transformation occurs. Following the martensitic transformation, compressive stress generation was observed. These experiments demonstrated the creation of hydrostatic compressive stresses in austenite as a consequence of the martensitic transformation. The findings of in-situ study were also supported with ex-situ synchrotron measurements at the EDDI station (HZB-BESSY II). Reflection geometry was applied for stress analysis in a θ–2θ configuration and the scattering angle was fixed at $2\theta = 8°$. The beam slit aperture was set to 0.5 mm to 0.5 mm, and the vertical aperture of the detector slit was 0.03 mm. The stresses were calculated by using $sin^2\Psi$ method.

Furthermore, energy dispersive synchrotron X-ray diffraction investigation was also conducted by Villa et al. to investigate the in situ the evolution of lattice strains and stresses in austenite and martensite during quenching and tempering of a soft martensitic stainless steel [156]. Heat treatment was conducted by using an Anton Paar DHS 1100 Domed Hot Stage under a continuous flow of protective Argon gas. During the investigation, martensitic stainless steel was quenched from an austenite temperature of 920 °C to 175 °C rapidly, and then the temperature is further reduced to room temperature with decreasing cooling rate. Investigation was performed in situ at the EDDI beamline of the BESSY II synchrotron facility. The acquisition time was 60 seconds per diffractogram and the experiments were conducted with a 0.5 to 0.5 mm slit configuration on the primary side that applies the diffraction geometry θ–2θ=7–14 deg. The equatorial slit aperture was set to 0.03 mm. The measurements were performed in both $sin^2\Psi$ configuration, i.e. Ψ angle was varied, and also configuration of perpendicular scattering vector and surface normal (constant Ψ angle). Diffraction lines were fitted with a pseudo-Voigt profile function for further analyses. Results gained from this study also confirm a compressive stress generation in austenite after martensitic transformation, and additionally show that stresses acting on martensite is also compressive from

the beginning of the austenite to martensite transformation (in presence of 5 ma. % martensite) until the end (93 ma. % martensite).

A similar study conducted by Allain et al. [157] also confirmed the generation of hydrostatic compressive stresses in austenite from the beginning of martensitic transformation until the end during quenching. This study was carried out at the DESY PETRA P07 beamline (Hamburg, Germany) by using a Bähr dilatometer for heat treatment. The monochromatic beam having energy of 100 keV combined with a fast 2D Perkin-Elmer detector were used in transmission mode. The 2D diffraction patterns produced during the experiments were integrated using the Fit2D software and further analyzed by the full Rietveld refinement procedure. Diffraction peaks were modeled with pseudo-Voigt functions using FullProf software.

Several in-situ quenching and partitioning investigations were conducted to investigate the microstructural changes during these treatments. Again, Allain et al.[158] conducted experiments at the European Synchrotron Radiation Facility (ESRF) in Grenoble, France, on beam line ID15B under a powder diffraction configuration by using commercial heating devices of Instron. The energy of the monochromatic beam was 87 keV and 2D Perkin-Elmer detector was used to gather data. Different acquisition time of 0.3 Hz and 10 Hz were set depending on the process step. The 2D diffraction patterns were integrated using the Fit2D and further analyzed with a full Rietveld refinement procedure. The diffraction peaks were modelled using a pseudo-Voigt function. During measurement, the sample underwent quenching from the austenitic temperature to a quench temperature of 230 °C, followed by reheating to 400 °C and a subsequent soaking period at that temperature for partitioning. During quenching after martensite formation, researchers observed a the generation of second order internal compressive stresses in austenite induced by the high level of martensite fraction. Throughout reheating, no change was observed in the microstructure. However, during holding at 400 °C, an increase in the body-centered cubic (BCC) structure was noted, attributed by the authors to the formation of bainite at that temperature. Additionally, increase of the austenite lattice parameter was observed during the holding step which is attributed to either carbon enrichment of austenite or relaxation of the stresses in martensite. The authors suggested that the former reason was more likely, considering the slow kinetics of stress relaxation at the given temperature

Huyghe et al.[159] also performed quenching and partitioning experiments at the high resolution ID11 beam line of the ESRF (Grenoble, France) with the beam energy of 65 keV. They also used an electrothermal mechanical testing system from Instron. A FReLoN CCD camera with 5 Hz acquisition rate was used for data collection. Similar to the previous studies, Fit2D software was used for azimuthal integration. Quenching and partitioning (Q&P) experiments were conductedat different quenching temperatures of 280 °C, 320 °C and 360°C along with single partitioning temperature of 400 °C. Carbon enrichment in austenite was observed during both reheating and also holding step. The study proposed two mechanisms for carbon enrichment which are bainite transformation and martensite carbon depletion. Carbon enrichment due to martensite carbon

depletion was found to be kinetically faster since it occured already during the reheating stage. On the other hand, the carbon enrichment following bainite transformation was slower as bainite formation and austenite carbon enrichment are coupled. The authors also highlighted that the specific contribution of each mechanism depends on the initial quenching temperature. For lower quench temperatures, carbon partitioning from martensite is stated as the major contributor while for higher quench temperatures carbon rejected from bainite transformation is attributed as the major contributor.

Hosseini et al.[160] also conducted quenching and partitioning investigations by using a high-temperature strip heater chamber HTK 2000 N (Anton Paar), mounted on a Panalytical Empyrean lab diffractometer. The in-situ XRD measurements were carried out using monochromatic Cu-Kα radiation at 40 kV and 45 mA. Two long 2θ ranges, (41-91)° and (27-85)° with scanning time of 109s, and two short 2θ ranges (41-46)° and (27-33)° with scanning time of 15s, were considered for phase identification. HighScore Plus v 4.8 software and PDF4 (2019) database were utilized to perform phase quantification. Heat treatments were conducted under high vacuum. Steel samples were quenched from austenite temperature to 165 °C and reheated to three different partitioning temperature of 280 °C, 400 °C and 500 °C followed by different holding times. For all samples, a decrease of the amount of austenite phase along with an increase of austenite lattice parameter were observed during the holding steps. This was attributed to the dissolution of retained austenite at enrichment of the austenite by carbon. Similar to the previous study, these changes were attributed to the carbon depletion from martensitic and bainitic transformation. The study also highlighted that the rate of bainitic transformation at 400°C was considerably higher in comparison to the 280 °C partitioning temperature. At 500 °C partitioning temperature, rapid depletion of martensite was observed, leading to the ferrite and tempered martensite at final microstructure. Finally, Fe_2C and $Fe_{2.5}C$ carbides were reported even in the very early stages of all partitioning temperatures.

In all of these in-situ investigations, researchers were able to observe the rate of phase transformation from austenite to martensite during quenching, noting a deviation in the austenite lattice parameter from linearity due to compressive stresses generated during martensitic transformation. During partitioning step, an increase in the austenite lattice parameter was observed, despite the phase content remaining the same, which was attributed to carbon partitioning.

As part of in-situ investigations into thermochemical treatments, studies on ion nitriding can also be found in the literature. Manova et al. [161] conducted a study investigating the phase formation during low energy ion nitriding of nickel-chrome alloys. An auxiliary heating stage was used for low energy treatment with process temperatures ranging from 350 °C to 500 °C. A Bragg–Brentano geometry diffractometer equipped with Cu cathode and 1D position sensitive detector was used for in situ XRD measurements. Authors were successfully able to observe the formation of tetragonal Ni_4N phase during implantation phase.

Similar experiments of ion nitriding of austenitic stainless steel were also conducted by again Manova et al [162] using same system and temperatures mentioned above. Further investigations of ion nitriding can also be found in literature [16,163].

Ion nitriding is conducted at lower temperatures compared to low-pressure carburizing, and it does not require hydrocarbon gases, making the implementation of this treatment in in-situ studies easier. Consequently, such studies have been performed previously. However, as of the author's best knowledge, there has been no in-situ XRD investigation of low-pressure carburizing followed by quenching.

3 Material and Experimental Method

3.1 Sample Preparation

The investigations were performed with conventional case hardening AISI 5120 (EN 20MnCr5) steel. The chemical composition of the steel measured by spark optical emission spectroscopy (S-OES) is given in Table 3-1.

Table 3-1: Chemical composition in ma. % of case hardening steels

	C	Si	Mn	P	S	Cr	Mo	Ni	Al	Cu
20MnCr5	**0.20**	0.25	1.26	0.017	0.031	1.26	0.030	0.039	0.03	0.024

Samples were machined into rectangular prism shapes with dimensions of 5 mm thickness, 14 mm length, and 14 mm width. In order to eliminate carbon diffusion from undesired sides during in-situ experiments, five surfaces of the samples were coated with a 5-8 µm thick Zirconium nitride (ZrN) by using PVD method, leaving the top surface that is aimed to be carburized uncoated. Figure 3-1 shows samples' sketch and optical micrograph of the initial ferritic-pearlitic microstructure.

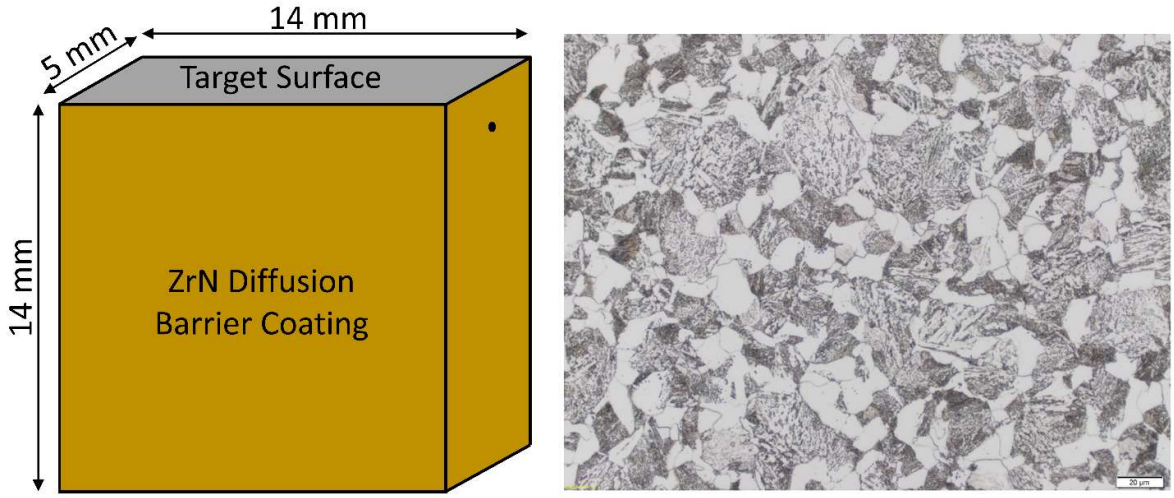

Figure 3-1: Drawing of the sample showing the dimensions, ZrN coating and target surface; and initial micrograph of the sample after standard metallographic preparation and 3.5 vol.% nital solution for 30 seconds.

The effectiveness of the coating was proved by comparing the carbon diffusion depth profiles of both coated and uncoated samples after the carburization process in an industrial furnace, specifically an Ipsen RVTC 224. Depth profile measurements were performed with GDOES (glow discharge optical emission spectrometry) and S-OES. For depths up to 80 µm, GDOES results were used, while S-OES results were taken for the depths beyond 90 µm. According to the measurement results given in Figure 3-2, increased carbon content is present in the coated sample in the first 5 µm, subsequently decreasing to 0.3 ma. % before stabilizing around the base carbon content at approximately 180 µm; on the other hand, the carbon content of the uncoated sample increased

from 0.2 ma. % up to 0.8 ma. %. Diffusion of carbon from side surfaces was mostly eliminated with ZrN coating. Since synchrotron XRD measurements in transmission give an integrated signal coming from the whole thickness of 5 mm, the increased carbon content within the first 5 µm represents 0.1 % of the total signal, which appears neglectable. Additionally, carbon would be able to diffuse under the coating up to 180 µm, resulting an average carbon content of 0.25 ma. % in these area, instead of 0.2 ma. %. Considering the 5 mm total thickness having 0.2 ma % carbon content, this penetration of the carbon only increase the average carbon content of the whole thickness from 0.2 to 0.2036 which can also be considered as neglectable.

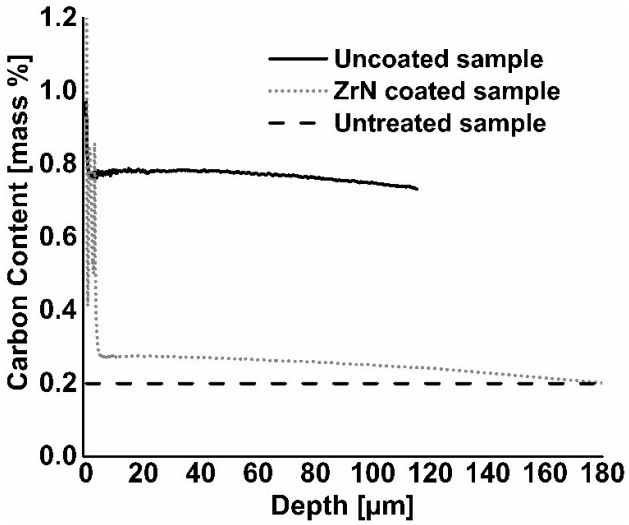

Figure 3-2: GDOES and S-OES results for depth profiles of carbon in uncoated and ZrN coated samples. Initial carbon content of untreated sample is also shown

3.2 Process Chamber and Control Units

In order to manufacture a process chamber for carburizing experiments, the cylindrical body and top cover were made out of stainless steel. Two circular windows were precision-machined to allow the beam path for transmission measurement. The chamber body also machined two supplementary longitudinal windows on the left and right sides for reflection measurement. Standard ISO-KF flanges were welded to the circular windows to form a viewport shape. These ISO-KF flanges and two longitudinal window openings were then covered with Kapton foils with 75 µm thickness to allow easy penetration of the X-ray beam while guaranteeing confinement of the chamber atmosphere.

Acetylene (C_2H_2) was used as carbon donor gas, and helium (He) was used as quench gas. Gas inlet pipe was positioned at the top, and vacuum outlet pipe was placed at the bottom to ensure that samples remained within the central portion of the gas flow. Gas supplies of the process were regulated with two mass flow controllers controlled by a Protherm 510 process control unit from United Process Controls GmbH/Germany. Pressure levels were monitored via a capacitance manometer and adjusted using a remotely-operated electro-pneumatic valve. In order to avoid any damage caused by high helium pressure during quenching in the case of failure of a vacuum pump

or electro-pneumatic valve, safety valve set to an open pressure of 33 mbar was connected to the chamber. Figure 3-3 shows the representative sketch of all components.

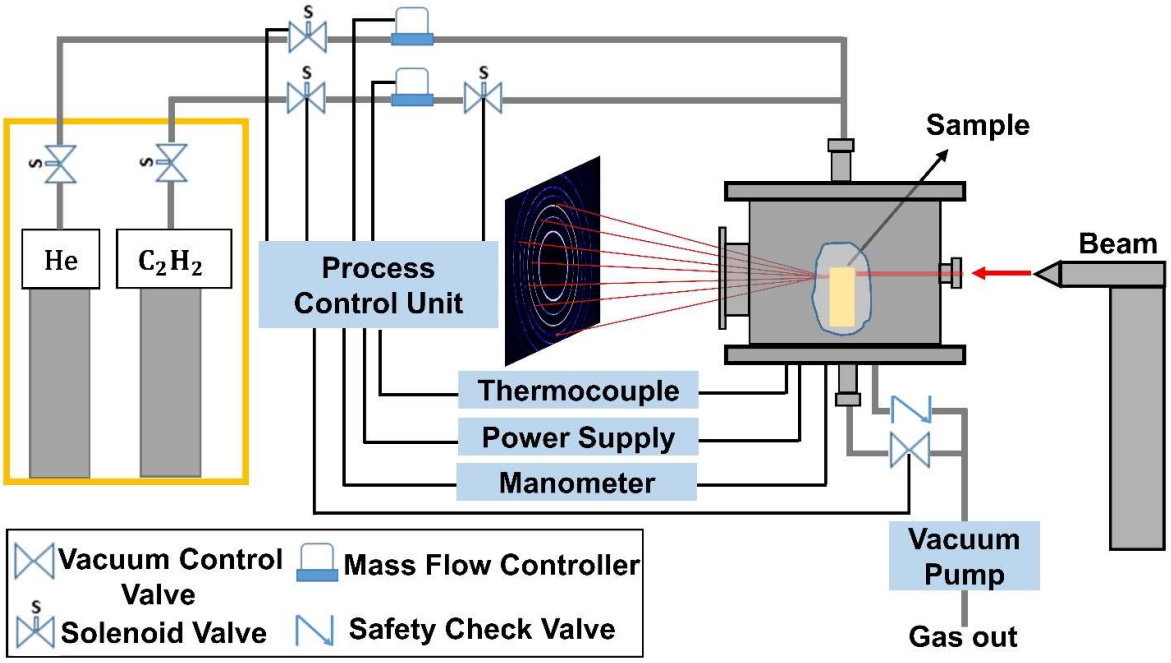

Figure 3-3: Representative sketch of the developed low pressure carburizing system

The sample was heated up using four SiN ceramic heating elements surrounding the sample and connected to an external power supply. The process control unit also adjusted the voltage of the power supply. The temperature was measured using a K-type mantle thermocouple inserted into a hole at the side of the sample, and data was recorded using Eurotherm temperature controller. One extra type-K thermocouple was also attached outside of the chamber to measure chamber temperature. All electrical components inside the chamber were made of copper-free material to eliminate any risk of acetylide formation since acetylides are sensitive to temperature, friction and bear a risk of explosion [164].

3.3 Process Scheme of In-situ Synchrotron Low Pressure Carburizing Experiments

Two synchrotron experiments were conducted in two different beam times. In the first, low pressure carburizing was applied to 20MnCr5 steel in transmission mode (see Figure 2-28), which is the main theme of this thesis. In the second beam time, the same steel grade was treated with the same parameters and measured in reflection mode with project partners (Karlsruhe Institute of Technology, Institute for Applied Materials – Materials Science and Engineering (IAM-WK)) in this collaborative project. In this measurement setup, sample is placed in the oven laterally to target only the surface with about 3 µm depth penetration to focus directly on the surface changes. As this method is not in the main scope of the thesis, detailed explanation of the measurement setup and

parameters are not given here. However, in the following sections, in related places, this method will also be explained briefly, and some results of this experiment will be presented and discussed to support the outcomes. In both beam times, several sets of process parameters were used and compared.

A representative example the process scheme for standard parameters is presented in Figure 3-4. Other process parameter variations will be explained in detail the results and discussion sections.

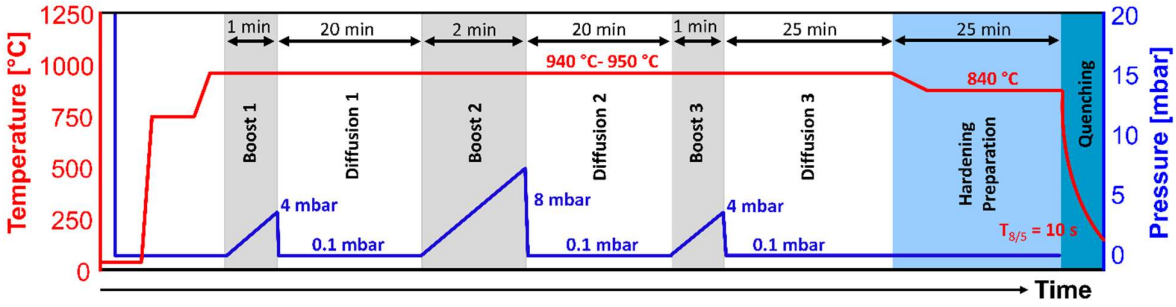

Figure 3-4: Standard process scheme of low pressure carburizing in in-situ chamber

Although low pressure carburizing in the experimental chamber gave very close results in comparison with that of industrial furnace (see comparative results in section 4.1), there are some differences that are required to be discussed. In the industrial furnace, carburizing and quenching were done in separate chambers, unlike the single chamber configuration in the experimental setup. Moreover, in the industrial process, all volumes of the furnace are heated rather than only the sample, and this makes temperature control easier compared to the experimental chamber. Furthermore, the absence of measurement windows makes the sealing of the industrial furnace better than that of the experimental chamber. The lowest vacuum reached in the experimental chamber was about 10^{-1} mbar, as seen in Figure 3-4, while in the industrial furnace, $5 \cdot 10^{-2}$ mbar can be achieved. Lastly, pressure control during boost step is not possible in the experimental chamber due to the relatively small volume compared to the capacity of the available vacuum control pump; therefore, a maximum limit of 33 mbar was set with the help of a check valve. For the shorter boost steps of 1-2 minutes, this caused minimal difference in the process compared to industrial furnace as pressure increased up to maximum 8 mbar (see Figure 3-4). However, for longer boost steps, pressure limit of 30 mbar was reached. These differences necessitate the comparison of the result of industrial furnace and the newly developed chamber to prove the reliability of the process.

The experiments and the results represented in this thesis are divided into four parts. In the first part, given in section 4.1 and section 4.2, the reliability of the chamber and repeatability of the process will be validated by comparing samples carburized in the industrial furnace and experimental chamber, using the same process parameters given in Figure 3-4. The main motivations to use these parameters were, first, to have 3 boost/diffusion cycles which give sufficient data for reliable comparison; and second, these parameters have been proven several times by

simulations and experiments to give approximately 0.8 % surface carbon content and targeted 0.6 mm case hardening depth (CHD).

In the second part, given in section 5.1, an investigation of microstructural changes for every step of low pressure carburizing and explanation of data analyses will be demonstrated

In the third part, section 5.2, microstructural changes during carburizing experiments conducted with different parameters will be presented. Three process parameters, which are temperature, boost diffusion/cycles and acetylene amounts, were varied. For each variation, two samples were investigated.

The fourth and final part will demonstrate and discuss the results of the change of stress state during different steps of carburizing experiments in section 6.

3.4 Set-up for In-Situ Synchrotron Experiment

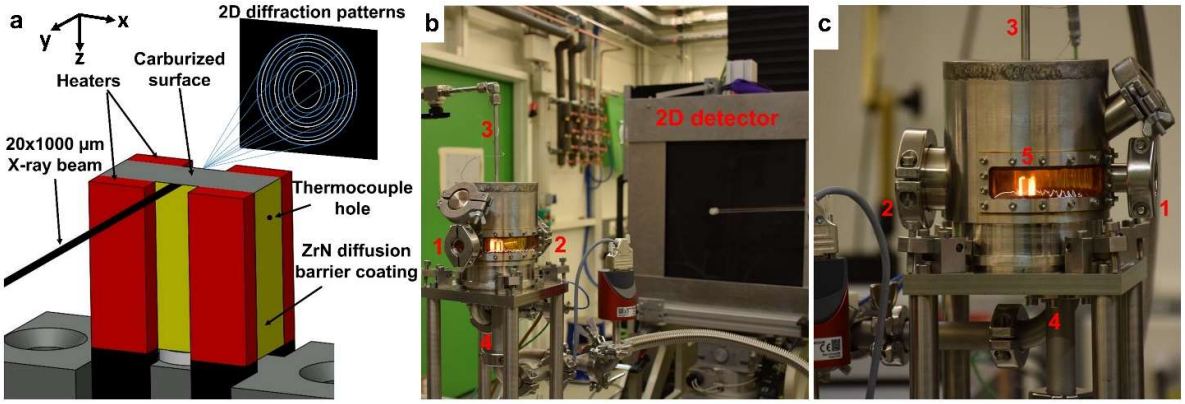

Figure 3-5: Drawing of sample alignment in transmission mode; (a) pictures of the chamber at high temperature (b,c).1 and 2 are beam in and out windows respectively; 3 and 4 are gas in and out pipes respectively and 5 is sample at process temperature.

The drawing of the sample alignment and photos of the chamber in operation are presented in Figure 3-5. The heaters were placed in such a manner that central sample region was accessible for the measurements by scanning over the vertical z-axis.

At the beginning of each process, the sample was placed between four SiN ceramic heating elements, and the chamber was evacuated until the pressure of 10^{-1} mbar was reached. The sample was then heated up to process temperature with an average heating rate of 120 °C/min to achieve a full austenitic state. Upon reaching the process temperature, first boost step was initiated by introducing acetylene into the chamber with 1.2 bar pressure and a rate of 10 ml/min (8.4 m^3/m^2h). In the presence of acetylene, the pressure inside the chamber increased. Following the end of the first boost step, the chamber was evacuated from the remaining gases and kept at process temperature for diffusion step to enable carbon diffusing in the sample to expand the carburizing region. This was the completion of one boost and diffusion cycle. This cycle was repeated as necessary according to the process plan to reach the desired carbon profile.

After the repetition of cycles, the temperature was gradually decreased to the hardening preparation temperatures and kept constant for homogenization, further diffusion and to ensure a low carbon content in solution in the austenite. Afterwards, the sample was quenched down to less than 100 °C using helium gas at 5 bar. The above-mentioned process parameters, such as process temperature, duration of boost and diffusion step, and hardening preparation temperature, varied depending on the experimental plan.

Several experiments with various process parameters were conducted, and each was repeated at least once to validate the repeatability/reproducibility of the findings. Table 3-2 provides the overview of the experiments conducted for the comparison of the effect of process parameters. The number of combinations in the process parameters shows the duration of boost and diffusion in minutes. For example, 5/20 means that the sample has a 5-min. boost step followed by a 20-min. diffusion step. Each cycle of this boost-diffusion is separated with double dots (..).

Sample names reflect the investigated process parameter. Designations of LF, HF, LT, HT, 4-BD and 3-BD represent “Low-flow,” “High-Flow,” “Low-Temperature,” “High-Temperature,” “4-Boost-Diffusion cycles” and “3-Boost-Diffusion” cycles, respectively. These designations also convey the effect of aimed process parameters. For example, LF-10ml and HF-80ml have 10 ml/ min and 80 ml/min flow rates, respectively, designed to investigate the effect of acetylene flow rate.

To demonstrate the repeatability of the processes and data analysis procedure, the repetition of sample 3-BD is named as 3-BD-R, facilitating a comparison of results.

Table 3-2: Overview of all experiments

Sample	Temperature	C_2H_2 Flow	Boost/Diffusion step time
LF-10ml	940 °C	10 ml min^{-1}	5/20..5/20
HF-80ml	940 °C	80 ml min^{-1}	10/20..10/20
LT-920C	920 °C	10 ml min^{-1}	1/20..1/20
HT-960C	960 °C	10 ml min^{-1}	1/20..1/20
4BD	940 °C	10 ml min^{-1}	1/20..1/20..1/30..1/45
3BD	940 °C	10 ml min^{-1}	1/20..2/20..1/25
3BD-R	940 °C	10 ml min^{-1}	1/20..2/20..1/25

3.4.1 Synchrotron X-ray Measurements Procedure

The transmission diffraction experiments were performed on Beamline P07-EH3 of the PETRA III Synchrotron at DESY/Hamburg. Table 3-3 gives general information about Hutch P07-EH3.

Table 3-3: General Information about P07-EH3

Photon Energy Range	tunable 33 - 200 keV
Optics	two bent Si(111) Laue crystals on Rowland geometry
Beam Height	1400 mm above the floor
Hexapod	heavy load of 1 t with resolution of +/- 1 µm
Detectors	Mar345 image plate, Perkin-Elmer XRD 1621, PILATUS3 X CdTe 2M
Available Software	image-viewer, a2tool DESY, fit2D, MARViewer

The energy of the monochromatic X-ray beam was set at 103.4 keV, which permits to work in transmission through the whole thickness of the steel sample. Measurements were done with a primary beam height of 20 µm to obtain a satisfying spatial resolution in the direction of the carbon gradient, while the beam width was chosen as 1000 µm for all experiments to obtain the best statistical conditions possible in terms of diffracting domains, as well as keep the measurement time as short as possible. Full diffraction rings were measured in the range of 0–12° 2θ angles with 0.2 s/frame to 1 s/frame time resolution depending on the duration of the experiment steps. Short acquisition times were used for the steps in which rapid changes happen, such as boost and quenching steps, while longer acquisition times were chosen for slow steps, such as diffusion and hardening preparation.

Data is collected using a 2D detector (Perkin-Elmer with 2048×2048 px and a pixel size of 200 µm) placed 1.325 m behind the sample. Temperature information was recorded through a thermocouple with a time resolution of 1 s/data. Special attention was paid to combining the temperature and diffraction data with different time resolutions to ensure perfect continuity between different steps without any artefacts.

For the whole experiment, approximately 150000 single 2D diffraction frames were recorded, averaging around 2500 frames per process. The 2D patterns were integrated using the fast PyFAI software [165] in order to generate 2θ vs. intensity graphs for further analyses.

3.4.1.1 Boost and Diffusion Steps

During measurement, one of the main focuses of the experiment was to observe the microstructural changes taking place in the surface region of the sample during the LPC. As a results, the X-ray beam position was consistently maintained directly below the surface, with an acquisition time of 0.2-0.5 s/frame during boost steps. Before each boost step, the determination of the surface position was achieved by surface entry scans.

In the surface entry scans, samples were systematically scanned from above the surface towards the surface itself, with 10-20 µm step size. The first detected peak was taken as a reference surface. However, measurements were performed 10-20 µm below the reference surface from the point that gave 800 - 1000 counts intensity for the first austenite γ {111) peak. Figure 3-6 illustrates the detected peaks as an example during surface entry scans.

It can be noticed that scans start from the air where no signal is detected. The initial signals originate from the edge of the sample, where there is only slight contact. Since the sample surface has some roughness from the production and the position of the sample is not perfectly flat, some minor portion of the beam passes through the sample's edge. A further step towards the depth having around 500 counts peak is the sample surface. However, measurements from this point do not provide sufficient intensity for peaks with high 2θ angles, and they are susceptible to intensity loss due to sample positon changes.

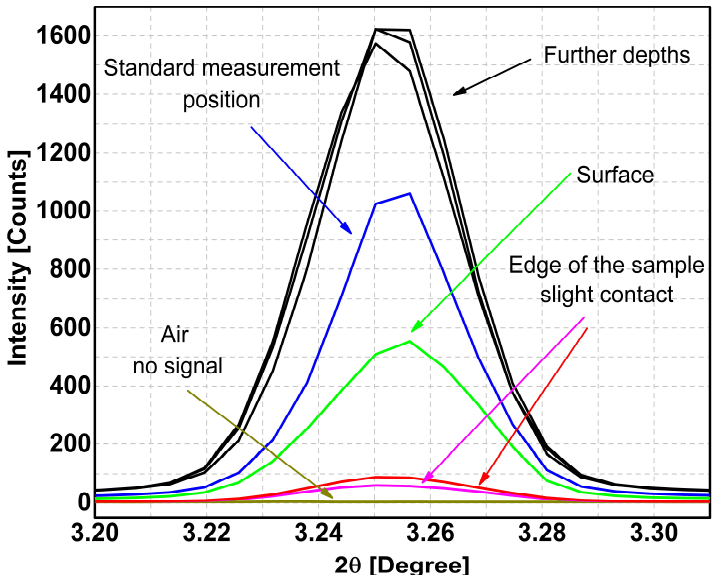

Figure 3-6: Austenite γ {111) peaks measured at different positions during surface entry scan.

It is important to address these sample positon changes here. Throughout the process, variations in the sample volume took place due to process-related temperature changes. Since the experimental chamber and samples are relatively small, these changes were induced because of any interference to the process atmosphere, such as the opening and closing of the vacuum valve, introduction of acetylene into the chamber, or thermochemical reactions on the sample surface. These changes led to sharp temperature changes of about 5-15 °C, which caused the stationary beam position to drift from the predefined position of the carburized surface. In response to such changes, the beam position was adjusted with this entry scan until the optimal intensity was attained. The impact of these changes on the measurement data and results will be discussed in further sections.

Therefore, to mitigate these challenges, instead of the position giving an intensity of around 500 counts, one further depth giving around 800 - 1000 counts for austenite γ {111) peak was chosen as the standard measurement position. After a step further, intensity continues to increase. This is an indication that some portion of the beam was still in the air at the standard measurement positon, which is desired since changes at the very top surface are aimed to be observed; while at further depths, all beam passes through the sample and no further increase is observed. These entry scans were repetitively conducted throughout the entire process to ensure consistent and accurate measurements.

During diffusion and hardening preparation steps, the beam position was either kept constant directly at the surface, or continuously scanning over the depth from the carburized surface with 0.5-1 s/frame acquisition time. This strategic adjustment in beam positioning allowed for the successful observation of microstructural evolution, carbide formations, and carbon diffusion.

3.4.1.2 Quenching Step

During the quenching step, the objective was to observe the evolution of microstructures and stresses near the surface region; consequently, the X-ray beam was kept at the surface. In previous steps, beam position adjustments due to temperature variations were made with entry scans since these changes were small and there was sufficient time to perform these scans. However, due to the sudden nature of the quenching process, placement of the beam at the precise position and additional adjustments during the process were impossible. Thus, the exact beam position in this step was not known during the experiments.

To address this challenge, the strategy for the quenching step was to estimate the precise beam position after the measurement based on the data and supplementary investigations, and interpret the results accordingly. One such supplementary investigation to estimate the beam position involved conducting heating/cooling tests within the same experimental system while simultaneously measuring the change in surface position using the laser triangulation method. During this measurement, an optoNCDT model blue laser triangulation device from Micro-Epsilon Messtechnik GmbH/Germany was utilized.

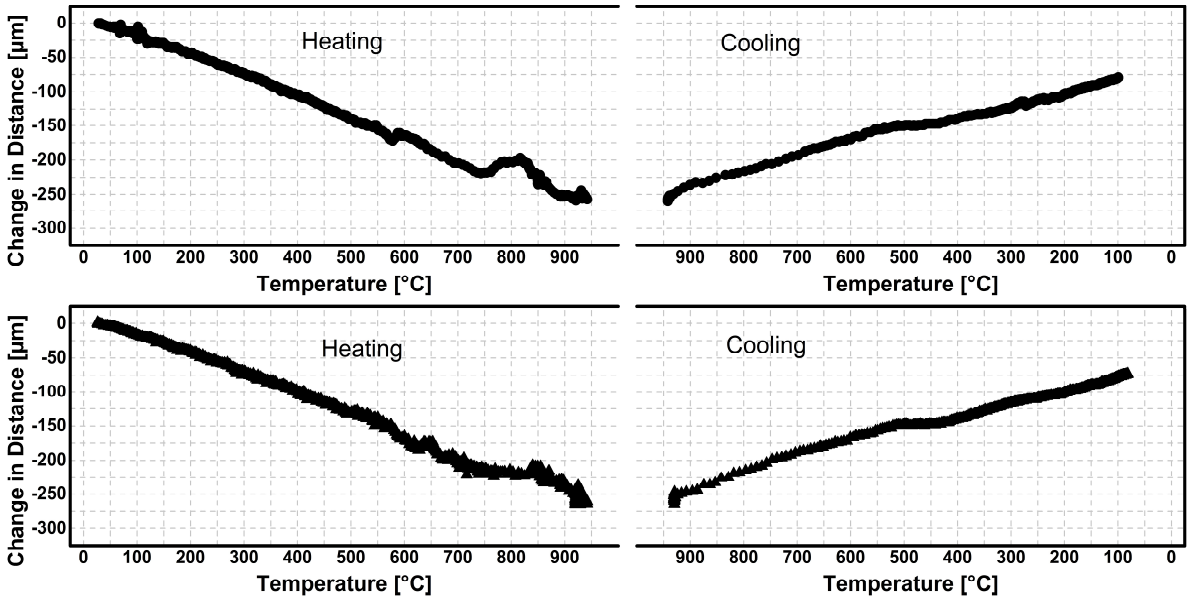

Figure 3-7: Change of surface position determined by laser triangulation during heating and cooling for two different samples

The results presented in Figure 3-7 show that the thermal expansion of the entire system is quite consistent and around 250 µm. The good precision of measurement can also be assumed by observing the effect of austenitic transformation on expansion at around 700 °C. This measurement provides the total thermal shrinkage of the system for the estimation of the change in beam position during quenching.

Since trial measurements were also made in the synchrotron to determine the effect of shrinkage, measurement positions for quenching were chosen around 200 µm below the standard

measurement position described in the previous section. Thus, the final position of the beam at the end of the quenching was near the surface area.

The determination of variations in beam position is especially important for stress analyses rather than phase analyses. Phase analyses mainly cover martensitic transformation, which starts at the surface around 210 °C – 250 °C depending on the carbon content and measured until around 90 °C was reached, the final quenching temperature of the system. Beam shifting between this temperature interval is around 25-30 µm at the near surface area where there is no sharp carbon gradient; thus, it can be neglected. In contrast, stress analyses start with generating thermal stresses in austenite at high temperatures, meaning that the measurement position is decisive for clarifying outcomes. Therefore, a detailed description of the change of beam position during quenching will be given in the stress analyses section 6.4 with related examples and illustrations.

3.4.2 In-situ Phase Analyses

For a detailed determination of the evolution of phase fractions and lattice parameters, the integrated diffraction patterns were analyzed using the Rietveld refinement in convolution-based fundamental parameters approach implemented in TOPAS 6.0 Academics (Coelho Software, Australia) [166].

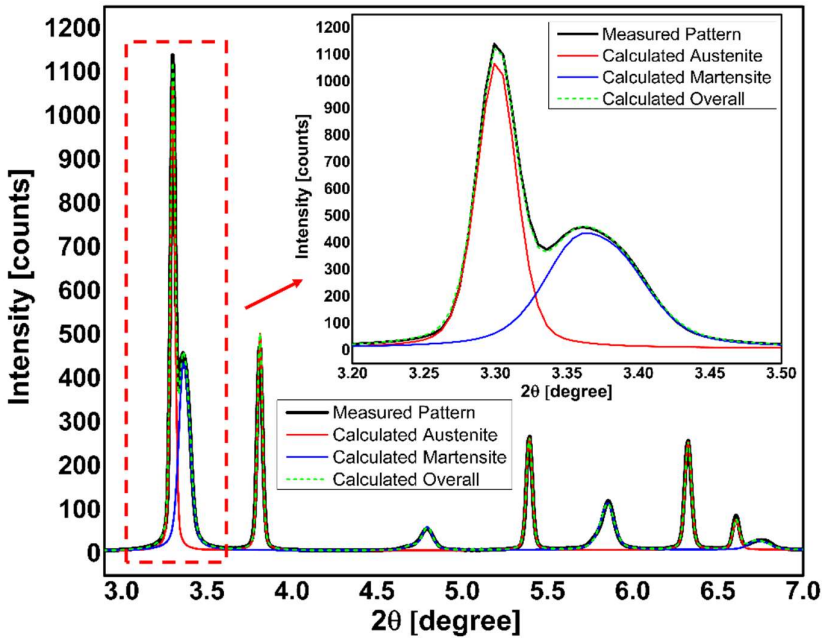

Figure 3-8: Example of X-Ray Diffraction Full Pattern Refinement using TOPAS version 6.0 for carburized 20MnCr5 steel.

In order to show the reliability of the program and fundamental parameter approach, one of the examples of diffraction data obtained from carburized 20MnCr5 sample is given in the Figure 3-8. This data was taken during the quenching of the sample, which has about 60 ma. % of austenite and 40 ma. % of martensite. As can be seen in the small part of the diffraction pattern, the double peak of γ {111} austenite and α' {110}/{101} martensite are separated successfully, which is particularly advantageous for obtaining reliable results. Moreover, the calculated overall pattern

shown with the green dashed line is in very good agreement with measured pattern shown with the black line.

TOPAS software uses the parameter called "*R-weighted pattern (Rwp)*" to quantify the goodness of the fit (GoF). It is a percentage value reflecting the difference between the measured and calculated pattern, meaning that a lower Rwp value is an indication of a better fit. This particular example in Figure 3-8 gave a 5.2 % Rwp value. For most of the data, calculated Rwp values were between 4 % and 8 %.

The instrumental contributions to the diffraction peak profiles were determined using measurements of 5 mm thick (same as sample thickness) standard LaB6 NIST SRM660C powder sample. Determined fitting parameters were then fixed and used as an instrumental data analysis function. For the first approximation, during the boost, diffusion and hardening preparation steps, only austenite and cementite $(Fe,Cr)_3C$ were taken into account. For the quenching step, the microstructural model containing austenite and martensite with a BCT lattice was used.

3.4.3 In-situ Stress Analyses

As it is already mentioned in section 2.7.3, cake analyses were performed to determine the change in stress state during in-situ measurements of different process steps. It was also pointed out that the quality of the peaks depends on the azimuthal degree interval of the cakes. Ideally, these intervals should be minimized to enhance the precision of directional stress determination. However, a balance must be found, as excessively small azimuthal angles may reduce peak quality for fitting. It is also shorlty mentioned in section 2.7.3.1 that total stress tensor can be expressed as the sum of two distinct stress tensors: hydrostatic tensor, responsible for the volume change of the material, and deviatoric tensor, responsible for the shape change of the material. These tensors have a different effect on the diffraction rings. Hydrostatic strains/stresses extend or constrict the ring equally in every direction, meaning the ring's radius can be determined equally at every azimuthal angle. On the other hand, deviatoric stresses deform the ring unequally, creating an elliptical shape or higher-order ring distortion.

In this thesis, both deviatoric stress and total stress were determined separately in the longitudinal direction (x-direction in Figure 3-5) separately for the different steps of the LPC treatment.

3.4.3.1 Determination of Deviatoric Stress

In order to determine deviatoric stress, each full diffraction rings of individual data were divided into 72 equally spaced 5° azimuthal cakes. A single peak of austenite γ {311} and martensite α' {211} were used to determine stresses in each phase and their position was determined by using the pseudo-Voigt function. Subsequently, from peak positions, 72 lattice spacings were found by using Bragg´s law. Stress-free lattice spacing (d_0) was then determined by taking the average of these 72 d-spacing. Following this, 72 strain values were calculated by using this stress-free lattice spacing. All these 72 strain data were then fitted by the fundamental equation given as

$$\varepsilon_{\varphi\delta} = \varepsilon_{xx}(cos^2\theta sin^2\delta) + \varepsilon_{xz}(cos^2\theta sin2\delta) + \varepsilon_{zz}(cos^2\theta cos^2\delta) \qquad \textit{Eq. 3-1}$$

This is the transformed and simplified version of the fundamental equation. Detailed mathematical background is given in Section 2.7.3.1. A representative figure of 72 cakes and the results of fitting are given in Figure 3-9.

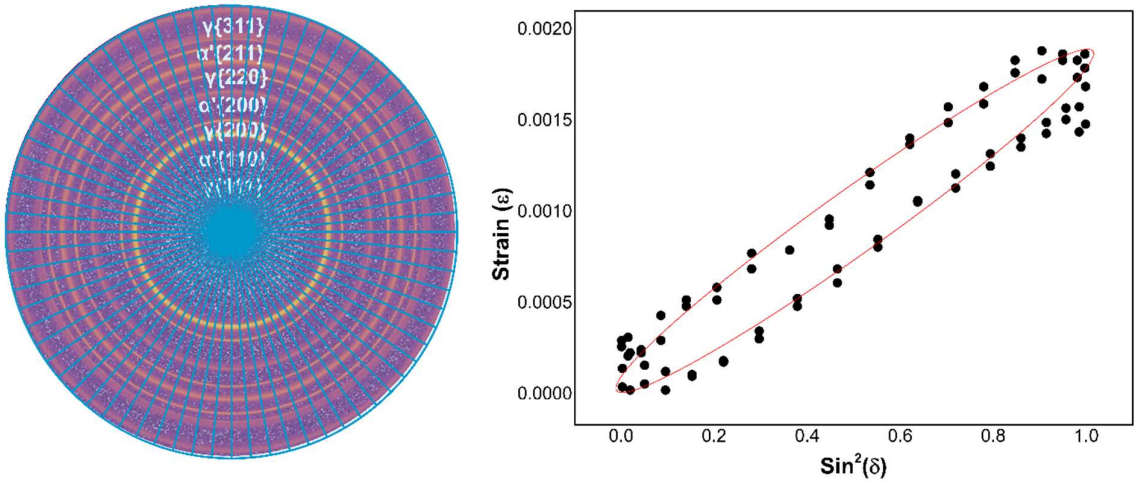

Figure 3-9: Representation image of 72 equally spaced 5° azimuthal cakes and fitting of fundamental equation.

As can be seen, the figure looks similar to that of a conventional $sin^2\Psi$ method with the modification of Ψ angle to δ angle due to synchrotron system.

From this fitting, the required strain values of ε_{xx}, ε_{xz} and ε_{zz} are determined. As a final step, strain values and material constants are introduced to Eq. 3-2 to find stress values.

$$\varepsilon_{\varphi\delta} = -\frac{v}{E}(\sigma_{xx} + \sigma_{zz}) + \frac{1+v}{E}(\sigma_{xx}cos^2\theta sin^2\delta + \sigma_{zz}cos^2\theta cos^2\delta) - \frac{1+v}{E}\sigma_{xz}cos\delta sin2\theta \qquad \textit{Eq. 3-2}$$

3.4.3.2 Determination of Total Stress

All processes of integration of the rings are the same for total stresses; therefore, they will not be repeated here. The only difference is the determination of stress-free lattice spacing (d_0). Unlike deviatoric stress, where an average value of 72 cakes is used as deviatoric stress creates a deviation from the perfect circle, the determination of total stress relies on the accurate determination of stress-free lattice spacing (d_0), which is quite challenging due to the carbon gradient in the measured volume and variation of temperature.

For austenite, full integration (360° azimuthal) of the data was performed during quenching and hkl specific lattice spacings of austenite (d^{311}) were determined by fitting the austenite γ {311} peak using the Pseudo Voigt function and Bragg's Law (Eq. 2-18). At the early stages of the quenching (800 °C-550 °C), linear change of d^{311} was determined and the linear thermal expansion coefficient (CTE) was calculated. It was then assumed that the sample was stress-free due to high temperature

in early stages of the quenching and this linearity of stress-free hkl specific lattice spacing (d_0^{311}) was valid until the end of quenching step. Therefore, data were extrapolated until the end of the quenching step and temperature-dependent stress-free lattice spacings ($d_0^{311}(T)$) were calculated. As each sample has a different carbon gradient, the CTE of austenite was determined individually.
For martensite (α') / ferrite (α), experimental data showed that thermal expansion is not linearly dependent on the temperature. The main reason for this is that these phases are generally present with the second phase (mainly austenite), which affects the accurate determination of CTE of pure bulk. There are still some models that suggest linear relations based on experiments conducted with very low carbon steels [34,167]. Additionally, some models propose quadratic equations for the CTE of martensite lattice parameters with respect to temperature based on experimental data [168–170]. In this thesis, the model suggested by Seki and Nagata [169] was adopted with an addition of carbon dependence. The reason for using this model is that Seki and Nagata have conducted an experiments using iron powder which is more reliable to measure stress-free lattice parameter changes, and they gas carburized the powder to see the effect of carbon content, which is quite similar to the experiments conducted in the scope of this thesis.
Suggested model for the Seki and Nagata can be seen in Eq. 3-3,

$$\alpha_0 = 1.602 \cdot 10^{-9} \cdot T^2 + 2.059 \cdot 10^{-6} \cdot T + 0.2860 \qquad \textit{Eq. 3-3}$$

where T is a temperature in Kelvin. Notably, this equation lacks carbon dependence since experiments by Seki and Nagata do not consider the effect of quenching and associated carbon trapped in martensite. In the context of this thesis, solely using the literature data would not give reliable results, as residual stress in martensite is influenced by factors such as carbon content, quenching rate, and quench finish temperature. Consequently, this equation had to be modified based on the experimental data of this study. This modification was made by addition of carbon dependence to the intercept (0.2860) of the equation, which Seki and Nagata originally assumed as a stress-free pure iron lattice constant at room temperature.
In order to introduce carbon dependence, in the first step, residual stresses of the samples at carburized surface were measured by using laboratory X-ray diffraction devices, with measurement parameters given in the next section, 3.5. Complementary Methods. Then, these residual stress values were taken as a reference for the measurements made at room temperature with synchrotron radiation. Afterwards, for all samples, intercept value of the formula was adjusted to a certain extent that gave the same reference stress values at room temperature synchrotron measurements. Then, linear fitting was applied to these values to create a formulation for carbon dependence. Figure 3-10 shows the intercept values that give the reference stresses and corresponding linear fitting. The value at 0 % carbon is 0.2860, which is the intercept value of Eq. 3-3, taking iron powder as a reference. Determined intercept and slope were then added to the formula.

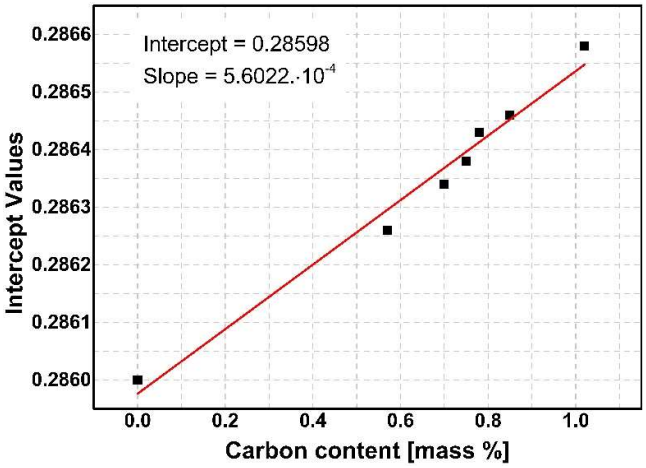

Figure 3-10: Intercept values that gives the reference stress values for synchrotron measurements

Then, final modified formula giving the stress free lattice parameter is obtained as given in Eq. 3-4;

$$\alpha_0 = 1.602 \cdot 10^{-9} \cdot T^2 + 2.059 \cdot 10^{-6} \cdot T + (0.28598 + 5.6022 \cdot 10^{-4} \cdot M_c^A) \qquad \textit{Eq. 3-4}$$

$$d_0^{hkl} = \frac{a_0}{\sqrt{h^2 + k^2 + l^2}} \qquad \textit{Eq. 3-5}$$

where M_c^A is the carbon content dissolved in austenite before quenching in ma. %. Additionally, for the determination of the stress-free lattice spacing in martensite, a cubic structure is assumed and Eq. 3-5 is used. After the determination of stress-free lattice spacing, similar to deviatoric stress calculation, strain values are determined by using the strain formula (Eq. 2-25).

It is necessary to mention here that the quenching rate is also very influential for the determination of stress-free martensite lattice parameter, which is not included in the formula. All in-situ experiments were conducted with the same system, and only the samples with the same quenching rate but different carbon contents will be presented. Therefore, the effect of the quenching rate is assumed to be negligible. In different systems, the proposed model might give different results.

Additionally, laboratory measurements penetration depth is only at 2-5 µm but synchrotron data is measured with 20 µm beam height. Moreover, it can be noticed that there is a difference between actual intercept values and the fitting line in Figure 3-10. As determined stress values are sensitively dependent on the stress-free lattice parameters, errors, to some extent, are inevitable, which should be kept in mind for interpretation of the results.

3.4.3.3 Determination of Elastic Constants

In section 2.7.3, the fundamental equation for stress determination was transformed to another form (see Eq. 2-38) that is suitable for synchrotron data. This form of the equation contains three stress components (σ_{xx}, σ_{zz}, σ_{xz}) and two hkl dependent elastic material constants for each phase, namely elastic modulus, E, and poisson's ratio, ν.

In order to investigate the generation and/or the relaxation of stresses at different temperatures, the knowledge of these elastic constants at each temperature is required. For this purpose, the data published by Richter [171] were used. These values, given in the reference, can be seen in appendix section 10.8. In order to obtain the temperature dependency for the whole LPC temperature range, polynomial fitting was applied to these values. Generated formulas from these fittings for austenite (γ) and martensite (α´) can be given as

$$E^{\alpha'}(T) = 212 - 0.5147 \cdot T - 5{,}15726 \cdot 10^{-5} \cdot (T)^2 \qquad \textit{Eq. 3-6}$$

$$E^{\gamma}(T) = 197.86 - 0.07945 \cdot T \qquad \textit{Eq. 3-7}$$

$$v^{\alpha'}(T) = 0.2847 + 2.8261 \cdot 10^{-5} \cdot T - 4.3296 \cdot 10^{-8} \cdot (T)^2 + 1.1757 \cdot 10^{-1} \cdot (T)^3 \qquad \textit{Eq. 3-8}$$

$$v^{\gamma}(T) = 0.2759 + 5.7219 \cdot 10^{-5} \cdot T \qquad \textit{Eq. 3-9}$$

The values presented in Richter's works are temperature depended macroscopic elasticity constants; therefore, they should be converted to crystallographic plane specific contents, called X-ray elastic constant (XEC). Formulation for this transformation is given as [120];

$$\frac{1}{2}S_2 = \frac{1+v}{E} \; and \; S_1 = \frac{-v}{E} \qquad \textit{Eq. 3-10}$$

$$\frac{1}{2}S_2^{\{hkl\}} = \frac{1}{2}S_2[1 + 3(0.2 - \Gamma^{\{hkl\}})\Delta] \qquad \textit{Eq. 3-11}$$

$$S_1^{\{hkl\}} = S_1 - \frac{1}{2}S_2[0.2 - \Gamma^{\{hk\}}]\Delta \qquad \textit{Eq. 3-12}$$

$$\Gamma^{\{hkl]} = \frac{h^2k^2 + k^2l^2 + l^2h^2}{(h^2 + k^2 + l^2)^2} \; and \; \Delta = \frac{5(A_{Rx} - 1)}{3 + 2A_{RX}} \qquad \textit{Eq. 3-13}$$

Where A_{Rx} for Fe-based materials having BCC and FCC structure are 1.49 and 1.72, respectively. Determined three strain values and XEC values are then introduced into Hooke´s law (Eq. 2-28) together with calculated material constants in order to find stress values.

The main focus would be the quenching step since stresses are predominantly generated during this step. Therefore, the results of the different samples with different carbon contents will be given in the following sections for quenching step. For other steps of the LPC, only the change of stress state of one sample will be presented exemplary.

3.5 Complementary Methods

After heat treatment, metallography, scanning electron microscope (SEM) and following electron back scattered diffraction (EBSD) analysis were performed to analyze the present microstructure and phases. For metallographic investigation, cross-section of the samples were ground, mechanically polished, and subsequently etched with 3 vol.% Nital solutions for 30 seconds. Microstructure images were captured using a light microscope and Phillips XL-30 model SEM with EBSD attachment. EBSD analyses were made with 25 kV voltage and 10-20 mm sample distance. OIM v8 pattern indexing software was used.

Additionally, electron micro probe analysis (EMPA) was utilized to verify the elemental distribution. EMPA measurements were performed with Joel JXA-8200 device with 15 kV acceleration voltage, and calibration of the device was made by using same grade of steel as the investigated sample. Measurements were taken from surface to 1 mm depth and width of 100 µm. The increment size was 1 µm in each direction with 20 ms/increment measuring time.

Micro-hardness measurements were conducted to obtain hardness distribution from the surface to the core. Leco-Universal LM series micro-Vickers hardness tester was used, applying different forces from 5 to 300 N for a dwell time of 15 seconds. Five measurements were taken, and then the average value of the hardness was calculated. The case hardening depth (CHD) was defined as the distance from the surface at which the hardness is 550 HV.

Carbon content depth profiles were determined by using either S-OES or GD-OES. A Thermo ARL 3460 device and LECO GDS-750A device are used for S-OES and GDOES, respectively.

In order to perform ex-situ residual stress measurements, an analytical X-ray MZ-VI-E diffractometer with Hecus position sensitive detector (PSD), and an ETA 3003 model with Braun PSD from GE Inspection Technologies were used. Measurements were made with chromium radiation with a 2 mm collimator using $\sin^2\Psi$ method on martensite α' {211} in 2θ range of 145°-164°. Psi angle was varied $\pm$45 in 13 equidistant steps with an exposure time of 150 seconds.

4 Functional Examination of In-situ Chamber

As mentioned before in Section 3.3, experiments conducted in the scope of this thesis were divided into four parts. The first part, proving the reliability of the chamber and the repeatability of the process, will be presented in this section.

4.1 Qualification of the In-situ Experimental Chamber for Low Pressure Carburizing

Although process recipes are the same, there are several differences between processes conducted in experimental chamber and industrial furnace. The existence of these process and equipment-related differences necessitates proof of the accuracy of the chamber.

4.1.1 Microstructural Comparison of Samples Carburized in Both Systems

The LPC treatments at 940 °C with boost/diffusion durations of 1/20, 2/20 and 1/25 (see Figure 3-4 and sample 3BD in Table 3-2) were conducted in the industrial furnace and experimental chamber. Then, the microstructure and surface-near region are compared by optical microscopy and EBSD. Figure 4-1 shows the metallography results of two samples.

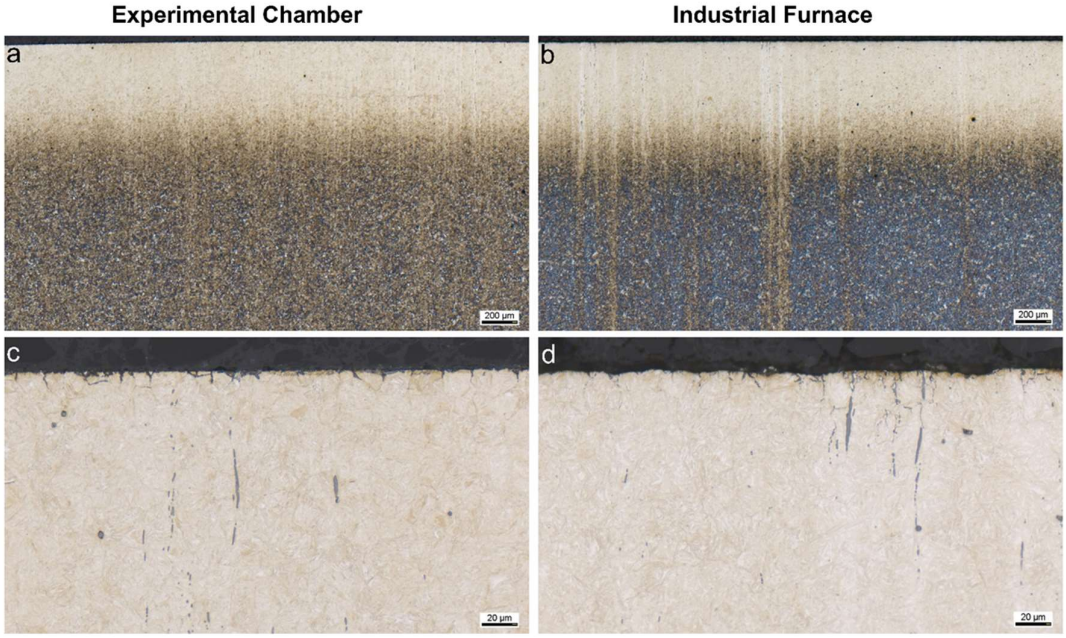

Figure 4-1: Comparison of microstructure obtained at the surface in industrial furnace and in the experimental process chamber after nital etching.

The overview pictures of the cross section show a comparable bright etching case and transition point to a dark-etched core region for both samples at approximately 550 µm depth. The surfaces have a martensitic structure with a similar amount of retained austenite in both samples. MnS

inclusions from base material are also observable in both samples. Slight color differences between the core structures can also be distinguished, which are attributed to slight differences in etching time. Also, it can be observed that the thermal etching of the grain boundaries of the sample treated in the experimental chamber is slightly more pronounced than the industrial chamber. The reason might be the higher amount of oxygen present in the experimental chamber than industrial furnace. The phase distribution at the first 100 µm from the surface was also determined with EBSD, and results are given in Figure 4-2. Distributions are rather similar. Austenite content determined by image analyses are 8.4 % for 3BD sample and 8.9 % for industrial furnace sample. The slightly higher retained austenite content of sample from industrial furnace can also be distinguished in the image. Although, the sample preparation for EBSD measurement generally reduces the amount of retained austenite, this data is still beneficial when combined with the other examinations to support the whole comparison.

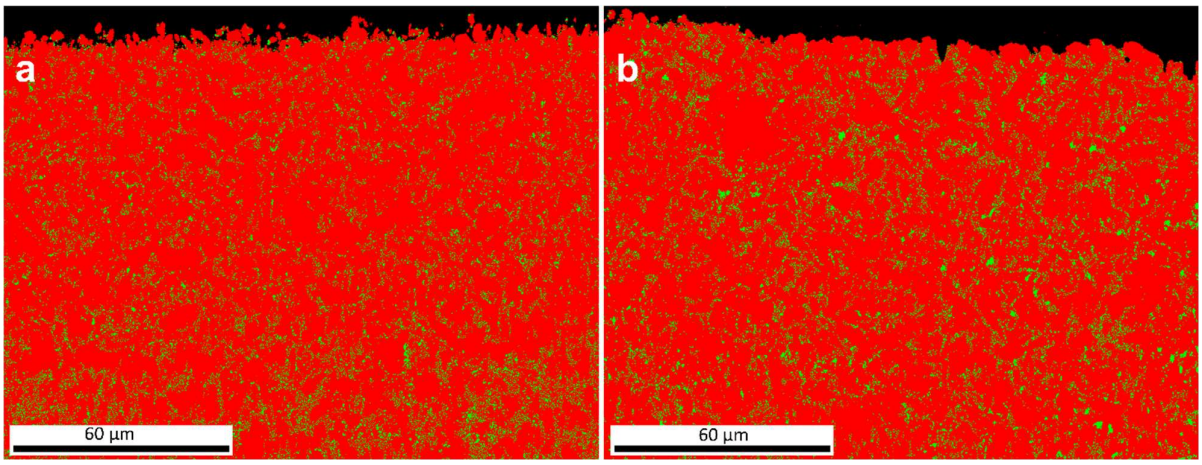

Figure 4-2: EBSD phase analyses of sample 3BD from the experimental chamber (a) and sample from the industrial furnace (b). The red phase is martensite/bainite, green phase is austenite.

4.1.2 Carbon Content and Micro-hardness of Samples Carburized in Both Systems

Figure 4-3 shows carbon content and micro-hardness depth profiles for sample 3BD, carburized in the experimental chamber, along with two other samples carburized in the industrial furnace with the same process parameters.

The overall carbon contents of all samples are close to each other. The sample carburized in the industrial furnace batch 1 has slightly higher carbon content, especially in the first 200 µm. Such variations can be observed in different batches, despite the same process parameters. Depending on the position of the sample in the furnace, even samples in the same batch can show some differences.

On the other hand, the overall hardness distributions of the samples are quite similar. The case hardening depth of the experimental chamber, batch 1 and batch 2 in the industrial furnace are 0.62, 0.64 and 0.66 mm, respectively. Therefore, no significant differences in the achieved case properties regarding microstructure, carbon content and hardness can be observed. According to

the results, it can be concluded that the resulting case properties of the sample carburized in the in-situ oven are fully comparable with that of the industrial furnace.

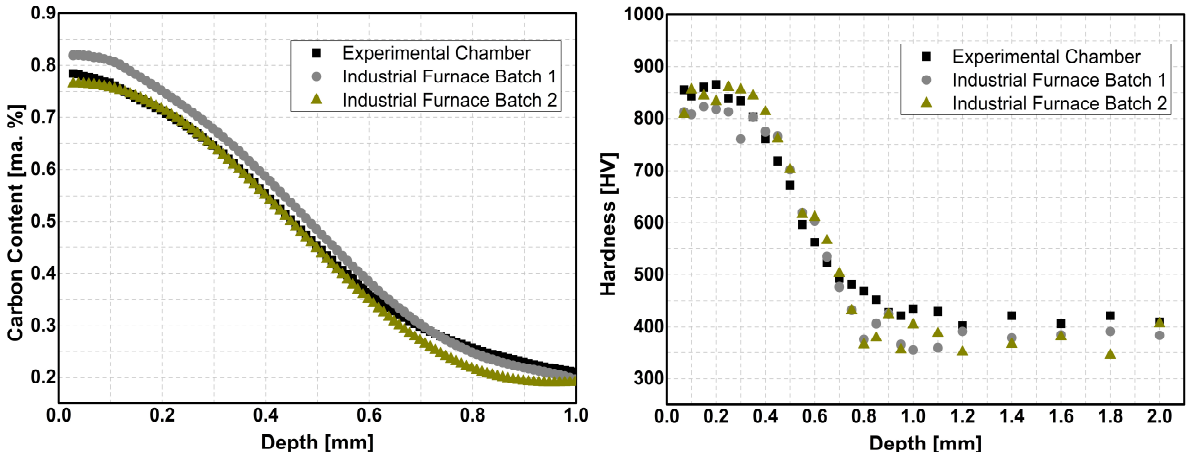

Figure 4-3: Comparison of carbon content (left) determined by Electron microprobe analyses (EMPA), and micro-hardness (right) depth profiles of sample 3BD, and two different samples from the industrial furnace.

4.2 Repeatability of Processes Conducted in In-situ Experimental Chamber

In order to demonstrate the repeatability of the processes, two samples, sample 3BD from the previous section and sample 3BD-R (see Table 3-2), were carburized in the experimental chamber with standard parameters given in Figure 3-4. Then, the two structures were compared in an optical microscope. Figure 4-4 shows the metallography results of the two samples.

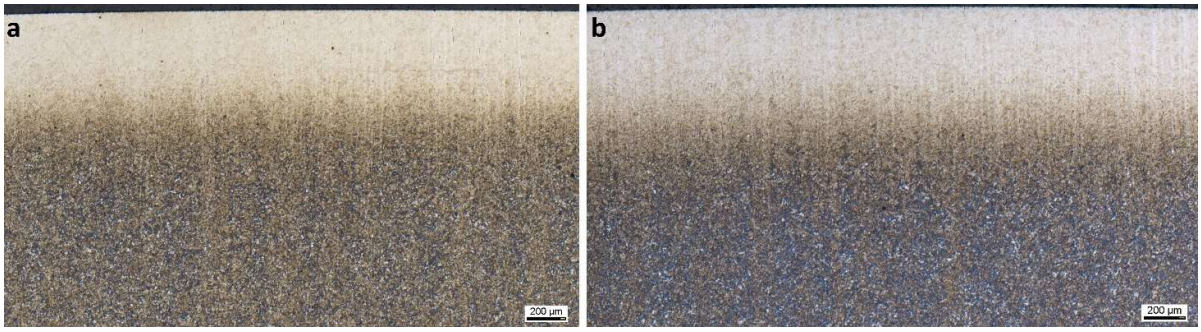

Figure 4-4: Comparison of nital etched microstructures obtained from Sample 3BD (a) and Sample 3BD-R (b) after carburization with same process parameters in the experimental chamber.

The overview pictures of the cross section show a similar transition point for both sample 3BD and sample 3BD-R at approximately 550 µm depth. The surfaces exhibit a martensitic structure with a comparable amount of retained austenite in both samples. Figure 4-5 shows the diffraction patterns measured at 40 µm depth of both samples at room temperature after the LPC and quenching. They show very similar final results with around 19 ma. % and 17 ma. % retained austenite for sample 3BD and sample 3BD-R respectively. The reason for this retained austenite difference can be attributed to slightly different measurement depth positions during scanning. As mentioned in section 3.4.1 and represented in Figure 3-6, measurement point that gave the first austenite γ {111)

peak after slight edge connection (see Figure 3-6) is considered as the surface, or the 0 µm position. From this point, depths are calculated based on that surface reference point multiplied by the step size. Due to sample roughness or uneven machining, the surface position might deviate from 0 µm, affecting the precise determination of further depths.

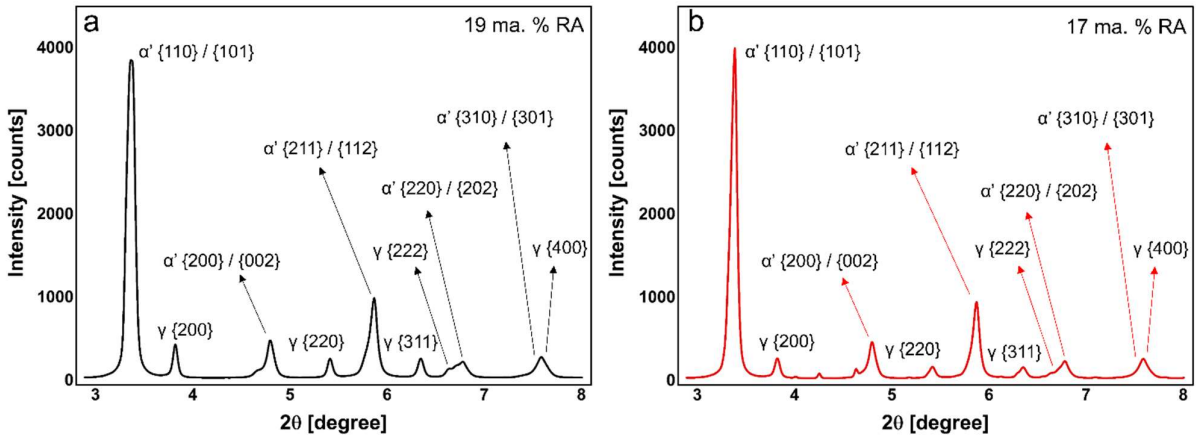

Figure 4-5: X-ray diffractograms of sample 3BD (a) and sample 3BD-R (b) gathered by Synchrotron at room temperature after the LPC with same parameters.

In addition to the metallographic structure and diffraction patterns, micro-hardness measurements were also conducted to compare both conditions. Figure 4-6 shows micro-hardness depth profiles of sample 3BD and sample 3BD-R. As can be seen from the figure, both samples have a comparable distribution of hardness over the depth.

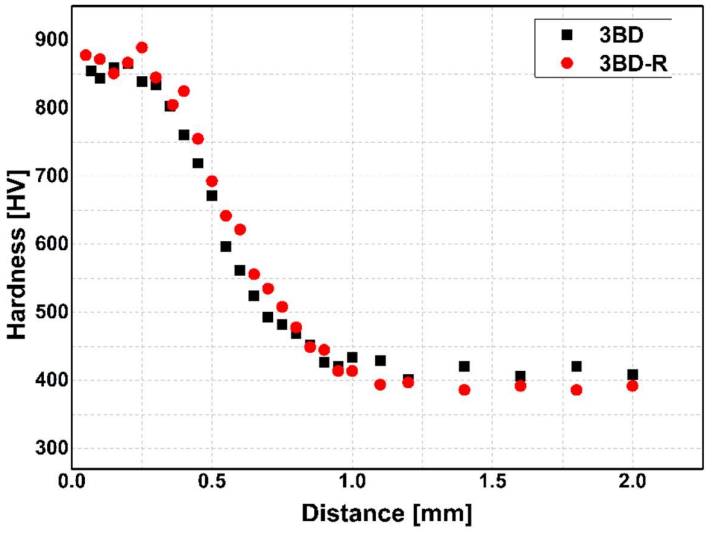

Figure 4-6: Comparison of micro-hardness depth profiles of sample 3BD and sample 3BD-R.

The post-process examination results indicate that, two samples carburized with the same parameters in different systems show very similar metallographic microstructure, and a comparison of carbon content and hardness distribution also supports this data. Considering the characteristics of both systems, slight differences in the carbon content distribution within the uncertainty range of

the investigation methods can be assumed as normal and expected. As low pressure carburizing is a non-equilibrium process in which carbon potential of the carburizing gas content cannot be controlled, the observed differences can be seen from time to time even between the different batches carburized with the same parameters and in the same system due to differences in the carburizing gas distribution in the furnace.

Therefore, it can be concluded that the newly developed experimental chamber is capable of producing comparable results to those of low pressure carburization and quenching conducted in an industrial furnace with very good repeatability, thus allowing its unrestricted use for fundamental research.

5 Results of In-situ Experiments and Discussion

In the first part of this section, the development of the data analyses procedure will be explained using two samples carburized with the same process parameters. The main focus will be the synchrotron measurements in transmission mode; however, results of the reflection mode and a description of the reflection measurement system will also be given to support the outcomes.
In the second part of this section, the results of the experiments with different LPC parameters will be presented and discussed. Three main parameter variations of process temperature, acetylene amount, and boost-diffusion cycle will be the discussion topic.
In the third and final part, the evolution of stress during different steps of the LPC will be observed. Samples with different carbon content gradients will be examined, and their stress profile will be discussed.

5.1 Development of Data Analyses Procedure

The primary measurement strategy in the synchrotron facility was to focus on changes in the carburized surface during the boost step, observe the carbon diffusion towards the depth during the diffusion steps, and focus on the surface again during the quenching step.

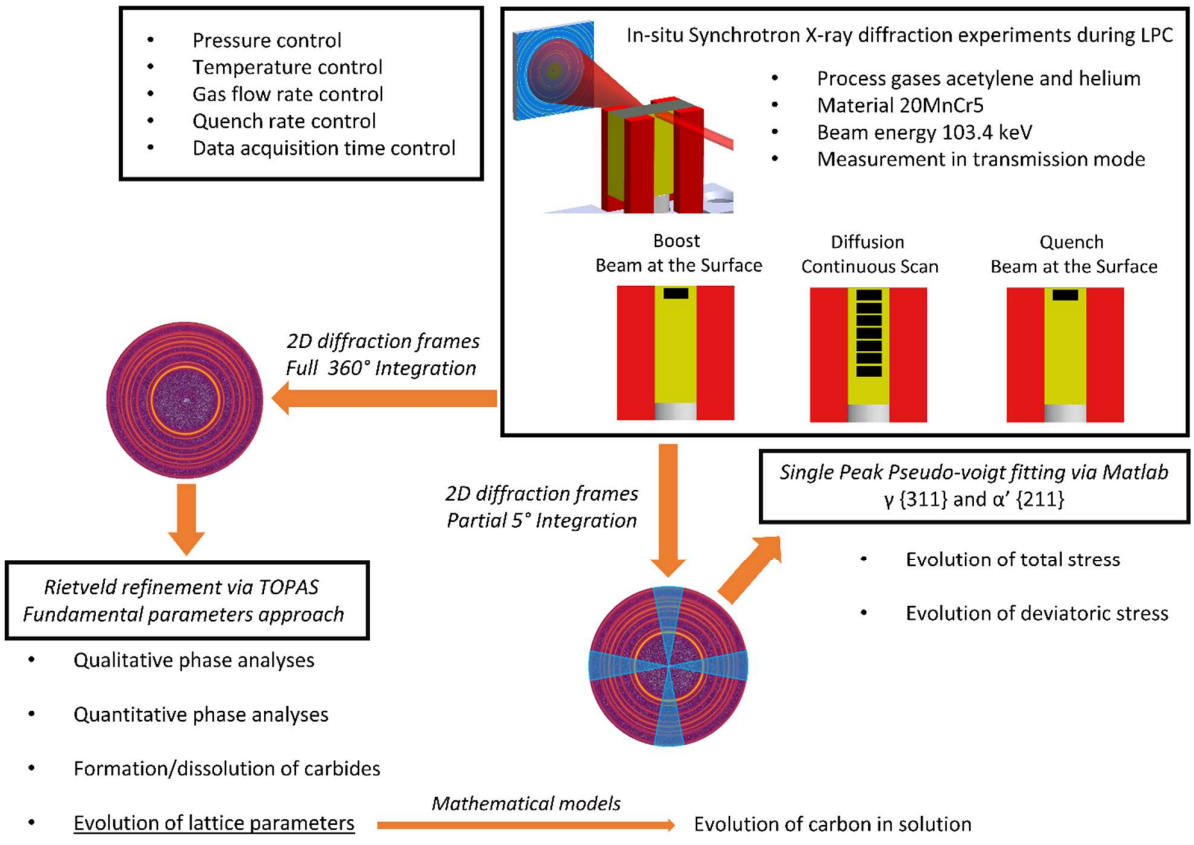

Figure 5-1: Flow chart that shows the synchrotron measurement strategy and data analyses procedure

Additionally, data analysis was separated into two parts: full and partial ring analyses. After full ring analyses, obtained diffractograms were further analysed with Rietveld refinement to gain information about phases, carbides and carbon content in solution. After full ring analyses, single peaks from obtained diffractograms were used for stress analyses. Figure 5-1 shows a flow chart that describes this procedure.

The data analyses procedure was started with the integration of raw synchrotron data by using Python-based, open-source software PyFAI, which is unified with a command line interface called Anaconda Prompt. A sequence of integrated diffraction patterns of sample 3BD from the previous section recorded at a fixed position directly below the carburized surface of the sample can be seen in Figure 5-2.

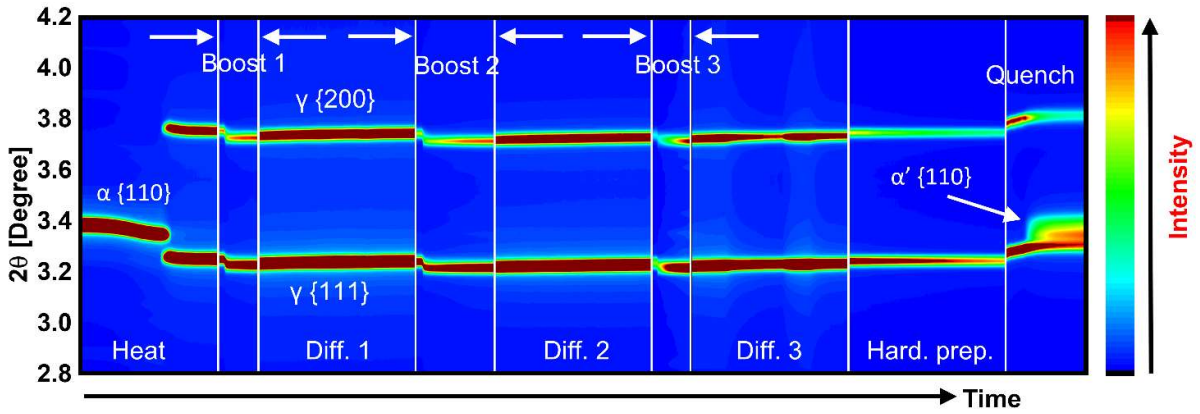

Figure 5-2: 2D contour plots of integrated diffraction patterns of sample 3BD during the whole process of heating, boost 1, diffusion 1, boost 2, diffusion 2, boost 3, diffusion 3, hardening preparation and quenching steps measured at the surface of the sample.

During the heating step, phase transformation could be identified by the disappearance of α {110} peak and appearance of γ {111} and γ {200} peaks. When the first boost step starts, austenite peaks shift to lower 2θ angles can be clearly observed. Figure 5-3 shows the shifting of the peaks during the first boost and diffusion step of the 3BD sample as an example.

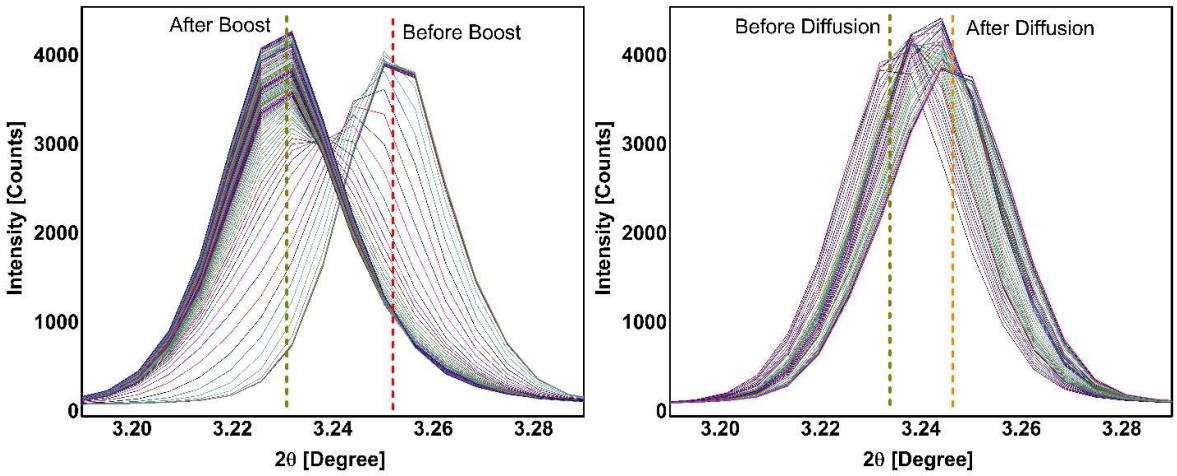

Figure 5-3: Austenite γ {111} peak shifting during boost and diffusion step. Dashed lines show the peak positions before and after corresponding step.

Given the peak is the diffractogram representation of the peak presented as a contour plot in Figure 5-2 in order to demonstrate the peak shifting more precisely. The shift can also be noticed from the contour plot.

Upon the impact of acetylene on the hot surface, peak shifting occurred rapidly in the initial seconds, followed by a relatively constant peak position despite the continuous presence of acetylene. In the following 20 minutes diffusion step, a gradual shift of the austenite peaks back to higher angles could be systematically observed.

During the second boost step, given in Figure 5-2, austenite peaks again shifted to lower 2θ angles further. Similar to the first boost step, a significant degree of shifting occurred within the first seconds of acetylene introduction, and peak positions remained almost constant until the end of the two minute duration. During the subsequent diffusion step, austenite peaks again slowly shifted back to higher 2θ angles. Images showing detailed peak shifting can be found in the appendix section 10.9.

During the final boost step, similar peak shifting to the lower 2θ angle could be detected, however, unlike other boost steps, after a very sharp initial shift, peak positions continued to shift to a lower 2θ angle instead of staying constant. Moreover, the intensity of the peaks are lower compared to previous boost steps, indicating that beam shifted slightly towards the top of the sample due to sample shrinkage. The effect of this phenomenon was already explained in section 3.4.1.1. However, during the following diffusion step, intensity increased back to the same level as previous diffusion steps. Nevertheless, in the following diffusion step, peaks shifted back to a higher 2θ angle very slowly as in previous diffusion steps. Images showing detailed peak shifting can also be found in the appendix section 10.9.

Sample 3BD-R also shows very similar behavior, which is hard to distinguish in 2D contour plots; therefore, the change of γ {111} austenite peak positions for both samples are given separately in the Figure 5-4. Very strong peak shifting in the early stages of the boost step can be seen clearly.

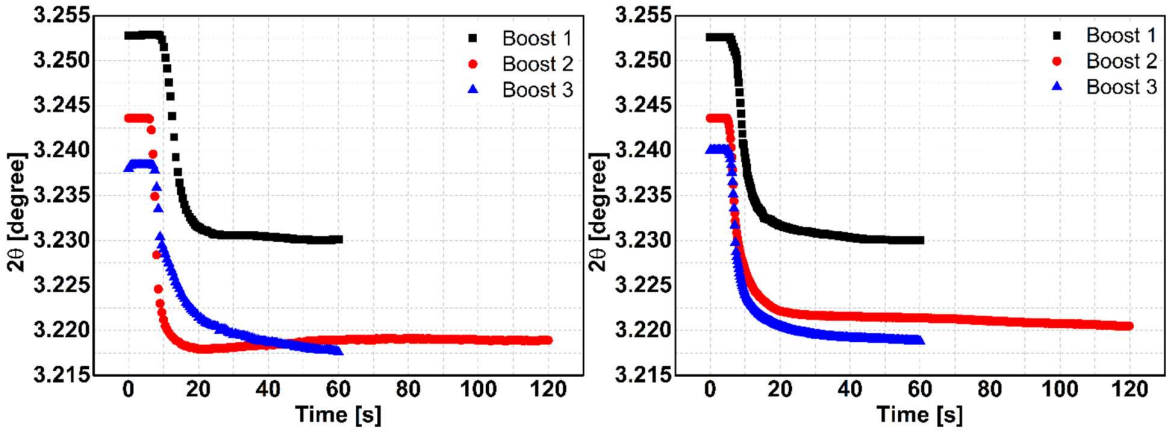

Figure 5-4: Change of γ {111} austenite peak position during boost step for sample 3BD (left) and sample 3BD-R (right).

After three boost and diffusion cycles, the temperature was reduced to 840 °C for the hardening preparation step. In this step, as seen in Figure 5-2 from the contour plot color change, the intensity of the peaks was reduced because of the previously mentioned thermal shrinkage of the sample

(see section 3.4.1). In the last steps of the process, the sample was quenched with high-pressure helium. Strong peak shifting towards higher 2θ angle could be observed in the first seconds, and then peaks continued to shift slowly. The martensitic transformation could also be observed in this step with the appearance of α' {110}/{011} and α' {200}/{002} martensite peaks displayed with a white arrow in the quench step. Also, austenite peaks are still present after quenching, indicating the presence of retained austenite.

Figure 5-5 shows the change of FWHM during the first and second boost steps of sample 3BD and sample 3BD-R as a representative example.

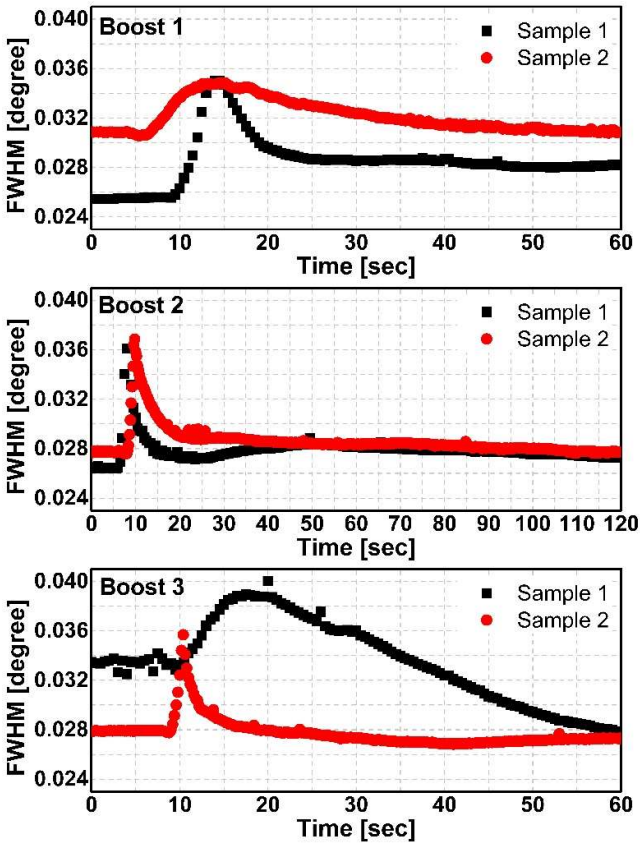

Figure 5-5: Change of FWHM of γ {111} austenite peak during first and second boost steps for sample 3BD and sample 3BD-R.

It can be seen that for both samples and both boost steps, FWHM increases when carbon uptake by the material starts. The increase in FWHM occurs together with peak shifting. This is attributed to lattice distortion due to increasing carbon in the interstitial solid solution. Although increase and decrease rates are not similar for all boost steps due to slightly different measurement positions, the trend is very similar. It can be concluded based on the comparison data of FWHM and carbon content that the processes are repeatable.

From the in-situ XRD measurements at the carburized surface of the sample, peak shifting towards lower and higher 2θ angles during boost and diffusion steps, respectively, and a sharp increase in FWHM during the boost step were observed. This is an indication of the change in lattice distances.

After analyzing integrated diffraction patterns, the austenite lattice parameter change of sample 3BD from the beginning of the first boost step to the end of the process was acquired by using Rietveld refinement. From the lattice parameter, the change of carbon content is then calculated by using the model developed by Onink (see Eq. 2-1). Evolution of both of these values is presented in Figure 5-6.

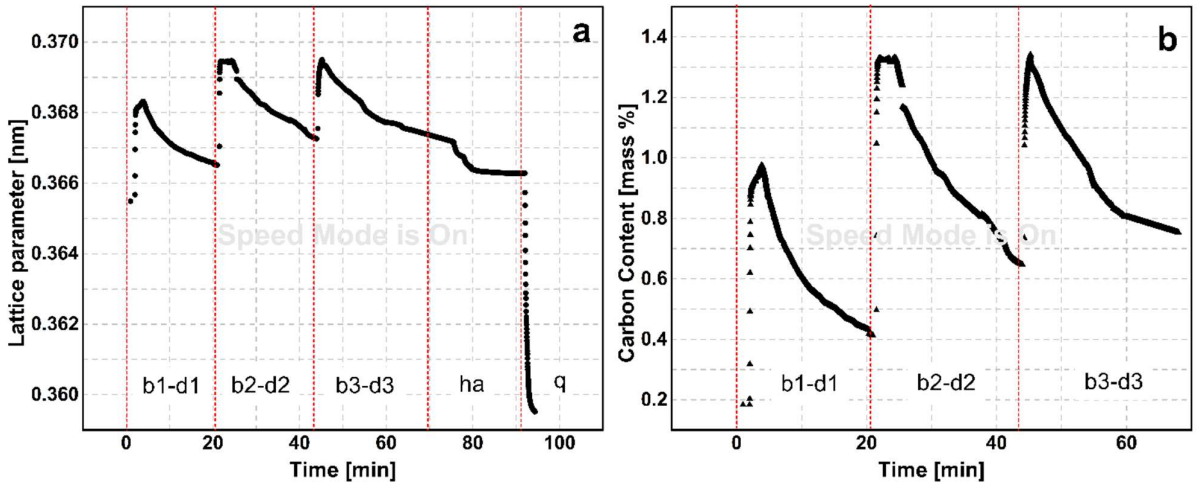

Figure 5-6: Evolution of lattice parameter of austenite (a) and of carbon content dissolved in austenite for sample 3BD measured from the top surface during boost 1 and diffusion 1 (b1-d1), boost 2 and diffusion 2 (b2-d2), boost 3 and diffusion 3 (b3-d3), hardening preparation (ha) and quenching (q).

A cyclic change of the lattice parameter and carbon content during boost and diffusion steps can be observed. The evolution of lattice parameter can be accounted for three contributions: chemical effect (changes in solid solution), thermal effect and stress-induced effect. During the boost and diffusion steps the temperature is mostly stable (within a few °C), and the sample is austenitic and relatively homogeneous in terms of compositions. Because of the present temperature, the effective stress relief and transformation from ferrite to austenite will relax all residual stresses previously present in the sample so that it can be considered stress-free. Therefore, the fast increase of lattice parameter at the beginning of each boost step was only attributed to the increasing carbon in solid solution in the austenite.

The following decrease in lattice parameter during diffusion and hardening preparation steps is a result of the redistribution of the carbon atoms induced by the diffusion towards the core. During the hardening preparation step, the lattice parameter decreases mainly due to temperature reduction, so other effects cannot be distinguished directly. In the last 15 minutes of the hardening preparation step, the lattice parameter stayed almost constant, indicating that no pronounced changes in local carbon content due to diffusion occurred during this period. In the quenching step, a very sharp decrease in lattice parameter can be seen due to thermal contraction.

The carbon content also follows a similar trend to the lattice parameter, as shown in Figure 5-6b. The evolution was given until the end of the third diffusion step, excluding the hardening preparation and quenching step, as the accuracy of the model of Onink decreases below 900 °C. In the following subsections, the change of carbon content will be examined in detailed for each step of the LPC.

5.1.1 Boost Steps

The evaluation of carbon content in solid solution can be calculated from the change of the austenite lattice parameter due to the occupation of octahedral sites within the austenitic lattice by the carbon atoms. As already mentioned in the previous section, the model developed by Onink from neutron diffraction experiment taking into account the thermal effect was used for the determination of carbon content [34]. According to the model, the lattice parameter of austenite is formulated as

$$a_\gamma = (0.363067 + 0.000783x_C^r) \cdot [1 + (24.92 - 0.51x_C^r) \cdot 10^{-6} \cdot (T - 1000)] \qquad \textit{Eq. 5-1}$$

where x_C^r is at. % carbon and *T* is the temperature in Kelvin. This formula was modelled by using pure iron, while the investigated steel has about 5 ma. % alloying elements (mainly Mn and Cr). Therefore, the initial nominal carbon content of 0.2 ma. % was taken as a reference, and the formula was tested according to this value. For most samples, the determined carbon contents at carburizing temperature before starting the first boost step were very accurate, so error margins were less than 0.02 ma. %. In a few cases, an error margin of up to $\pm$ 0.04 ma. % was also observed. Based on the determined deviation, all values were corrected and $\pm$ 0.04 ma. % error margin can be assumed as the maximum possible error range. Additionally, values determined by the given formula gave very close results to those of electron microprobe analyses. Therefore, it can be concluded that the formula gives a good and reliable estimation of carbon content in the austenite.

Figure 5-7 shows the change of average carbon content dissolved in austenite during boost steps for two different samples after conversion in ma. %.

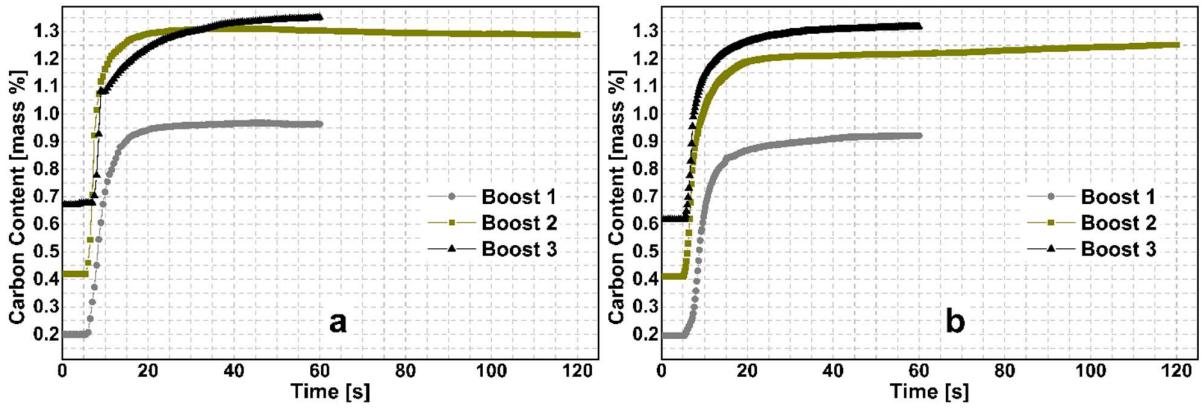

Figure 5-7: Calculated change of average carbon content dissolved in austenite in measured surface area of sample 3BD (a) and sample 3BD-R (b) for three different boost steps. Measured region is averaging from surface to maximum 20 µm below (beam height).

All boost steps of the two samples exhibit very similar tendencies, indicating good experimental consistency. During the first boost step, the carbon content increase is steep at the beginning and stays almost constant for both samples. The average carbon content of sample 3BD increases from 0.2 up to 0.92 ma. % in the first 20 seconds and then continues to increase very slowly to 0.94 ma. % until the end. Similarly, the average carbon content of sample 3BD-R also increases from 0.2

up to 0.87 ma. % in 20 seconds and then slowly increases to 0.91 % until the end. These values are significantly lower than the saturation point of the austenite at 940 °C, which is about 1.3 ma. % carbon according to the Thermocalc model. The reason for this difference in carbon contents is attributed to the carbon gradient within the 20 µm beam height. Prior to the first boost step, the sample contains a base carbon content of about 0.2 ma. %. In the early seconds of the boost steps, the carbon content in a few microns of the surface increases, creating a steep gradient within the probed height of 20 µm. This leads to an average carbon content of about 0.95 ma. % in the probed region. Before the second and third boost steps, this difference is strongly reduced since the carbon gradient is less steep and diffusion is slowed down.

Additionally, despite continuous acetylene introduction at the same rate into the chamber, a constant carbon content can be observed in the measured volume of the two samples after 20 seconds, so apparently, some steady-state was reached. The same steady-state behavior can also be observed for subsequent boost steps; however, the amount of carbon dissolved in austenite is very close to the solubility limit.

With the applied strategy in transmission mode, it is challenging to detect the behavior of carbon within the first µm of the surface due to the beam height (20 µm). Consequently, finding an explanation to above mentioned steady-state observation by using solely transmission measurements is not possible. As the signal is averaged within this height during measurement, any carbon from the surface to a 20 µm depth cannot be resolved precisely. Additionally, even minimal changes in the temperature and volume due to carbon intake can result in 1-2 µm expansion or shrinkage of the sample towards the z-direction (See Figure 3-5), potentially influencing the beam position and leading false interpretations of carbon content variations attributed to the carbon gradient. Consequently, the hypothesis explained in the top paragraph requires more precise measurement, which can be achieved with reflection mode measurements presented in following subsection.

5.1.1.1 Measurement System in Reflection Mode

In order to increase the precision in the near surface area, this experiment was additionally conducted in reflection mode at P05 of the PETRA III Synchrotron at DESY/Hamburg. In this approach, the sample is laterally positioned in the oven so that the beam hits the carburized surface directly, and it is reflected through the side windows. Four different line detectors, precisely positioned to capture two martensitic/ferritic and three austenitic peaks were used to gather the required data. The energy of the beam was 10.9 keV and the mean penetration depth was around 3 µm. Figure 5-8 shows the sample alignment in this method.

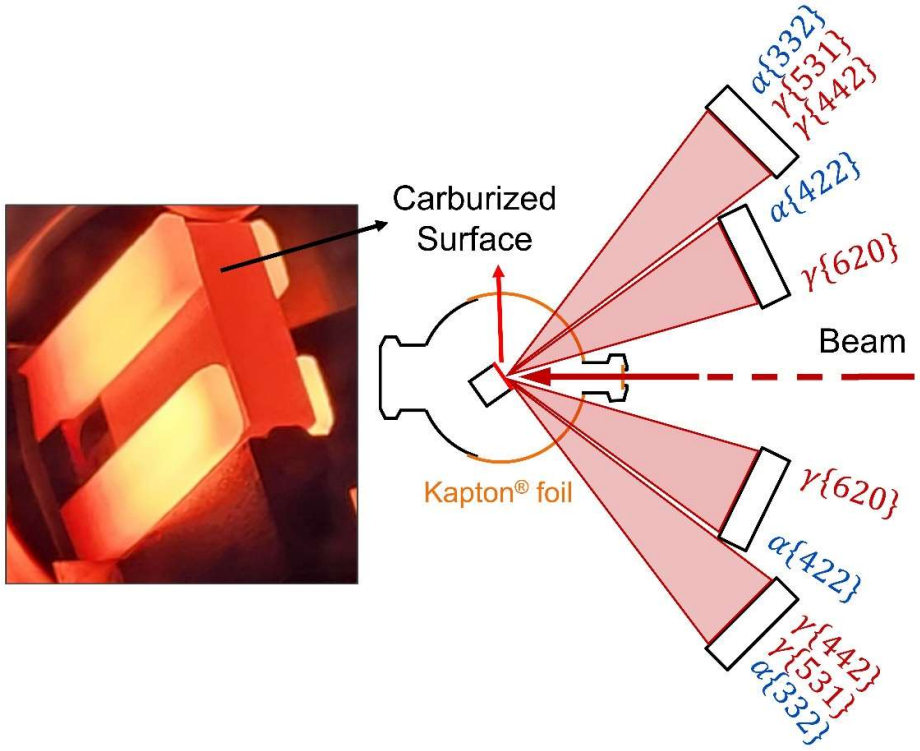

Figure 5-8: Measurement setup in reflection mode with 4 detectors capturing different peaks [172].

This measurement method is less affected by thermal expansion compared to the transmission method since measurement regions do not change due to the lateral sample position.

Additionally, the shallow penetration depth focuses only on the near surface area, which allows the detection of changes at the very surface of the sample.

Figure 5-9 shows the change of a sequence of integrated diffraction patterns measured by reflection mode at the sample surface during the whole carburization process (same process parameters as Figure 3-4). Similar changes as those seen in Figure 5-2 during the transmission mode measurements are also evident in this figure.

During the heating step, a phase transformation could be identified by the disappearance of the α {322} ferrite peak and appearance of the γ {442} and γ {531} austenite peaks. Upon the initiation of the first boost step, the austenite peaks shift to lower 2θ angles, from around 138° to 135° for γ {442} and from around 134° to 131° for γ {531}, as marked with a yellow dashed arrow. Up to this point, observations are comparable to those made in transmission mode. However, after this sudden shift of peak positions to lower angles in the early seconds of boost steps, an asymptotic increase is observed, showing that the peaks shift back to the higher angles until the end of the stage (marked with red arrows). This observation differs from transmission mode, where the peak position stays constant until the end of the boost step. In the following 20 minutes diffusion step, a gradual shift of the austenite peak positions further back to higher angles is systematically observed, similar to the transmission mode. The behaviors of the peaks during the hardening preparation and quenching steps are the same as those in the transmission mode.

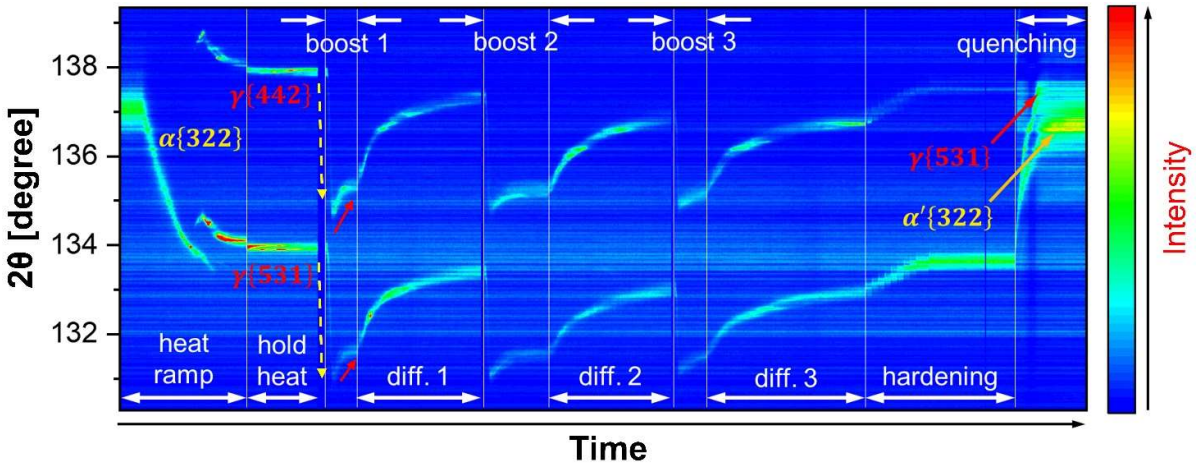

Figure 5-9: 2D contour plots of integrated diffraction patterns of the carburized sample during whole process measured in reflection mode [172].

Similar to the transmission mode, the change of carbon content was calculated for the reflection mode using Eq. 5-1 and shown in Figure 5-10.

It can be seen for all boost steps that after a sudden increase of the carbon content, despite a continuous supply of the carbon donor acetylene gas, there is a decrease after reaching the maximum solubility limit of the austenite for this steel grade. This decrease confirms the asymptotic increase of 2θ peak positions observed in Figure 5-9.

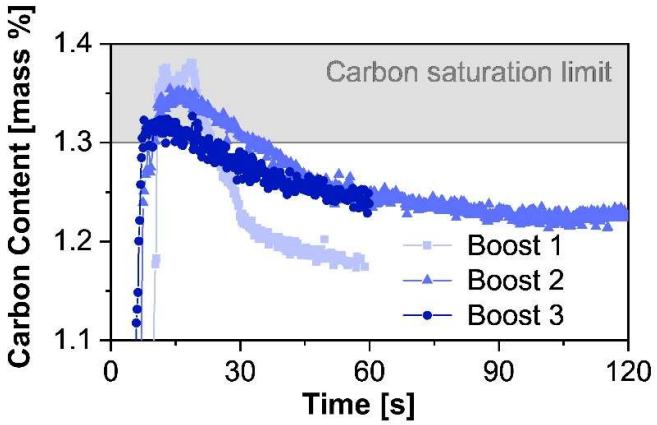

Figure 5-10: Calculated change of average carbon content dissolved in austenite from the surface to 3 µm depth from the data measured in reflection mode [172].

This is because the formation of the carbide layer at the surface hinders further acetylene decomposition. Consequently, this reduces the carbon intake of the surface, although acetylene is still present. As a result, surface carbon content is reduced. This phenomenon occurs only a couple of micron at the surface, so it could not be observed in transmission experiments.

It can also be noticed that the decrease of carbon content after saturation in boost 1 is very sharp, but the degree of this decrease is getting smaller for the following boost 2 and boost 3. These results are expected since the carbon gradient is steeper in the first boost step, a stronger driving force for diffusion. Initial carbon contents increase in the following boost steps due to preceding carbon

accumulation, leading to reduced differences in carbon content between the saturated surface and the initial state. Consequently, diffusion slows down in subsequent boost steps.

Another phenomenon that becomes evident is the increase in carbon content beyond the saturation limit of austenite during all boost steps. This observation was consistent in both transmission and reflection modes. The underlying reason for this occurrence could be the imprecise determination of the saturation limit of austenite, since 1.3 ma. % value relies on Thermocalc modeling. Alternatively, this behavior may be attributed to an oversaturation phenomenon of austenite for a short duration, induced by a rapid influx of carbon that creates temporary segregation points.

One additional phenomenon related to oversaturation is that maximum carbon contents during boost steps decrease from boost 1 to boost 3. During boost 1, carbon content reaches up to 1.38 ma. %, whereas this value decreases to 1.32 ma. % in the third boost step. This phenomenon might be attributed to the manganese effusion during the process. Figure 5-11 shows GDOES measurement results of evolution of manganese, chromium and carbon over 65 µm depth for the sample carburized in the industrial furnace with the same process parameters of sample 3BD. According to the results, Mn content reduced from the nominal content of 1.25 ma. % down to 0.5 ma. % in the surface.

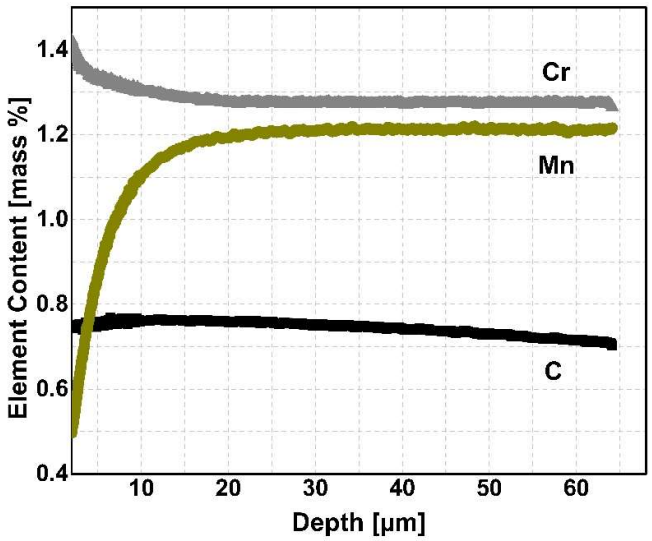

Figure 5-11: Change of contents of carbon (C), manganese (Mn) and chromium (Cr) in first 65 µm of the sample measured by GDOES

The calculation of carbon content based on an austenitic lattice with the model provided in Eq. 5-1 relies on the assumption that the amounts of all other alloying elements stay constant; however, due to low pressure, Mn at the surface tends to evaporate. This might cause an increasing underestimation of carbon content. Considering that this phenomenon occurs mostly in less than 5 µm, its effect on the carbon content calculation is difficult to determine.

5.1.1.2 Qualitative Determination of Carbides

The formation and dissolution kinetics of carbides are highly depend on various parameters such as their size [173,174], on the base carbon content, favorable formation sites and on the alloying elements [48]. Moreover, if carbides are formed locally without covering the entire carburizing surface, they may affect the carbon diffusion rates from the atmosphere to the sample in an inhomogeneous manner. Thus, carbon uptake may still continue in the presence of carbides but in a reduced rate. If the surface manages to stay active for acetylene decomposition, carbon atoms can still diffuse through the carbide layer. In such cases, carbon absorption from the atmosphere does not completely stop but slows down, as cementite has a lower diffusion coefficient for carbon than austenite, as previously given [57,58].

Carbide formation during boost steps was also confirmed experimentally for sample 3BD, as growing diffraction peaks belonging to cementite could clearly be observed. Figure 5-12 shows respective time frames belonging to first, second and third boost diffusion cycle. The peaks are aligned from bottom to top starting from the early seconds of the each boost step (8th or 10th) to respective seconds of following diffusion steps.

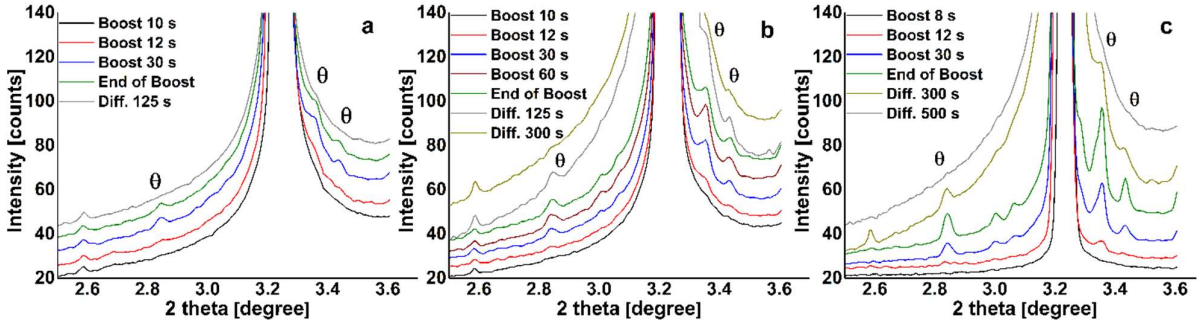

Figure 5-12: Cementite (Fe_3C / θ) formation and dissolution in (a) boost 1-diffusion 1, (b), boost 2-diffusion 2, (c) boost 3-diffusion 3 around {111} austenite peak of sample 3BD after different times. Time at the end of the steps gives seconds along each boost.

During the initial 10 seconds of the first boost step, no indication of carbide peaks is observed since the saturation limit was not reached yet, so the amount of carbon that could be dissolved in austenite was still continuously increasing.

After reaching the saturation limit, carbides start to form and small carbide peaks can be identified near {111} austenite peak in the diffraction pattern already after 12 seconds. Saturation of the austenite at the surface is assumedly only 1-2 µm from the top because the average carbon content at measured height stayed constant at 0.94 %. This is an indication that there is a steep carbon gradient within the first 20 µm from the surface.

When the acetylene flow is turned off at the end of the boost step, carbides start to dissolve slowly in the following diffusion step. After approximately 2 minutes of diffusion, carbides are completely dissolved, so carbide peaks disappear. According to the measured data, carbides have fully dissolved during the diffusion phase, so no alloy element aggregation in carbides has happened in a significant amount. Otherwise, a full dissolution of carbides could not have happened during the

diffusion phase, because manganese or chromium are stabilizing carbides and would have forced a significantly higher dissolution temperature (above 1000 °C) [175].

The carbide formation behavior of sample 3BD in the second boost step is also similar to the first boost step. Upon reaching the saturation limit of austenite, carbides start to form and remain present until the conclusion of the boost step. In the following diffusion step, carbides start to dissolve gradually. Figure 5-12c shows carbide peaks of sample 3BD for the third boost step. Full dissolution of carbides at the surface takes about 500 seconds, significantly longer than the first two boost steps. Therefore, it is important to consider that as the duration or number of boost step is increases, the duration of the diffusion step should be extend accordingly, while the time required for full dissolution of carbides increases in each boost step.

In order to visually observe the carbide formation at the surface, a different sample was gas quenched with helium directly after 5 min boost step at 940 °C, and the surface was scanned using synchrotron X-rays. Figure 5-13 shows the metallographic examination of the sample and diffraction peaks of the surface. Carbide layer formed at the surface with a grey color is easily noticeable in the figure. Also it can be seen from the diffractograms that carbide peaks appear near main austenite peaks, as expected.

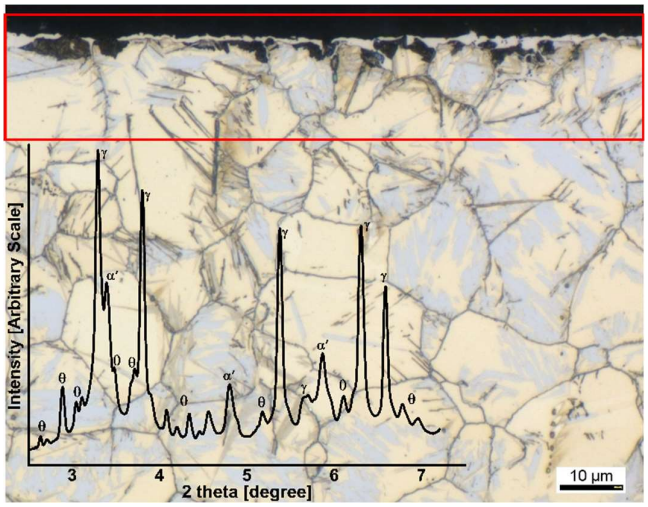

Figure 5-13: Metallographic examination and synchrotron X-ray diffraction results of a sample quenched directly after the boost step. γ -Phase in diffraction pattern is austenite, α'-phase is martensite and θ is M_3C carbides. Conventional optical microscopy was used and sample was etched with 3.5 % nital. The XRD-probed area is indicated in red.

Overall, It can be concluded that acetylene decomposes to atomic carbon and gaseous hydrogen immediately when it comes in contact with the thermally activated metal surface at low pressure [80]. Consequently, free carbon diffuses directly into the sample with a very fast diffusion rate in the early seconds of the boost step and accumulates in the austenite grains at the surface. When the surface reaches the maximum solubility, a very fine continuous cementite Fe_3C layer in the first few microns of the surface forms.

Other hydrocarbons, such as propane or methane, undergo thermal decomposition, breaking down to their components under heat. Acetylene, however, is a catalytically decomposable hydrocarbon,

requiring both heat and a metal catalyzer for decomposition [4,79,176,177]. Therefore, it is also expected that this carbide layer influences acetylene decay negatively by blocking the reaction sides, and autocatalytic acetylene decomposition reaction is suppressed or maybe completely stopped [178–182]. Although the carbon diffusion continues in the material saturation of the austenite and carbide layer, it may decelerate carbon uptake from the atmosphere to the steel sample. Consequently, a decrease in the carbon content might result after reaching saturation. Further carbon absorption of the sample becomes possible in only two ways: first, by dissolution of carbides, which is very slow compared to the diffusion of carbon from the atmosphere to the sample, and second, by diffusion of carbon through the cementite layer, which is also slow due to lower diffusion speed of carbon in cementite [57,58] as explained previously in section 2.3.2.

The diffusion coefficients of cementite and austenite, calculated by using Eq. 2-9 and Eq. 2-10, are approximately $2x10^{-9}$ cm^2/s and $7x10^{-7}$ cm^2/s at 940 °C, respectively, showing two orders of magnitude lower diffusion in cementite than in austenite [48].

In conclusion, the observed steady-state condition and following decrease of the dissolved carbon within the top micrometers of the sample was due to carbon accumulation on the surface and the formation of a cementite layer. This layer effectively slows down further carbon absorption of the sample from the atmosphere. Either way, introducing new carbon into the system was very slow compared to carbon diffusion from the atmosphere to sample and compensate for the carbon diffusion inside the material.

5.1.1.3 Quantitative Determination of Carbides

Carbides formed during the boost step for sample 3BD were quantitatively analyzed using Rietveld refinement. Only cementite structure was used as carbide, so other structures such as $Cr_{23}C_6$, Cr_3C_2 or Cr_7C_3 were not taken into account. It was assumed that all previously present carbides were dissolved at 940 °C right before the first boost step, so this point was taken as a reference of zero. Figure 5-14 shows the amount of carbides formed in each boost step. Since the amount of carbides were very low compared to the main austenite phase, intensities of the carbide peaks are also very low, reducing the accuracy of quantitative determination. According to figure, for the first boost step, cementite starts to form after 10 seconds and reaches its peak point after about 30 seconds, which is a very short time for diffusion of carbon; after that, there is a decreasing trend. The reason for this behavior can be hypothesized that in the first 30 seconds of boosts, carbon accumulation occurred at the very surface of the sample, while right below the surface, the carbon content remained at the nominal level of 0.2 ma. %. This difference created a very steep slope of carbon content from the edge through the core, which generated a high driving force for cementite dissolution and further carbon diffusion towards the core. Thus, cementite dissolution predominated over carbide formation after about 30 seconds, which causes a decrease in the cementite content despite the fact that acetylene is still present in the chamber. This decrease could be confirmed in Figure 5-12a, in which

the intensities of the cementite peaks at the 30th second are slightly higher than the peaks at the end of the boost step.

In the second boost step, carbon content exhibits a sharp increase from 10 to 30 seconds, after which the rate of increase reduces. Because of the lower carbon gradient compared to the first boost step, cementite formation slightly predominated over dissolution, resulting in a gradual increase in the amount of cementite until the end of the second boost step.

During the third boost step, cementite formation rates are considerably higher than in the first two boost steps because the force for cementite dissolution decreases as the carbon content gradient flattens out

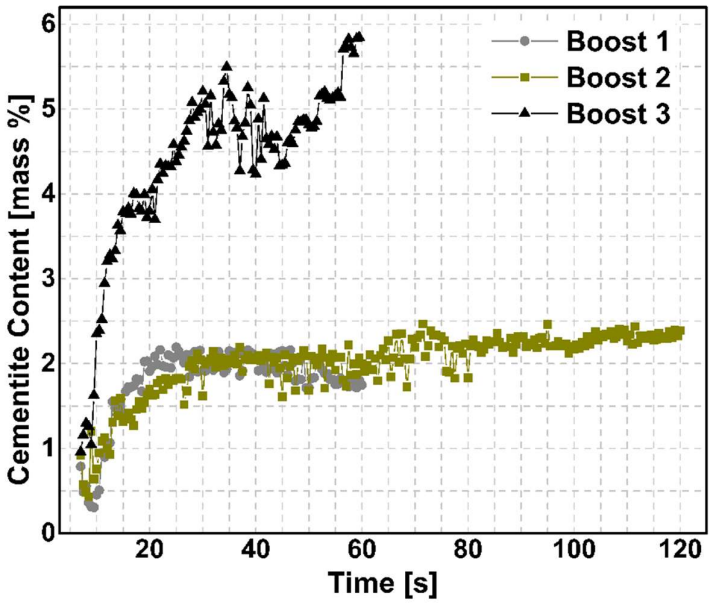

Figure 5-14: Amount of carbides formed in boost steps at the surface of sample 3BD

It is important to mention that the amount of carbon content dissolved in austenite is determined using the lattice parameter, which is primarily based on the peak position, rather than the peak intensity. However, quantitative analyses of the carbides are conducted by using peak intensity. Between the steps, the sample position was manually adjusted to account for slight variations in peak intensity due to thermal expansion/shrinkage of the material. Although these variations were not significantly high, they might still affect the peak intensity of minority phases and cause a difference in the quantitative results, considering that carbides are only present within the first 1-2 µm at the surface. Therefore, each carbide peak figure should be interpreted individually for quantitative evolution. This means that almost three times higher carbide content of the third boost step in Figure 5-14 compared to the previous boost step might be misleading. The safe interpretation of the figure is that carbides start to from in the very early stages of all boost steps and then reach to steady state after around 30 seconds.

5.1.2 Diffusion and Hardening Preparation Steps

The carbon gradient built up in the material is extremely large in boost steps. This leads to very high potential differences, resulting in the redistribution of the carbon along the gradient. Figure 5-15 shows the carbon content change calculated using Eq. 5-1 for two samples during the following diffusion steps after each boost step. For sample 3BD, the beam kept constant directly at the surface; for sample 3BD-R, continuous scanning from the surface to 0.5 mm depth was applied with a rate of approximately 4 µm/sec. Therefore, carbon content at the surface and also carbon content distribution over the depth could be observed.

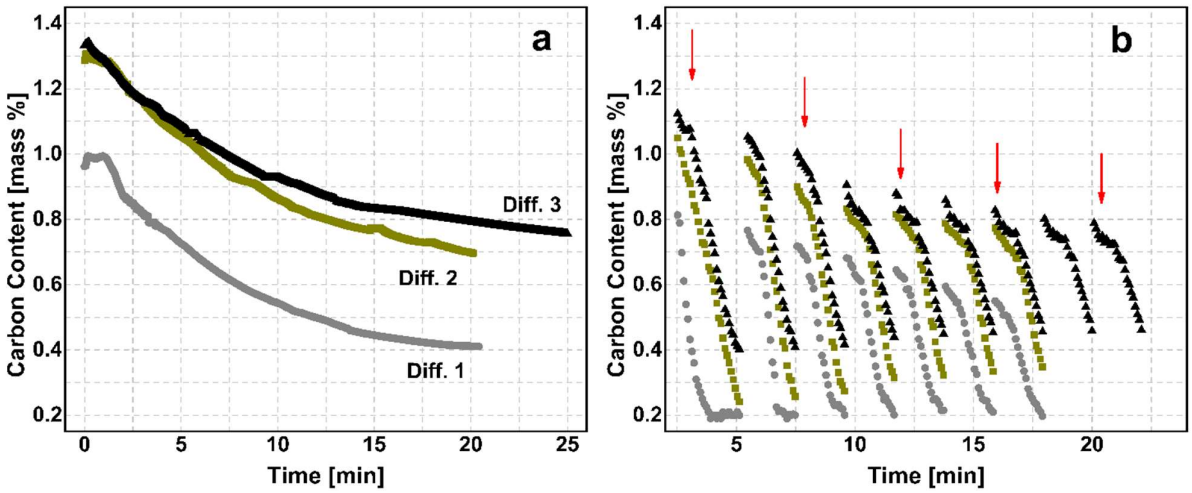

Figure 5-15: Change of average carbon content at the top surface of sample 3BD (a) and scanning of carbon content distribution up to 0.5 mm depth for sample 3BD-R (b).

Due to the initially high carbon gradient during the diffusion step, the driving force for diffusion was also high. Thus, carbon diffused faster at the early stages and slowed down afterward, creating an expected rate decrease in the overall graph for both samples. For all diffusion steps, the rate of decrease is slowing down and the gradient is getting reduced. The initial carbon content of samples was 0.2 % and after three boost and diffusion cycles, 0.78 % and 0.76 % carbon content was reached at the surface for sample 3BD and sample 3BD-R respectively.

The carbon contents of both samples follow the same trend and give very close results during the whole process. This observation proves the repeatability of the experiment. The carbon content distribution of sample 3BD-R with time over 500 µm depth is given in Figure 5-15b. At the end of the first scan of diffusion 1, represented with grey circle in Figure 5-15b, carbon content stays constant at nominal carbon content of 0.2 ma. % for about 1 minute, indicating that carbon had not diffused all the 0.5 mm at this point. In the following scans of the first diffusion step, carbon content at the surface reduces while at 500 µm it increases, making carbon gradient flatter. After around 16 minutes, carbon content at the surface reduces down to 0.52 ma. %.

In the second and third diffusion step, carbon content at 0.5 mm depth gradually increases to about 0.37 ma. % and 0.45 ma. % respectively. Additionally, the rate of carbon content decrease at the

surface (reduction of the top of each scans over the time) and the rate of carbon content increase at 500 µm (increase of the bottom each scans over the time) depth are quite different. This indicates that carbon diffusion slows down through the depth due to lower driving force.

Detailed carbon depth profiles marked with red arrows in Figure 5-15b are given in Figure 5-16. Carbon accumulation in the first 100 µm can be noticed from flatter gradient for all diffusion steps, especially for the first 2.5 minutes of the scan. Additionally, there is a noticeable carbon content difference between the first scan and the following scans especially for 2nd and 3rd diffusion steps, which can also be attributed to the higher driving force of diffusion caused by higher carbon gradient.

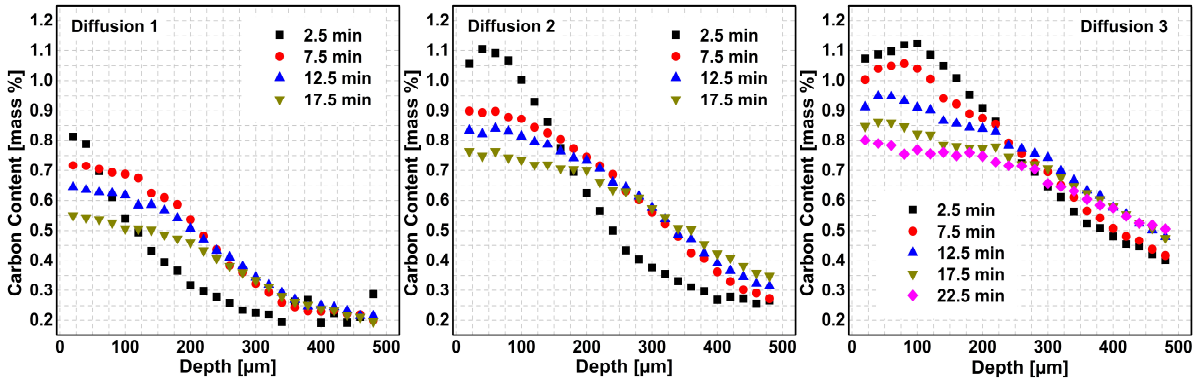

Figure 5-16: Change of average carbon content over the depth during diffusion steps for sample 3BD-R.

Upon closer examination of the early stages of the diffusion steps of sample 3BD, an increase in the carbon content in austenite becomes apparent, even though there is no presence of acetylene gas.

Figure 5-17 shows the first two minutes of all three diffusion steps of sample 3BD from Figure 5-15a. Within the first 10 seconds, the carbon content increases and then either stays constant or reduces slowly. The reason for this slight increase is attributed to the dissolution of carbides formed in boost steps. Following this small increase in the first two diffusion steps, the carbide dissolution rate and the carbon diffusion rate reache an equilibrium for about a minute, so carbon content in the probed layer of about 20 µm stayed nearly constant.

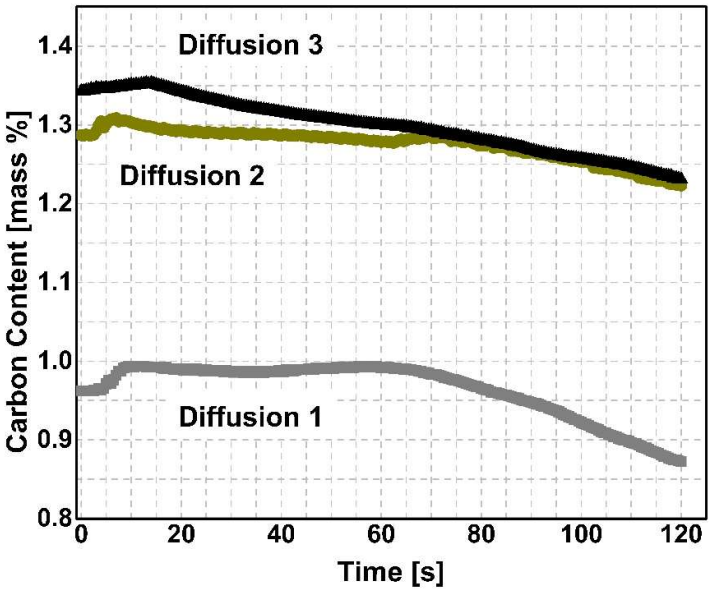

Figure 5-17: Amount of carbon dissolved in austenite in the first two minutes of diffusion steps for sample 3BD

After the first minute, the carbon diffusion rate overpasses the carbide dissolution rate, leading to a decrease in carbon content because of the transportation of carbon atoms into the depth of the sample.

Figure 5-18 shows the change of cementite content during the first two minutes of the diffusion. In the first 10 seconds, fluctuations of the values can be observed, especially for the first two diffusion steps, due to difficulties in detecting lower amount of carbides. In the first diffusion step, cementite content stays stable until around 40 seconds and then starts to reduce. The second and the third boost steps show similar behavior. The amount of cementite increases in the beginning of the diffusion steps and reaches the maximum value at the end of the first minute. After that point, it starts to decrease. It can be said that after the boost step, cementite can still form, although there is no acetylene present in the oven as a primary carbon source. This would be because of carbon accumulation at the surface of the metal as an alternative, secondary, carbon source, allowing further cementite formation in the first stage of the diffusion step.

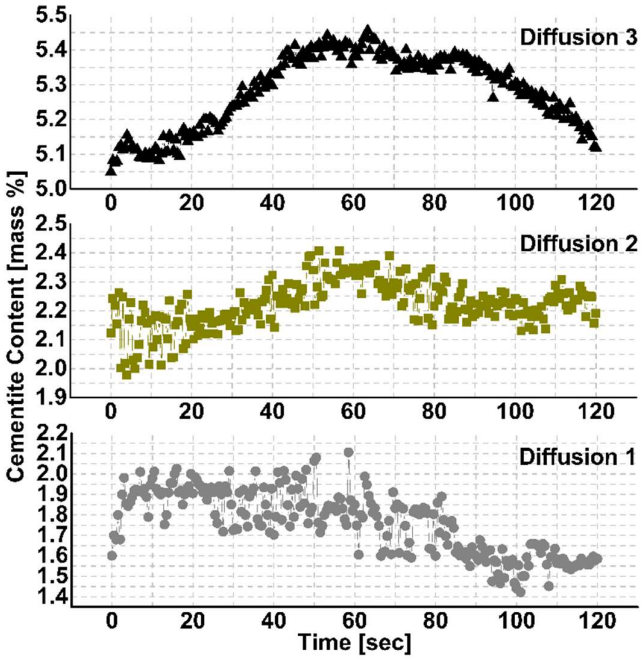

Figure 5-18: Change of cementite content during first two minutes of each diffusion step.

5.1.3 Quenching Step

In most cases, carbon enrichment in the surface region alone does not adequately improve the mechanical properties of a component. Therefore, additional phase transformation by quenching is necessary. In this experiment, the cooling rate achieved by high-pressure helium quenching was 30 °C/s in the first 10 seconds and reduced exponentially until 90 °C was reached. Due to limitations of the system, better cooling rates were not possible. After that temperature, quench gas was stopped, and samples were let to cool down to room temperature.

The quenching step of sample 3BD was examined in detail. Rietveld analysis of diffraction patterns during quenching provided a precise evolution of phase fractions in the near-surface region. Figure 5-19 gives the phase changes and cooling curve of sample 3BD during quenching.

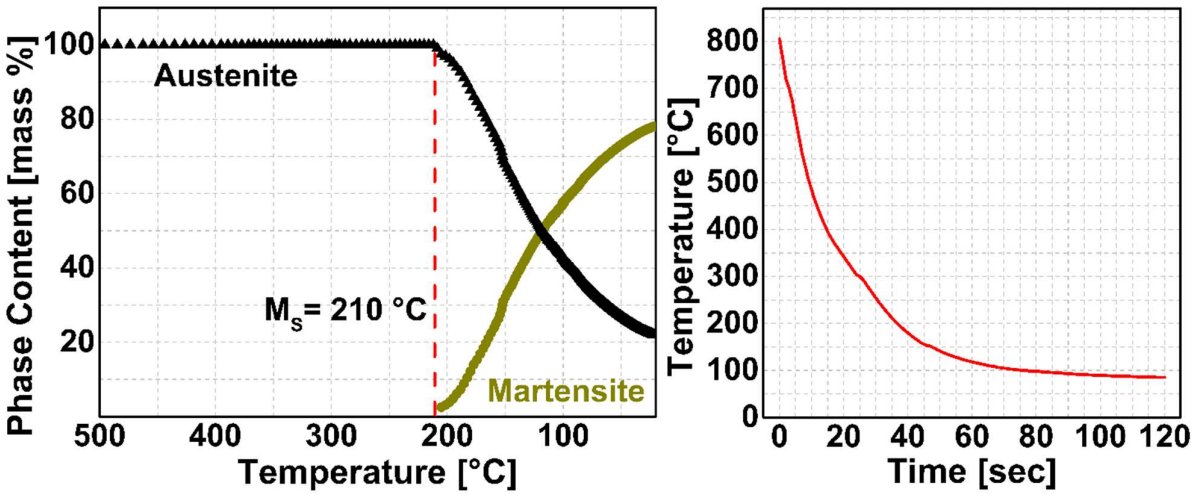

Figure 5-19: Evolution of phase fractions of sample 3BD during quenching from austenite region.

High carbon content on the case retarded bainite transformation, thus the near-surface region does not show any transformation until the martensite start temperature (M_s) is reached despite a relatively moderate cooling rate. It can be seen from the graph that the martensite start temperature is about 210 °C.

Based on the experimentally determined M_s temperature, carbon content dissolved in austenite before quenching can be determined with good accuracy by using the model developed by van Bohemen [183]. The model aims to calculate the M_s temperature of steels having 0.1-1.9 ma % C and less than 7 ma % other alloying elements. According to the model, M_s can be formulated as

$$M_s = 565 - \sum_i K_i x_i - 600[1 - exp(-0.96 x_C)] \qquad \textit{Eq. 5-2}$$

Where x_C is amount of carbon in ma. % and $\sum_i K_i x_i = 31x_{Mn} + 13x_{Si} + 10x_{Cr} + 18x_{Ni} + 12x_{Mo}$ describes the effect mass percentage of other substitutional elements.

The equation gives about 0.73 % carbon dissolved in austenite for a 210 °C M_s temperature. This value correlates well with the final carbon content obtained by EMPA given in Figure 4-3; however, the carbon content determined from Onink's formula based on the lattice parameter of austenite gives approximately 0.67 % at the end of the hardening preparation step at 840 °C, right before quenching. This 0.06 % difference corresponds to about +17 °C on the M_s temperature. This deviation is acceptable since alloying elements are not the sole influential factors for the determination of martensitic transformation kinetics by mathematical calculations. It is known that a difference in the defect structure of austenite and prior austenite grain size can shift the M_s temperature of the same material [183–188]. Furthermore, the thermal expansion coefficient of the face centred cubic (FCC) lattice might also deviate from linearity when the temperature reduces [189]; therefore, the error margin of Onink's formula slightly increases when the temperature drops from the carburizing temperature (940-950 °C) to the hardening preparation temperature (840 °C). Consequently, the possible reason for this deviation is a combination of the error margins of calculations caused by external influential factors.

On the other hand, the carbon content in the solution in the martensite can be evaluated based on the lattice parameters. A linear relationship between the tetragonality of martensite and carbon content in martensite can be found in Eq. 5-3 [21].

$$c/a = 1 + 0.045 x_C \qquad \textit{Eq. 5-3}$$

Where c and a lattice parameters of martensite and x_C is the amount of ma. % carbon in martensite. Other alloying elements, such as chromium and manganese, substitute iron, so they only have a minor effect on c/a ratio of martensite. The evolution of determined lattice parameters as well as calculated carbon content in martensite is presented in Figure 5-20.

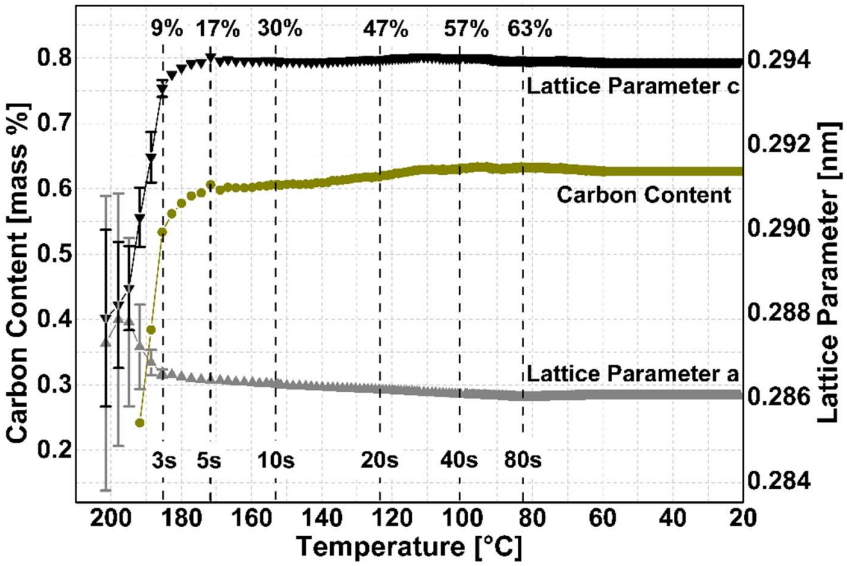

Figure 5-20: Evolution of lattice parameters of martensite and carbon content in solution for sample 3BD as a function of temperature. Carbon content is calculated based on average lattice parameter values so error bars are not considered. Doted vertical lines show the time from the beginning of martensitic transformation in seconds.

In the early stages of transformation, the measured lattice parameters display high standard deviations since the amount of martensite is quite low. In the first 3 seconds, until reaching 185 °C, lattice parameter “c” increases steeply and stays almost constant; while parameter “a” decreases rapidly in the first 5 seconds and then decreases at a much slower rate. After the first minute, around 90 °C, both values stay almost constant until the end of the quenching step.

Tetragonality of the martensite, expressed as the c/a ratio, increases during the transformation, so the first 15 % of martensite formed in the first 5 seconds has a lower c/a ratio than later-formed martensite. This could be due to phase-specific 2nd kind hydrostatic compressive stresses generated in the early stages of transformation because martensite at these early stages is a minority phase. As the transformation progresses and martensite becomes the dominant phase, the compressive stress reverses, resulting in a higher c/a ratio. A similar phenomenon was reported in previous studies [156,159].

Another possible reason for the lower c/a ratio at the early stages of the transformation might be the lower carbon content of fresh martensite. Increasing carbon content reduces the M_s temperature, thereby delaying the martensitic transformation. Before quenching, there might be some prior austenite grains that have slightly lower carbon content than the majority of them, causing them to transform earlier due to their higher M_s temperature. This may also be an indication that carbon atoms were not evenly distributed in the measured area during the diffusion and hardening preparation steps. Although carbon atoms had sufficient time and temperature for homogeneous distribution, some of the carbides that dissolved later during the final diffusion step might leave some carbon agglomerates in austenite, making local inhomogenities.

Additionally, carbon content calculated via Eq. 5-3 at the end of quenching is about 0.62 ma. % which is lower than the surface carbon content of the sample. The reason for this difference might be self-tempering/carbon partitioning from martensite during quenching.

In the case of martensitic transformation, which involve both chemistry (partitioning) and internal stress changes, an XRD study alone is generally limited to semi-quantitative conclusions based on assumptions for the measurement of carbon content. Therefore, determination of the exact carbon content of all phases in order to make a certain judgement about the carbon partitioning kinetics is not easy. Nonetheless, if the given XRD results are combined with literature studies using advance characterization techniques, the following conclusions about the present case can be deduced in different extents.

Transformation of martensite is usually described as occuring without diffusion of interstitials, so changes in carbon are usually neglected because of very low temperatures and short times. Previous studies, however, exhibit evidence of self-tempering and even carbon partitioning from martensite to retained austenite during fast quenching [190–194]. Besides the redistribution of carbon from martensite to retained austenite or cementite, carbon segregation to microstructural features like dislocations or martensite lath boundaries is also very common in the literature [241–243], especially for the cases where a lower M_s temperature restricts the mobility of carbon. The depletion of martensite during cooling is highly dependent on the cooling rate. It was studied that cooling rates under 25 K/s are highly favorable for carbon partitioning from martensite to retained austenite for medium carbon steels [192]. In the present study, the average cooling rate from the hardening preparation temperature (840 °C) to M_s temperature was 17 K/s and further reduced to lower values after the martensite start temperature. Although cooling rates correlate, the M_s temperature of the mentioned literature results is quite higher, so relatedly, carbon mobility during quenching is greater compared to the present study. However, there are also some studies in which a minor effect of self-tempering of martensite could be observed for M_s temperature down to 200 °C [19,195].

The change of austenite lattice parameter during quenching was also determined and is shown in Figure 5-21. The austenite thermal expansion coefficient is calculated as $2.12 \cdot 10^{-5}\ K^{-1}$, which is consistent with previous studies [159,196]. Contraction in the austenite lattice can be noticed from the reduction of austenite lattice parameter after M_s temperature, which is mostly an indication of compressive stresses in austenite, which will be discussed in further sections.

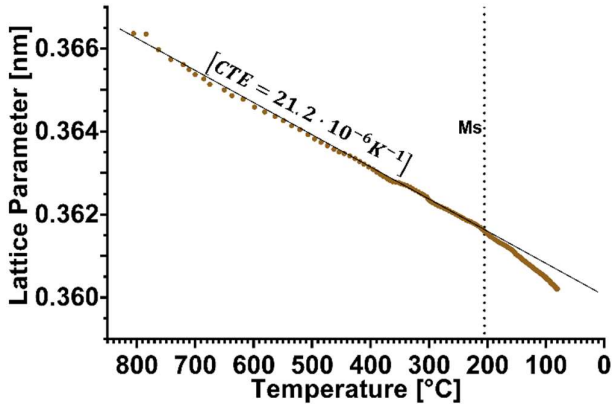

Figure 5-21: Change of austenite lattice parameter during quenching of sample 3BD and coefficient of thermal expansion calculated by linear fitting to the data between T = 750-450 °C.

Figure 5-22 shows the XRD diffraction pattern of the studied sample at room temperature both before and after low pressure carburizing treatment. Before treatment, along with the main α-peaks, several low intensity carbide peaks are easily distinguishable; but after treatment, they all disappear. However, the figure is on a large scale to determine carbides. This still weakens the possibility of carbon rejection from martensite to precipitate as cementite or any other carbides.

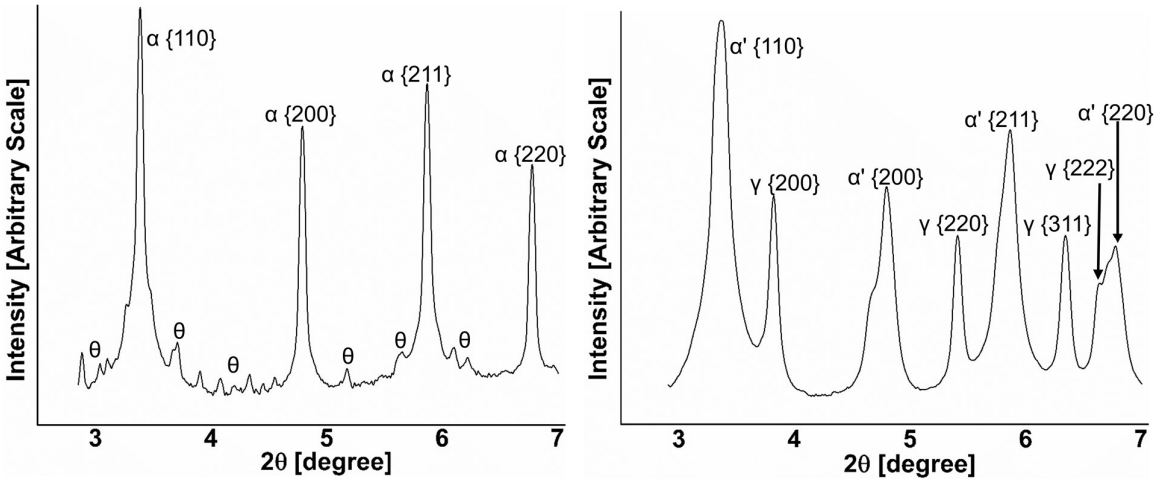

Figure 5-22: X-ray diffraction peak measured at sample 3BD at room temperature before (a, and after (b) low pressure carburizing treatment. Small peaks in the diffraction pattern before heat treatments are mainly carbides.

5.2 Effect of Process Parameters on the Carbon Content and Microstructure Evolution

In this section, the results of the effect of three process parameters, which are process temperature, acetylene amount and boost diffusion cycle, on the evolution of carbon content during the process will be given and discussed.

5.2.1 Effect of Process Temperature

The industrially used temperature range for LPC is generally 880 °C–1050 °C, but most of the processes are conducted between 910 °C-and 980 °C for conventional case hardening grades. Higher processing temperatures significantly shorten the processing time, reducing the cost. On the other hand, temperatures higher than 980 °C are generally not desired due to detrimental grain growth [84,108], and because of the risk of soot formation [197].

Table 5-1: Process parameters for the experiments with varying temperature

	Boost 1	Diff. 1	Boost 2	Diff. 2
Duration (min)	1	20	1	20
Pressure (mbar)	4	10^{-1}	4	10^{-1}

In order to investigate the effect of temperature on the microstructural evolution, two low pressure carburizing experiments were conducted at 920 °C and 960 °C, respectively, with the same parameters given in Table 5-1 (See Table 3-2, sample LT-920C and HT-960C).

Before the process, the chamber was evacuated to 10^{-1} mbar and the samples were heated up to the process temperature with a heating rate of 2 K sec^{-1} in order to achieve a full austenitic state. Subsequently, acetylene was continuously introduced into the furnace. The bottle outlet pressure of acetylene was adjusted to a slight over atmospheric pressure of 1.2 bar and a flow rate of 10 ml min^{-1} (~ 8 m^3 $m^{-2}h^{-1}$) to initiate the boost step, and process pressure went up to 4 mbar. In the following diffusion step, the remaining acetylene was extracted from the furnace; hence, the pressure was reduced to 10^{-1} mbar again. Following the final diffusion step, the samples were quenched with 5 bar helium gas with the gas flow directed at the top surface of the sample. The representative process scheme can be seen in Figure 5-23.

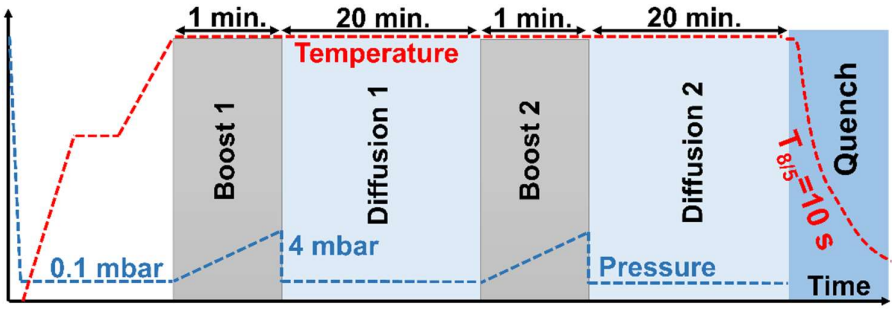

Figure 5-23. Process scheme of two boost-diffusion cycle LPC experiments

During the process, changes in the peak position, full width half maximum (FWHM) and integrated intensity were observed. Figure 5-24 shows these changes of the γ {111} austenite peak during the boost steps for both temperatures.

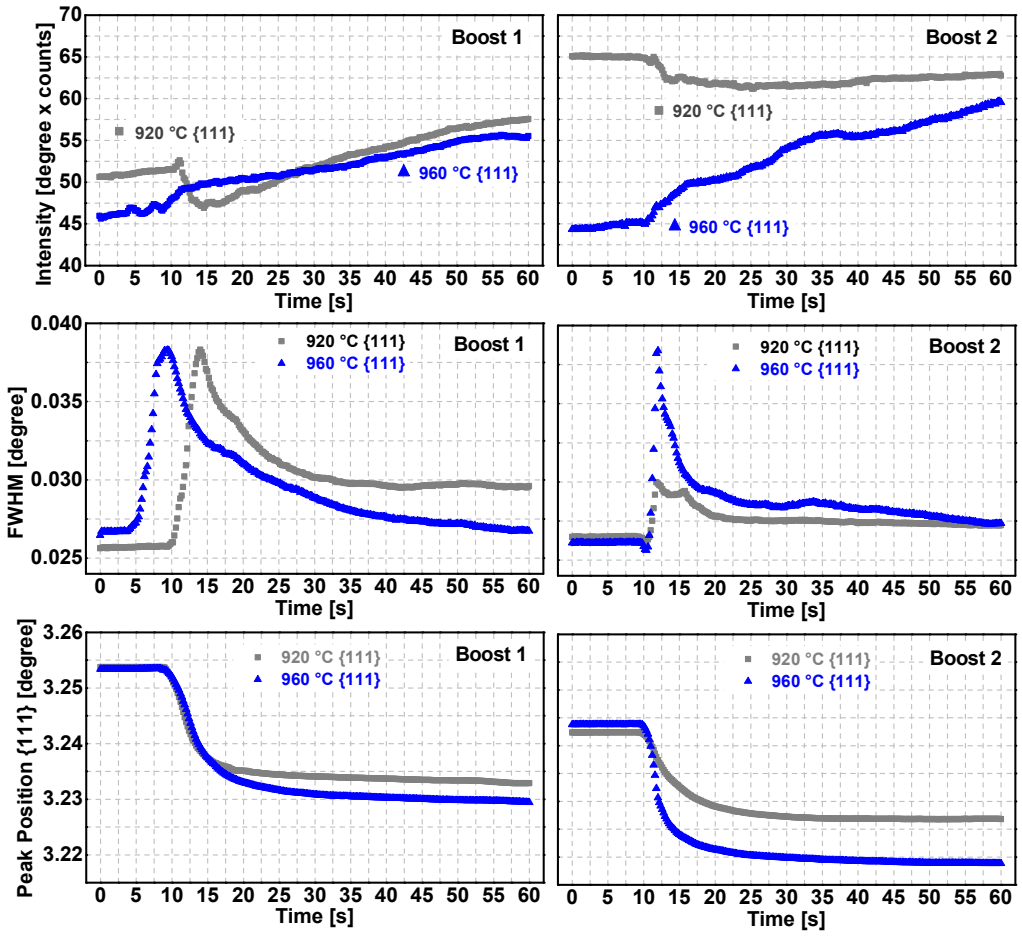

Figure 5-24: Change of integrated intensities, FWHM and peak positions of γ {111} austenite peak vs. duration of the boost step for samples LT-920C and HT-960C. Average error margin for integrated intensity and FWHM is ± 5 % of data points and $4 \cdot 10^{-4}$ degree respectively which are not presented in the figure due to high number of data point. Error margins of peak positions are smaller than symbols.

During the boost steps of both samples, peak shifting to lower angle can be observed. The initial peak positions of both samples are 3.255° for the γ {111} peak. Notably, peaks of the HT sample shift to smaller angles than those of the LT sample.

The boost steps were followed by diffusion steps with a 20 minutes duration. The change of peak positions and FWHM of the γ {111} austenite peak over depth during the first diffusion step of LT-920C can be seen in Figure 5-25 as a representative example. No data are available in the first and the last 2 min, which is the time required for the transition of measurement modus from fixed mode to scanning mode.

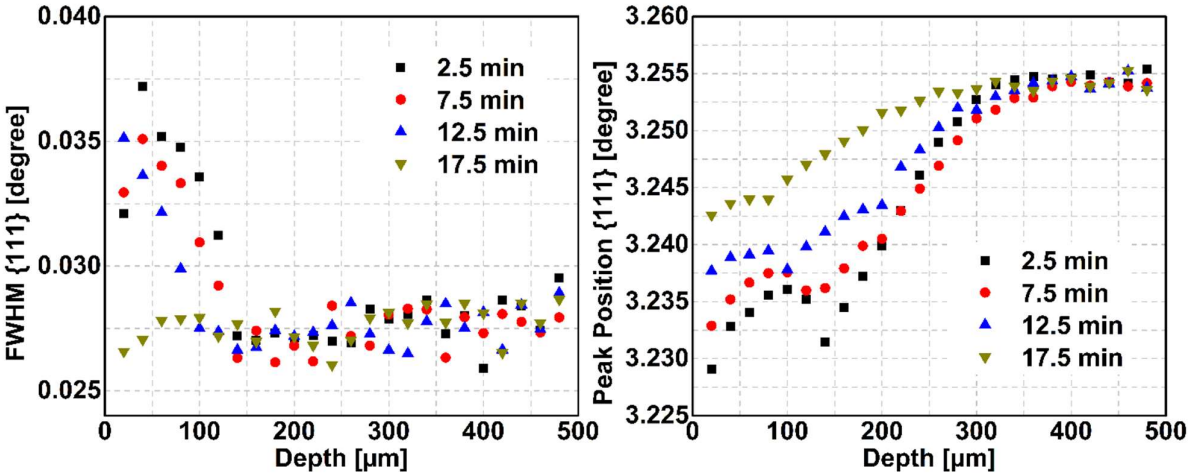

Figure 5-25: Change of FWHM and peak positions of γ {111} austenite peak during scanning over z axis for first diffusion step of the sample carburized at 920 °C. The 1st, 3rd, 5th and 7th scan were given with corresponding time.

During the diffusion steps, the sample was scanned continuously seven times (same as previously represented with sample 3BD-R in Figure 5-15) from the top to approximately 0.5 mm depth. FWHM values are higher at the beginning of the scan (at the top surface) due to smaller peak heights and the carbon inhomogeneity of the sample at the top surface. When scanning continues towards the depth, FWHM values of γ {111} austenite peak decrease to values between 0.026 and 0.030 degrees. A slow shift of the austenite peaks back to higher angles can be systematically observed in both individual scans and also in the overall evolution during the whole diffusion step.

It can also be noticed that FWHM of the γ {111} values fluctuate between 0.026 and 0.030 degrees, although the whole 20 µm beam height was within the sample. The possible reason for this is the continuous change of carbon content in the probed volume due to diffusion from the surface to the depth, which might generate local microstrains across the probed area. Another reason may be the mentioned minor temperature changes during the entire process.

5.2.1.1 Determination of the Evolution of Carbon Content

Peak shift toward lower and higher 2θ angles in the process is directly related to the change of lattice parameter. After analyzing integrated diffraction patterns, the change of austenite lattice parameter from the beginning of the first boost step to the end of the second diffusion step was evaluated and presented in Figure 5-26 for both samples.

During boost and diffusion steps, temperature is mostly stable (±15 °C of the process temperature). The sample is at fully austenitic temperatures and is homogeneous in terms of composition, so it can be considered almost stress-free. Thus, at a constant temperature, changes in the lattice parameter can be attributed to the changes in the chemistry, i.e. in the present case, most likely to the amount of carbon in the solid solution in austenite.

During the boost step, carbide formation was observed at the surface of the samples, potentially induces stress in the austenite. The effect of this stress on the peak shifting is presumed to be minimal due to the high process temperature, very low amounts of carbides, and fast carbide

dissolution; therefore, it is neglected in calculations, and peak shifting is only attributed to the carbon content change.

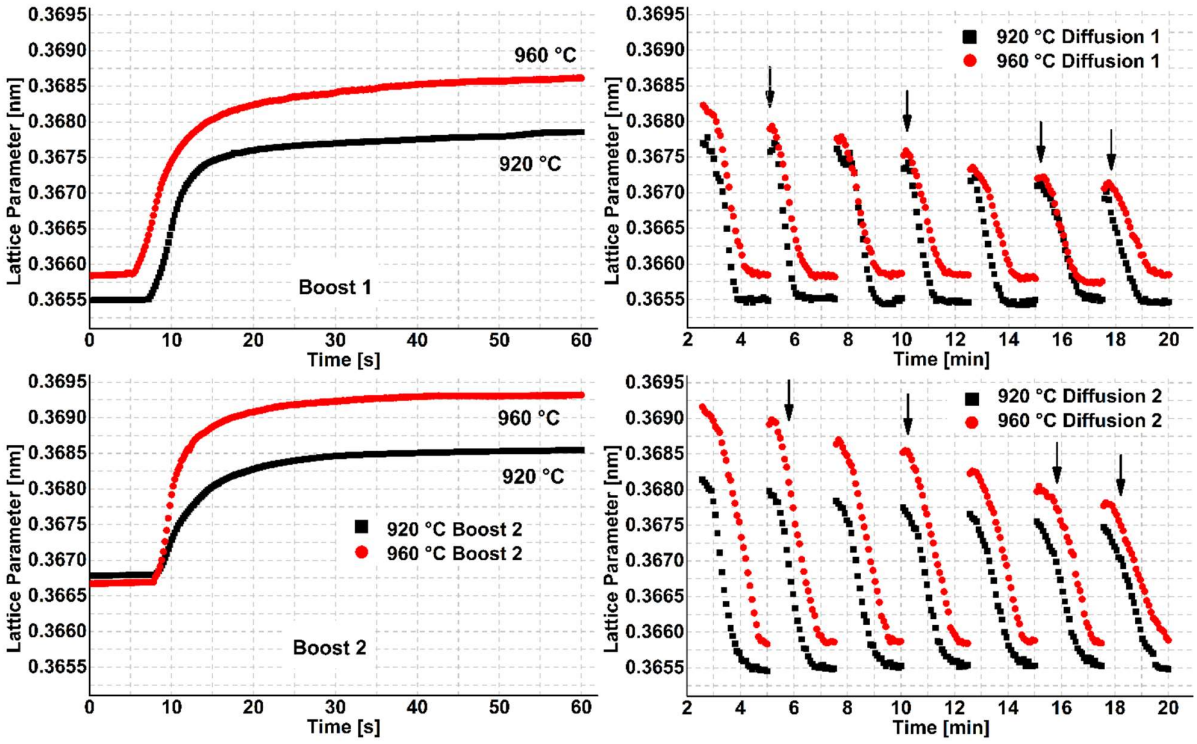

Figure 5-26: Evolution of the lattice parameter of austenite for sample LT-920C and HT-960C Beam kept stable at the surface during boost steps, and continuously scanned over 500 µm depth during diffusion.. Black arrows in diffusion graphs show further investigated scans for the change of carbon content determination. Average error bars are $\mp 5 \cdot 10^{-5}$ *and it is smaller than symbols.*

As already explained in the previous sections, the assessment of the carbon content can be done from the dilation of the austenite lattice parameter due to the occupation of octahedral sites of the austenitic lattice by the carbon atoms. For this, the model developed by Onink is also used (see Eq. 5-1).

Figure 5-27 shows the calculated average carbon content change in the solid solution in austenite during boost and diffusion steps for two different samples carburized at different temperatures. During boost steps, the beam position was kept constant at the surface, while during the diffusion steps, samples were scanned from the top to approximately a 500 µm surface distance. Investigated diffusion scans are shown in Figure 5-26 with black arrows.

Carbon content before the first boost step is calculated as 0.2 ma. %, which corresponds to the base carbon content of the steel. During the first boost step, the average carbon content of the low-temperature sample increases up to about 0.95 ma. % while that of the higher temperature experiment goes up to about 1.05 ma. %. This difference is attributed to the higher solubility limit of austenite at a high temperature. According to calculations using Thermocalc software, the maximum carbon solubility of the given steel is about 1.33 ma. % for 960 °C and about 1.26 ma. % for 920 °C.

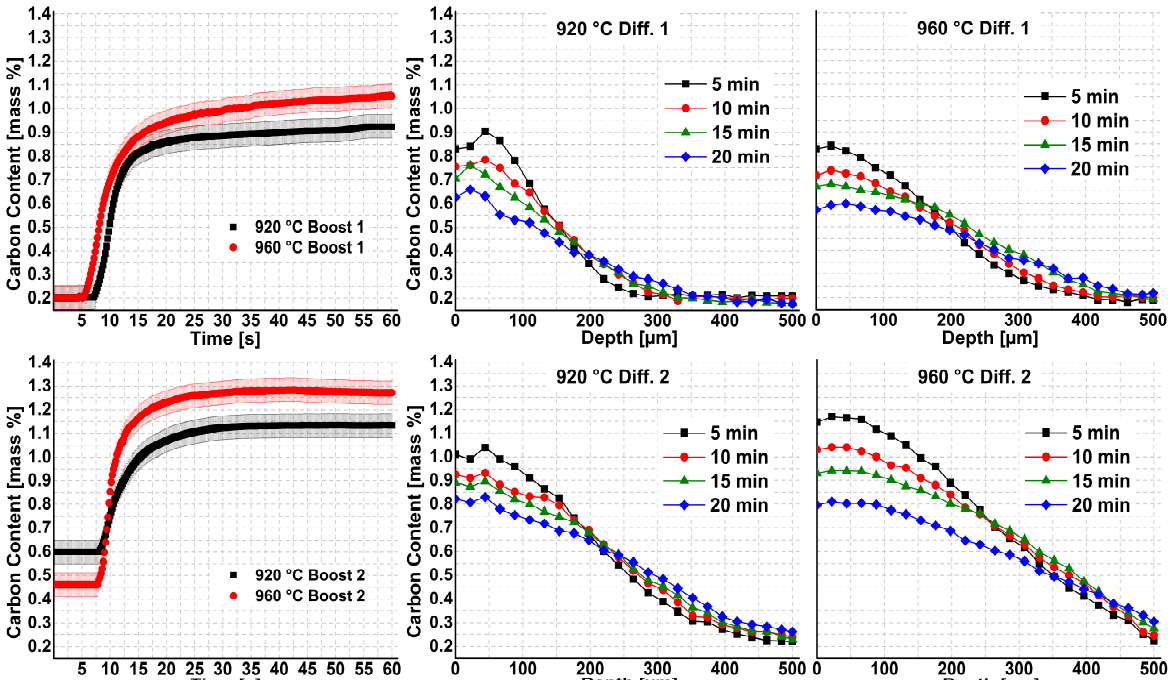

Figure 5-27: Evolution of carbon content dissolved in austenite during the boost and diffusion steps of LT-920C and HT-960C. t=0 is the time that the acetylene valve was opened. Error margins for all graphs are. $\pm\ 0.04\ ma.\ \%$ *as shown in boost steps. For diffusion steps, they are not given on the figure for the sake of clarity.*

Given that the beam height is limited to a maximum of 20 µm, and considering that carbon accumulation in the austenite initially occurs with a steep gradient over the first microns from the surface, the average carbon content in the measured area is notably lower than the maximum solubility limit of austenite at the specified temperatures. Nevertheless, the carbon content approaches its maximum value in each boost step. Acetylene rapidly decomposes into carbon and hydrogen upon contact with the hot steel surface [80,176,177], leading to a sharp carbon content increase. Subsequently, the rate of increase gradually decelerates and eventually converges towards a steady-state condition.

One reason for this rate decrease for both samples can be the accumulation of carbon at the surface and following formation of a very fine continuous cementite (Fe_3C) layer in the first few microns of the surface. If the concentration of carbon in the case during the boost step exceeds the solubility limit of austenite, M_3C carbides, with M being mostly Fe and Cr, can be generated at the surface [198]. This carbide layer decelerates the carbon uptake from the atmosphere to the sample and possibly hampers the diffusion of carbon in the near-surface region of the sample due to the lower diffusion rate of carbon in cementite [57,58]. Moreover, this carbide layer may hinder/slow down further carbon uptake by blocking the reaction sites; therefore, the autocatalytic acetylene decomposition reaction is slowed down, so the available carbon amount decreases [178–181].

In the diffusion steps after the first boost steps, carbon contents for both samples are the same after 5 minutes, although a higher carbon content is reached during the boost steps for the higher temperature process. Moreover, the carbon content at the surface for the high-temperature process decreases faster in the following minutes of the diffusion step. This is due to the increased diffusion

coefficient at high temperatures as well as an increased driving force provoked by the steeper carbon gradient. A similarly rapid decrease in surface carbon content can be observed analogously for the second diffusion step. Additionally, the reached depth is much higher for the high-temperature process. At the end of the second diffusion step, carbon contents at 0.5 mm depth are about 0.32 ma. % and 0.25 ma. % for the high-temperature and low-temperature processes respectively.

During the second boost step, similar to the first one, carbon content rise very fast at the beginning for both samples. However, the initial value is no longer the nominal carbon content of the steel but a higher value that remained after the previous diffusion step. After the first rapid increase within about 10 to 20 seconds, the carbon content in the solution of austenite at the surface remains mostly constant over the remaining boost duration, although acetylene was continuously introduced into the chamber at the same rate. The carbon content at the saturation level increases up to about 1.12 ma. % at 920 °C while reaching up to about 1.26 ma. % is reached at 960 °C, which is still lower than the maximum solubility limit. Measuring lower values than the indicated maximum limits is an indication that there is still a carbon gradient in the probed beam height of max. 20 µm area close to the very surface.

Based on the results, it could be observed that samples carburized at a higher temperature exhibit a steeper carbon content increase rate than a sample carburized at a lower temperature for both boost steps. Moreover, the final carbon content in the sample carburized at a high temperature is higher than that of a sample processed at a lower temperature, which was expected.

Additionally, it can be concluded for diffusion steps that the effect of temperature is more dominant at the early stages of the process, and its effect is getting lower during each additional step. This indicates that the main driver is the carbon gradient, which flattens during the process. Carbon in the high-temperature process reached higher depths, but the sample had a slightly lower surface carbon content due to the increased diffusion coefficient. It can be noticed from the final scans of the diffusion steps that the difference of 40 °C temperature for the two processes conducted with the given parameters results in a variation of the surface carbon content of around 0.05 ma. % in the final carbon profiles.

5.2.1.2 Formation of Carbides

The formation of carbides during the boost steps was confirmed as growing diffraction peaks belonging to cementite could be observed during the boost steps as indicated in Figure 5-28.

There is no obvious difference between the carbide peak intensities of both samples in two boost steps. As it is mentioned earlier in section 5.1.1.3 that carbides formed only at 2-3 µm from the surface while they are probed with 20 µm beam height, making them difficult to analyze or compare in quantitatively. However, it can be seen from the partial figures that carbides start to form in the very early stages of the boost steps to different amounts as soon as the surfaces of the samples

are saturated with carbon and grew until the end. Therefore, carbide formation is confirmed for both samples.

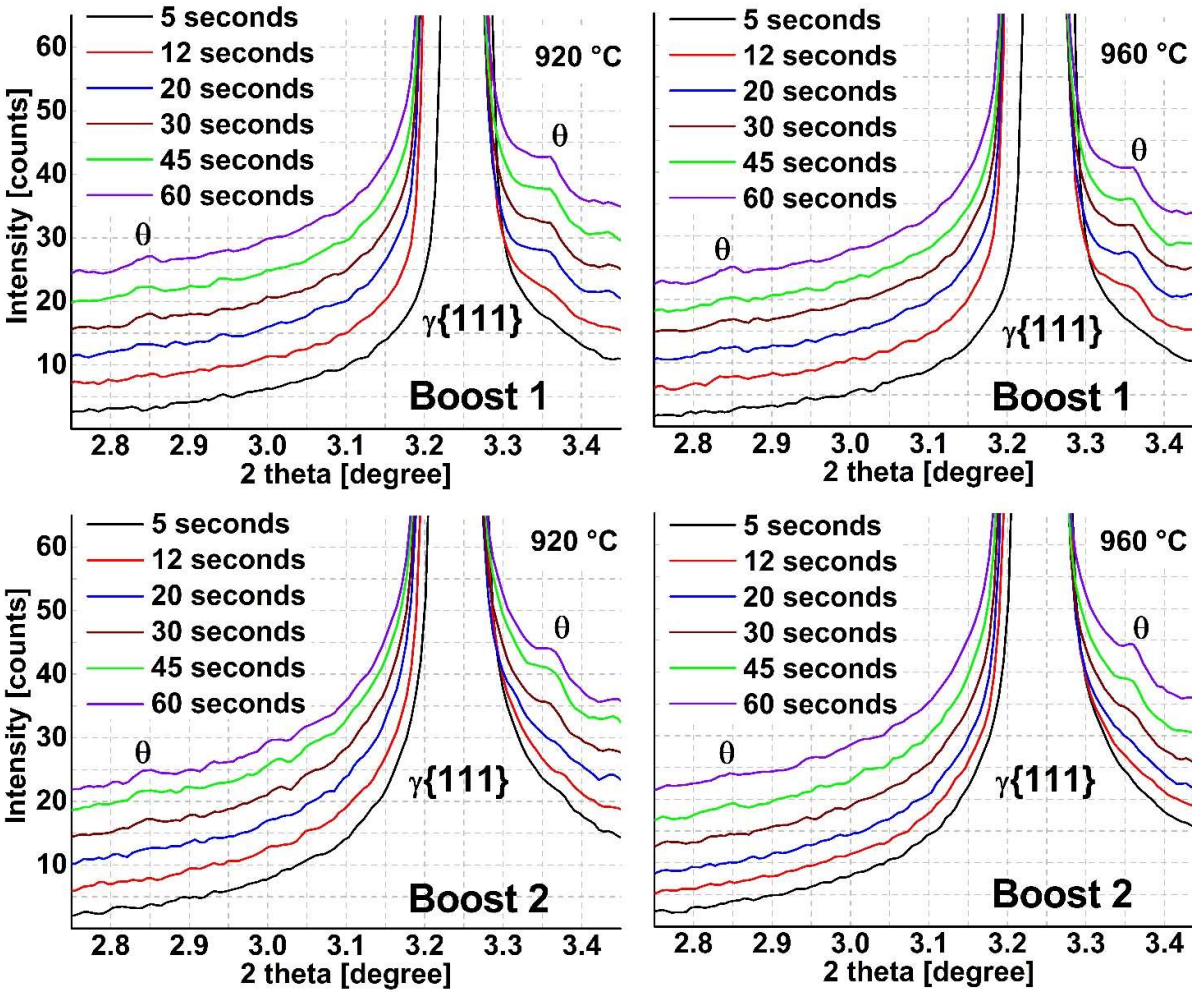

Figure 5-28: Cementite (Fe_3C / θ) formation near main γ {111} peak during the boost steps of samples LT-920C and HT-960C. 5 seconds peak is reference; each peak after that was offset +3 in intensity from previous one in y-axis for easy examination.

It can also be noticed from the 5th seconds of the second boost step that carbides formed in the previous steps are already dissolved during the following diffusion, as already observed previously at 940 °C in Figure 5-12. Since the carbide peaks exhibit very low intensity, drawing conclusive insights into the effect of temperature on carbide formation for the given example is challenging.

5.2.2 Effect of Acetylene Amount

The degree of dissociation of the carburizing gas depends on the temperature and flow rate, so the appropriate selection of the flow rate of the carbon donor gas is very significant for the process efficiency [83,199]. An optimum amount of carburizing gas varies considerably depending on the process temperature, batch size and complexity of the sample geometry; therefore, modern LPC processes are conducted using an excess amount of carbon donor gas. This creates a very high carbon potential and leads to the fast saturation of the austenite. Therefore, understanding the

microstructural evolution during the boost steps is crucial for gaining an appropriate comprehension of the process.

In order to investigate the effect of acetylene on microstructural evolution, two different low-pressure carburizing experiments with two boost-diffusion cycles were planned and conducted at 940 °C.

The amount of acetylene in the system can be varied by increasing the duration of the boost step, by increasing the acetylene flow rate or by increasing both simultaneously. Simply increasing the duration of the boost to achieve the desired effect would result in a substantial difference in the total process times between the two experiments, making them difficult to compare. Similarly, solely increasing the flow rate would not yield the desired effect, as acetylene could not be kept in the furnace with pressure control due to design limitations (see section 3.3). This would cause pressure to increase above the suggested limits. Therefore, in the experiments given in Table 5-2, both parameters were varied.

Table 5-2: Process parameters for the experiments with varying acetylene amount

		Boost 1	Diff. 1	Boost 2	Diff. 2
Sample LF-10ml	**Duration (min)**	5	20	5	20
	Pressure (mbar)	10	10^{-1}	10	10^{-1}
	Flow rate (ml min^{-1})	10	0	10	0
Sample HF-80ml	**Duration (min)**	10	20	10	20
	Pressure (mbar)	2	10^{-1}	2	10^{-1}
	Flow rate (ml min^{-1})	80	0	80	0

For both experiments, the chamber was first evacuated down to 10^{-1} mbar, and subsequently the sample was heated to 940 °C with a heating rate of 2 K sec^{-1}. Then acetylene was introduced into the furnace. Details about flow rates and durations are indicated Table 5-2. During the boost steps of sample LF-10ml, the vacuum valve was closed. In consequence, the average pressure in the chamber during the boost step was 10 mbar; instead, for sample HF-80ml, the vacuum valve stayed open, so the sample was showered with acetylene at a constant 2 mbar pressure.

The primary motivation for this approach was to maintain all process parameters as close as possible with the ranges recommended for modern low-pressure carburizing. As indicated earlier, achieving precise pressure control within the furnace was not possible. When acetylene was introduced into the closed system at a rate of 80 ml/min in the given experimental chamber, the pressure rapidly rose to 30 mbar and remains constant throughout the boost step. This could lead to soot formation on the chamber and the sample, potentially affecting the quality of the experiments.

The experimental chamber was designed to ensure that the gas inlet pipe was placed directly above the carburized and investigated surface, and the vacuum outlet pipe was placed right at the bottom of the sample. Consequently, the sample was placed in the direction of the gas flow. With this strategy, the optimum pressure range for the processes was not exceeded and the sample was exposed to a continuous flow of a very high amount of acetylene. The acetylene amount is linked with pressure; thus, adjusting different acetylene amounts under the same pressure was not

possible in the designed system due to technical limitations. However, according to a study performed in a thermogravimetric measurement device to determine the mass gain during carburizing, no significant differences were observed between absolute acetylene pressures of 3 to 15 mbar [48], which was taken as a reference to design processes. Therefore, values were tried to be adjusted as close as possible to this pressure interval and the effect of pressure was neglected in this study. However, pressure information is still included in the table to be more specific about the experiments.

Figure 5-29 presents the change of FWHM and peak positions of γ {111} austenite peaks during boost steps.

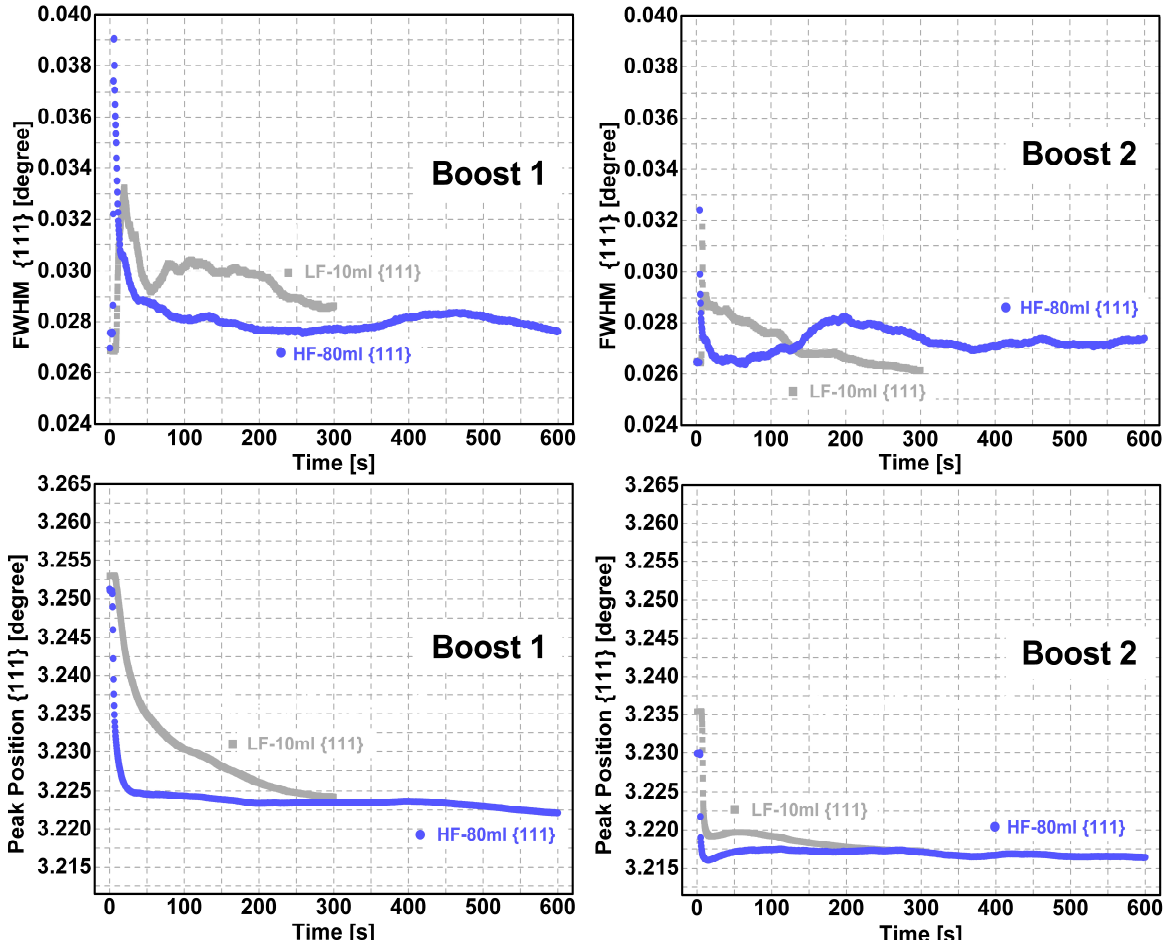

Figure 5-29: Evolution of FWHM and peak positions of γ {111} austenite peaks with time for the boost step of two different samples carburized with different acetylene amounts. Average error margin for FWHM is $3.7 \cdot 10^{-4}$ degrees.

Similar to previous investigations, peak shifts can be observed during the boost and diffusion steps of both experiments. These peak shifts are again directly related to carbon intake and diffusion via the lattice parameter evolution. Final peak positions in 2θ of the γ {111} peak for sample LF-10ml and sample HF-80ml are comparable for both boost steps with slightly more shifting of sample HF-80ml to lower angles. Additionally, an FWHM increase at the point where peak shift occurs can also be observed for both samples. After this increase, values decrease slowly to about 0.028-0.030

degrees again. Moreover, there are fluctuations of varying degrees in the FWHM of both samples, exhibiting local minima and maxima. This phenomenon may be attributed to the generation of local microstrains caused by the diffusion of carbon across the probed area.

Integrated diffraction frames were analyzed, and the lattice parameter changes were found using the same procedure as previously presented. Figure 5-30 shows the change of lattice parameter of austenite during the boost and diffusion steps of the two samples carburized with different acetylene amounts. During the boost step, the beam was kept constant at the surface and continuous scans were applied during diffusion. The change of lattice parameter during the first and the last scan is presented for simplification.

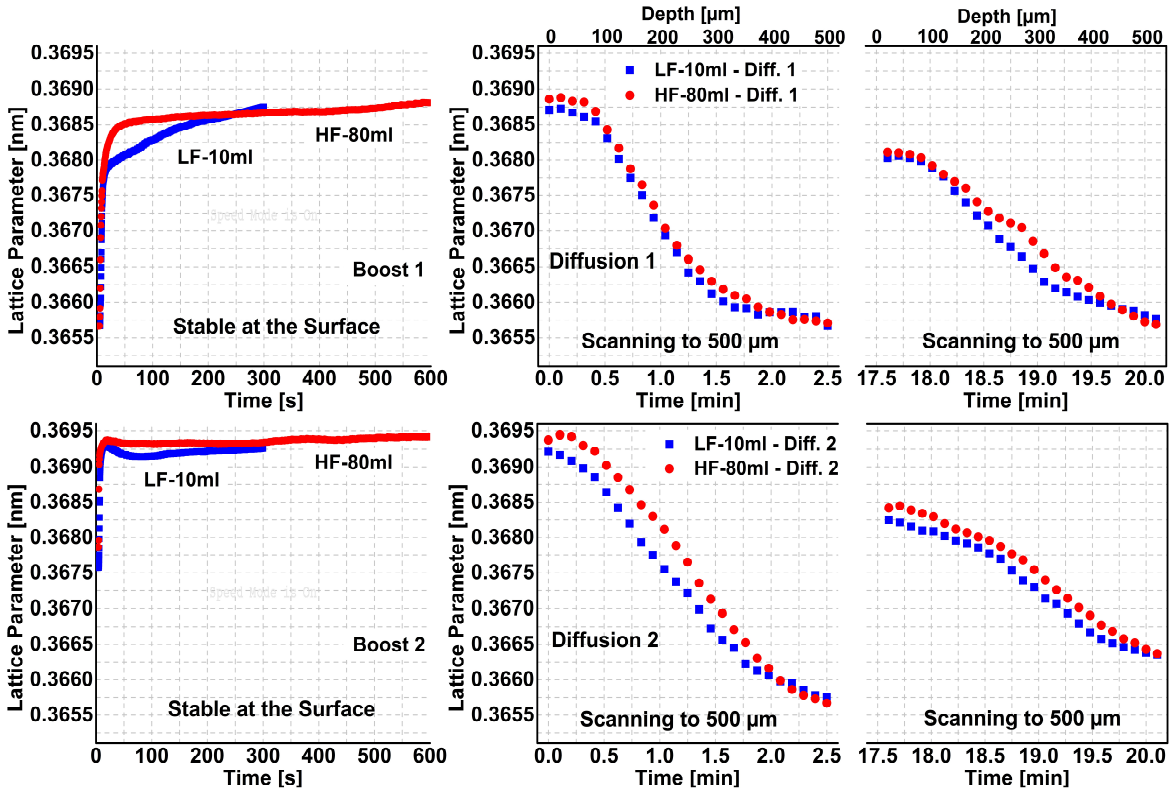

Figure 5-30: Evolution of the lattice parameter of austenite for samples carburized with different acetylene amounts. Distances from the surface were given at the top of each scan figure. Average error bars scale is $\mp 5 \cdot 10^{-5}$ and it is smaller than symbols.

Slightly higher lattice parameter values for sample HF-80ml can be observed from the graph, especially for the second boost-diffusion cycle. By using the given lattice parameters in Figure 5-30, carbon contents dissolved in austenite were calculated with Eq. 5-1 for each of the boost and diffusion steps and are given in Figure 5-31.

In the first boost steps, at the very early stages, the carbon content in the measured volume increases rapidly. Carbon contents at the end of 60 seconds are about 0.95 ma. % and 1.18 ma. % for sample LF-10ml and sample HF-80ml respectively, which indicates that increasing the acetylene flow rate positively affected carbon absorption from the atmosphere to the sample in the first minute.

After the first minute of the experiment of sample HF-80ml, carbon content stays almost constant at about 1.18 ma. %; however, during that of sample LF-10ml, it increases continuously.

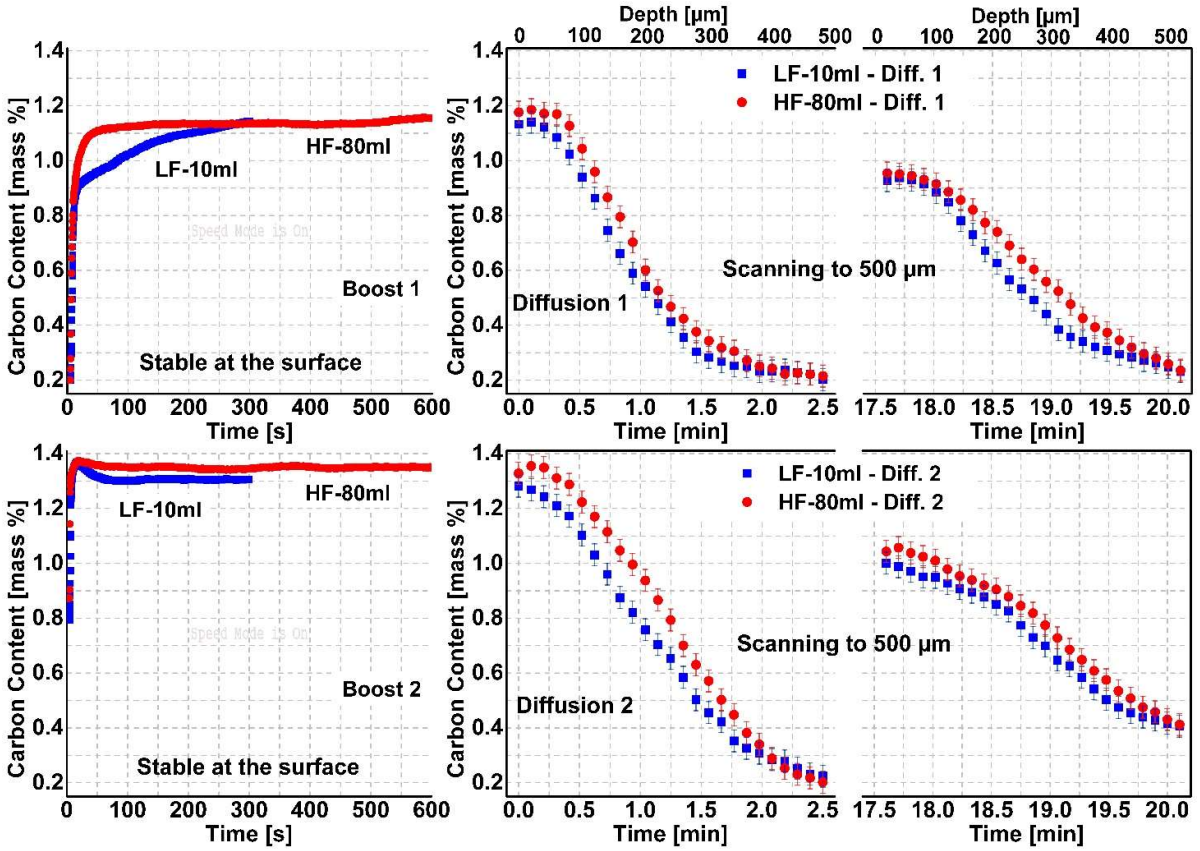

Figure 5-31: Change of carbon content dissolved in austenite over time during the boost and the diffusion steps of two samples carburized at 940 °C with different acetylene amount. Average error bar scale of ± 0.04 ma. % is only given for scanning stages due to higher number of data points but the scale is the same for all graphs.

It is notable that carbon supply to the surface of the sample during sample LF-10ml still continued very slowly after the first minute, whereas for sample HF-80ml, it stopped. Although the rate of carbon uptake decreases after the first minute, increasing the duration of the boost without changing the acetylene flow rate can still supply carbon to the surface at a very low rate. Hence, it is interesting to notice that the final carbon contents at the surface after the first boost step of these two experiments are very close despite the very different flow rates and durations. This is an indication that, after a certain point, which is most probably the coverage of the surface with carbides that block the reaction sides, it is not possible to increase the carbon further before the formed carbides are dissolved.

In the second boost step, the amount of carbon content at the end of 60 seconds is about 1.3 ma. % and 1.34 ma. % for sample LF-10ml and sample HF-80ml respectively. Increasing the boost step duration by two times and flow rate by eight times to higher values do not significantly affect the final carbon content.

It can also be noticed that there is a peak point of carbon content after 20 seconds of the second boost steps for both experiments and then carbon content decreases slightly by approx. 0.02 ma. %.

The reason for this might be an accumulation of carbon at the beginning due to the high reactivity of the surface until cementite is formed.

Similar to the temperature variation case, carbide formation during the boost steps was also observed. Figure 5-32 shows cementite peaks formed at different stages of the second boost steps.

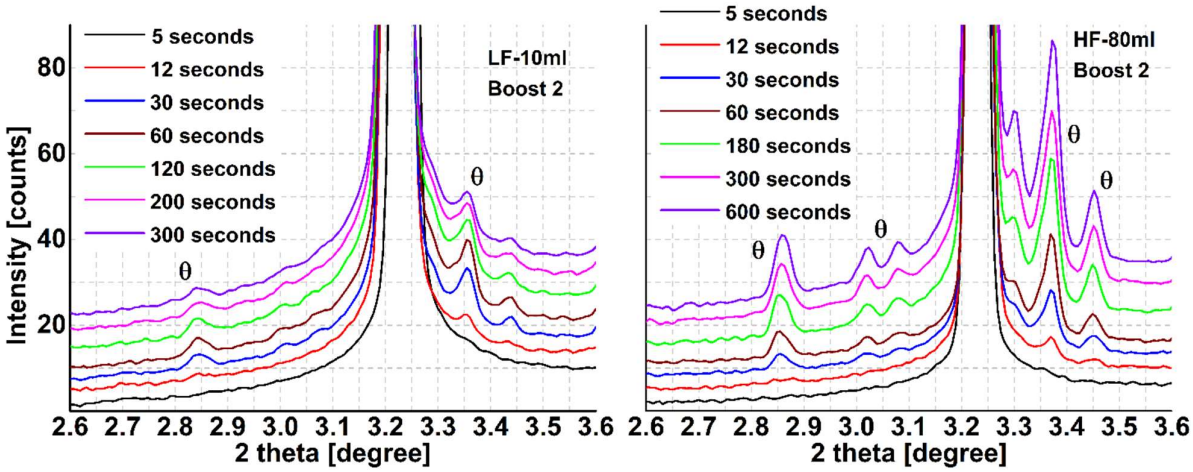

Figure 5-32: Diffraction patterns showing cementite (Fe_3C / θ) formation during boost steps of samples carburized with different acetylene amounts (see Table 5-2). 5 seconds peak is reference, each peak after that was offset +3 from previous one in y-axis for easy examination.

Similarly to previous samples, cementite starts to form during the boost step in the early seconds, with its' amount increasing steadily until the end of the boost step. Notably, cementite peak intensities at the second boost step of sample HF-80ml are apparently much higher than those in that of LF-10ml. It might lead to a deduction that a higher acetylene flow rate correlates with higher carbide formation. However, the position of the beam also highly affects the intensity of the carbide peak. Therefore, a quantitative comparison of the carbides between the two samples requires further data.

After the second boost steps, it is noticed that the final carbon contents show no significant difference for sample LF-10ml and sample HF-80ml. However, if carbide formation is taken into account, which should contribute to the final carbon profile by dissolution during the diffusion step, the overall effect can be seen more clearly.

Despite variations in the duration of the boost steps and the acetylene flow rates, the carbon depth profiles of sample LF-10ml and sample HF-80ml are very close to each other for the first diffusion step (see Figure 5-31 right). During the second diffusion step, the difference in the carbon profiles of these two samples expands, especially at the surface; however, they are still close through the depths, especially for the final scan. This phenomenon is ascribed to undissolved carbides at the surface, which have yet to contribute additional carbon to the solution. Sample HF-80ml, subjected to a prolonged 10-minute boost step with a substantial acetylene influx, exhibits pronounced carbide formation, particularly during the second boost step. The following 20-minute diffusion proved insufficient to dissolve all carbides, as evidenced in Figure 5-33, which shows carbide peaks at the end of the 20 minutes diffusion step for all samples. The figure indicates that there are still noticeable

cementite peaks at the surface for sample HF-80ml, while the sample LF-10ml shows minimal intensity carbides or secondary phases. The cementite contents of sample LF-10ml and sample HF-80ml are 2±1 ma. % and 5±1 ma. %, respectively, with austenite being the remaining phase for both samples.

In conclusion, increasing the duration of the boost step requires also a longer diffusion step for complete carbide dissolution. Nevertheless, these results also clearly show that the carburizing strategy, in particular, the duration of the boost step, is a key parameter in designing suitable and short carburizing processes. Prolonged boost steps with elevated acetylene amounts cause thick carbide layer formation, slowing down the acetylene diffusion from the atmosphere to the sample. Subsequently, these carbides contribute to the final carbon content through dissolution in the following steps, which is not as effective as a direct contribution.

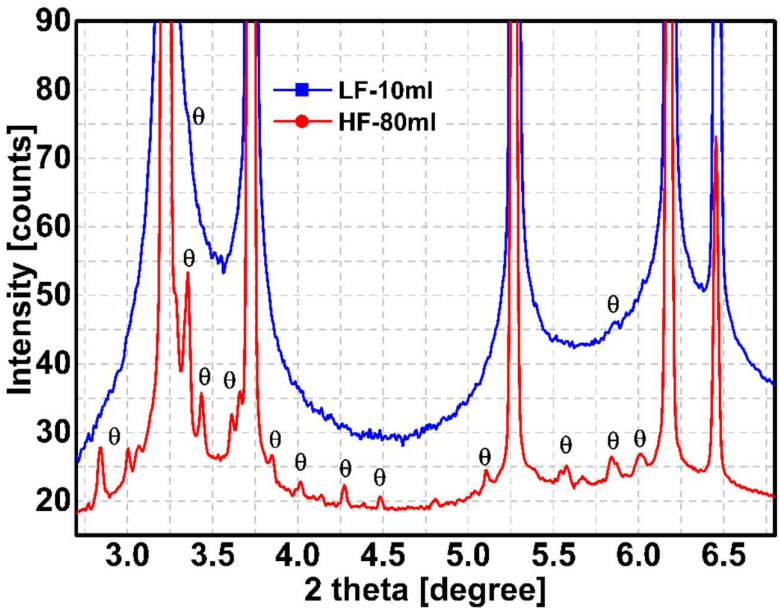

Figure 5-33: Diffractograms showing carbide peaks near main austenite peaks at the end of the second diffusion step measured at the surface of the samples. Sample LF-10ml peaks were offset +10 on y-axes respectively for easy examination.

In order to investigate the contribution of the carbides to the final boost step, a quantitative carbide analyses were conducted for the final boost step of sample HF-80ml. The higher amount of carbides made quantitative data evaluation more precise for this sample. Figure 5-34 illustrates the determined change of cementite content during the second boost step.

The increase of the cementite content is similar to some examples of carbon content in austenite represented in previous sections. It starts to increase sharply in the early stages, followed with deceleration in the increase rate. The formation rate of cementite is higher in the first 100 seconds of the boost step and then slows down. Upon closer examination of the enlarged region of the figure, showing the carbide evolution in the first 10 seconds, it can be noticed that cementite formation starts after about 5 seconds, meaning that the complete elimination of cementite formation by reducing the boost durations is not possible due to this immediate formation. Therefore, for this

case, the austenite saturation limit was reached within the first seconds, and during the following 100 seconds of the boost step, cementite formed at a notably high rate.

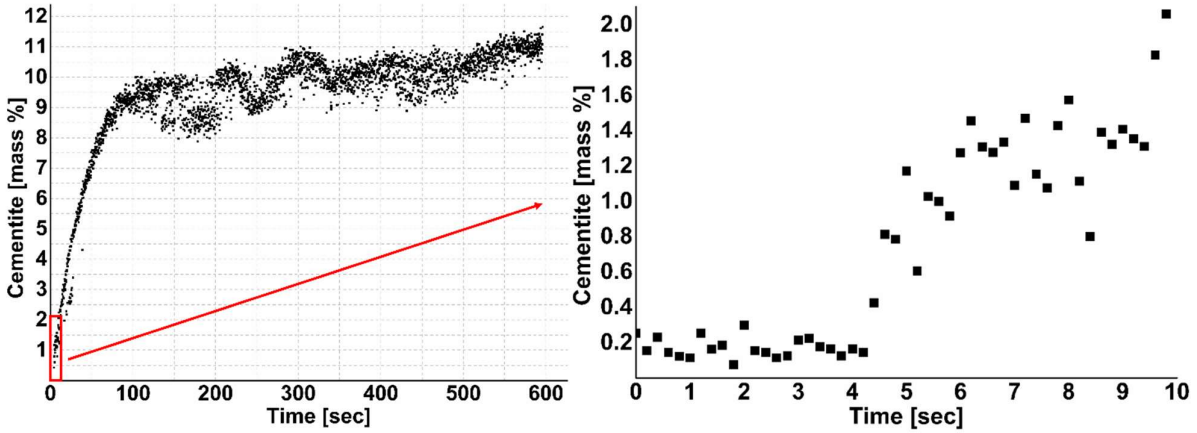

Figure 5-34: Change of cementite content during the second boost step of sample HF-80ml. The small figure shows only the first 10 second in which cementite started to form. The rest of the phase fraction is austenite. Only average error bar scale is given at top left corner due to higher number of data points.

Considering that the cementite dissolves and contributes to the final carbon content, it can be inferred that a boost step duration of 100 seconds is not necessarily detrimental to process efficiency because the given acetylene is still decomposing and forms cementite. However, beyond the initial 100 seconds of the boost step, the cementite formation rate reduces to very low levels, indicating that further acetylene introduction to the furnace does not contribute in a pronounced way to the carburizing process.

Figure 5-35 shows the initial and the final carbon content distribution of the sample from sample HF-80ml during the second diffusion step, without the contribution of dissolved cementite. By analyzing the change of area under the curve, the contribution of cementite to the full carbon content in the solution given in Figure 5-31 can be estimated.

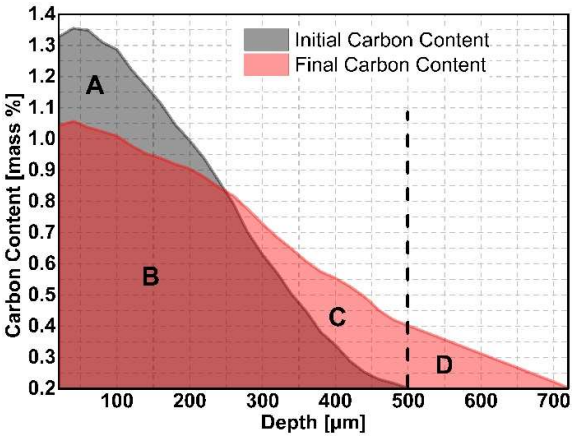

Figure 5-35: Initial and final carbon content distribution over depth during diffusion step 2 of sample HF-80ml. Area A+B represents the first 2.5 minutes, area B+C represents the last 2.5 minutes of the 20 min diffusion. Since scanning was done until a depth of 500 µm, area D is extrapolated to a base carbon content of 0.2 ma. %.

The selection of this particular sample is deliberate, as for this sample, cementite formation is the highest among others due to the higher acetylene flow rate. Therefore, quantitative detection of cementite is more precise. The combined area A+B amounts to 1.43 units, while area B+C is 1.45 units. The extrapolated area D is 0.11 units. According to this estimation, about 8.5 % of the total carbon comes from the dissolution of cementite, and this value has the potential to increase as it is known from the results presented in Figure 5-33 that there is still about 5 ma. % of undissolved cementite at the surface of the sample after 20 minutes of the diffusions step. While acknowledging the simplicity of this estimation, it serves as a useful example to show the significance of considering the impact of cementite on the final carbon content, especially for higher acetylene amounts or longer boost durations. Such considerations should be considered for modeling of carbon content depth profiles.

5.2.3 Effect of Boost-diffusion Cycles

When a high case hardening depth (CHD) is desired, the number of boost-diffusion cycles is generally increased and the carbon gradient becomes flatter. The addition of each supplementary boost step induces a complexity in predicting the microstructural evolution. Therefore, understanding the effect of a higher number of boost steps is crucial to provide appropriate models. In order to investigate the effect of the number of cycles, an additional experiment with four boost-diffusion cycles was conducted at 940 °C, and the results were compared with those of sample 3BD. Consistent to previous examples, experiments were started by heating the samples to the process temperature in a vacuum environment. The diffusion pressure was 10^{-1} mbar, the flow rate and the bottle outlet pressure of acetylene were 10 $ml.min^{-1}$ and 1.2 bar, respectively. Process pressures and durations of four boost-diffusion cycles are given in Table 5-3**.** Experiments were designed in a way that the total duration of the boost steps kept constants while adding one more boost diffusion cycles.

Table 5-3: Duration and pressure for boost and diffusion steps of two experiments

		B1	D1	B2	D2	B3	D3	B4	D4
Sample 4BD[2]	**Duration (min)**	1	20	1	20	1	30	1	45
	Pressure (mbar)	4	10^{-1}	4	10^{-1}	4	10^{-1}	4	10^{-1}
Sample 3BD	**Duration (min)**	1	20	2	20	1	25		
	Pressure (mbar)	4	10^{-1}	8	10^{-1}	4	10^{-1}		

Similar to previous investigations, the change of FWHM and peak positions of the γ {111} austenite peak during boost steps was investigated, and then the evolution of lattice parameters during boost

[2] First two boost-diffusion cycles of this sample are same with Table 5-1**;** therefore, this sample can also be compared with samples in **4.2.2.1. Process Temperature** as an example of 940 °C. To eliminate the repetition, results of this sample was not also given in that section.

and diffusion steps was determined. To eliminate repetition, these results will not be presented here. Details can be found in appendix section 10.10.

By using lattice parameters and Eq. 5-1, the change of carbon content during the boost and the diffusion steps was determined and presented in Figure 5-36.

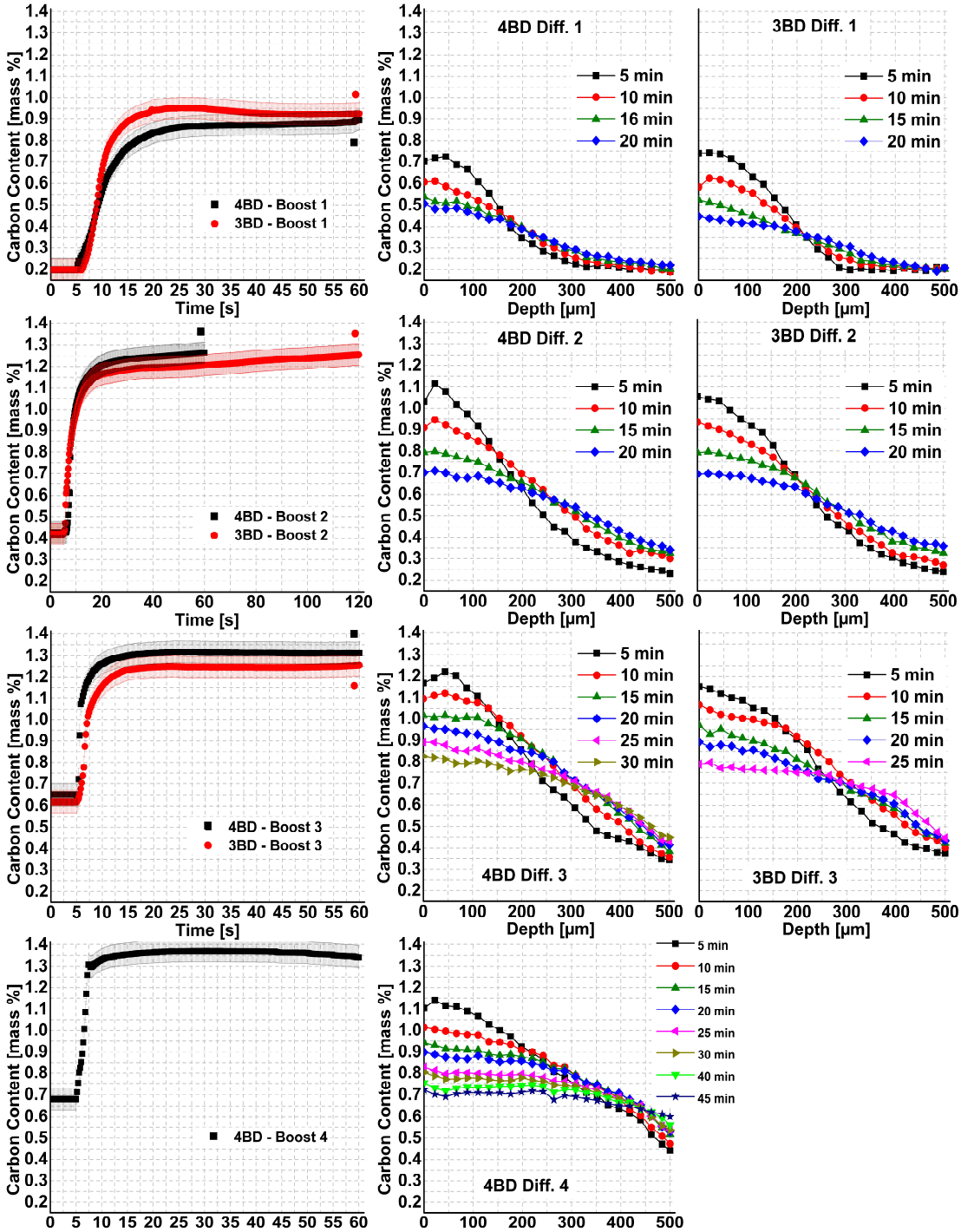

Figure 5-36: Carbon content change during the boost steps of the sample 4BD (a) and sample 3BD sample (b) carburized at 940 °C with 10 ml min^{-1} acetylene. Error bars scale is same for diffusion steps as given in boost steps but they are not shown in the figure for the sake of clarity.

The first boost and diffusion steps of the two samples show a very similar tendency, as the process parameters were almost identical. However, some gap between the values after the 10th second of the boost step is also noticeable. The reason for this is the reaction of the sample to the acetylene contact.

As it is mentioned in section 5.1.1, for some samples when acetylene contacts to the sample surface, it causes either a decrease due to cold contact or an increase due to an exothermic decomposition reaction, which causes the beam to shift from predefined positions. Although this problem is compensated by process control unit, it could not be fully eliminated. This can be understood from the fact that carbon contents getting closer to each towards the other at the end of the step due to the response of the process control unit.

The final carbon contents at the end of the second boost step are also very close to each other, although sample 3BD has a minute longer duration of the second boost step. As hypothesized in previous sections, the reason for this is the early saturation of austenite by carbon. The carbon absorption rate of the surface decreases rapidly after about 20 seconds in each boost step primarily due to austenite saturation. Prolonging the boost steps beyond this point leads to the formation of carbides at the surface, which also contributes to the overall carbon profile by dissolution in the diffusion step; however, this contribution is not as effective as the direct absorption of carbon from the atmosphere. These results signify the importance of applying a short but high number of boost steps when maximum process efficiency is desired.

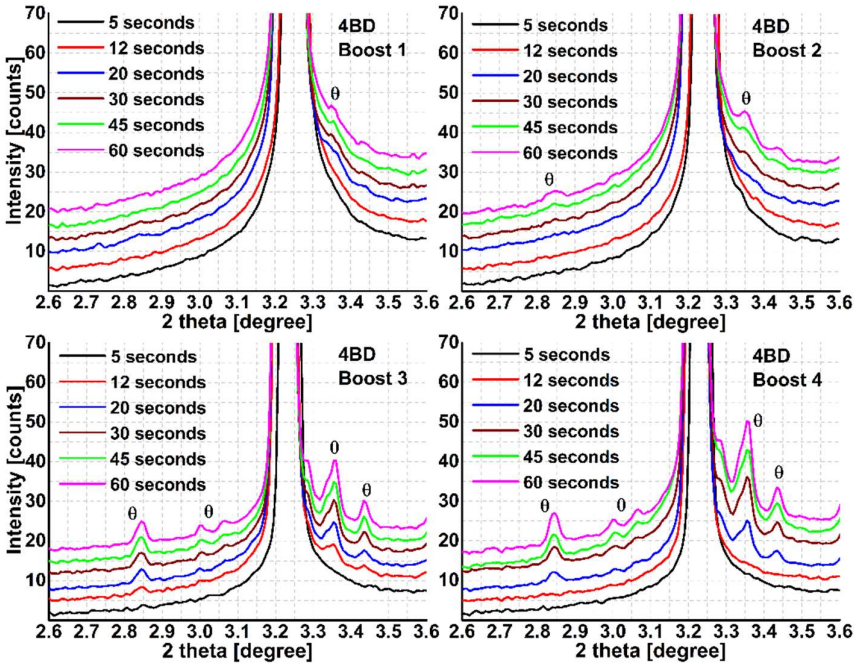

Figure 5-37: Diffractograms showing cementite formation during boost steps of sample 4BD. 5 seconds peak is reference, each peak after that was offset +3 from previous one in y-axis for easy examination.

Similar to the previous cases, carbide formation during the boost steps was also observed in the early seconds. Since carburizing parameters for sample 3BD are the same as those for sample

4BD, except for one minute longer second boost step, carbide peaks look very similar. Therefore, only diffractograms of sample 4BD are given in Figure 5-37 in order to eliminate repetition.
Carbides form directly after saturation, which is about 10 seconds. The intensity of the carbide peaks increases for each boost step. This is because of the increase in the phase fraction of carbides.
Quantitative analyses of carbides were also performed for boost 3 and boost 4 and are represented in Figure 5-38. Cementite contents start to increase after about 10 seconds for both samples, where austenite saturation is reached, according to Figure 5-36. For both steps, the increase rate is faster in the early stages and subsequently reduces until the end. However, for boost 3, this difference in increase rate is not as apparent as boost 4.

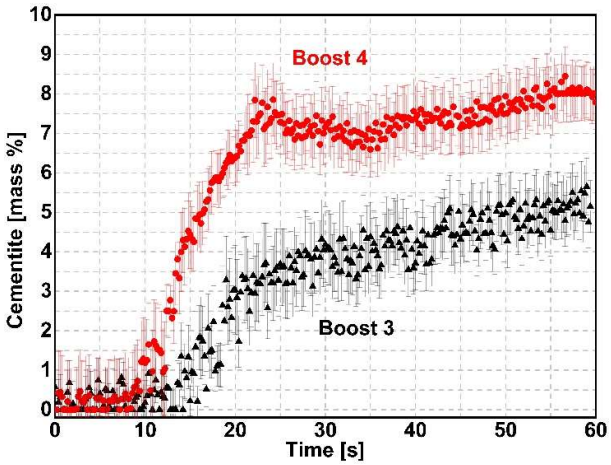

Figure 5-38: Change of cementite content during the 3rd and 4th boost steps of sample 4BD.

Similar to previous quantitative cementite analyses, it can be concluded that until 25th second of the boost 4, acetylene supplied into the system decomposes and forms cementite. This cementite will contribute to the final carbon content by dissolution in the following diffusion step. However, after around 25 seconds, the cementite formation rate reduces significantly, which means that further acetylene introduced into the system neither goes into solution with austenite nor forms cementite. Thus, it is assumed that there is no further substantial contribution to the final carbon profile.

5.3 General Discussion and Comparison with the LPC Process Model

As it is described in section 2.6, the movement of carbon atoms in the sample follows the same diffusion laws in both LPC and atmosphere gas carburizing. The key difference is the determination of initial parameters or equations, which are difficult to ascertain for the LPC due to its non-equilibrium nature. Thus, the results of the in-situ synchrotron X-ray experiments gave very important findings that can be useful in determining these parameters of the simulation.
One of the significant observations made during in-situ measurements was the very fast saturation of the austenite phase during boost steps, less than 5 seconds in some cases, which led to very rapid carbide formation. These carbides can cover the surface of the sample and reduce the carbon intake of the surface, causing a carbon flux reduction after the early seconds of the boost step. Additionally, oversaturation of the austenite was observed during boost steps. This leads to the

conclusion that the process becomes diffusion-controlled after the first seconds of the boost step, and carbon content at the sample surface slightly surpasses the thermodynamic limit. Both observations should be applied to the parameters.

Moreover, another critical finding was the stable carbon content observed during the early minutes of the diffusion step following the completion of each boost. The reason for this was hypnotized that the carbides formed during the boost step serve as an extra carbon source. This leads to the conclusion that carbon flux should be determined in a way that continues during the early minutes of the diffusion step by taking the dissolution of carbides into consideration. There are some diffusion models that assume carbon flux on the specimen surface as zero after the boost step [200], neglecting the carbide dissolution. According to this observation, this assumption is not correct.

Furthermore, results from in-situ experiments showed that carbides formed during boost steps, except for the HF-80ml sample, dissolve in the first 5-10 minutes of the diffusion steps, which means standard diffusion duration is adequate for dissolving carbides on the surface of the sample. Carbide formation/dissolution parameters should be adjusted in this way to dissolve all carbides in these conditions.

5.3.1 Comparison of Measurement Data with Numerical Process Simulation Results

The results of the in-situ synchrotron X-ray diffraction experiments were compared with results from thermodynamic simulations (see section 2.6.2) in order to refine the corresponding model parameters.

Comparison analyses showed notably good agreement between the in-situ experimental results and the simulated data for low-pressure carburizing within common parameter ranges (1 - 1.5 hours carburizing time and 920 – 950 °C process temperature).

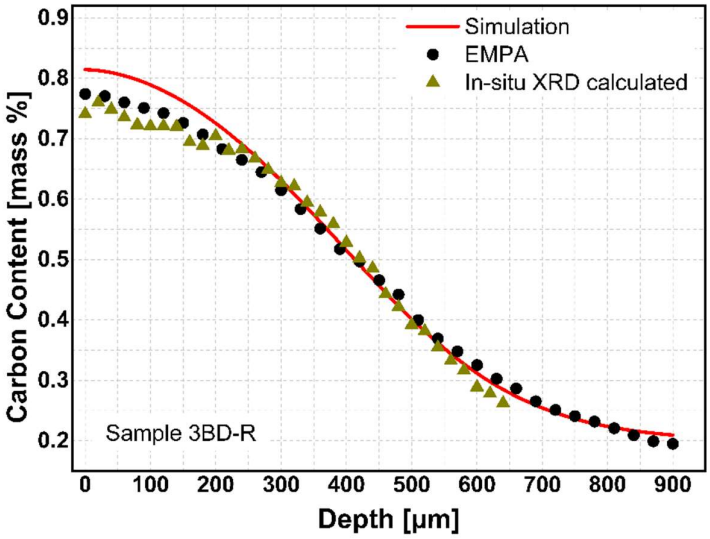

Figure 5-39: Simulation, EMPA and in-situ calculated results of carbon content depth profile of the sample 3BD-R carburized in experimental chamber.

Figure 5-39 shows the comparison of carbon content distribution over depth determined by EMPA, simulation and in-situ XRD measurement calculations for 3BD-R sample. Process parameters are given in Table 3-2 in section 3.4.

As the plot shows, EMPA data and calculated carbon content show close agreement, indicating the reliability of the calculations. There are, however, small deviations between these two and simulation data at the surface. One of the possible reasons for this difference might be slight decarburization in the experimental chamber. However, it is reported similar to this study that heat treatment of steel having 0.9 ma. % of carbon in air at 900 °C for two hours caused a 200 µm decarburized layer [201]. In the present data, the deviation also starts from 200 µm despite the fact that the process was conducted in vacuum and the duration was 1.5 hours. Additionally, a 200 µm depth of oxides must be easily noticeable from the diffraction peak, which was not the case. Therefore, the reason for this deviation to be solely decarburization is not probable.

The contributing reason to this difference might be the effect of the carbide layer formed at the surface. As mentioned several times in previous sections, carbides formed during boost steps slow down carbon intake from the atmosphere to the sample. An inaccurate description of this effect on the carbide dissolution conditions might cause deviations.

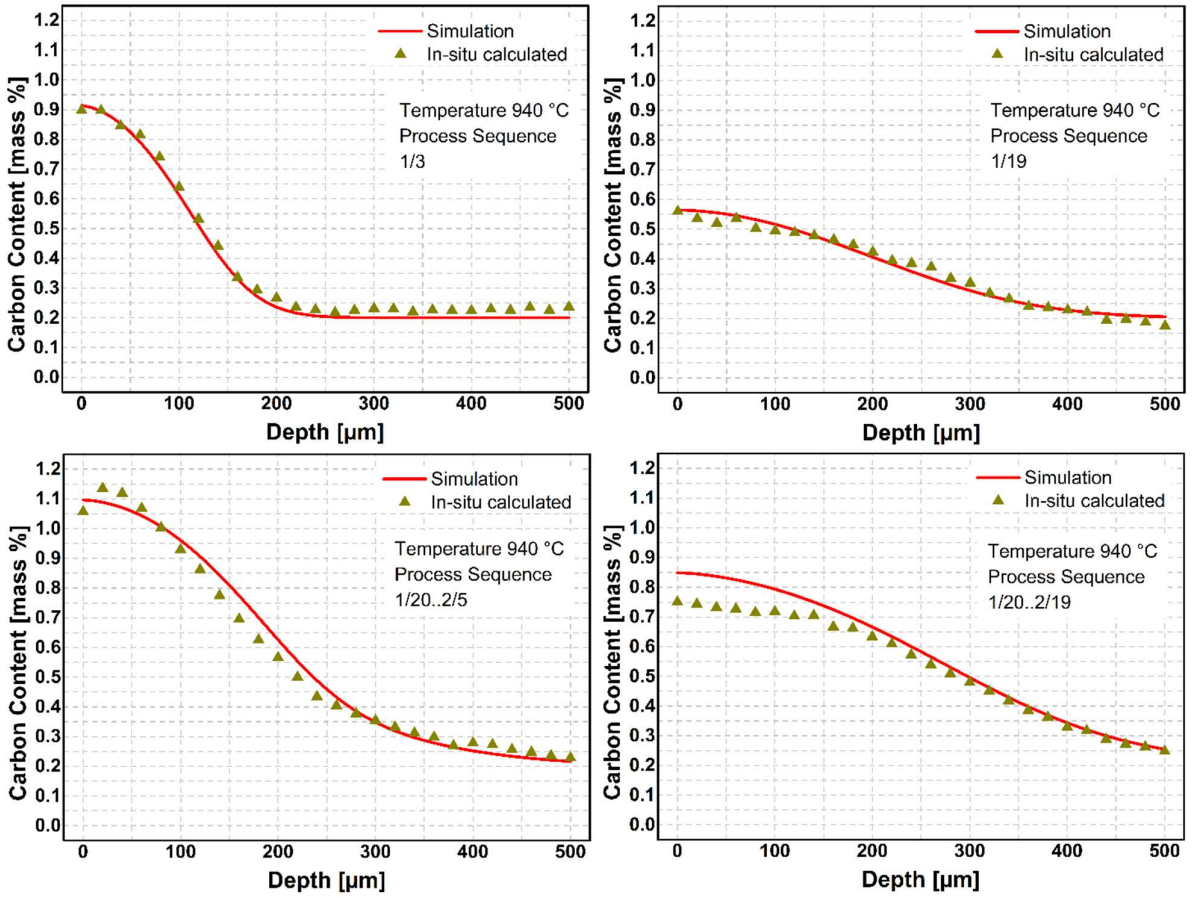

Figure 5-40: Simulation and in-situ calculated results of carbon content depth profile of the sample carburized in experimental chamber for different periods of the whole process.

Since boost and diffusion steps are entirely different from each other, in addition to comparative analyses of final results, observation of the behavior of carbon in each step of the LPC process can also give valuable information. Then, these observations can be used to optimize the related parameters and modelling kinetics to increase the precision. One of the advantages of in-situ measurements is the capability of gathering data from these individual steps.

In order to observe this, carbon content depth profiles at the particular moments of the whole process sequence were observed, and the results were compared with simulation predictions. The comparison can be seen in Figure 5-40. Calculated carbon content and simulation give very close results, except for the near surface area in the final step (Figure 5-40d). The deviation observed in Figure 5-39 is also present in this case. The reason for this deviation is probably also the deceleration of diffusion of carbon due to the formation of the carbides layer and partial decarburization at the surface.

In order to observe the effect of the above mentioned carbide layer, two samples were investigated with short boost steps. Figure 5-41 shows two samples carburized with less than a minute boost steps. For the simulation, the same parameters used for Figure 5-39 are also used for consistency. In Figure 5-41a, in which a 30 seconds boost step is followed by a 3 minutes diffusion step, carbon content is underestimated for the entire gradient. The possible reason for this is that the model calculates the carbon intake of the sample in a way that is directly proportional to the boost step. However, it was observed from in-situ experiments that after the early seconds, when the carbide layer is formed at the surface of the material, acetylene decomposition reactions slow down or stop. This implies that the most efficient carbon intake occurs within the initial seconds of the boost steps. Afterwards, further carbon intake relies on the dissolution of the carbides and diffusion of the accumulated carbon at the surface of the sample.

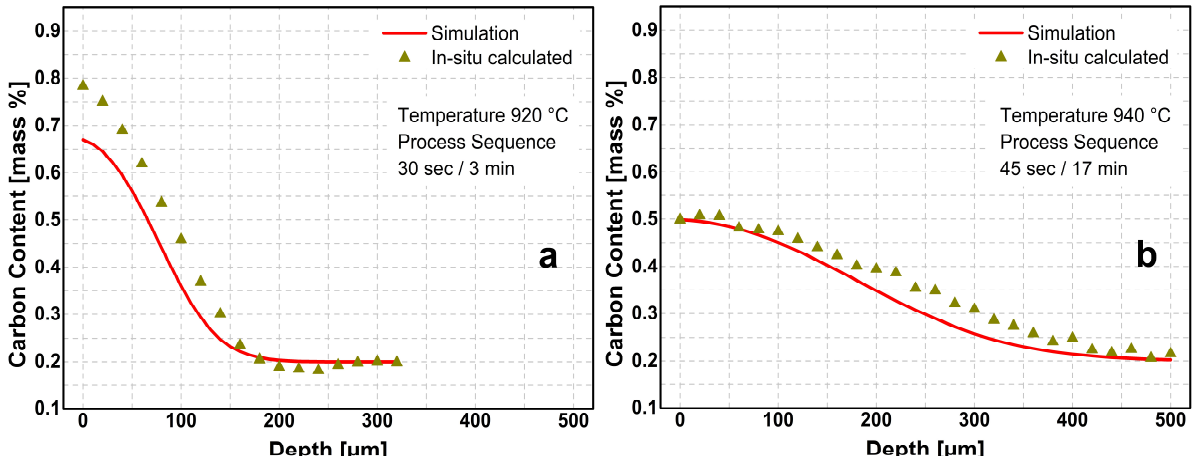

Figure 5-41: Simulation and in-situ calculated results of carbon content depth profiles for samples having less than a minute boost steps. Process temperatures and plans are given in the figure.

In Figure 5-41b, a comparable behavior can also be seen. The difference in the carbon content is not as much as the difference observed in Figure 5-41a. The reason for this might be that the boost step is closer to the standard value of 1 minute. Another possible explanation might be that, due to

longer diffusion steps, accumulated carbon at the sample surface has diffused through the sample and contributed to the final carbon gradient.

If the same observation were made with the standard parameters, simulation and calculated carbon contents would give very close results, as seen in Figure 5-42a. If the duration of the boost step is extended to very high values, such as 10 min as given in Figure 5-42b, then carbon contents are strongly overestimated in the depth. The reason for this that parameters do not fully take account the carbide formation and related deceleration of carbon intake.

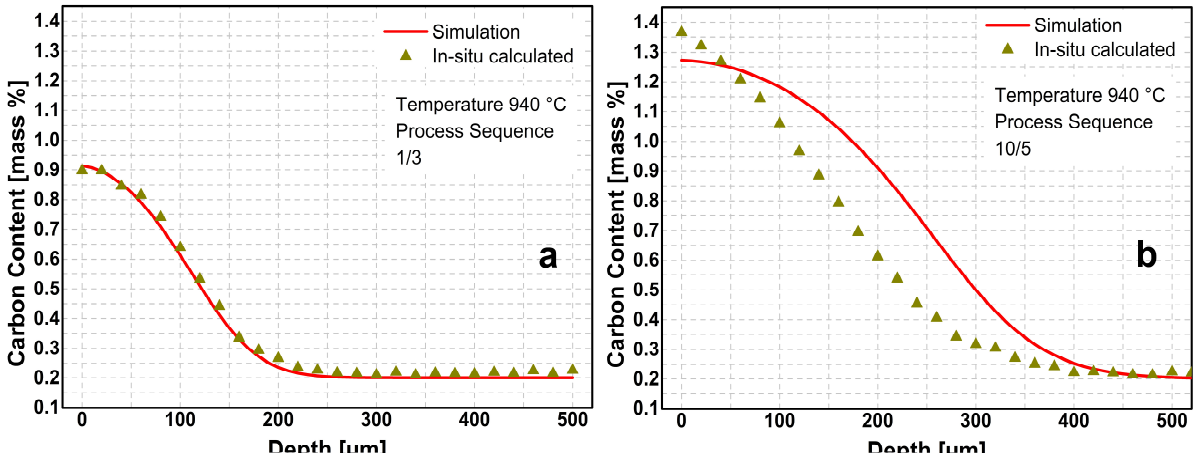

Figure 5-42: Simulation and in-situ calculated results of carbon content depth profiles for samples having 1 min and 10 min boost steps. Process temperatures and plans are given in the figure.

In conclusion, thermodynamic simulation is capable of giving very accurate results when applied to conventional boost step duration in the range of 45 seconds to a few minutes. However, if the duration of the boost step is increased or reduced in a certain extent, a modification of standard parameters becomes necessary to adequately model the impact of the carbide layer on diffusion. In-situ measurements reveal a non-linear relationship between carbon uptake and boost step duration, owing to rapid saturation and carbide formation. Therefore, in order to predict the carbon depth profile of the LPC processes with complex process sequences, effect of carbides should also be considered. Based on the results, this effect can be added to parameters defining carbide formation and dissolution.

6 Evolution of Stress during Different Steps of Low Pressure Carburizing

Stresses generated at high temperatures are generally considered negligible since the yield strength is so low. For the investigated steel 20MnCr5, the yield strength at 700 °C is around 100 MPa [202], and it is even lower at the 940 °C process temperature. Additionally, relaxation of the stress due to recovery is expected to be very fast. While the quenching step is the most critical in terms of stress generation during the case hardening process, the stresses generated at each step will be presented and discussed in this section for the sake of completeness and consistency.

6.1 Before Boost Step

It is expected that before the boost steps, all stresses are relaxed due to the 940 °C process temperature. In order to confirm this, deviatoric stress was calculated by using the procedure described in sections 2.7.3 and 3.4.3 for the sample 3BD. Change of deviatoric stress in longitudinal direction (x direction in Figure 3-5) at 940 °C before the first boost step is given in Figure 6-1.

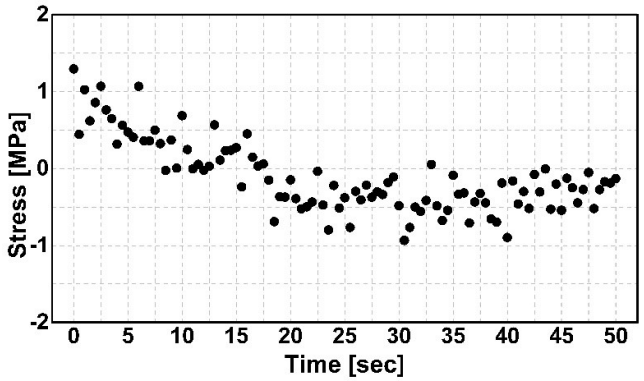

Figure 6-1: Evolution of deviatoric stress in austenite in longitudinal direction before first boost step of Sample 3BD.

There is no stress before the first boost step as expected. Consequently, it is safe to take stress values before boost step as a reference zero and adjust other values accordingly. The reason for doing that is to eliminate miscalculation caused by small sample position fluctuations.

6.2 Boost Step

As already discussed in previous sections, during the boost step, a sharp decrease in the peak position and an increase in the FWHM were observed mainly due to carbon uptake. Along with these changes, a change in the deviatoric stress state was also calculated. Stresses at 940 °C before each boost step were taken as a reference zero due to stable environmental conditions and high temperature, and changes in stresses were adjusted accordingly. The change of the values deviatoric stress for austenite during boost steps can be seen in Figure 6-2.

Stresses are generated in the 5th second of the graph, coinciding with the point where carbon content starts to increase in Figure 5-7. For all boost steps, stresses in the longitudinal direction are first compressive, and their values progressively increase. After reaching a certain point, which is pointed out with yellow arrows in the figure, stresses values reach the maxima in compression direction. This maxima corresponds to the point where the saturation limit of the austenite is reached. After this, compression stresses start to relax. From the first to the last boost step, the duration between the beginning of compression stresses and the change of direction is getting shorter, as can be seen from the arrows getting closer to each other. This phenomenon is attributed to the reduced time required for the saturation of austenite in each successive boost step.

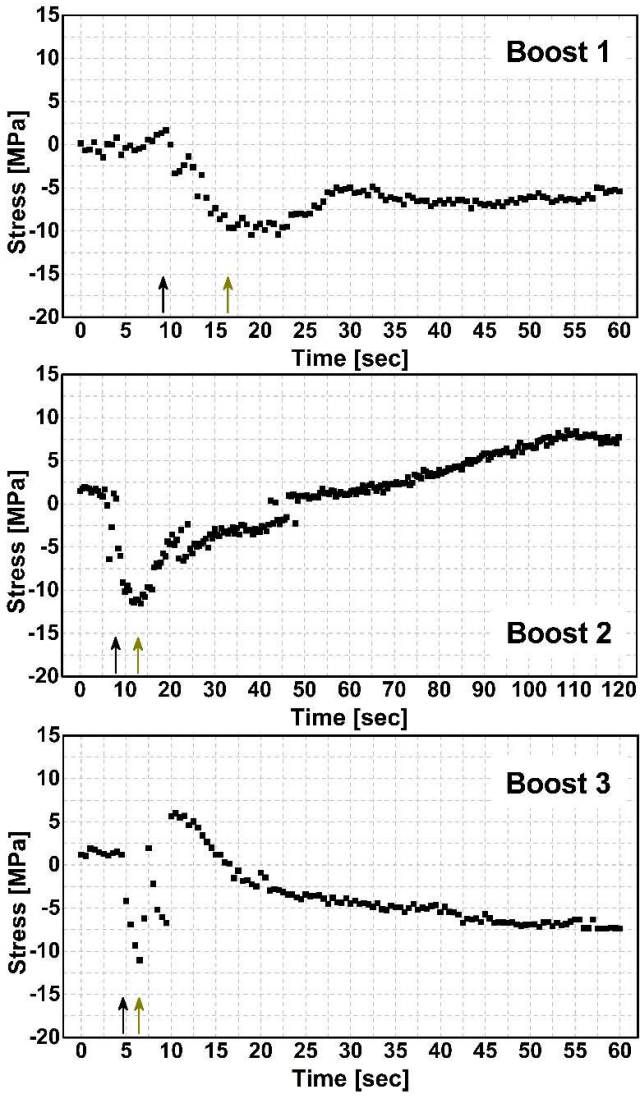

Figure 6-2: Evolution of deviatoric stress in longitudinal direction in austenite during boost steps of Sample 3BD.

The observed changes in stresses are attributed to the sudden introduction of carbon into the austenite lattice, creating a saturated austenite layer at the top of the sample. This leads to a lattice expansion, generating tensile stresses. Notably, this expansion only happens at the very top 2-3 µm of the surface, while the remaining area probed by the X-ray beam still maintains lower carbon

content. Therefore, tensile stresses occurring 2-3 µm at the top of the surface due to this expansion are counterbalanced by deviatoric macroscopic compression stresses in this low carbon area (remaining 17-18 µm from the top, considering that all 20 µm beam height passes through the sample). Consequently, compressive stresses are observed at the beginning of the boost step. However, due to the high temperature, they relax quickly and the total stress approaches zero.
Although some changes are observed in the deviatoric stress state during the boost step, the values of stresses are very small, so it is not suitable to make certain judgements. They are less than 20 MPa for both tensile and compression direction despite very sharp lattice expansion. Therefore, the effect of stresses is negligible compared to the carbon absorption of the austenite lattice. However, it is still important to show that despite very high temperatures, stresses in some extent were generated.

6.3 Diffusion Step

There is also no stress expected during the diffusion step due to the high temperatures and the slow carbon mobility in the austenite lattice compared to the boost steps. In order to observe the changes during the diffusion step, deviatoric stress was calculated for the sample 3BD. The change of deviatoric stress in longitudinal direction is given in Figure 6-3.

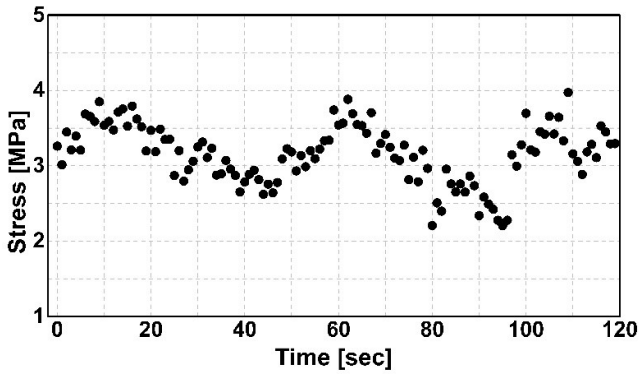

Figure 6-3: Evolution of deviatoric stress in austenite in longitudinal direction during first 2 minutes of first diffusion step directly after first boost step for Sample 3BD.

It can be seen that almost no stress was observed during the diffusion step, which was expected. Fluctuations in the stress are most probably because of regulation of the voltage that controls the temperature or continuous diffusion of the carbon atoms. In both cases, values are negligible.

6.4 Quenching Step

Stress generation during quenching was determined for both phases of austenite and martensite. Samples with different carbon profiles were investigated, which can be seen in Figure 6-4 along with cooling curves. Sample names are given based on the surface carbon contents. For example, sample C58 and C86 have a surface carbon content of 0.58 ma. % and 0.86 ma. %, respectively.

As can be seen from the figures, the cooling curves are very close to each other, suggesting that the key parameter influencing stress evolution is the carbon content distribution. The sample named as C78 is the 3BD sample that was examined in earlier sections. The other two samples belong to new experiments designed for stress analyses.

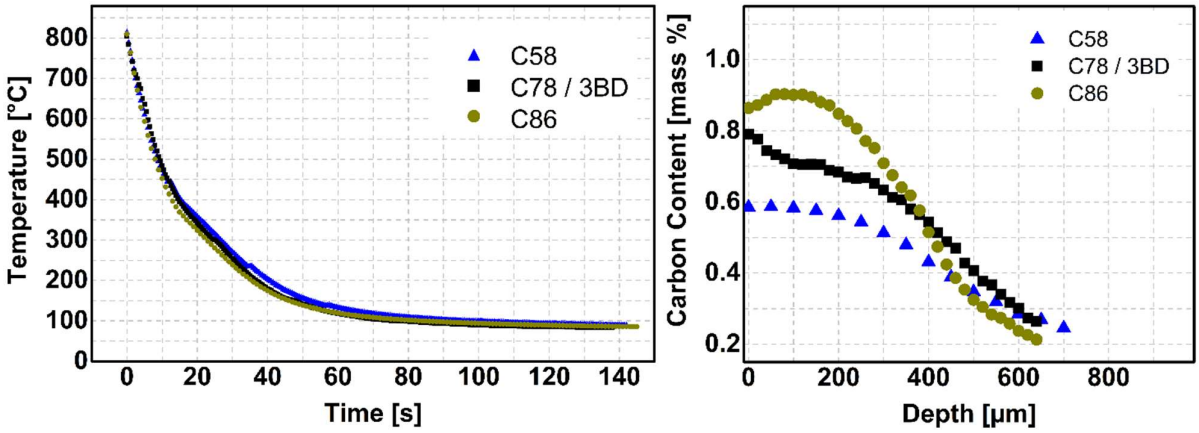

Figure 6-4: Evolution of temperature during quenching and carbon content depth profiles of investigated samples.

For the quenching step, both deviatoric stresses and total stress were determined. Each stress type includes phase-specific stresses as well as macro stress, calculated using the direct phase proportion of each phase based on Eq. 6-1.

$$\sum_{\xi=1}^{n} c^{\xi}(\sigma_x)^{\xi} = \sigma_x^T \qquad \textit{Eq. 6-1}$$

ξ represents the austenite and martensite phases $(\sigma_x)^{\xi}$ is phase specific stresses in longitudinal direction (x-direction, see Figure 3-5) and c^{ξ} is mass fraction of the phase each phase. A detailed explanation of the determination of stress is given in Section 3.4.3.

C78 (Sample 3BD)

As mentioned in section 3.4.1, beam position changes during quenching due to shrinkage of the sample. Therefore, finding the degree of this shifting is important to interpret the results. It is demonstrated in section 3.4.1.2 with laser triangulation measurements that the change of beam position from the beginning (840 °C) to the end (85 °C) of the quenching is around 200 µm. Therefore, the first surface position was determined by entry scans and then measurement was performed around 200 µm below the surface to account for this shrinkage. Figure 6-5 illustrates this measurement strategy.

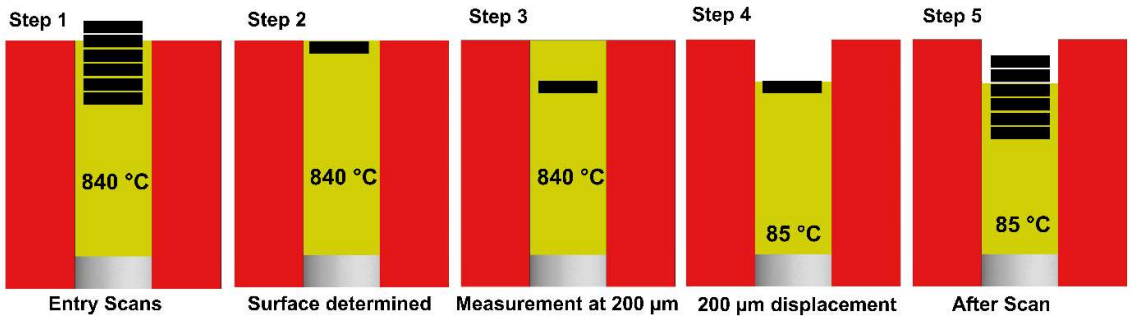

Figure 6-5: Strategy to determine measurement position during quenching. Yellow area represent the measured opening between heating elements (in red).

In order to confirm the final positions, values of lattice parameter of austenite at the end of the quenching are compared with the values from the scanning after quenching. Figure 6-6 shows the lattice parameter comparison data.

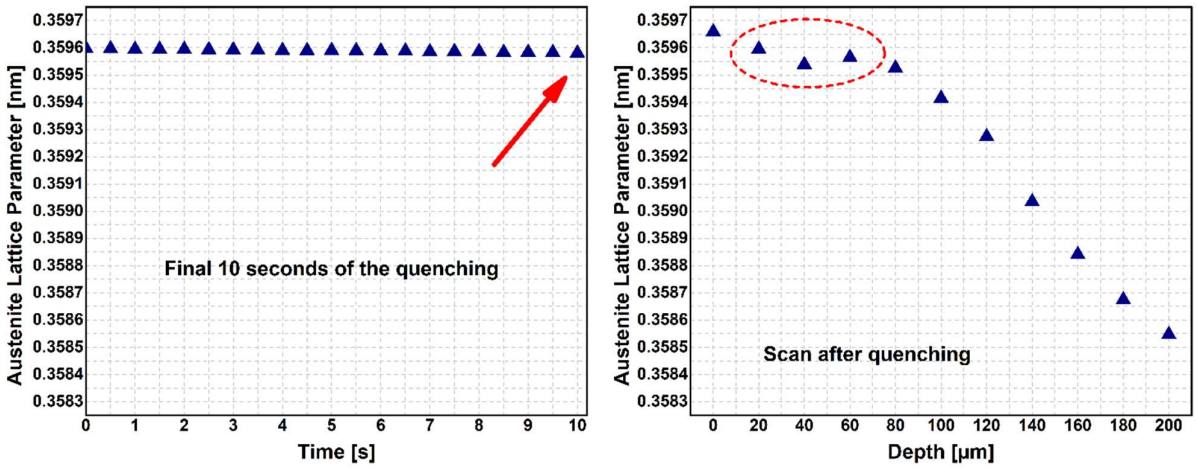

Figure 6-6: Evolution of austenite lattice parameter in final 10 seconds of the quenching over time and directly after quenching over depth.

It can be noticed from the depth scan values that lattice parameters in the first 60 µm are quite close due to similar carbon content near the surface. Comparing the final quenching lattice parameter value of around 0.35955 (shown with a red arrow) with the depth profile scan, it can be assumed that the final measurement position is within the first 20-60 µm (showed with dashed ellipse). Then it can be concluded that measurement started at around 200 µm depth at 840 °C (step 3 of Figure 6-5), then the beam shifted towards the surface during quenching up to 20-60 µm depth. Determination of beam position with better precision is not possible with the available data.

The evolution of deviatoric stress for sample C78 in austenite and martensite can be seen in Figure 6-7. The deviatoric total stress in the figure is calculated by using the proportion of each phase given in Figure 6-8.

It can be noticed that the first stresses are generated around 700 °C in the tensile direction and then gradually increase up to 50 MPa. This is because of the higher specific volume of the core since the core cools slower than the surface. Subsequently, at around 450 °C, strong further increase to the

tensile direction can be observed. This is linked to the martensitic/bainitic transformation of the core, which has around 0.2 ma. % carbon and M_s temperature around 410 °C according to the formula developed by van Bohemen (Eq. 5-2). The reason for this difference in the theoretical and observed M_s temperature can be the position of the thermocouple, which is closer to the surface. Another possible reason for this difference is that this observed transformation is bainitic, although it is unlikely due to the higher theoretical bainite start temperature, around 560 °C.

This preceded transformation of the core before the surface creates a further increase of the specific volume of the core and this expansion could not be compensated by still soft austenite at the surface, which ultimately created a further tensile stress in the austenitic surface.

From 450 °C to 220 °C, there is a continuous increase of the tensile stress; however, there are also certain points where sudden jumps are observed, such as at 360 °C, 300 °C and 240 °C. The reason for this is the carbon gradient from the measurement start point to the surface (end point) which creates an M_s temperature gradient. As measurements started from 200 µm depth and ended around 20-60 µm (see Figure 6-5), they are affected from carbon gradient. The transformation that started from the core proceeds towards the surface, and each transformed area along the way generates a further tensile stress at the surface, which is the measured area.

Towards the end of the quenching process, there is another turning point in the compression direction at about 215 °C, corresponding to the approximate martensitic transformation temperature of the surface. Since the surface has a higher carbon content, it has a lower M_s Temperature. In the final stage, the sample has compression stresses at the surface as expected. This transformation also generates the same lattice expansion; however, this expansion is restricted by an already hardened, rigid core. Thus, tensile stresses at the surface are reduced and inverted into the compression stresses.

Compression stresses in martensite could be properly detected around 195 °C, which is 20 °C lower than the observed temperature of slope change in austenite. These compression stresses in martensite were initially around -25 MPa and continued to increase until the end of the quenching step to -150 MPa, while stresses in austenite reached about -75 MPa at the end of the quenching.

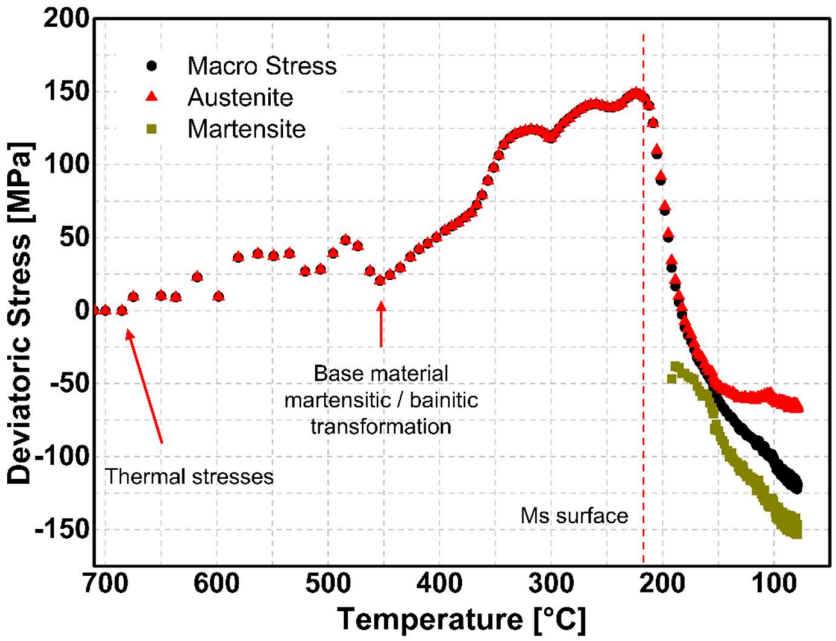

Figure 6-7: Evolution of deviatoric stresses in longitudinal direction for both austenite and martensite and deviatoric macro stress during quenching for C78.

For the same sample, total stresses were also calculated for both martensite and austenite, which requires a precise calculation of stress-free lattice spacing. The CTE of austenite was determined based on the evolution of the d-spacing of γ {311} from full integration of the diffraction rings, and then the linear part of the data above the M_s temperature was extrapolated down to the final temperature. This requires the assumption of a linear dependence of stress-free lattice spacing to the temperature until the end of quenching. Figure 6-8 shows the evolution of austenite d-spacing during quenching and the theoretical stress-free d-spacing.

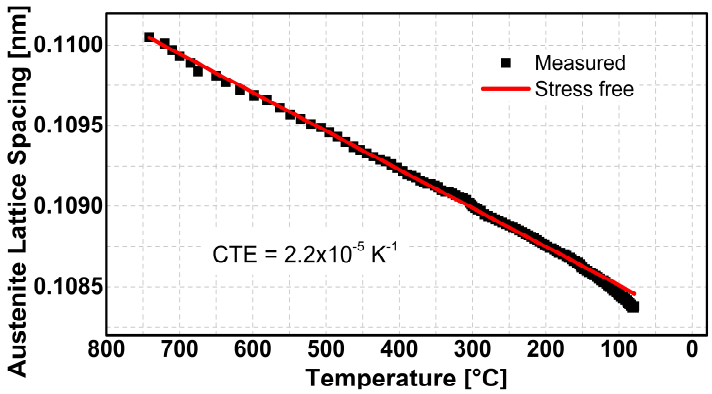

Figure 6-8: Evolution of measured austenite d-spacing during quenching and linear fitting extrapolation showing theoretical stress-free lattice spacing (left) and evolution of phases (right) during quenching for sample C78

For martensite, in order to determine stress-free lattice parameter (α_0), a quadratic equation of lattice parameter depending on temperature (Eq. 3-4) was used from literature with modification based on ex-situ laboratory stress measurements, and stress-free lattice d-spacing (d_0) was

determined by a cubic structure assumption by using Eq. 3-5. A detailed explanation of the procedure is given in Section 3.4.3.2.

The evolution of total stress in longitudinal direction for sample C78 in austenite and martensite can be seen in Figure 6-9. It can be noticed from the figure that the same turning points are present in austenite as it is observed in evolution of deviatoric stresses in Figure 6-7. Initially, thermal stresses are started to form around 620 °C in the tensile direction and then slowly increases up to 100 MPa, surpassing the deviatoric part. Around 450 °C, a notable further increase in the tensile direction can be seen, with values again exceeding those in the deviatoric part. At about 215 °C, a change of evolution can be observed with decreasing tensile/increasing compression, which is about the martensitic transformation temperature of the surface. Following this point, stresses in austenite goes down to -400 MPa at the end of the quenching step.

Evolution of the total stress of martensite is different than that of deviatoric stress. After the M_s temperature, compression stresses of around -250 MPa are detected in firstly formed martensite grains, and then these stresses relax until the end of the quenching step down to around -25 MPa. Total stresses are the sum of deviatoric and hydrostatic parts. It was determined that both hydrostatic and deviatoric stresses are in compression in the austenite, which gives around -400 MPa total stresses at the end. However, for martensite, deviatoric stresses are in compression around -150 MPa, while hydrostatic stresses are in tension, which gives at the end around -25 MPa total compression stresses.

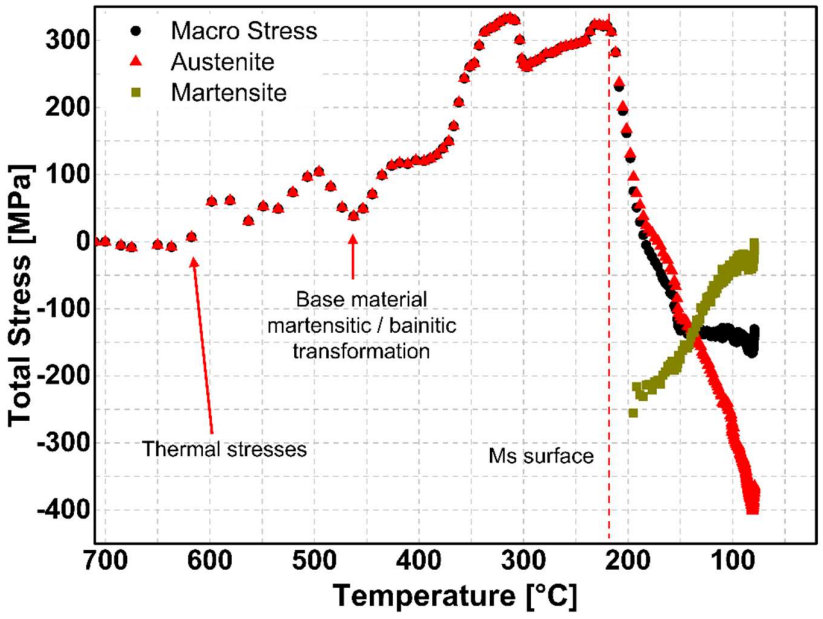

Figure 6-9: Evolution of total stresses in longitudinal direction for both austenite and martensite along with total macro stress for sample C78 during quenching.

The generation of high hydrostatic compression stresses in austenite after martensitic transformation has already been reported [19,154,155]. It is possible that some portion of these stresses are compensated by hydrostatic tensile stresses in martensite.

The depth profile of residual stresses in the longitudinal direction was measured at the different samples, which are carburized and quenched with the same LPC parameters and given in Figure 6-10 as an example.

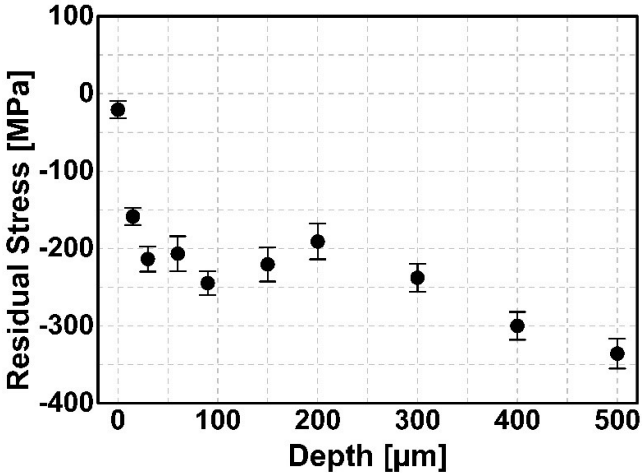

Figure 6-10: Residual stress depth profile of the sample treated with same conditions with sample C78. Measurements were done by using α' {211} martensite peak with $Sin^2\Psi$ method.

At the end of the quenching of sample C78, martensite exhibits around -20 MPa residual stress, which is measured from the surface to 20-60 µm depth, as explained in the beginning of this section. If this value is compared with the residual stresses at the same depth obtained by ex-situ measurement in Figure 6-10, it can be argued that the final beam position is closer to the surface than the 60 µm depth. Since both the measurement techniques and measured volumes are different, some deviation in the final stress values is also expected

Sample C58 and C86

The same procedure was applied to samples C58 and C86 having lower and higher carbon content at the surface, respectively. The final beam position at the end of the quenching was calculated as 40 µm for sample C58 and 60 µm for sample C86 by using the same procedure described in Figure 6-6, which will not be given to eliminate repetition. Figure 6-11 shows the evolution of lattice spacing of austenite along with theoretical stress-free d-spacing and evolution of phases during quenching for both samples.

It can be noticed for sample C58 that the M_s temperature of the surface is higher than that of sample C78; however, for sample C86 it is lower. The reason for this observation is the difference in carbon content at the surface as confirmed by the carbon depth profile comparison of the samples in Figure 6-4.

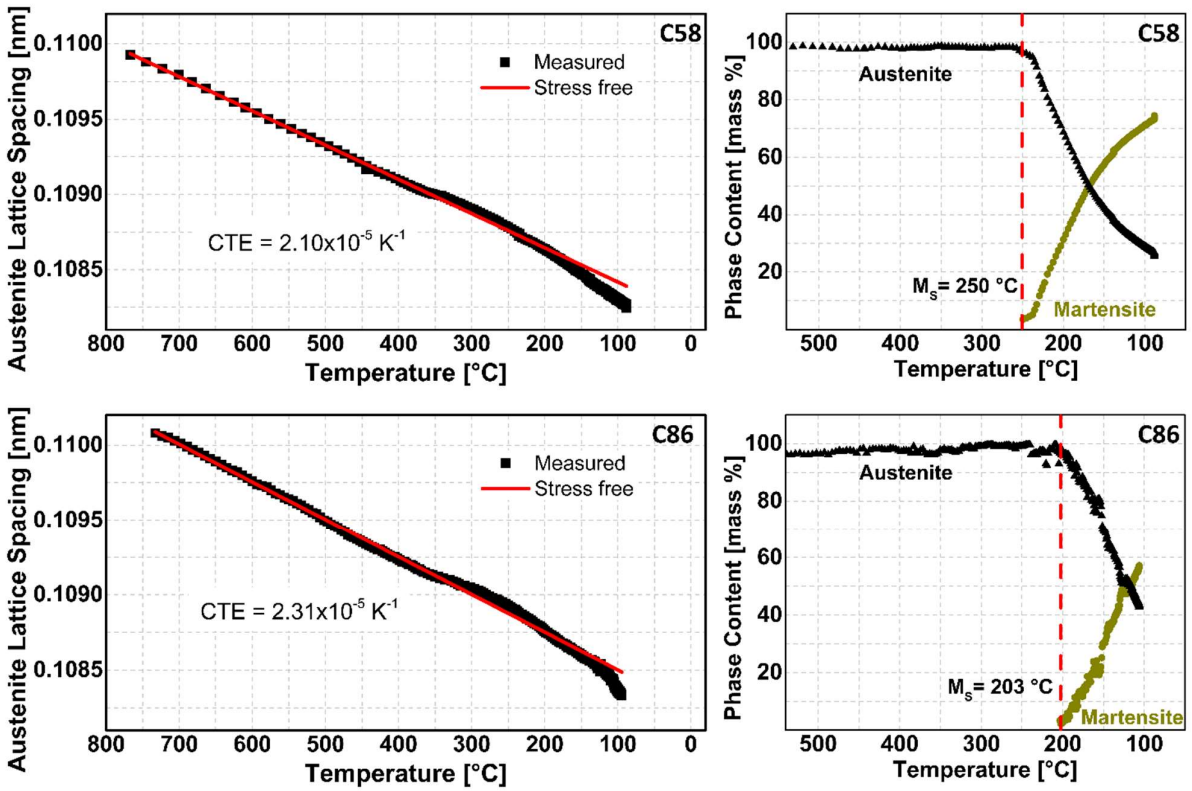

Figure 6-11: Evolution of measured austenite d-spacing during quenching and linear fitting extrapolation showing theoretical stress-free lattice spacing (left) and evolution of phases (right) during quenching for sample C58 and C86.

The evolution of deviatoric stress in austenite and martensite along with macro stress can be seen in Figure 6-12 for both samples. Both of these samples have same distinct stress points observed in sample C78 only at slightly different temperatures because of different carbon content distribution. The reasons behinds these behaviors were already explained in detailed on sample C78. Therefore, they will be shortly summarized here.

The base material transformation point at around 450 °C, leading to stress generation in tensile direction is also present for both samples. Similar to C78, these tensile stresses increases until martensite start temperature of the surface, and then turns towards the compression direction after martensite transformation begins. In the final state, both samples have compression stresses in both austenite and martensite. Additionally, transformation of intermediate points between core and the surface can be identified from a strong increase of the stress in tensile direction as indicated with blue arrows.

Conversely to the behavior of sample C78 and C86, generation of thermal stresses in the early stages of the quenching is not observed for sample C58. Moreover, the compression stresses observed in austenite from around 145 °C to the end of quenching are either stable or have a slight tendency to relax. The main reason for this stable behavior of the stresses is the reduction of quenching rate at the end of the process due to equipment limitations. This slowed down the transformation; thus, thermal stresses between the phases compensated the transformation stresses keeping them in balance. It can also be noticed that, the peak point of the tensile stresses

right before martensitic transformation of the surface is 150 MPa for C86 and 125 MPa for C58. The reason for this difference can be attributed to delayed transformation of the surface for sample C86 due to lower M_s temperature. However, due to this delay, the same quenching rate generated higher compression macro stresses at the surface of sample C58 as the tensile stresses needed to be compensated were less than that of C86.

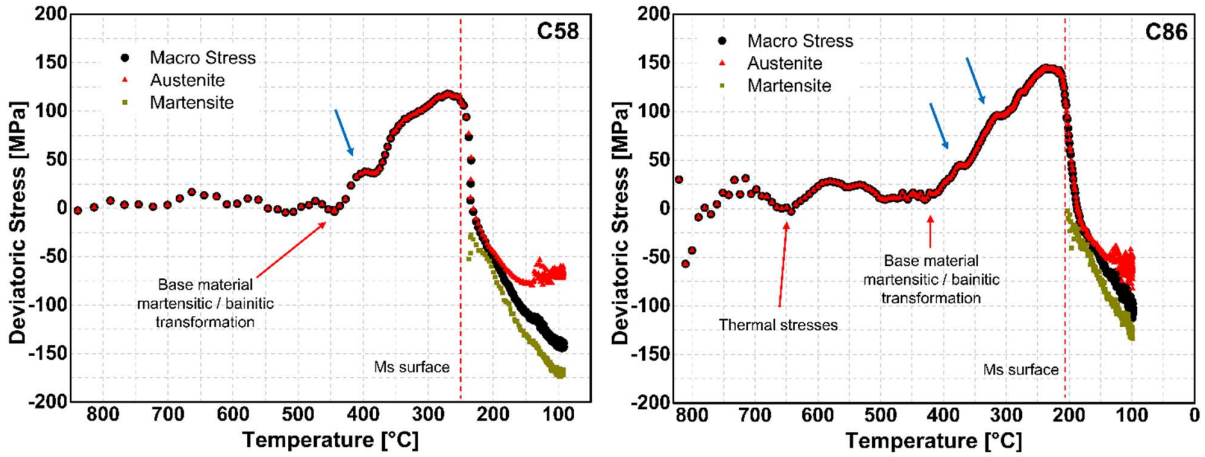

Figure 6-12: Evolution of deviatoric stresses in longitudinal direction for both austenite and martensite along with macro deviatoric stress during quenching for sample C58

Evolution of total stress in longitudinal direction in austenite and martensite along with macro stress is given in Figure 6-13 for sample C58 and C86. Same distinct stress generation points are also observed in total stresses.

Contrary to deviatoric stress evolution of the C58 sample, thermal stresses in the range of 50 MPa can be noticed from the figure. Since these stresses are not observed in deviatoric stress evolution, they are most likely hydrostatic. The reason for this might be flatter carbon gradient of sample C58 compared to the other sample, creating similar shrinkage rates during the cooling at the near surface area which causes only low magnitude hydrostatic stresses.

Another finding that stands out is the compression stresses around -580 MPa. Residual stresses in this range is not common to observe; therefore, difficult to explain. The reason for this might be lower surface carbon content of sample C58 and its flat carbon gradient. It is know from the data that core transformation precedes the surface transformation due to M_s temperature gradient caused by carbon gradient. However, It can be seen in the carbon profile of C58 from Figure 6-4 that, carbon contents at first 200 µm are very close, which might imply the disappearance of the M_s gradient from surface to 200 µm depth. Therefore, if transformation proceeds from the surface to the core until 200 µm depth, and then reverts to the surface, creating a retained austenite stuck in the probed area (probed area is 40 µm from the surface for C58 sample), then residual stresses in this range can be observed. If there is no M_s gradient, then it is expected for the surface to cool faster, and transform faster. This makes remaining austenite between two martensite layers more prone to the larger compression stresses caused by volume increase in both direction.

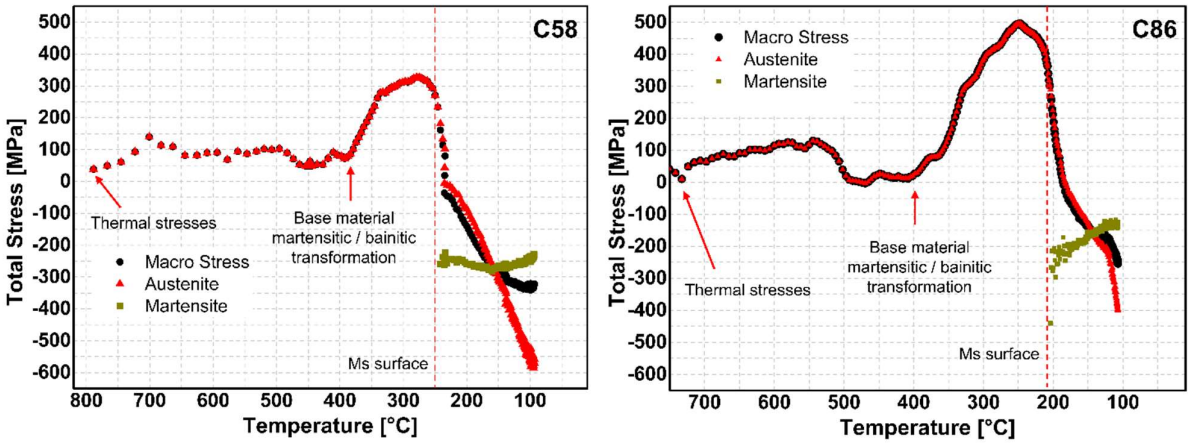

Figure 6-13: Evolution of total stresses in longitudinal direction for both austenite and martensite along with total macro stress during quenching for C58 and C86.

6.4.1 General Discussion Regarding Stress Generation During Quenching

The quenching of carburized steel samples in this thesis can be divided into three main parts. Part 1 is from the beginning of the quenching until around 420 °C, which can be called the “thermal stress part”; part 2 is from 420 °C to the martensite start temperature of the surface, which can be called “base material transformation part”; part 3 and the final part is from the M_s temperature of the surface to the end of quenching which can be called as “surface transformation part”.

Thermal stress part

Thermal stresses are generated in the early stages of the quenching. It can be said for the first part that they are generated at the surface in the tensile direction in the early stages of the quenching step. The main reason for this is that the surface and the core experience different cooling rates. The surface cools more rapidly than the core and tends to shrink stronger than the core. Consequently, the shrinkage of the surface is impeded by the core that has less volumetric change, resulting in compression stresses in the core and tensile stresses at the surface. The generation of thermal stresses does not have a certain temperature but rather have a temperature range. It starts earliest around 750 °C and lowest around 650 °C.

Moreover, fluctuations or "ups and downs" in the thermal stresses can also be noticed. One potential explanation for this behavior could be variations in the beam position during quenching, particularly in the early stages, due to sample shrinkage. These variations can result in measurements being taken across a carbon gradient, leading to varying stress behaviors. Additionally, the effect of formation of bainite at the core might be a reason. This formation could not be observed with X-ray since in-situ measurement during quenching were only conducted at the surface. For ex-situ measurements, it is difficult to distinguish bainite from martensite or ferrite from x-ray diffractograms and same problem also present for metallographic investigations especially for low amounts.

Furthermore, another possible reason is the plastic deformation of the surface during quenching. The yield stress of the material is at very low levels at high temperatures. If the generated thermal stresses during quenching exceed the yield strength, the material may undergo plastic deformation.

Thus, leading to this fluctuation phenomenon. Demonstration of this using a theoretical values of the yield strength and thermal stresses were given in appendix Section 10.11.

Base material transformation part

It can be said for the second part that for all samples, the bainitic/martensitic transformation of the core preceded the surface transformation. The main reason for this is the higher carbon content of the surface that shifts the martensite start temperature to the lower values. Given the relatively small, 5 mm thickness of the examined samples, the temperature gradient from the surface to the core is not expected to be steep. Consequently, the region with lower carbon content (mostly the core) transforms earlier due to its higher martensite start temperature. This early transformation of the core creates an expansion, and since the surface is still in the austenitic phase, it is soft enough to be easily strained. This leads to a strong increase of the tensile stresses at the surface until the martensitic transformation of the surface. Similar to thermal stress generation, the base material transformation temperate is not the same for all samples, it has a range between 450 °C to 380 °C. This temperature range is close to the martensite start temperature of the core which has 0.2 ma. % and 410 °C M_s temperature.

Even though the temperature gradient was not expected to be strong from the surface to the core, it still exists, like all quenching processes in any quenching media. Due to this temperature gradient, for particular samples, areas close to the surface that have more than 0.2 ma. % reach the transformation temperature faster than areas with base carbon content. This leads to a delayed increase of the stresses in tensile direction. Thus, every change happening below the non-measured area has a reaction at the surface, the measured area, which could be observed as an increase of stresses in the tensile direction.

Surface transformation part

As a third and final step, the near surface and surface region transform to martensite, which also generates lattice expansion; however, this expansion is restricted by an already hardened, rigid core. Thus, tensile stresses at the surface are reduced and inverted into the compression stresses. The amount of stress in each time interval of the quenching depends on the carbon content depth profile and cooling rate. In this present study, consistent cooling rates were maintained for all samples i.e. the key factor was carbon content distribution. Although there are not much samples to draw certain conclusions, some comments can still be made based on the available results. It was observed that sample C58, having lower carbon content at the surface has higher compressive residual stress in retained austenite at the end of the quenching. These results were already reported estimated in the literature [19]. The main reason for this is most probably the amount of austenite. When the carbon content of the material is lower, M_s temperature increases, and the amount of retained austenite reduces. Therefore, lower amount of retained austenite experiences more compression by the surrounding martensite.

Additionally, for all samples, higher total compression stresses are generated in the first formed martensite, and then these stresses are reduced during further martensitic transformation. The

reason for this might be that martensite is a minority phase at the beginning and its expansion could be restricted by surrounding bulk austenite. Another possible reason might be that in the early state of transformation temperature is still high enough so stresses continues to relax during further cooling. Not as apparent as the relation of carbon content and residual stress in austenite, sample C58, having the lowest carbon content at the surface also has higher compression stresses in martensite at the end of the quenching.

The literature also reports a similar relation between carbon content and residual stress. Katemi et. Al. reported lower residual stresses for samples having higher carbon content for both austenite and martensite [203]. Zimmerman et al. also investigated the effect of carbon content on final residual stresses for both atmosphere and low pressure carburized samples for three different surface carbon content of 0.7 ma. %, 0.9 ma. % and 1.1 ma. %. They found that samples with lower carbon content for both treatments have higher compression surface residual stresses in martensite [204]. Nelson et. al. reported results that were quite similar to the data given in this present study [205]. They investigated the residual stress state of the steels having carbon contents of 0.2 ma. %, 0.35 ma. %, 0.45 ma. %, 0.80 ma. % and 1.0 ma. % after quenching. They found out that lowest residual stresses were present for the steel having 1.0 ma % carbon content while highest residual stresses were observed for steels having 0.35 ma. %, 0.45 ma. % and 0.80 ma % with very close values. However, despite having the lowest carbon content of 0.2 ma. %, residual stress values for this steel were in the middle.

However, it is important to mention that this study covers a few numbers of steel samples, having low alloy content and very basic geometry. In transferring these results to components of a more complex nature, careful considerations of the existing type of alloy contents as well as the geometric and process-specific parameters are always necessary.

7 Conclusion

In-situ synchrotron experiments were performed at the high energy synchrotron beamline P07-EH3 of the PETRA III ring at DESY/Hamburg. Complete low pressure carburizing treatments were conducted in a specially designed experimental heat treatment chamber with 20MnCr5 steel samples. The recorded data were analyzed using the convolution-based Rietveld refinement to obtain information about the microstructural evolution. The level of knowledge about microstructural changes and the generation of stresses during all steps of the treatment could be considerably improved.

Initially, experiments conducted in experimental heat treatment chambers were compared with those conducted in industrial furnaces to prove that the newly developed system is suitable for performing low pressure carburizing treatments comparable to those in industrial furnaces. This comparison involved S-OES and EMPA analyses for comparison of carbon content distribution over the depth, micro-hardness analyses to compare the hardness depth profiles and EBSD analyses to compare the phase contents.

Then, two samples were carburized using the same parameters in the experimental chamber to validate the consistency of the chamber and the repeatability of the processes within the chamber. Microstructural changes and stress generation during the low pressure carburizing steps were demonstrated.

In the third part, microstructural changes during carburizing experiments conducted with different process parameters were investigated and discussed. These parameters included process temperature, acetylene amount and the number of boost diffusion cycles.

In the fourth and final part, the results of the change of stress state during different steps of carburizing experiments were demonstrated.

Conclusions based on all findings are given and represented in this section for every step of the low pressure carburizing.

Boost Steps

The austenite saturation limit was reached within a few seconds of the boost steps due to the very fast carbon uptake rate from the atmosphere into the sample. This fast increase was observed regardless of the process parameters. Carbon atoms accumulated at the surface, and carbides rapidly precipitated. Therefore, carbon diffusion from the atmosphere to the surface was decelerated. After that point, the carburizing reaction shifted from an atmosphere-dominated to a material-dominated, so further carbon transfer from the atmosphere to the surface of the sample became controlled by both cementite dissolution and possibly the diffusion of carbon through cementite at depth. Therefore, increasing the duration of the boost step to very long times does not directly increase the carbon profile; instead, this would only increase the amount of carbides formed

at the surface and possibly grain boundaries, which will contribute to the carbon profile by dissolution in the following steps.

Supportive experiments conducted in reflection mode to the main transmission mode experiments revealed that carbon content in solid solution in austenite reached the saturation limit after 20 seconds of boost steps and then decreased due to diffusion of carbon, although acetylene was still present in the atmosphere. This is attributed as a strong evidence for the deceleration of carbon uptake due to the carbide layer, mainly cementite, formed at the surface of the material.

This carbide layer formation could be confirmed experimentally by both cementite peaks in X-ray diffraction during boost steps, and metallographic and SEM analyses of the samples that were quenched directly after the boost step. For some samples, carbide peaks were not observed during boost steps. The reason for this, however, was not attributed to the absence of carbides but rather to the slightly shifted measurement point away from the surface due to temperature changes. Although these shifts are systematically corrected by surface scans, data loss due to time required for correction could not be completely eliminated.

Overall, it was determined that splitting the total boost duration to shorter but more steps is more efficient since carbides decelerate the carbon uptake from atmosphere to sample after a certain point.

Diffusion and Hardening Preparation Steps

Carbides formed at the surface of the material during the early seconds of the boost steps started to dissolve in the following diffusion steps. The formation and dissolution kinetics of the carbides highly depend on the amount of carbides and on the base carbon content in the austenitic matrix. When the number of boost steps increases, the stability of the formed cementite also increases due to increasing overall carbon content.

Quenching Steps

During quenching, early-formed martensite, especially the martensite that was formed in the first 5 seconds, exhibited a lower c/a ratio compared to the martensite formed later. This is attributed to the early phase transformation of austenite grains having lower carbon content. On the other hand, instantaneous self-tempering, second order stresses between austenite and martensite, and carbon redistribution/ordering leading to lower tetragonality are also expected.

Effect of Temperature and Acetylene Amount

To investigate the effect of temperature, two experiments with the same process parameters were conducted at 960 °C and 920 °C.

It was observed that higher temperatures resulted in increased carbon absorption during the boost step. The influence of higher temperature was more pronounced in the early stages of the process, with its effect decreasing in subsequent steps. This proves that the major driver of carbon diffusion is the carbon gradient, which tends to flatten during the process.

Regarding the investigation of the effect of acetylene amount, two experiments were conducted with different acetylene flow rates and different durations of boost steps. Duration of boost steps was doubled and acetylene flow rate increased eightfold. In the first minute of the boost steps, a noticeable difference in the carbon contents dissolved in austenite was observed, indicating that increasing the acetylene flow rate positively affected carbon absorption from the atmosphere to the sample in the early seconds of boost steps. However, at the end of boost steps for two samples, the final carbon contents at the surface were very close, despite very different flow rates and durations. This is an indication that, after formation of carbides at the surface, further carbon increase is mostly blocked until formed carbides are dissolved. Increasing the flow rate helps to reach that point faster by enhancing the carbon absorption from the surface to the sample. Nevertheless, by the end of the process, the carbon content gradient was comparable despite one sample exposing to a significantly greater amount of acetylene in the system.

Comparison of the Simulation with Measured Data

In order to determine precise parameters and equations for modelling, in-situ data were compared with simulation. For standard process sequences, calculated data correlated very well with simulation. However, a comparison of process sequences having different boost steps showed that shorter boost steps of less than a minute caused underestimation of the carbon content by simulation. The reason for this is suggested that carbon intake from the atmosphere to the sample is very fast in the early seconds of the boost steps; however, it then slows down strongly due to austenite saturation and carbide formation. Moreover, if the boost step duration was increased, an overestimation of the carbon content was observed. This phenomenon is attributed to the formation of carbides at the surface that decelerate the carbon intake. The simulation program takes carbide formation into account but does not fully consider the negative effect of carbides on acetylene decomposition, which leads to the slight over calculation of the carbon gradient.

Overall, the simulation program gave results very close to calculated data for the standard process sequence. This shows that by using this new system, new data required for high alloyed steels and out-of-standard process sequences can be gathered and used as input. The main difference between calculated and simulated data was a slight deviation in the near surface area due to the diffusion deceleration effect of carbide formation. This could be successfully determined by in-situ data and can be adapted in the future by changing the related parameters.

Evolution of Residual Stresses

The evolution of both deviatoric and total stresses during every step of the LPC treatment was systematically analyzed by a specific methodology. Residual stresses during the quenching step were the primary focus. Precise determination of the beam position was not possible due to temperature-related sample shrinkage; however, with the aid of complementary experiments and a comparison of lattice parameters before and after quenching, final measurement position was estimated to be around 20-60 µm from the surface.

Thermal stresses were generated at the surface in the tensile direction during the initial stages of the quenching step. The main reason for this is that the surface and the core experiences different cooling rates. Subsequently, a martensitic/bainitic transformation of the core was observed, which created an expansion at the core. This expansion caused further tensile stress on the austenitic surface. As the transformation progresses, the near-surface and surface regions undergo martensitic transformation, inducing lattice expansion. However, this expansion is constrained by the already hardened, rigid core, resulting in the gradual mitigation and reversal of tensile stresses to compression stresses at the surface.

In summary, the surface response to phase transformations along the carbon gradient was effectively observed, characterizing the behavior of stress evolution during the LPC treatment.

8 Outlook

Implementation of novel techniques and in-situ experimental methods to the synchrotron facilities has been increasing in recent years. As a noteworthy contribution to this trend, in-situ synchrotron LPC experiments with a newly developed system were successfully conducted. The current state of knowledge about the process and measurement technique has been significantly improved. Based on the present results, several potential advancements in the existing system can be made. A crucial improvement should be the implement of surface positioning setup within the system. In the current thesis, the shift of the beam from a pre-defined place due to temperature-related sample expansion and shrinkage was one of the main challenges. Therefore, a positioning system that precisely determines the surface position during the entire process and gives feedback for the relative sample movement can be designed. The implementation of the laser system used in this study to determine the rate of thermal expansion is currently in progress and successful trials have already been made.

Another improvement could be investigations of high alloyed steels. A comparison with the simulation and industrially carburized samples showed that very accurate carbon content distribution could be determined at different steps of the process. This knowledge can be extended to high alloy steels, and then gained knowledge can be used for further improvements. Thus, the demonstrated capability of the new system suggests potential applicability to high-alloy steels.

One of the advancements could also include the extending the capacity of the system to utilize diverse thermochemical treatments, such as nitriding or nitrocarburizing. Additionally, the integration of the current system into more complex geometries, such as samples with blind holes, or industrial components, such as gears, could also be a logical progression for the next step.

9 References

[1] D. Herring, A comprehensive guide to heat treatment, Industrial Heating, BNP Media, Troy, 2018.

[2] B. Edenhofer, D. Joritz, M. Rink, M. Rink, Carburizing of steels, in: Thermochem. Surf. Eng. Steels Improv. Mater. Perform., Woodhead Publishing., 2015: pp. 485–553. https://doi.org/10.1533/9780857096524.3.485.

[3] B. Clausen, E. Hoffmann, H.W. Zoch, Beeinflussung der Randschicht Durch die Einsatzhärtung, HTM - J. Heat Treat. Mater. 63 (2008) 326–336. https://doi.org/10.3139/105.100473.

[4] Daniel H. Herring, Robert V. Peters Jr., New-Formula Acetylene Cool for Heat Treatment, Gear Technol. (2013).

[5] H. Altena, F. Schrank, Niederdruck-aufkohlung mit Hochdruck-Gasabschreckung: Grundlagen, Einsatzmöglichkeiten und anlagentechnik, HTM – Härterei Tech. Mitteilungen. 57 (2002) 247–256.

[6] H. Altena, Niederdruck- und Plasmaaufkohlung. Aufkohlungsprozesse in Vakuumanlagen, HTM – Härterei Tech. Mitteilungen. 49 (1994) 58–63. https://doi.org/doi.org/10.1515/htm-1994-490116.

[7] K. Yada, O. Watanabe, Reactive flow simulation of vacuum carburizing by acetylene gas, Comput. Fluids. 79 (2013) 65–76. https://doi.org/10.1016/j.compfluid.2013.03.005.

[8] R. Gorockiewicz, The kinetics of low-pressure carburizing of alloy steels, Vacuum. 86 (2011) 448–451. https://doi.org/10.1016/j.vacuum.2011.09.006.

[9] M.Y. Semenov, A.E. Smirnov, M.Y. Ryzhova, Computation of carbon concentration curves in vacuum carburizing of steels, Met. Sci. Heat Treat. 55 (2013) 38–42. https://doi.org/10.1007/s11041-013-9576-x.

[10] M. Steinbacher, B. Clausen, F. Hoffmann, P. Mayr, H.W. Zoch, Thermogravimetrische messungen zur charakterisierung der reaktionskinetik beim niederdruckaufkohlen, HTM - Haerterei-Technische Mitteilungen. 61 (2006) 186–194. https://doi.org/10.3139/105.100385.

[11] H. Ikehata, K. Tanaka, H. Takamiya, H. Mizuno, Effect of chemical compositions of case hardening steels for distribution of carbon and cementite during vacuum carburizing, ISIJ Int. 52 (2012) 1348–1355. https://doi.org/10.2355/isijinternational.52.1348.

[12] V.A. Esin, B. Denand, Q. Le Bihan, M. Dehmas, J. Teixeira, G. Geandier, S. Denis, T. Sourmail, E. Aeby-Gautier, In situ synchrotron X-ray diffraction and dilatometric study of austenite formation in a multi-component steel: Influence of initial microstructure and heating rate, Acta Mater. 80 (2014) 118–131. https://doi.org/10.1016/j.actamat.2014.07.042.

[13] M. Villa, K. Pantleon, M.A.J. Somers, In situ investigation of the martensitic transformation in Fe-12 wt.%Ni-0.6 wt.%C steel at subzero temperatures, J. Alloys Compd. 557 (2013) 543–548. https://doi.org/10.1016/j.jallcom.2011.12.162.

[14] J. Epp, T. Hirsch, C. Curfs, In situ X-ray diffraction analysis of carbon partitioning during quenching of low carbon steel, Metall. Mater. Trans. A Phys. Metall. Mater. Sci. 43 (2012) 2210–2217. https://doi.org/10.1007/s11661-012-1087-7.

[15] F. Niessen, M. Villa, F. Danoix, J. Hald, M.A.J. Somers, In-situ analysis of redistribution of carbon and nitrogen during tempering of low interstitial martensitic stainless steel, Scr. Mater. 154 (2018) 216–219. https://doi.org/10.1016/j.scriptamat.2018.06.004.

[16] J. Feugeas, B. Gómez, A. Craievich, Ion nitriding of stainless steels. Real time surface characterization by synchrotron X-ray diffraction, Surf. Coatings Technol. 154 (2002) 167–175. https://doi.org/10.1016/S0257-8972(02)00017-8.

[17] J. William D. Callister, Materials Science and Engineering 7th Ed. : An Introduction, 7th ed., John Wiley & Sons, Inc., New York, 2007.

[18] H. Berns, W. Theisen, Eisenwerkstoffe - Stahl und Gusseisen, 4th ed., Springer-Verlag Berlin Heidelberg, 2008. https://doi.org/10.1007/978-3-540-79957-3.

[19] J. Epp, Time Resolved Investigations Of Phase Transformations and Stress During Heat Treatments of Steel Samples by Meams of Diffraction Experiments, Bremen University, 2016. https://doi.org/10.2370/9783844045475.

[20] G. Krauss, Physical metallurgy of steels: An overview, in: Automot. Steels Des. Metall. Process. Appl., 2017. https://doi.org/10.1016/B978-0-08-100638-2.00004-3.
[21] H.K.D.H. Bhadeshia, R.W.K. Honeycombe, Steels: Microstructure and Properties: Fourth Edition, Elsevier Inc, Amsterdam, 2017.
[22] H.K.D.H. Bhadeshia, Cementite, Int. Mater. Rev. 65 (2020). https://doi.org/10.1080/09506608.2018.1560984.
[23] W. Bleck, Materials Science of Steel - Textbook for RWTH Aachen University Students, 4th ed., IEHK 2016, 2016.
[24] M. Hunkel, H. Surm, T. Lübben, O. Kessler, F. Hoffmann, P. Mayr, Modeling the formation of austenite from ferrite-carbide aggregates, in: Mater. Sci. Technol. 2003 Meet., 2003.
[25] G. Krauss, Steels: heat treatment and processing principles, ASM International, Cleveland, 1990.
[26] M.J. Speich, G. R. ; Szirmae, A. ; Richards, Formation of Austenite from Ferrite and Ferrite-Carbide Aggregates, Met Soc AIME-Trans. 245 (1969) 1063–1074.
[27] E.V.D. Pereloma Elena, Phase transformations in steels 2 Diffusionless Transformations, High Strength Steels, Modelling and Advanced Analytical Techniques, Woodhead Publishing Limited, Cambridge, 2012.
[28] M. Militzer, Phase field modelling of phase transformations in steels, in: Phase Transform. Steels, Woodhead Publishing Limited, Cambridge, 2012: pp. 405–432. https://doi.org/10.1016/B978-1-84569-971-0.50013-2.
[29] M. Militzer, H. Azizi-Alizamini, Phase field modelling of austenite formation in low carbon steels, in: Solid State Phenom., 2011: pp. 1050–1059. https://doi.org/10.4028/www.scientific.net/SSP.172-174.1050.
[30] W. Bleck, Wolfgang Bleck (ed.) Materials Characterisation, Textbook for RWTH Students, 2013.
[31] H.K.D.H. Bhadeshia, Bainite in steels, transformations, microstructure and properties, 2nd ed., IOM Communications Ltd, London, 2001.
[32] J.M. Moyer, G.S. Ansell, The volume expansion accompanying the martensite transformation in iron-carbon alloys, Metall. Trans. A. 6 (1975) Article Nr. 1785. https://doi.org/10.1007/BF02642308.
[33] E.C. Bain, N.Y. Dunkirk, The nature of martensite, Trans. AIME. 1 (1924) 25–47.
[34] M. Onink, C.M. Brakman, F.D. Tichelaar, E.J. Mittemeijer, S. van der Zwaag, J.H. Root, N.B. Konyer, The lattice parameters of austenite and ferrite in FeC alloys as functions of carbon concentration and temperature, Scr. Metall. Mater. 29 (1993) 1011–1016. https://doi.org/10.1016/0956-716X(93)90169-S.
[35] W.F. Hosford, Iron and steel, Cambridge University Press, New York, 2012. https://doi.org/10.1017/CBO9781139086233.
[36] G.N. Haidemenopoulos, N. Aravas, I. Bellas, Kinetics of strain-induced transformation of dispersed austenite in low-alloy TRIP steels, Mater. Sci. Eng. A. 615 (2014). https://doi.org/10.1016/j.msea.2014.07.099.
[37] D.H. Herring, A discussion of retained austenite, Ind. Heat. (2005).
[38] R.H. Richman, R.W. Landgraf, Some effects of retained austenite on the fatigue resistance of carburized steel, Metall. Trans. A. 6 (1975) Article Nr. 955. https://doi.org/10.1007/BF02661347.
[39] ASM Handbook, Volume 19: Fatigue and Fracture, ASM International, Materials Park, OH, 1996. https://doi.org/doi.org/10.31399/asm.hb.v19.9781627081931.
[40] D.E. Laughlin, K. Hono, Physical Metallurgy: Fifth Edition, Elsevier B.V., 2014. https://doi.org/10.1016/C2010-0-65716-6.
[41] G. Gottstein, Physical Foundations of Materials Science, 1st ed., Springer-Verlag Berlin Heidelberg GmbH, New York, 2004. https://doi.org/10.1007/978-3-662-09291-0.
[42] R.E. Smallman, A.H.W. Ngan, Modern Physical Metallurgy: Eighth Edition, Butterworth-Heinemann, 2013. https://doi.org/10.1016/C2011-0-05565-5.
[43] W. Dahl, Eigenschaften und Anwendungen von Stählen Band 1: Grundlagen; Inst. Eisenhüttenkunde der RWTH Aachen, Verlagsgruppe Mainz, 1998.
[44] J. Ågren, A revised expression for the diffusivity of carbon in binary FeC austenite, Scr. Metall. 20 (1986) 1507–1510. https://doi.org/10.1016/0036-9748(86)90384-4.
[45] C. Wells, W. Batz, R.F. Mehl, Diffusion coefficient of carbon in austenite, JOM. 188 (1950)

533–560. https://doi.org/10.1007/bf03399032.
[46] R.H. Siller, R.B. McLellan, The application of first order mixing statistics to the variation of the diffusivity of carbon in austenite, Metall. Trans. 1 (1970) 985–988. https://doi.org/10.1007/BF02811782.
[47] H.K.D.H. Bhadeshia, Diffusion of carbon in austenite, Met. Sci. (1981) 477–479. https://doi.org/10.1179/030634581790426525.
[48] M. Steinbacher, Thermogravimetrische Messungen beim Niederdruckaufkohlen als Grundlage für Simulationen, Universität Bremen, 2012.
[49] R.P. Smith, The diffusivity of carbon in iron by the steadystate method, Acta Metall. 1 (1953) 578–587. https://doi.org/10.1016/0001-6160(53)90088-1.
[50] G. Leyens, G. Woelk, J. Wuenning, Berechnung der Aufkohlung nach dem Sättigungs-Ausgleichs-Verfahren, Arch Eisenhuettenwes. 47 (1976) 385–390. https://doi.org/10.1002/srin.197603742.
[51] AWT-Fachausschuß 5 Arbeitskreis 4 (Hrsg.), Die Prozessregelung beim Gasaufkohlen und Einsatzhärten, Expert Verlag, 1997.
[52] H.-J. Eckstein, Wärmebehandlung von Stahl, VEB Dtsch. Verlag Für Grundstoffindustrie. 22 (1971) 748. https://doi.org/doi.org/10.1002/maco.19710220829.
[53] J. Kučera, K. Stránský, The dependence of carbon diffusion coefficients in austenitic ternary alloys on concentration of additive elements, Acta Tech. CSAV (Ceskoslovensk Akad. Ved). 48 (2003) 353–364.
[54] R.P. Smith, Trans. AIME, 230 (1964) 476.
[55] P. Grieverson, E.T. Turkdogan, Trans. AIME, 230 (1964) 407.
[56] A.E. Lord, D.N. Beshers, The mechanical damping of iron from room temperature to 400°c at 7 megacycles/sec, Acta Metall. 14 (1966) 1659–1672. https://doi.org/10.1016/0001-6160(66)90018-6.
[57] A. Schneider, G. Inden, Carbon diffusion in cementite (Fe3C) and Hägg carbide (Fe5C2), Calphad Comput. Coupling Phase Diagrams Thermochem. 31 (2007) 141–147. https://doi.org/10.1016/j.calphad.2006.07.008.
[58] B. Ozturk, V.L. Fearing, J.A. Ruth, G. Simkovich, The diffusion coefficient of carbon in cementite, Fe3C, at 450°C, Solid State Ionics. 12 (1984) 145–151. https://doi.org/10.1016/0167-2738(84)90141-3.
[59] M. Bepari, Carburizing: A Method of Case Hardening of Steel, in: Compr. Mater. Finish., Elsevier, Amsterdam, 2017: pp. 73–104.
[60] J. Franke, Entwicklung von Niederdruck-Carbonitrierprozessen zur Festigkeitssteigerung hochbelasteter Bauteile, Universität Bremen, 2018.
[61] J. Wünning, Weiterentwicklung der Gasaufkohlungstechnik, HTM. 23 (1968) 101–110.
[62] R. Chatterjee-Fischer, Internal oxidation during carburizing and heat treating, Metall. Trans. A. 9 (1978) 1553–1560. https://doi.org/10.1007/BF02661937.
[63] G. Parrish, Carburizing : microstructures and properties, ASM International, Ohio, 1999. https://doi.org/10.31399/asm.tb.cmp.9781627083379.
[64] D. Buchholz, R.U. Khan, S. Bajohr, R. Reimert, Computational fluid dynamics modeling of acetylene pyrolysis for vacuum carburizing of steel, in: Ind. Eng. Chem. Res., 2010. https://doi.org/10.1021/ie900996h.
[65] H. Altena, F. Schrank, Low Pressure Carburizing with High Pressure Gas Quenching, Gear Technol. March/Apri (2004).
[66] G. Hiller, Advantages of low pressure carburising and high pressure gas quenching technology in manufacturing, Int. Heat Treat. Surf. Eng. 8 (2014) 35–41. https://doi.org/10.1179/1749514813Z.00000000087.
[67] B. Gornicki, Klaus Loeser, Low Pressure Carburizing of Large Transmission Parts, Gear Technol. September (2009).
[68] D. Beauchesne, A. Goldsteinas, W. Tang, D. Zhao, Quenching after vacuum carburizing, Jinshu Rechuli/Heat Treat. Met. (2005).
[69] D. Beauchesne, A. Goldsteinas, A user's guide to quenching after vacuum carburizing, Heat Treat. Prog. (2004).
[70] H. Altena, F. Schrank, S. Heineck, B. Haase, F. Hoffmann, F. Graf, D. Liedtke, S. Bajohr, Prozessüberwachung und regelung von niederdruck-aufkohlungsprozessen, HTM - Haerterei-Technische Mitteilungen. 61 (2006) 195–206. https://doi.org/10.3139/105.100382.

[71] V.F. Da Silva, L.F. Canale, D. Spinelli, W.W. Bose-Filho, O.R. Crnkovic, Influence of retained austenite on short fatigue crack growth and wear resistance of case carburized steel, J. Mater. Eng. Perform. 8 (1999) pages 543–548. https://doi.org/10.1007/s11665-999-0007-5.
[72] D. Liedtke, Stand des Einsatzhärtens aus industrieller Sicht, HTM - Haerterei-Technische Mitteilungen. 64 (2009) 323–337. https://doi.org/10.3139/105.110041.
[73] B. Clausen, K. Klenke, R. Kohlmann, F. Hoffmann, Legierungskonzept 20CrMo5 — Härtbarkeit und Kornwachstumsverhalten des Einsatzstahles für Hochtemperaturaufkohlungsbehandlungen, HTM J. Heat Treat. Mater. 65 (2010) 299–304. https://doi.org/10.3139/105.110077.
[74] G. Prunel, B. Stauder, Advantages of low pressure carburizing in the heat treatment, Cailiao Rechuli Xuebao/Transactions Mater. Heat Treat. 25 (2004) 364–369.
[75] W. Gräfen, B. Edenhofer, Acetylene low-pressure carburising – a novel and superior carburising technology, Heat Treat. Met. 4 (1999) 79–83.
[76] F. Graf, S. Bajohr, R. Reimert, Pyrolysis of propane during vacuum carburizing of steel, HTM - Haerterei-Technische Mitteilungen. 58 (2003) 20–23.
[77] W. Gräfen, Untersuchungen zur Kohlenstoffübertragung bei der Niederdruckaufkohlung., Universität Bremen, 2002.
[78] R.U. Khan, S. Bajohr, D. Buchholz, R. Reimert, H.D. Minh, K. Norinaga, V.M. Janardhanan, S. Tischer, O. Deutschmann, Pyrolysis of propane under vacuum carburizing conditions: An experimental and modeling study, J. Anal. Appl. Pyrolysis. 81 (2008) 148–156. https://doi.org/10.1016/j.jaap.2007.09.012.
[79] D.H. Herring, A Case for Acetylene Based Low Pressure Carburizing of Gears, Therm. Process. (2012).
[80] B. Esper, Acetylene: The Right Carbon Source For Low-Pressure Carburizing, Ind. Heat. November (2009).
[81] B. Edenhofer, M. Lohrmann, W. Gräfen, Novel Thermochemical Diffusion Processes in Vacuum Furnaces for Steel Components, in: ASM Proc. Heat Treat., 2000.
[82] P. Rokicki, K. Dychton, Acetylene Flow Rate as a Crucial Parameter of Vacuum Carburizing Process of Modern Tool Steels, Arch. Metall. Mater. 61 (2016) 2009–2012. https://doi.org/10.1515/amm-2016-0324.
[83] E. Wołowiec-Korecka, M. Korecki, M. Sut, A. Brewka, P. Kula, Calculation of the mixture flow in a low-pressure carburizing process, Metals (Basel). 9 (2019) 439. https://doi.org/10.3390/met9040439.
[84] B. Gornicki, High Temperature Vacuum Carburizing Drives Alloy Development, Gear Solut. ALD-Holcro (2015).
[85] B. Huchtemann, V. Schuler, E. Wulfmeier, Hochtemperaturaufkohlung von Einsatzstahlen, HTM J. Heat Treat. Mater. 45 (1990) 57–65. https://doi.org/10.1515/htm-1990-450119.
[86] B. Clausen, C. Laumen, T. Holm, F. Hoffmann, P. Mayr, Einfluss des prozessgases auf kohlenstoff-aufnahme und rußbildung in niederdruck- und plasmaaufkohlungsprozessen, HTM - Haerterei-Technische Mitteilungen. 56 (2001) 23–29.
[87] B. Liscic, H.M. Tensi, L.C.F. Canale, G.E. Totten, Quenching Theory and Technology, Second Edition, 2nd ed., CRC Press, Boca Raton, 2010. https://doi.org/10.1201/9781420009163.
[88] B. Lhote, O. Delcourt, Gas Quenching with Helium in Vacuum Furnaces, Mater. Sci. Forum. 102–104 (1992) 867–884. https://doi.org/10.4028/www.scientific.net/msf.102-104.867.
[89] R. Hill, High-pressure gas cooling: The case for hydrogen, Heat Treat. Prog. (2006).
[90] S. Midea, T. Holm, S. Segerberg, J. Bodin, T. Thors, K. Swärtstrom, High pressure gas quenching--technical and economical considerations, in: Proc. 2nd Int. Conf. Quenching Control Distortion, 1996.
[91] P. Stratton, I. Shedletsky, L. Maurice, Gas Quenching with Helium, Solid State Phenom. 118 (2006) 221–226. https://doi.org/doi.org/10.4028/www.scientific.net/SSP.118.221.
[92] J.I. Goldstein, A.E. Moren, Diffusion modeling of the carburization process, Metall. Trans. A. 9 (1978) 1515–1525. https://doi.org/10.1007/BF02661934.
[93] G.S. Gupta, A. Chaudhuri, P. Vasanth Kumar, Modelling, simulation, and graphical user interface for industrial gas carburising process, Mater. Sci. Technol. 18 (2002) 1188–1194. https://doi.org/10.1179/026708302225007349.
[94] G. sheng SONG, X. hua LIU, G. dong WANG, X. qiu XU, Numerical Simulation on Carburizing

and Quenching of Gear Ring, J. Iron Steel Res. Int. 14 (2007) 47–52. https://doi.org/10.1016/S1006-706X(07)60089-2.
[95] P. Cavaliere, G. Zavarise, M. Perillo, Modeling of the carburizing and nitriding processes, Comput. Mater. Sci. 46 (2009) 26–35. https://doi.org/10.1016/j.commatsci.2009.01.024.
[96] S.R.E. Hosseini, Simulation of Case Depth of Cementation Steels According to Fick's Laws, J. Iron Steel Res. Int. 19 (2012) 71–78. https://doi.org/10.1016/S1006-706X(13)60023-0.
[97] H. Dubitzky, W., Wolkenhauer, O., Cho, KH., Yokota, Parabolic Differential Equations, Diffusion Equation, in: Encycl. Syst. Biol., 2013: pp. 1621–1624. https://doi.org/https://doi.org/10.1007/978-1-4419-9863-7_273.
[98] H. Jiménez, M.H. Staia, E.S. Puchi, Mathematical modeling of a carburizing process of a SAE 8620H steel, in: Surf. Coatings Technol., 1999: pp. 358–365. https://doi.org/10.1016/S0257-8972(99)00464-8.
[99] C. Sudha, N. Sivai Bharasi, R. Anand, H. Shaikh, R.K. Dayal, M. Vijayalakshmi, Carburization behavior of AISI 316LN austenitic stainless steel-Experimental studies and modeling, J. Nucl. Mater. 402 (2010) 186–195. https://doi.org/10.1016/j.jnucmat.2010.05.023.
[100] Metallurgical Society of AIME. Ferrous Metallurgy Committee, Decomposition of Austenite by Diffusional Processes, in: Ferr. Metall. Comm. Inst. Met. Div., 1960.
[101] T. Murakami, H. Fukuyama, K. Nagata, Mechanisms of carburization and melting of iron by CO gas, ISIJ Int. 41 (2001) 416–421. https://doi.org/10.2355/isijinternational.41.416.
[102] S.J. Lee, D.K. Matlock, C.J. Van Tyne, An empirical model for carbon diffusion in austenite incorporating alloying element effects, ISIJ Int. 51 (2011) 1903–1911. https://doi.org/10.2355/isijinternational.51.1903.
[103] M. Zajusz, K. Tkacz-Śmiech, M. Danielewski, Modeling of vacuum pulse carburizing of steel, Surf. Coatings Technol. 258 (2014) 646–651. https://doi.org/10.1016/j.surfcoat.2014.08.023.
[104] W.M. Gao, L.X. Kong, P.D. Hodgson, Integral approach and numerical improvement to calculate carbon concentration profiles in carburising, in: Adv. Mater. Res., 2011: pp. 1494–1499. https://doi.org/10.4028/www.scientific.net/AMR.264-265.1494.
[105] D.W. Kim, Y.G. Cho, H.H. Cho, S.H. Kim, W.B. Lee, M.G. Lee, H.N. Han, A numerical model for vacuum carburization of an automotive gear ring, Met. Mater. Int. 17 (2011) 885–890. https://doi.org/10.1007/s12540-011-6004-x.
[106] J.O. Andersson, J. Ågren, Models for numerical treatment of multicomponent diffusion in simple phases, J. Appl. Phys. 72 (1992) 1350. https://doi.org/10.1063/1.351745.
[107] A. Borgenstam, A. Engström, L. Höglund, J. Ågren, DICTRA, a tool for simulation of diffusional transformations in alloys, J. Phase Equilibria. 21 (2000) pages269–280. https://doi.org/10.1361/105497100770340057.
[108] J. Rudnizki, B. Zeislmair, U. Prahl, W. Bleck, Thermodynamical simulation of carbon profiles and precipitation evolution during high temperature case hardening, Steel Res. Int. 81 (2010) 472–476. https://doi.org/10.1002/srin.201000048.
[109] P. Thibaux, A. Métenier, C. Xhoffer, Carbon diffusion measurement in austenite in the temperature range 500 °C to 900 °C, Metall. Mater. Trans. A Phys. Metall. Mater. Sci. 38 (2007) 1169–1176. https://doi.org/10.1007/s11661-007-9150-5.
[110] O. Karabelchtchikova, R.D. Sisson, Carbon diffusion in steels: A numerical analysis based on direct integration of the flux, in: J. Phase Equilibria Diffus., 2006: pp. 598–604. https://doi.org/10.1361/154770306X153611.
[111] Y. Wei, L. Zhang, R.D. Sisson, Modeling of carbon concentration profile development during both atmosphere and low pressure carburizing processes, J. Mater. Eng. Perform. 22 (2013) 1886–1891. https://doi.org/10.1007/s11665-012-0353-6.
[112] J.G. Charney, R. FjÖrtoft, J. Von Neumann, Numerical Integration of the Barotropic Vorticity Equation, Tellus. 2 (1950) 237–254. https://doi.org/10.3402/tellusa.v2i4.8607.
[113] F. Neumann, B. Person, Beitrag zur Metallurgie der Gasaufkohlung. Zusammenhang zwischen dem C-Potential der Gasphase und des Werkstückes unter Berücksichtigung der Legierungselemente, HTM - Härterei-Technische Mitteilungen. 23 (1968) 296–308.
[114] J. Chipman, Thermodynamics and phase diagram of the Fe-C system, Metall. Trans. 3 (1972) 55–64. https://doi.org/10.1007/BF02680585.
[115] V.S. Ramachandran, J.J. Beaudoin, Handbook of Analytical Techniques in Concrete Science and Technology - Principles, Techniques, and Applications, Noyes Publications, New Jersey, 2001.

[116] J. Epp, X-Ray Diffraction (XRD) Techniques for Materials Characterization, in: Mater. Charact. Using Nondestruct. Eval. Methods, 2016: pp. 81–124. https://doi.org/10.1016/B978-0-08-100040-3.00004-3.
[117] L. Spieß, G. Teichert, R. Schwarzer, H. Behnken, C. Genzel, Moderne Röntgenbeugung, 2nd Editio, Teubner Verlag, Wiesbaden, 2009. https://doi.org/https://doi.org/10.1007/978-3-8349-9434-9.
[118] J.A. Kaduk, S.J.L. Billinge, R.E. Dinnebier, N. Henderson, I. Madsen, R. Černý, M. Leoni, L. Lutterotti, S. Thakral, D. Chateigner, Powder diffraction, Nat. Rev. Methods Prim. 1 (2021) 77. https://doi.org/10.1038/s43586-021-00074-7.
[119] P.S. Prevey, X-Ray Diffraction Residual Stress Techniques, in: Asm Handb. Vol. 10 - Mater. Charact., ASM International, Almere, 1986: pp. 380–392. https://doi.org/doi.org/10.31399/asm.hb.v10.a0001761.
[120] B.B. He, Two-Dimensional X-Ray Diffraction, 2nd ed., John Wiley & Sons, Inc., Hoboken, 2018. https://doi.org/10.1002/9781119356080.
[121] DESY Photon Science, Machine Parameters PETRA III (Design Values), (2016). http://photon-science.desy.de/facilities/petra_iii (accessed February 7, 2023).
[122] G. Will, The Rietveld Method, in: Powder Diffr. Rietveld Method Two-Stage Method, 1st Ed, Springer, Berlim, 2006: pp. 41–72. https://doi.org/doi.org/10.1007/3-540-27986-5_2.
[123] H.M. Rietveld, Line profiles of neutron powder-diffraction peaks for structure refinement, Acta Crystallogr. 22 (1967) 151–152. https://doi.org/10.1107/s0365110x67000234.
[124] H.M. Rietveld, A profile refinement method for nuclear and magnetic structures, J. Appl. Crystallogr. 2 (1969) 65–71. https://doi.org/10.1107/s0021889869006558.
[125] R.W. Cheary, A.A. Coelho, J.P. Cline, Fundamental parameters line profile fitting in laboratory diffractometers, in: J. Res. Natl. Inst. Stand. Technol., 2004: pp. 1–25. https://doi.org/10.6028/jres.109.002.
[126] L. Spieß, G. Teichert, R. Schwarzer, H. Behnken, C. Genzel, Beugung von Röntgenstrahlung, in: Mod. Röntgenbeugung - Röntgendiffraktometrie Für Mater. Phys. Und Chem., 3rd Ed, Springer Spektrum, Wiesbaden, 2019: pp. 41–94. https://doi.org/doi.org/10.1007/978-3-8348-8232-5.
[127] J. Epp, J. Dong, H. Meyer, A. Bohlen, Analysis of cyclic phase transformations during additive manufacturing of hardenable tool steel by in-situ X-ray diffraction experiments, Scr. Mater. 177 (2020) 27–31. https://doi.org/10.1016/j.scriptamat.2019.09.021.
[128] A. Kern, A.A. Coelho, R.W. Cheary, Convolution Based Profile Fitting, in: P. Mittemeijer, E., Scardi (Ed.), Diffr. Anal. Microstruct. Mater., vol. 68, Springer Series in Materials Science, 2004: pp. 17–50. https://doi.org/10.1007/978-3-662-06723-9_2.
[129] E. Macherauch, H. Wohlfahrt, U. Wolfstieg, Zur zweckmaßigen Definition von Eigenspannungen, HTM - Haerterei-Technische Mitteilungen. 28 (1973) 201–211. https://doi.org/doi.org/10.1515/htm-1973-280305.
[130] A. Schlueter, Phase Field Modeling of Dynamic Brittle Fracture, Technische Universität Kaiserslautern, 2019.
[131] M.E. Fitzpatrick, A.T. Fry, P. Holdway, F.A. Kandil, J. Shackleton, L. Suominen, Measurement Good Practice Guide No. 52: Determination of Residual Stresses by X-ray Diffraction - Issue 2, 2005.
[132] M. Sepsi, V. Mertinger, M. Benke, Sample cutting-free pole figure measuring method for centreless diffractometers in modified X mode, Mater. Charact. 151 (2019) 351–357. https://doi.org/10.1016/j.matchar.2019.03.031.
[133] I.C. Noyan, J.B. Cohen, Residual Stress - Measurement by Diffraction and Interpretation, 1st ed., Springer-Verlag, New York (US), 1987. https://doi.org/https://doi.org/10.1007/978-1-4613-9570-6.
[134] B. Eigenmann, E. Macherauch, Röntgenographische Untersuchung von Spannungszuständen in Werkstoffen, Materwiss. Werksttech. 27 (1995) 426–437. https://doi.org/https://doi.org/10.1002/mawe.19960270907.
[135] H. Behnken, Mikrospannungen in vielkristallinen und heterogenen Werkstoffen, Postdoctor, Shaker Verlag Aachen, 2003.
[136] A. Zeilinger, J. Todt, C. Krywka, M. Müller, W. Ecker, B. Sartory, M. Meindlhumer, M. Stefenelli, R. Daniel, C. Mitterer, J. Keckes, In-situ Observation of Cross-Sectional Microstructural Changes and Stress Distributions in Fracturing TiN Thin Film during

Nanoindentation, Sci. Rep. 6(1):22670 (2016) 1–14. https://doi.org/10.1038/srep22670.
[137] M. Stefenelli, J. Todt, A. Riedl, W. Ecker, T. Müller, R. Daniel, M. Burghammer, J. Keckes, X-ray analysis of residual stress gradients in TiN coatings by a Laplace space approach and cross-sectional nanodiffraction: A critical comparison, J. Appl. Crystallogr. 46 (2013) 1378–1385. https://doi.org/10.1107/S0021889813019535.
[138] F. Heidelbach, C. Riekel, H.R. Wenk, Quantitative texture analysis of small domains with synchrotron radiation X-rays, J. Appl. Crystallogr. 32 (1999) 841–849. https://doi.org/10.1107/S0021889899004999.
[139] M. Sedighi, R. Nazemnezhad, Effect of Peak Positioning Method on Accuracy of X-Ray Diffraction Residual Stress Measurement, Exp. Tech. 40 (2016) 295–302. https://doi.org/10.1007/s40799-016-0033-9.
[140] H.O. Di Roccoa, A. Cruzado, The voigt profile as a sum of a gaussian and a lorentzian functions, when the weight coefficient depends only on the widths ratio, Acta Phys. Pol. A. 122 (2012) 666–669. https://doi.org/10.12693/aphyspola.122.666.
[141] T. Ida, M. Ando, H. Toraya, Extended pseudo-Voigt function for approximating the Voigt profile, J. Appl. Crystallogr. 33 (2000) 1311–1316. https://doi.org/10.1107/S0021889800010219.
[142] T. Hirsch, Entwicklung von Eigenspannungszuständen im Fertigungsprozess, HTM - Härterei-Technische Mitteilungen. 58 (2003) 110–126.
[143] A. Rose, Eigenspannungen als Ergebnis von Wärmebehandlung und Umwandlungsverhalten, HTM - Härterei-Technische Mitteilungen. 21 (1966) 1–6.
[144] T. Ericsson, Residual Stress Caused by Thermal and Thermochemical Surface Treatments, 1987. https://doi.org/doi.org/10.1016/B978-0-08-034923-7.50012-7.
[145] O.D. Sherby, J. Wadsworth, D.R. Lesuer, C.K. Syn, Revisiting the structure of martensite in iron-carbon steels, Mater. Trans. 49 (2008) 2016–2027. https://doi.org/10.2320/matertrans.MRA2007338.
[146] T. Reti, Residual stresses in carburised, carbonitrided and case-hardened components (Part 1), Heat Treat. Met. 30 (2003) 83–96.
[147] E. Macherauch, O. Vöhringer, Residual Stresses After Quenching, in: Theory Technol. Quenching, 1992. https://doi.org/10.1007/978-3-662-01596-4_6.
[148] J. Epp, H. Surm, O. Kessler, T. Hirsch, In situ X-ray phase analysis and computer simulation of carbide dissolution of ball bearing steel at different austenitizing temperatures, Acta Mater. 55 (2007) 5959–5967. https://doi.org/10.1016/j.actamat.2007.07.022.
[149] J. Epp, H. Surm, O. Kessler, T. Hirsch, In-Situ X-Ray Investigations and Computer Simulation during Continuous Heating of a Ball Bearing Steel, Metall. Mater. Trans. A. 38 (2007) 2371–2378. https://doi.org/doi.org/10.1007/s11661-007-9314-3.
[150] T.G.R. Clarke, A. da Silva Rocha, A. Reguly, T. Hirsch, In situ XRD measurements during plasma nitriding of a medium carbon steel, Surf. Coatings Technol. 194 (2005) 283–289. https://doi.org/10.1016/j.surfcoat.2004.06.037.
[151] J. Dong, H. Prekel, M. Dethlefs, J. Epp, A. Fischer, In-situ-Untersuchung von Randschichten während des Gasnitrierens mittels Röntgendiffraktometrie und photothermischer Radiometrie, HTM J. Heat Treat. Mater. 72 (2017) 154–167. https://doi.org/doi.org/10.3139/105.110322.
[152] J. Epp, Investigation of triaxial stress state in retained austenite during quenching of a low alloy steel by in situ X-ray diffraction, Adv. Mater. Res. 996 (2014) 525–531. https://doi.org/10.4028/www.scientific.net/AMR.996.525.
[153] J. Epp, Effects of Hydrostatic 2nd Kind Residual Stresses and of Carbon Partitioning During Martensitic Quenching of Low Alloy Steel, Mater. Res. Proc. 2 (2017) 283–288. https://doi.org/10.21741/9781945291173-48.
[154] M. Villa, F.B. Grumsen, K. Pantleon, M.A.J. Somers, Martensitic transformation and stress partitioning in a high-carbon steel, Scr. Mater. 67 (2012) 621–624. https://doi.org/10.1016/j.scriptamat.2012.06.027.
[155] M. Villa, K. Pantleon, M.A.J. Somers, Evolution of compressive strains in retained austenite during sub-zero Celsius martensite formation and tempering, Acta Mater. 65 (2014) 383–392. https://doi.org/10.1016/j.actamat.2013.11.007.
[156] M. Villa, F. Niessen, M.A.J. Somers, In Situ Investigation of the Evolution of Lattice Strain and Stresses in Austenite and Martensite During Quenching and Tempering of Steel, Metall.

Mater. Trans. A Phys. Metall. Mater. Sci. 49 (2018) 28–40. https://doi.org/10.1007/s11661-017-4387-0.
[157] S.Y.P. Allain, S. Gaudez, G. Geandier, J.C. Hell, M. Gouné, F. Danoix, M. Soler, S. Aoued, A. Poulon-Quintin, Internal stresses and carbon enrichment in austenite of Quenching and Partitioning steels from high energy X-ray diffraction experiments, Mater. Sci. Eng. A. 710 (2018) 245–250. https://doi.org/10.1016/j.msea.2017.10.105.
[158] S.Y.P. Allain, G. Geandier, J.C. Hell, M. Soler, F. Danoix, M. Gouné, In-situ investigation of quenching and partitioning by High Energy X-Ray Diffraction experiments, Scr. Mater. 131 (2017) 15–18. https://doi.org/10.1016/j.scriptamat.2016.12.026.
[159] P. Huyghe, M. Caruso, J.L. Collet, S. Dépinoy, S. Godet, Into the quenching and; partitioning of a 0.2C steel: An in-situ synchrotron study, Mater. Sci. Eng. A. 743 (2019) 175–184. https://doi.org/10.1016/j.msea.2018.11.065.
[160] N. Hosseini, F. Forouzan, E. Vuorinen, In-situ microstructural evolution during quenching and partitioning of a high-carbon steel by high-temperature X-Ray Diffraction, Mater. Today Commun. 31. 31 (2022) 103503. https://doi.org/doi.org/10.1016/j.mtcomm.2022.103503.
[161] D. Manova, D. Hirsch, J.W. Gerlach, S. Mändl, H. Neumann, B. Rauschenbach, In situ investigation of phase formation during low energy ion nitriding of Ni80Cr20 alloy, Surf. Coatings Technol. 259 (2014) 434–441. https://doi.org/10.1016/j.surfcoat.2014.10.054.
[162] D. Manova, S. Mändl, H. Neumann, B. Rauschenbach, Analysis of in situ XRD measurements for low energy ion beam nitriding of austenitic stainless steel, Surf. Coatings Technol. 256 (2014) 64–72. https://doi.org/10.1016/j.surfcoat.2014.03.047.
[163] S. Sienz, S. Mändl, B. Rauschenbach, In situ stress measurements during low-energy nitriding of stainless steel, Surf. Coatings Technol. 156 (2002) 185–189. https://doi.org/10.1016/S0257-8972(02)00081-6.
[164] J.C. Oxley, J.L. Smith, F.L. Steinkamp, J. Gorawara, V. Kanazirev, Study on exposing supported copper compounds to acetylene, J. Chem. Heal. Saf. 24 (2017) 26–33. https://doi.org/10.1016/j.jchas.2016.06.001.
[165] G. Ashiotis, A. Deschildre, Z. Nawaz, J.P. Wright, D. Karkoulis, F.E. Picca, J. Kieffer, The fast azimuthal integration Python library: PyFAI, J. Appl. Crystallogr. 48 (2015) 510–519. https://doi.org/10.1107/S1600576715004306.
[166] A.A. Coelho, TOPAS and TOPAS-Academic: An optimization program integrating computer algebra and crystallographic objects written in C++: An, J. Appl. Crystallogr. 51 (2018) 210–218. https://doi.org/10.1107/S1600576718000183.
[167] H.K.D.H. Bhadeshia, S.A. David, J.M. Vitek, R.W. Reed, Stress induced transformation to bainite in Fe-Cr-Mo-C pressure vessel steel, Mater. Sci. Technol. (United Kingdom). 7 (1991). https://doi.org/10.1179/mst.1991.7.8.686.
[168] S.J. Lee, M.T. Lusk, Y.K. Lee, Conversional model of transformation strain to phase fraction in low alloy steels, Acta Mater. 55 (2007). https://doi.org/10.1016/j.actamat.2006.09.008.
[169] I. Seki, K. Nagata, Lattice constant of iron and austenite including its supersaturation phase of carbon, ISIJ Int. 45 (2005). https://doi.org/10.2355/isijinternational.45.1789.
[170] R. Subramanian, H. Tripathy, A.K. Rai, R.N. Hajra, S. Saibaba, T. Jayakumar, E. Rajendra Kumar, Thermal expansion characteristics of Fe-9Cr-0.12C-0.56Mn-0.24V-1.38W-0.06Ta (wt.%) reduced activation ferritic-martensitic steel, J. Nucl. Mater. 459 (2015) 150–158. https://doi.org/10.1016/j.jnucmat.2015.01.026.
[171] F. Richter, Die physikalischen Eigenschaften der Stähle -Das 100 -Stähle -Programm -Teil I: Tafeln und Bilder, Mühlheim an der Ruhr, 2010.
[172] M.G. Zürn, O.B. Tapar, J. Epp, J. Gibmeier, Real-time monitoring of the near-surface stress development during quenching after low-pressure carburizing, in: Int. Conf. Residual Stress., 2022.
[173] J. Ågren, G.P. Vassilev, Computer simulations of cementite dissolution in austenite, Mater. Sci. Eng. 64 (1984) 95–103. https://doi.org/10.1016/0025-5416(84)90076-4.
[174] C. Wert, C. Zener, Interference of growing spherical precipitate particles, J. Appl. Phys. 21 (1950) 5–8. https://doi.org/10.1063/1.1699422.
[175] J. Agren, Kinetics of carbide dissolution, Scand. J. Metall. 19 (1990) 2–8.
[176] M. Sugiyama, K. Ishikawa, H. Iwata, Vacuum carburizing with acetylene, Adv. Mater. Process. 155 (1999) 29–33.
[177] R.U. Khan, D. Buchholz, F. Graf, R. Reimert, Pyrolysis of acetylene for vacuum carburizing

of steel: Modeling with detailed kinetics, Int. J. Chem. React. Eng. 7 (2009) A10. https://doi.org/10.2202/1542-6580.1781.
[178] R.J. Madix, Reaction Kinetics and Mechanism on Metal Single Crystal Surfaces, Adv. Catal. 29 (1980) 1–53. https://doi.org/10.1016/S0360-0564(08)60119-4.
[179] R. Neubauer, C.M. Whelan, R. Denecke, H.P. Steinrück, The thermal chemistry of saturated layers of acetylene and ethylene on Ni(100) studied by in situ synchrotron x-ray photoelectron spectroscopy, J. Chem. Phys. 119 (2003) 1710–1718. https://doi.org/10.1063/1.1582432.
[180] R. Byron Bird Warren E. Stewart Edwin N. Lightfoot, R.B. Bird, W.E. Stewart, E.N. Lightfoot, Concentration Distributions with More than One Independent Variable, in: Transp. Phenomena, Revis. 2nd Ed., John Wiley & Sons, Inc., New Jersey, 2006: pp. 612–656.
[181] P. Kula, R. Pietrasik, K. Dybowski, Vacuum carburizing - Process optimization, J. Mater. Process. Technol. 164–165 (2005) 876–881. https://doi.org/10.1016/j.jmatprotec.2005.02.145.
[182] C. Sauerborn, Modellierung der Stoffübertragung beim Niederdruckaufkohlen mit Acetylen, karlsruhe institute of technology, 2008.
[183] S.M.C. Van Bohemen, Bainite and martensite start temperature calculated with exponential carbon dependence, Mater. Sci. Technol. 28 (2012) 487–495. https://doi.org/10.1179/1743284711Y.0000000097.
[184] A.S. Sastri, D.R.F. West, Effect of austenitizing conditions on kinetics of martensite formation in certain medium-alloy steels, J. Iron Steel Inst. 203 (1965) 138–149.
[185] P.J. Brofman, G.S. Ansell, On the effect of fine grain size on the Ms temperature in Fe-27Ni-0.025C alloys, Metall. Trans. A, Phys. Metall. Mater. Sci. 14 A (1983) 1929–1931. https://doi.org/10.1007/BF02645565.
[186] C. Celada-Casero, C. Kwakernaak, J. Sietsma, M.J. Santofimia, The influence of the austenite grain size on the microstructural development during quenching and partitioning processing of a low-carbon steel, Mater. Des. 178 (2019) 107847. https://doi.org/10.1016/j.matdes.2019.107847.
[187] M. Tupaj, A.W. Orłowicz, A. Trytek, M. Mróz, G. Wnuk, A.J. Dolata, The effect of cooling conditions on martensite transformation temperature and hardness of 15% cr chromium cast iron, Materials (Basel). 13 (2020) 2760. https://doi.org/10.3390/ma13122760.
[188] T.Y. Hsu (Xu Zuyao), J. Li, Z. Zeng, Effect of solution strengthening of austenite on martensite transformation in Fe-Ni-C alloys, Metallography. 19 (1986). https://doi.org/10.1016/0026-0800(86)90018-2.
[189] S.M.C. Van Bohemen, The nonlinear lattice expansion of iron alloys in the range 100-1600 K, Scr. Mater. 69 (2013) 315–318. https://doi.org/10.1016/j.scriptamat.2013.05.009.
[190] H.K.D.H. Bhadeshia, Carbon content of retained austenite in quenched steels, Met. Sci. 17 (1983) 151–152. https://doi.org/10.1179/030634583790421087.
[191] M. Sarikaya, G. Thomas, J.W. Steeds, S.J. Barnard, G.D.W. Smith, Solute Element Partitioning and Austenite Stabilization in Steels, Berkeley, 1982. https://doi.org/10.2172/7031961.
[192] D.H. Sherman, S.M. Cross, S. Kim, F. Grandjean, G.J. Long, M.K. Miller, Characterization of the carbon and retained austenite distributions in martensitic medium carbon, high silicon steel, Metall. Mater. Trans. A Phys. Metall. Mater. Sci. 38 (2007) 1698–1711. https://doi.org/10.1007/s11661-007-9160-3.
[193] C. Lerchbacher, S. Zinner, H. Leitner, Atom probe study of the carbon distribution in a hardened martensitic hot-work tool steel X38CrMoV5-1, Micron. 43 (2012) 818–826. https://doi.org/10.1016/j.micron.2012.02.005.
[194] R.C. Thomson, M.K. Miller, An atom probe study of carbon distribution in martensite in 2 1/4 Cr1Mo steel, Scr. Metall. Mater. 32 (1995) 149–154. https://doi.org/10.1016/S0956-716X(99)80028-4.
[195] R.A. Vorobev, V.N. Dubinskii, V. V. Evstifeeva, Effect of The Processes of Self-Tempering and Tempering on The Mechanical Characteristics and the Character of Fracture of Low-Carbon Martenstic Steel Quenched in Air, Phys. Met. Metallogr. 120 (2019) 989–994. https://doi.org/10.1134/S0031918X19100132.
[196] Y. Wang, Y. Tomota, T. Ohmura, S. Morooka, W. Gong, S. Harjo, Real time observation of martensite transformation for a 0.4C low alloyed steel by neutron diffraction, Acta Mater. 184 (2020) 30–40. https://doi.org/10.1016/j.actamat.2019.11.051.

[197] T. Mendiara, M.P. Domene, A. Millera, R. Bilbao, M.U. Alzueta, An experimental study of the soot formed in the pyrolysis of acetylene, J. Anal. Appl. Pyrolysis. 74 (2005) 486–493. https://doi.org/10.1016/j.jaap.2004.11.019.
[198] M. Steinbacher, B. Clausen, F. Hoffmann, H.W. Zoch, Steigerung der vorhersagegenauigkeit bei der berechnung des kohlenstoffprofils von niederdruckaufkohlungsprozessen, HTM - J. Heat Treat. Mater. 63 (2008) 33–39. https://doi.org/10.3139/105.100437.
[199] H.W. Antes, Calculating the gas flow rate for vacuum carburization, Heat Treat. Prog. 8 (2005) 51–53.
[200] M. Jung, S. Oh, Y.K. Lee, Predictive model for the carbon concentration profile of vacuum carburized steels with acetylene, Met. Mater. Int. 16 (2009) 971–975. https://doi.org/10.1007/s12540-009-0971-1.
[201] G. Parrish, Decarburization, in: Carburizing Microstruct. Prop., Ohio, 1999: pp. 37–49. https://doi.org/10.31399/asm.tb.cmp.t66770037.
[202] J. Brnic, G. Turkalj, D. Lanc, M. Canadija, M. Brcic, G. Vukelic, Comparison of material properties: Steel 20MnCr5 and similar steels, J. Constr. Steel Res. 95 (2014) 81–89. https://doi.org/10.1016/j.jcsr.2013.11.024.
[203] R.J. Katemi, J. Epp, F. Hoffmann, M. Steinbacher, Investigations of residual stress distributions in retained austenite and martensite after carbonitriding of a low alloy steel, in: Adv. Mater. Res., 2014. https://doi.org/10.4028/www.scientific.net/AMR.996.550.
[204] C. Zimmerman, J. Hall, D. McCurdy, E. Jamieson, Comparison of residual stresses from atmosphere and low pressure carburization, Heat Treat. Prog. (2007).
[205] D. V. Nelson, R.E. Ricklefs, W.P. Evans, Residual stresses in quenched and tempered plain carbon steels, in: SAE Tech. Pap., 1971. https://doi.org/10.4271/710283.
[206] H.H. A. Rose, Atlas of steels heat treatment, Verlag Stahleisen, Düsseldorf, 1972.
[207] L. Cheng, A. Böttger, T.H. de Keijser, E.J. Mittemeijer, Lattice parameters of iron-carbon and iron-nitrogen martensites and austenites, Scr. Metall. Mater. 24 (1990) 509–514. https://doi.org/10.1016/0956-716X(90)90192-J.
[208] Z. Nishiyama, Martensitic Transformation., Academic Press, London, 1978.
[209] J.W. Christian, Basic crystallography and kinetics, in: E.R. Petty (Ed.), Martensite Fundam. Technol., Longman Group, London, 1970.
[210] G. Krauss, Martensite in steel: Strength and structure, Mater. Sci. Eng. A. 273–275 (1999). https://doi.org/10.1016/s0921-5093(99)00288-9.
[211] L. Kaufman, M. Cohen, Thermodynamics and kinetics of martensitic transformations, Prog. Met. Phys. 7 (1958) 165–246. https://doi.org/10.1016/0502-8205(58)90005-4.
[212] A.R. Entwisle, The kinetics of martensite formation in steel, Metall. Trans. 2 (1971) pages 2395–2407. https://doi.org/10.1007/BF02814877.
[213] H. Kitahara, N. Tsuji, Y. Minamino, Martensite transformation from ultrafine grained austenite in Fe-28.5 at.% Ni, Mater. Sci. Eng. A. 438–440 (2006) 233–236. https://doi.org/10.1016/j.msea.2006.02.082.
[214] Q. Gao, C. Wang, F. Qu, Y. Wang, Z. Qiao, Martensite transformation kinetics in 9Cr-1.7W-0.4Mo-Co ferritic steel, J. Alloys Compd. 610 (2014) 322–330. https://doi.org/10.1016/j.jallcom.2014.05.060.
[215] H.S. Yang, H.K.D.H. Bhadeshia, Austenite grain size and the martensite-start temperature, Scr. Mater. 60 (2009) 493–495. https://doi.org/10.1016/j.scriptamat.2008.11.043.
[216] J.C. Zhao, M.R. Notis, Continuous cooling transformation kinetics versus isothermal transformation kinetics of steels: a phenomenological rationalization of experimental observations, Mater. Sci. Eng. R. (1995). https://doi.org/10.1016/0927-796X(95)00183-2.
[217] S. Da Silva De Souza, P.S. Moreira, G.L. De Faria, Austenitizing temperature and cooling rate effects on the martensitic transformation in a microalloyed-steel, Mater. Res. 23 (2020). https://doi.org/10.1590/1980-5373-MR-2019-0570.
[218] Z. Babasafari, A. V. Pan, F. Pahlevani, R. Hossain, V. Sahajwalla, M. Du Toit, R. Dippenaar, Effects of austenizing temperature, cooling rate and isothermal temperature on overall phase transformation characteristics in high carbon steel, J. Mater. Res. Technol. 9 (2020) 15286–15297. https://doi.org/10.1016/j.jmrt.2020.10.071.
[219] V.M. Mirzaev, D.A.; Shtejnberg, M.M.; Ponomareaa, T.N.; Schastlivtsev, Effect of cooling rate on martensite point position. Carbon steels, Fiz. Met. i Metalloved. 47 (1979) 125–135.
[220] L.Z. Chengcheng Liu, Minping Huang, Qiang Ren, Ying Ren, Effect of Grain Size and Cooling

Rate on the Martensite Start Temperature of Stainless Steel, Steel Res. Int. 93 (2022). https://doi.org/doi.org/10.1002/srin.202200044.
[221] H. Schwendemann, Die Thermische Restaustenitstabilisierung bei den Stählen 100Cr6 und X210Cr12, Universität Karlsruhe, 1983.
[222] W. Reimche, S. Zwoch, O. Bruchwald, F.-W. Bach, H. Klümper-Westkamp, J. Lütjens, H.-W. Zoch, Hochtemperatur-Prüftechnik ermöglicht Einblick in die Werkstoffumwandlung und Phasenausbildung bei Hochleistungsbauteilen, in: DGZfP-Jahrestagung 2011, 2011.
[223] P. Payson, C.H. Savage, Martensite Reactions in Alloy Steels, Trans. ASM. 33 (1944) 261–275.
[224] C. Liu, Z. Zhao, D.O. Northwood, Y. Liu, A new empirical formula for the calculation of MS temperatures in pure iron and super-low carbon alloy steels, in: J. Mater. Process. Technol., 2001. https://doi.org/10.1016/S0924-0136(01)00625-2.
[225] D.P. Koistinen, R.E. Marburger, A general equation prescribing the extent of the austenite-martensite transformation in pure iron-carbon alloys and plain carbon steels, Acta Metall. (1959). https://doi.org/10.1016/0001-6160(59)90170-1.
[226] M. Wildau, Zum Einfluß der Werkstoffeigenschaften auf Spannungen, Eigenspannungen und Maßänderungen von Werkstücken aus Stahl, Technische Hochschule Aachen, 1986.
[227] H. zhuang ZHAO, X. hua LIU, G. dong WANG, Progress in Modeling of Phase Transformation Kinetics, J. Iron Steel Res. Int. 13 (2006) 68–73. https://doi.org/10.1016/S1006-706X(06)60064-2.
[228] D.H. Herring, R.L. Houghton, The influence of process variables on vacuum carburizing, in: Proc. Sec. Intern. Conf. Carburizing Nitriding with Atmos., Cleveland, 1995: pp. 103–108.
[229] K. Dybowski, R. Niewiedzielski, Distortion of 16MnCr5 Steel Parts During Low-Pressure Carburizing, Adv. Sci. Technol. Res. J. 11 (2017) 201–207. https://doi.org/10.12913/22998624/67674.
[230] G.E. Totten, Steel Heat Treatment Handbook, Second Edition, CRC Press, Boca Raton, 2006.
[231] F. Limque, F. Bless, Erfahrungen mit Überdruck-Gasabschrecken sowie Aufkohlen in Vakuumöfen, Haerterei-Technische Mitteilungen. 35 (1980) 238–244. https://doi.org/doi.org/10.1515/htm-1980-350504.
[232] F.W. Eysell, E. Heumüller, Entwicklungstendenzen auf dem Gebiet der Unterdruckaufkohlung, HTM Härterei-Techn. Mitt. 34 (1979) 83–89. https://doi.org/doi.org/10.1515/htm-1979-340204.
[233] F. Graf, Pyrolyse- und Aufkohlungsverhalten von C2H2 bei der Vakuumaufkohlungs von Stahl, Universität Karlsruhe, 2007. https://doi.org/10.5445/KSP/1000007244.
[234] J. Naudot, Process and oven for low-pressure cementation, 1991.
[235] B. Edenhofer, Einsatzhärten - Ein prozess mit neuen entwicklungen und perspektiven, HTM - Haerterei-Technische Mitteilungen. 56 (2001) 14–22.
[236] AWT Fachausschuss 5, Arbeitskreis 4 (Hrsg.): Die Prozeßregelung beim Gasaufkohlen und Einsatzhärten., Expert-Verlag. (1997).
[237] F. Hoffmann, D. Liedtke, U. Wyss, H.W. Zoch, Der Aufkohlungsvorgang, HTM - Haerterei-Technische Mitteilungen. 50 (1995) 86–93.
[238] Neumann F, Wyss U, Aufkohlungswirkung von Gasgemischen im System H2 / CH4 / H2O - CO / CO2 - N2, HTM - Haerterei-Technische Mitteilungen. 25 (1970) 253–266.
[239] K. Rimmer, E. Schwarz-Bergkampf, J. Wuenning, Geschwindigkeit der Oberflächenreaktion bei der Gasaufkohlung, HTM - Haerterei-Technische Mitteilungen. 30 (1975) 152–160. https://doi.org/doi.org/10.1515/htm-1975-300303.
[240] P. Willmott, An introduction to synchrotron radiation: Techniques and applications, 2011. https://doi.org/10.1002/9781119970958.
[241] G. Malmros, J.O. Thomas, Least-squares structure refinement based on profile analysis of powder film intensity data measured on an automatic microdensitometer, J. Appl. Crystallogr. 10 (1977) 7–11. https://doi.org/10.1107/s0021889877012680.
[242] P. Scardi, Diffraction Line Profiles in the Rietveld Method, Cryst. Growth Des. 20 (2020) 6903−6916. https://doi.org/10.1021/acs.cgd.0c00956.
[243] R.A. Young, P.E. Mackie, R.B. von Dreele, Application of the pattern-fitting structure-refinement method of X-ray powder diffractometer patterns, J. Appl. Crystallogr. 10 (1977) 262–269. https://doi.org/10.1107/s0021889877013466.

[244] G.K. Wertheim, M.A. Butler, K.W. West, D.N.E. Buchanan, Determination of the Gaussian and Lorentzian content of experimental line shapes, Rev. Sci. Instrum. 45 (1974) 1369. https://doi.org/10.1063/1.1686503.
[245] J.I. Langford, A rapid method for analysing the breadths of diffraction and spectral lines using the Voigt function, J. Appl. Crystallogr. 11 (1978) 10–14. https://doi.org/10.1107/s0021889878012601.
[246] A. Immirzi, Constrained powder-profile refinement based on generalized coordinates. Application to X-ray data of isotactic polypropylene, Acta Crystallogr. Sect. B Struct. Crystallogr. Cryst. Chem. B36 (1980) 2378–2385. https://doi.org/10.1107/s0567740880008771.
[247] R.A. Young, The Rietveld Method, in: The Rietveld Method, Oxford University Press, New York (US), 1993: pp. 1–38.
[248] P.W. Stephens, Phenomenological model of anisotropic peak broadening in powder diffraction, J. Appl. Crystallogr. 32 (1999) 281–289. https://doi.org/10.1107/S0021889898006001.
[249] P. Thompson, D.E. Cox, J.B. Hastings, Rietveld refinement of Debye–Scherrer synchrotron X-ray data from Al2O3, J. Appl. Crystallogr. 20 (1987) 79–83. https://doi.org/10.1107/S0021889887087090.
[250] D. Balzar, Voigt-function model in diffraction line-broadening analysis, in: Defect Microstruct. Anal. by Diffr., 1999: pp. 94–126.
[251] R.W. Cheary, A. Coelho, Fundamental parameters approach to x-ray line-profile fitting, J. Appl. Crystallogr. 25 (1992) 109–121. https://doi.org/10.1107/S0021889891010804.
[252] L. Alexander, The synthesis of x-ray spectrometer line profiles with application to crystallite size measurements, J. Appl. Phys. 25 (1954) 155. https://doi.org/10.1063/1.1721595.
[253] H. Klug, L. Alexander, X-ray Diffraction Procedures: For Polycrystalline and Amorphous Materials, 2nd Edition, Willey, New York, EUA. (1974).
[254] E. Macherauch, H.-W. Zoch, Praktikum in Werkstoffkunde, 12th Ed, Springer Fachmedien Wiesbaden, Wiesbaden, 2014. https://doi.org/10.1007/978-3-658-05038-2.

10 Appendix

10.1 Structural Transformation in Steel

10.1.1 Description of Austenitization via TTA Diagram

Upon heating the steel above the austenite formation temperature, the carbides begin to dissolve, leading to a homogeneous distribution of carbon. Figure 10-1 shows the isothermal austenitization TTA diagram for steel C45 with a heating rate of 130 K/s as an example.

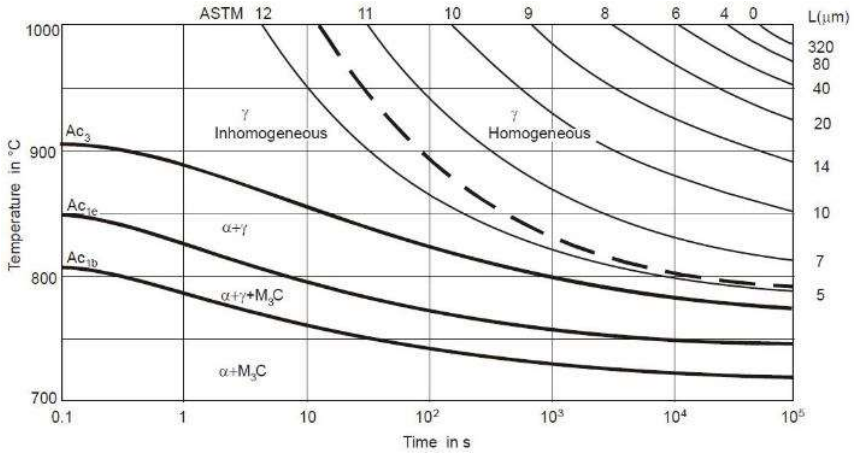

Figure 10-1: Schematic TTA diagram for isothermal austenitization of the steel C45; vA = 130 K/s. Grain size values of austenite is given in above x- and right y-axis [206] [23].

Taking 800 °C as an illustrative example from the graph, the temperature surpasses the Ac_{1b} line after a 0.3-second holding period, indicating the initiation of austenite formation.
After 9 seconds, where Ac_{1e} temperature is exceeded, all carbides dissolve in austenite, resulting in a microstructure composing solely of ferrite and austenite. Approximately 1600 seconds later, surpassing the Ac_3 temperature, the microstructure undergoes complete transformation into austenite. Upon quenching from this point, the steel exhibits a grain size of less than ASTM 12. However, it's important to note that increasing holding time can lead to an increase in grain size[3].
For instance, a holding time of 105 seconds after austenitizing at 820 °C yields fine austenite grains with an ASTM grain size of 11, corresponding to approximately 7 µm. In addition, if 950 °C is considered, with the given heating rate, the microstructure transforms completely into austenite within 0.1 seconds. Following a 1.5-hour holding period at this temperature, the austenite grains coarsen to 14 µm. Prolonged holding for 7 hours results in a final grain size of 20 µm.

[3] ASTM grain size number decreases with increasing grain size

10.1.2 Characterization of Final Microstructure Upon Cooling via CCT Diagram

Continuous cooling transformation (CCT) diagrams illustrate the degree of transformation as a function of time for consistently decreasing temperature, as desired for most hardening operations including carburizing. In practical terms, this involves cooling a sample from the austenite state at a predetermined rate, with the degree of transformation assessed using techniques such as dilatometry [1]. The final quenched microstructure resulting from the heat treatment process can be effectively characterized and predicted through the utilization of CCT diagrams. Figure 10-2 shows a CCT diagram specifically for steel 34Cr4.

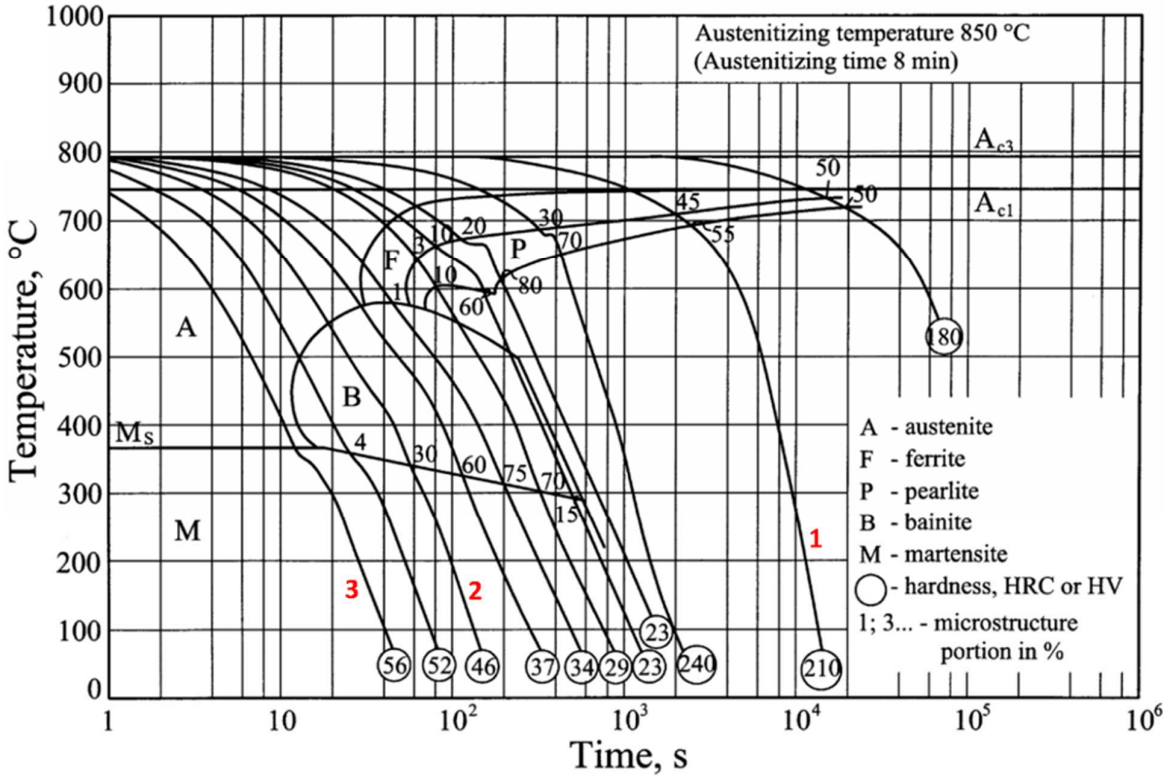

Figure 10-2: Continuous-cooling transformation (CCT) diagram of steel 34Cr4. Numbers near the curves shows the relative amounts of structural components [206].

In the depicted figure, A_{C3} and A_{C1} temperatures represent upper and lower critical temperatures, respectively. These temperatures signify the range below which pearlite formation (A_{C1}) and ferrite formation (A_{C3}) occur for very slow cooling.

Additionally, the figure gives various cooling rates, each associated with distinct hardness values in the final microstructure. For instance, if steel is cooled along the path 1, the final microstructure comprises 45 vol. % ferrite and 55 vol. % pearlite, resulting in a final hardness of 210 HV. On the other hand, following the cooling rate labeled as 2, austenite transforms into 30 vol. % bainite and 70 vol. % martensite, resulting in a final microstructure with a hardness of 46 HRC.

The cooling rate represented by path 3 is significant as it suppresses all other transformations except the transformation to martensite. This critical cooling rate is referred to as the *upper critical*

cooling rate, or simply the *critical cooling rate*, and holds particular importance in the hardening process of steels.

10.2 Further Details of Martensitic Transformation

Crystal Structure of Martensite

Martensite forms from a slight displacement of atoms relative to its neighbors. Shear and tensile forces lead to a polymorphic transformation from FCC austenite to body-centered tetragonal (BCT) lattice [17,30]. The crystallographic model to explain this transformation is formulated by Edgar Collins Bain and called “Bain model” [33]. Figure 10-3 gives the representative figure of the “Bain model”.

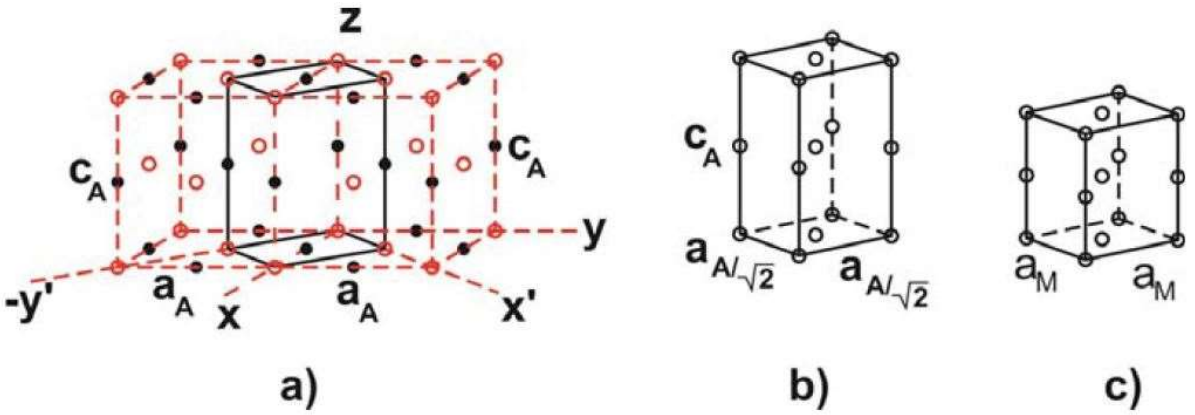

Figure 10-3: The transformation of FCC austenite into BCT martensite according to the Bain model; two face-centered cubic cells (austenite) with embedded tetragonal cell (a), tetragonal cell from (b), martensite cell (c) [30].

According to the model, a pair of FCC unit cells, with the lattice constant a_A is a starting point and they already contain a virtual tetragonal body-centered lattice, as seen in Figure 10-3a. The virtual tetragonal unit cell has the lattice constants $c_V = a_A$ and $a_V = a_A/\sqrt{2}$. The c-axis is compressed by approximately 20% through a homogeneous deformation and the a-axis is enlarged by 12% in order to agree with the final lattice measurement of martensite [30].

Occupancy of some octahedral vacancies in the iron lattice with the interstitial dissolved carbon atoms causes the tetragonal lattice distortion. Carbon atoms settle preferable to the larger octahedral vacancies in the z-plane; therefore, tetragonality of martensite increases with carbon content [30]. Relationship between the tetragonality of martensite, and lattice constant with the carbon content has been shown to follow the relation given as [21,207]

$$c_M/a_M = 1 + 0.045x_C \qquad \textit{Eq. 10-1}$$

$$c_M = 0.28664 + 0.0247x_C^r \qquad \textit{Eq. 10-2}$$

$$a_M = 0.28664 + 0.00028x_C^r \qquad \textit{Eq. 10-3}$$

where x_C is ma. % and x_C^r is atomic percent of carbon. Lattice constants c_M and a_M are in nm. This relationship can be used to determine the carbon content of martensite.

Although the explanation of the deformation of the crystal lattice during the transformation from the FCC to the tetragonally distorted BCC by Bain model is appropriate, it is not complete because of the absence of invariant plane between parent and product phase [30,208]. This invariant plane can only be determined experimentally, requiring a further deformation step. This second deformation step must have the characteristic that it should be macroscopically homogeneous but microscopically inhomogeneous so the structure of the previously produced martensite lattice is preserved [30,208]. The phenomenological theory of martensite crystallography describes this mechanism (Figure 10-4). Crystal slipping and twinning compensates for the lattice distortion caused by pure lattice-altering transformations.

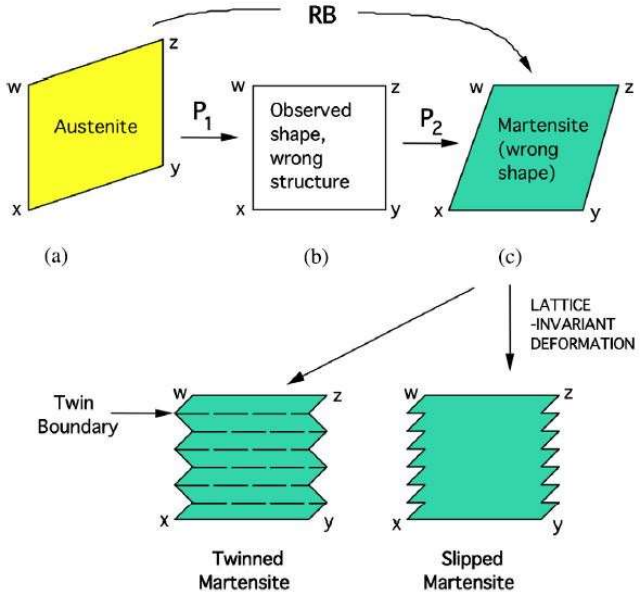

Figure 10-4: The phenomenological theory of martensite crystallography [21]

Combination of rigid body rotation, **R,** and Bain strain, **B, (RB)** creates a deformation called deformation invariant-line strain (from a to c in Figure 10-4). During the transformation, the observed shape deformation P_1 and the second homogeneous shear P_2 created the correct structure but were still in the wrong shape. These conflicts are fixed when the shape-changing effect of P_2 is eliminated macroscopically by an inhomogeneous lattice-invariant deformation, which is slip or twinning [21,30]. The theory explains all the observed features of the martensite crystallography. Figure 10-5 shows schematically the two types of lattice invariant deformation occurring within a martensite plate.

Therefore, the austenite-martensite transformation can be completed in two steps: the lattice-changing deformation (Bain) and the lattice-retaining deformation (invariant deformation).

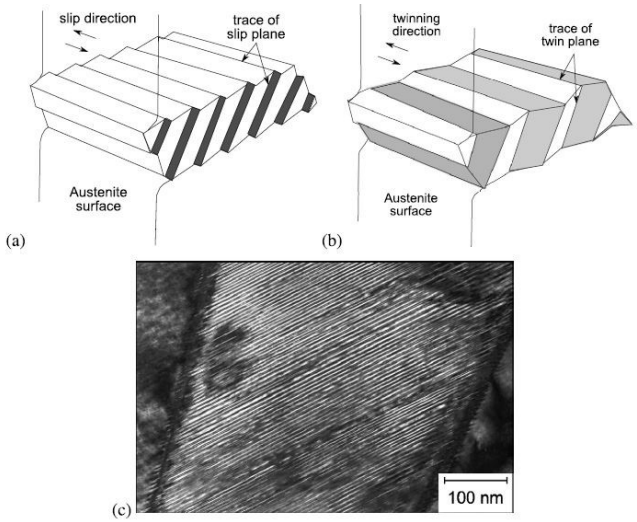

Figure 10-5: Two types of lattice deformation. The broad faces in these schematics represent the habit planes: (a) slip and (b) twinning [209]. *(c) Transmission electron micrograph showing a finely twinned plate of martensite in Fe-22Ni-20Co-0.6C steel* [21].

In order to reduce the strain energy due to the distortion, martensite forms as thin plates or laths when the transformation of martensite is restrained by its surroundings [21]. The names of the morphologies are derived from their appearances. Lath martensite has an appearance of laths, a thin and narrow strips; while plate martensite is has an appearance of needle-like structure. Figure 2-6 shows these two different morphologies of martensite.

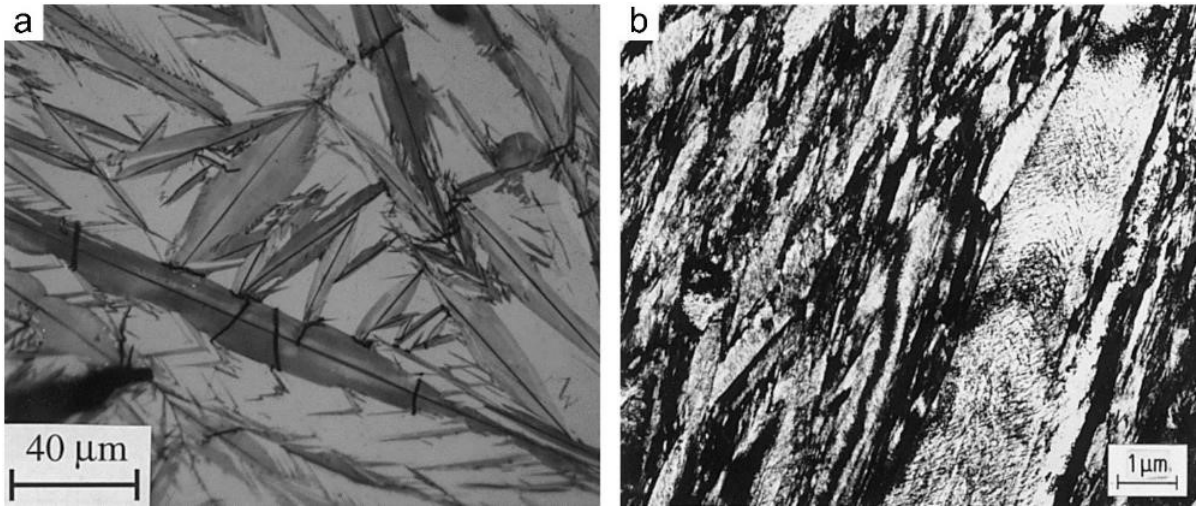

Figure 10-6: a) Microstructure of plate martensite in an Fe–1.86 wt.% C alloy taken by light microscope, b) microstructure of lath martensite in 4140 steel tempered at 150°C taken by TEM bright field imaging. [210].

The morphology of martensite is particularly affected by the carbon content. For alloys containing less than approximately 0.6 ma. % carbon, morphology is dominated by lath-like martensite. Plate martensite is found exclusively in alloys containing more than approximately 1.0 ma % carbon. For carbon contents between 0.6 and 1 ma. %, the martensite present is a mixture of both. In general, lath martensite exhibits lower strength but relatively higher toughness and ductility, while plate martensite structure is associated with much higher strength but also brittleness.

As mentioned earlier in this section, this transformation is accompanied by volume expansion which creates, due to interstitial solute atoms, (residual) stresses. At high carbon concentrations, the amount of these stresses can reach to the levels that could lead cracks during transformation. Thus, plate martensite is less desirable structures in most applications [1,21].

Kinetics of Martensite Formation

Austenite is a stable phase at high temperatures, possessing a lower Gibbs free energy than martensite. When the temperature decreases (sufficiently fast enough to prevent all diffusion reactions), Gibbs free energy of austenite and martensite increases with different rates. There is a certain temperature where both become equal. This temperature is called Equilibrium Temperature (T_E). However, reaching the equilibrium temperature alone is not adequate for the initiation of martensite transformation, as there is no Gibbs free energy difference to favor one phase over the other. To initiate the transformation, a certain nucleation Gibbs free energy (ΔG_{A-M}) should be supplied through additional undercooling (ΔT) until M_s temperature [30,211,212]. Figure 10-7 illustrates this transformation.

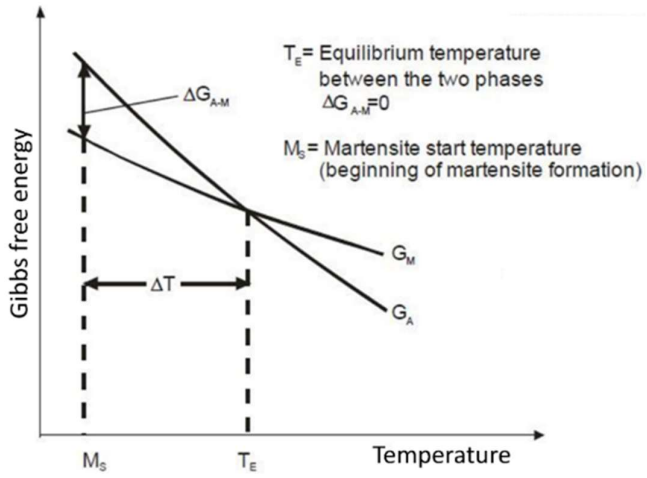

Figure 10-7: Effect of temperature on the free Gibbs free energy of austenite and martensite. G_A is for austenite, G_M is for martensite and ΔT is undercooling [21,30].

During rapid cooling, martensitic transformation starts immediately after martensite start temperature (M_s) is reached, and continues until martensite finish (M_f) temperature. Generally, M_s temperature is influenced by chemical compositions [30], austenite grain size [213–215] and cooling rate [214,216].

The size of the austenite grains tends to increase with higher austenitizing temperatures, leading to a higher M_s temperature [215,217]. Regarding the cooling rate, different observations have been reported, indicating both decreases [214] and also increase [218] of M_s in higher cooling rates. However, the prevailing trend, especially for higher austenitizing temperatures, is often a decrease in M_s temperature [214,217,219,220].

After the martensite finish temperature (M_f), no further transformation occurs. However, it's essential to note that this does not imply a complete transformation of 100 % of the parent austenite phase into martensite [19,221,222].

Most of the alloying elements that go into solution in austenite reduces the M_s and M_f temperatures. One of the first model to describe this effect is given by Payson and Savage in 1944 [223] as

$$M_s\ (°C) = 499 - 308w_c - 32.4w_{Mn} - 16.2w_{Ni} - 27w_{Cr} - 10.8w_{Mo} - 10.8w_w - 10.8w_{Si} \qquad \textit{Eq. 10-4}$$

Since then, several other models have been developed. An overview of these models can be seen in chronological order in the work done by Liu et al. [224]. While many of these models suggest a linear relation between alloying elements and M_s temperature, some recent models deviate by demonstrating an exponential relationship between carbon content and M_s temperature. One notable example of such a model is the work developed by van Bohemen [183], which is also used in this thesis. The model aims to calculate the M_s temperature of steels having 0.1-1.9 ma % C and less than 7 ma % other alloying elements. According to the model, M_s can be formulated as

$$M_s = 565 - \sum_i K_i x_i - 600[1 - exp(-0.96x_C)] \qquad \textit{Eq. 10-5}$$

Where x_C is amount of carbon in ma. % and $\sum_i K_i x_i = 31x_{Mn} + 13x_{Si} + 10x_{Cr} + 18x_{Ni} + 12x_{Mo}$ describes the effect mass percentage of other substitutional elements. This particular model has been used in this thesis and will be comprehensively discussed further in the subsequent discussion section.

Figure 10-8 presents the effect of carbon content on M_s and M_f temperature. As stated before in section 2.1, carbon atoms occupy the octahedral sites in FCC lattice. Since transformation take place without or with minimal diffusion, carbon atoms retain their positions. This causes a remaining distortion of the BCT lattice in the z-direction; thus, stronger undercooling has to be supplied in order to reach the required Gibbs free energy. Consequently, the M_s and M_f are shifted to lower temperatures as the carbon content increases [30].

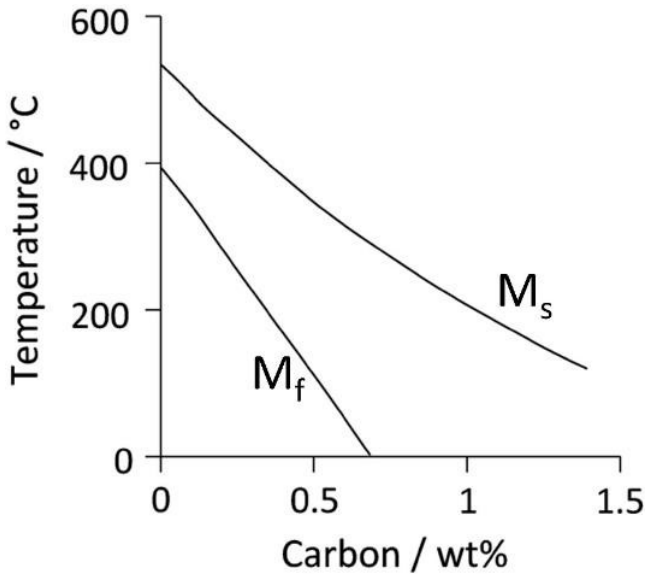

Figure 10-8: Effect of carbon content on M_s and M_f temperatures [21].

There are several models to describe the kinetics of martensitic transformation but the most widely accepted one is “Koistinen and Marburger (KM) model”. The model is given as

$$V_m = X - exp\left[0.011 \cdot \left(M_s - T_q\right)\right] \qquad \textit{Eq. 10-6}$$

Where V_m is the volume of martensite formed at the temperature T_q below the martensite start temperature (M_s) in °C, *X* is the volume fraction of austenite available just above M_s [225]. Several modifications of this model were presented in the literature such as the model of Wildau which is based on dilatometry measurements [226].

$$V_m = X - exp\left[\frac{1}{T_0}\left(M_s - T_q\right)^n\right] \qquad \textit{Eq. 10-7}$$

The parameters T_0 and n are dependent on the carbon content related to the M_s temperature. Based on the dilatometry curves, the relation between parameters and M_s temperature can be given as

$$^1/_{T_0} = -(0.36x10^{-3} + 0.10x10^{-4}xM_s - 0.34x10^{-6}xM_s^2 + 0.32x10^{-8}xM_s^3 - 0.52x10^{-1}\ xM_s^4) \qquad \textit{Eq. 10-8}$$

$$n = 2.08 - 0.76x10^{-2}xM_s + 0.16x10^{-4}xM_s^2 - 0.90x10^{-8}xM_s^3. \qquad \textit{Eq. 10-9}$$

Another modified version of the KM formula is proposed by Zhao et al. using a temperature dependence of the parameter b_1 and b_2 which can be fitted to experimental data [227]. The formula given as

$$V_m = X - exp\left[(b_1 \cdot T_q - b_2) \cdot (M_s - T_q)\right] \quad \textit{Eq. 10-10}$$

For AISI 1080 steel grade with M_s=200 °C the authors found b_1=0.000019 and b_2=0.0146.
The final quenched microstructure resulting from the heat treatment process can be effectively characterized and predicted through the utilization of CCT diagrams, which were briefly explained in the previous section.

10.3 Development of Low Pressure Carburizing Process

Low-pressure carburizing is the carburization of a component below atmospheric pressure, achieved by introducing a controlled amount of hydrocarbon gases. The major advantages of low-pressure carburizing include the ability to carburize complex geometries with satisfactory homogeneity and the elimination of surface oxidation [2].
It is known that increasing the partial pressure of hydrocarbon gases enhances the carbon transfer from the atmosphere to the surface [228,229]. This discovery dates back to the 1960s, and research on the opportunities for low-pressure carburizing was extensively conducted [230]. In the early years of the process, long-chained hydrocarbons were used as a carbon source, resulting in an oversupply of carbon and the formation of soot particles in the atmosphere. This led to contamination of the furnace systems. In the 1980s, attempts were made to overcome the soot problem by utilizing soot sensors and propane gas as a carbon source. The concept was to cut the supply of propane when the sensor detected soot particles [231–233], but this solution did not completely eliminate the soot problem. Another challenge was the required distance between carburized components, reducing the number of components per charge and increasing the overall cost. Therefore, despite the advantages of the process, its industrial application was not broadly adopted [48].
The significant step towards a reliable, soot-free process was finally achieved in the early 1990s by Naudot [234]. In this method, pressure was lowered to the 3-7 mbar and cyclic enrichment and diffusion steps were applied at same pressure. During the enrichment step (or boost step) the furnace was filled with propane, and during the diffusion step propane was replaced with nitrogen. This controlled gas introduction and gas extraction was used to maintain the same process pressure during the whole process. The process temperature was 950-1000 °C. By lowering the pressure below 10 mbar and using a gas nozzle to eliminate propane decomposition before reaching the sample, the soot formation problem was solved. Subsequent developments in the process involved using acetylene as the process gas [75]. Carburizing complex geometries, reduced process times, elimination of intergranular oxidation as well as the good reproducibility of the results made the process increasingly interesting for the industry.

10.4 Reactions of Gas Carburizing and Their Effect on Carbon Potential

Examples of possible carburizing reactions are given below:

$$CO + H_2 \leftrightarrow C + H_2O \quad (1)$$

$$2CO \leftrightarrow C + CO_2 \quad (2)$$

$$CO \leftrightarrow C + \frac{1}{2}O_2 \quad (3)$$

The carbon potential of the work piece should be lower than the carbon potential of the furnace atmosphere in order to provide the required driving force for the transportation of carbon [235]. The addition of hydrocarbon gases is used to control the carbon potential [59]. It is assumed that the carburizing is taking place directly due to the CO content in the atmosphere. An example of reactions to generate required CO using natural gas is given below:

$$CH_4 + H_2O \leftrightarrow CO + 3H_2 \quad (4)$$

$$CH_4 + CO_2 \leftrightarrow 2CO + 2H_2 \quad (5)$$

$$CH_4 + O_2 \leftrightarrow 2CO + 4H_2 \quad (6)$$

and carbon potentials for reaction 1, 2 and 3 are calculated by the following formulations [60,236];

For reaction 1 $a_c = \frac{1}{K} \cdot \frac{p(CO) \cdot p(H_2)}{p(H_2O)}$ *where logK =* $-\frac{7100}{T} + 7.496$ *Eq. 10-11*

For reaction 2 $a_c = \frac{1}{K} \cdot \frac{p(CO)^2}{p(CO_2)}$ *where logK =* $-\frac{8817}{T} + 9.071$ *Eq. 10-12*

For reaction 3 $a_c = \frac{1}{K} \cdot \frac{p(CO)}{p\left(O_2^{\frac{1}{2}}\right)}$ *where logK =* $-\frac{5927}{T} + 4.545$ *Eq. 10-13*

K is the equilibrium constant, p(gas) is the partial pressures of the corresponding gases (measured in fractions of an atmosphere) in the furnace, and *T* is the furnace temperature in Kelvin.
Calculations and reactions given above describe the phenomenon at the equilibrium stage. Carbon flux transfer from the atmosphere to the steel surface before reaching the equilibrium can be described with the equation below [60,237];

$$J_c = \beta \cdot \left(a_c^{gas} - a_c^{steel}\right) \quad in\ \frac{cm}{s} \quad \text{Eq. 10-14}$$

$$\beta = \frac{M_c}{\Delta t \cdot 7.85 \cdot \left(C_g - \frac{c_{t_1} + c_{t_2}}{2}\right) \cdot 100} \quad in \frac{cm}{s} \qquad \textit{Eq. 10-15}$$

Where J_c is a carbon flux ($\frac{\text{cm}}{\text{s}}$) which is proportional to the carbon activity differences in atmosphere and steel, and β is the proportionality factor ($\frac{\text{cm}}{\text{s}}$), which is a non-constant carbon transfer coefficient highly depending on the used gas. M_c is the amount of carbon absorbed in the sample. C_g is the equilibrium carbon content. c_{t_1} and c_{t_2} are carbon contents measured at different times of t_1 and t_2 where $t_2 > t_1$. Figure 10-9 shows the gas dependence of the carbon transfer coefficient.

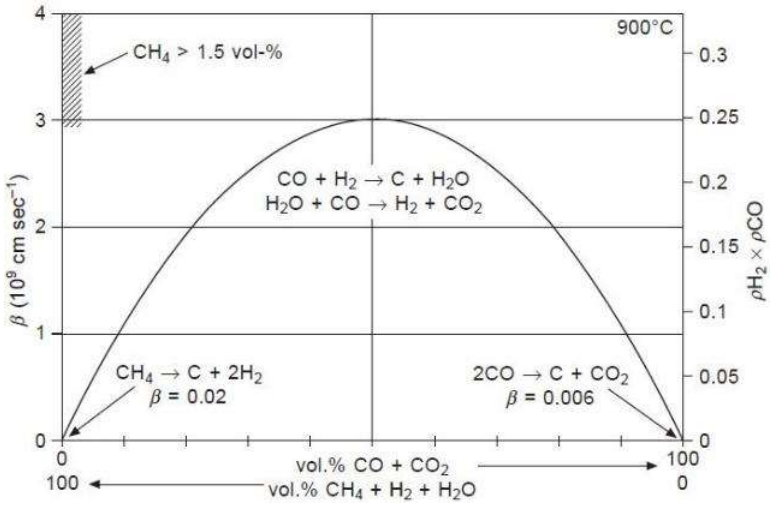

Figure 10-9: Gas composition dependence of carbon transfer coefficient [2,238]

In Figure 10-10, Rimmer et. al. showed the significance of the carbon transfer coefficient by determining its effect on the time required to reach 1.15 % surface carbon content at 920 °C. An atmosphere containing 50 % CO and 50 % H_2 ($\beta = 2.5 \cdot 10^{-5}$) as compared to one with 20 % CO and 40% H_2 ($\beta = 1.25 \cdot 10^{-5}$) reduced the time for the surface carbon content to reach the value of the carbon potential (1.15 ma. %) from about 20 hours to 4 hours. Therefore, the carbon flux into the surface and the carbon flux diffusing into the steel are two competing carbon fluxes that influence the time required for surface carbon content to reach carbon potential. [2,239].

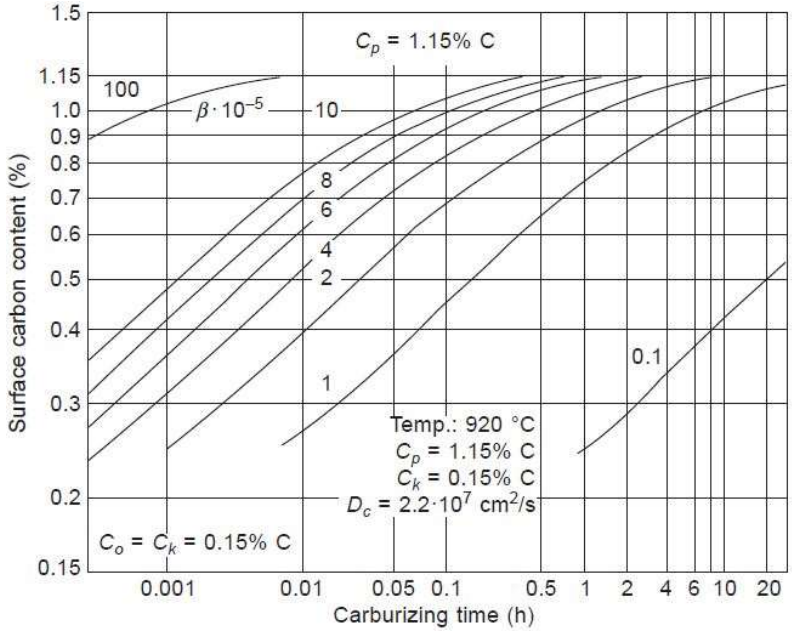

Figure 10-10: Effect of carbon transfer coefficient on the increase of the surface carbon content in gaseous carburizing [2,239].

10.5 Schematic Representation of Synchrotron and Description of Main Components

Figure 10-11 shows the schematic representation of the Synchrotron ring.

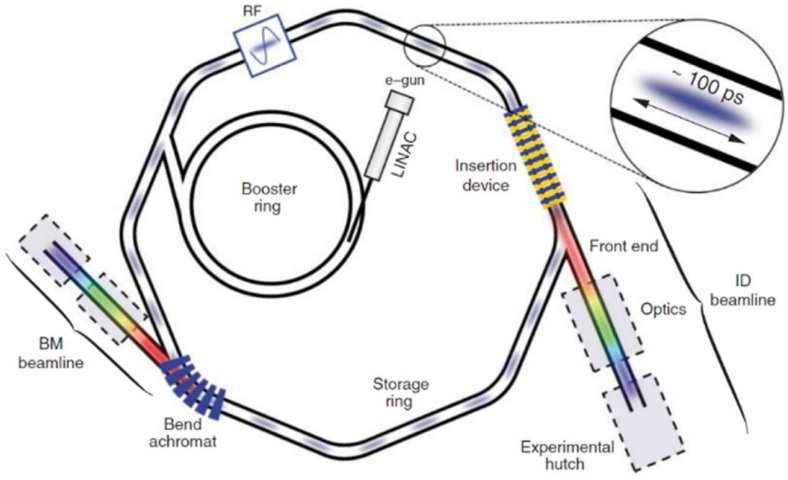

Figure 10-11: A schematic of the most important components of a modern synchrotron facility. E-gun is an electron gun which is the source of electrons. LINAC is linear accelerator. ID is insertion device. BM is bending magnets and RF is radio frequency supply [240].

A synchrotron consists of five main components [240];

1. Electron gun: It is a source of electrons which are normally generated by thermionic emission from a heated filament. The electron gun supplies a steady amount of electrons since collisions with remaining gas particles in the storage ring cause continual losses. Electrons are afterwards accelerated by a linear accelerator (LINAC) to about 100 MeV.

2. Booster ring: Electrons from the LINAC are pumped into the booster ring for further acceleration up to an energy level at which they travel in the main storage ring. The storage ring current has to be maintained; thus, bunches of electrons are periodically injected. In order to prevent the loss of operation time in the beamline due to such large injections, modern facilities operate in a so-called 'top-up' mode, in which the stored current in the ring is injected into the booster in small amounts but frequently to keep the ring always "full".
3. Storage ring: It keeps electrons on a closed path by the use of a magnet array. The electrons have kinetic energies, $\mathcal{E}$, measured in GeV, and their velocities are highly relativistic, i.e. they are very close to the velocity of light. The relative spread in electron energy $\Delta\mathcal{E}/\mathcal{E}$ is of the order of 0.1%. The storage ring structure consists of arc-shaped sections containing the above-mentioned magnets that bend the electrons and straight sections to generate the highest brilliance of synchrotron radiation by using insertion devices (IDs).

   Additionally, there is also special line up of bending magnets, which are called wigglers, to increase the intensity of synchrotron radiation by the number of magnet poles. Modern facilities also use undulators for the same purpose instead of wigglers. Similar to wigglers, they generate an alternating static magnetic field which deflects the electron beam sinusoidally with the help of periodic arrangements of dipole magnets.
4. Radio frequency (RF): It is used to supply the compensation energy to the electron as they pass through to eliminate the energy loss caused by the emission of synchrotron radiation.
5. Front end: This is the first section of the beamline and has several functions and safety features such as separation of the vacuum of the beamline and storage ring for isolation; determination of the position of the photon beam; adjustment of the angular acceptance of synchrotron radiation; blocking and filtering out radiations which can cause damage to the optical components in the next section.

Finally, before entering the experimental hutch, the beam is focused and/or monochromatized in the optics hutch. Lead-lined, thick concrete walls are used in the experimental hutch to protect users from radiation.

10.6 Diffraction Line Profiles in Rietveld Method

The Rietveld method was originally designed as a method of refining crystal structure data obtained by neutron powder diffraction with low resolution by Hugo M. Rietveld in 1967 [123,124]. At that time, the Gaussian peak profile function was appropriate to describe this low resolution data. When there was a need for an extension of the method to powder X-ray diffraction (PXRD), it was realized that the line profiles could not be described by Gaussians alone. Malmros and Thomas first proposed a modified Lorentzian [241,242], whereas Young, Mackie, and von Dreele compared results obtained with Gaussian or Lorentzian line profiles [242,243]. The authors mentioned that the option of using the Lorentzian function rather than Gaussian improved the peak profile description.

In the following years, several profile functions were proposed, including the so-called split-functions (different left/right peak width parameters) to account for peak asymmetry [242].

By the end of the 1980s, the domain of the pseudo-Voigt (pV) [242,244], Voigt (V) [242,245], and Pearson VII (PVII) [242,246] profile functions were introduced. Among all, the pV function was the most preferred one, which is the weighted average of Gaussian or Lorentzian functions. The pV function is flexible enough to adapt to the most common experimental data and is an excellent approximation of the Voigt function with a faster calculation ability.

In the 1990s, in order to obtain microstructural parameters from the width and shape of line profiles refined by the Rietveld method, several interpretations have been proposed. Since the pV profile function was a popular a choice due to its simplicity, most interpretations of the line broadening caused by microstructural features, such as domain size and microstrain, were given in terms of Lorentzian and Gaussian profile components [247]. Although this interpretation was not entirely justified by theory, it was highly used due to its practical and fast approach.

It was realized that the quality of the structural refinement could be negatively affected if the line broadening anisotropy (hkl-dependence of peak width and shape) is not properly considered. Therefore, hkl-dependent expressions were proposed by some authors to solve this problem, for example, the spherical harmonics model of Stephens [242,248].

Some further modifications of pV functions, such as Modified Thompson-Cox-Hasting pV (TCHZ) [242,249] or double-Voigt function [242,250], were the main choice as a profile fitting function, including anisotropy if necessary, such as the model of Stephens given above. This choice of the profile function was based on computational speed and flexibility, aiming to improve the description of the Bragg peaks, especially in the case of peak overlapping.

The microstructural interpretation was most often given in terms of parameters, such as the “volume-weighted mean column length” or a spherical harmonics representation of the size anisotropy. Although these parameters are informative, they were not directly comparable with the results from complementary methods such as transmission electron microscopy [242].

At this point, the fundamental parameter approach (FPA) [166,242,251] has brought significant modification in the instrumental line profile description by using the convolutive approach of Alexander [242,252,253].

10.7 Residual Stress Analyses with Omega (ω) and Chi (χ) Mode.

In ω-mode, only two circles are required (θ and ω). While keeping the angle between the X-ray source and the detector constant, different Psi (Ψ) angles are determined by rotating the sample parallel to the 2θ rotation axes. Eq. 10-16 is then used to calculate the Ψ angle. For all orientations, this measurement setup results in beam path asymmetry. Moreover, depending on the position of the recorded peak, the feasible Ψ angles can be severely limited. Furthermore, for high Ψ angles, significant elongation of the beam on the sample due to the flat angle of the incoming beam causes measurement errors.[116].

$$\psi = \frac{2\theta}{2} - \omega \qquad \textit{Eq. 10-16}$$

In χ mode, three or four circle diffractometers are used to perform the measurement. The sample is tilted out of the plane around a rotation axis perpendicular to the 2θ rotation axes, making the Ψ angle equal to the χ angle. With this alignment, beam path symmetry for all orientations can be achieved; additionally, the sample can be tilted to high angles irrespective of the peak position. As a result, this approach is well established for measuring stress [148]. Figure 10-12 depicts a graphic explanation of both measurement types.

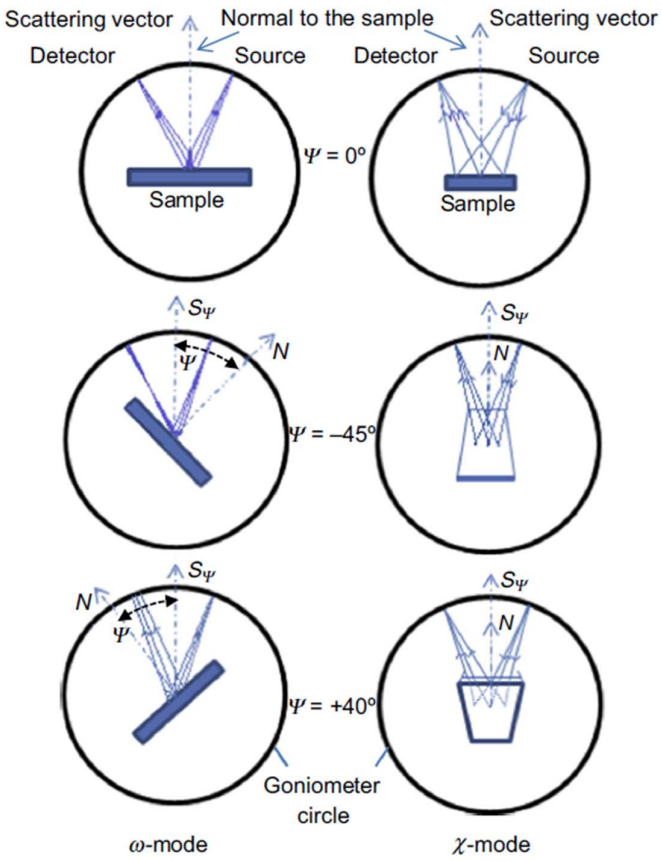

Figure 10-12: Principle of residual stress measurements in Omega (ω) and Chi (χ) mode [116,254].

10.8 Determination of Elastic Constants

Table 10-1: Temperature dependence of elastic contants

Temperature (°C)	*Austenite E (Gpa)*	*Austenite ν*	*Martensite E (Gpa)*	*Martensite ν*
-100	206	0.271	217	0.282
-50	202	0.274	215	0.283
0	198	0.276	213	0.284
20	196	0.277	212	0.285
50	194	0.279	210	0.286
100	190	0.282	207	0.287
150	186	0.284	203	0.288
200	182	0.287	199	0.29
250	178	0.29	196	0.291
300	174	0.293	192	0.293
350	170	0.296	188	0.295
400	166	0.298	184	0.297
450	162	0.301	179	0.299
500	158	0.304	175	0.302
550	154	0.307	170	0.306
600	150	0.31	164	0.311
650	146	0.313	155	0.318
700	142	0.316		
750	138	0.32		
800	134	0.323		
850	131			
900	127			

10.9 Change of Peak Positions During Boost and Diffusion Cycles

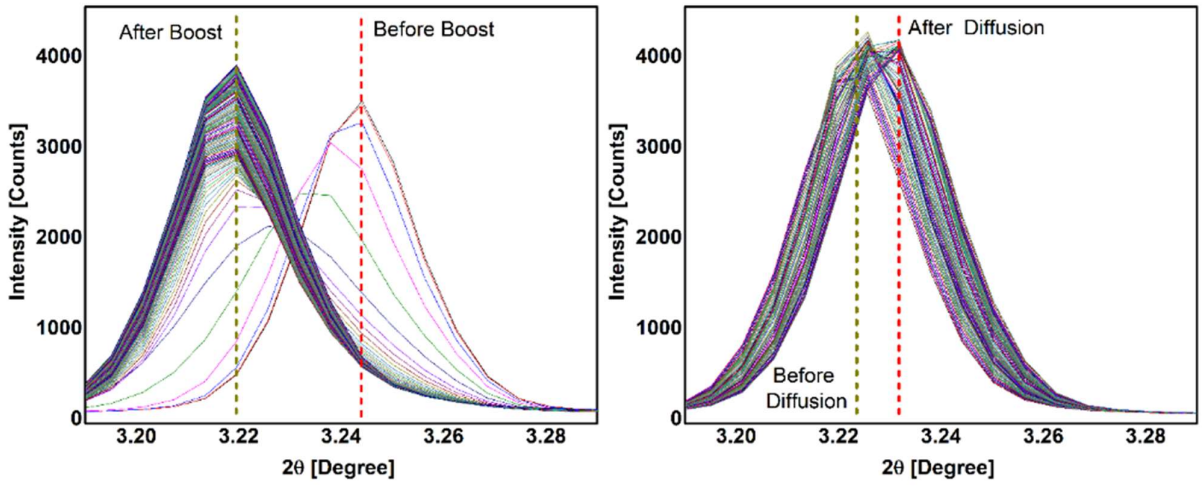

Figure 10-13: Austenite γ {111} peak shifting during second boost and diffusion step. Dashed lines show the peak positions before and after corresponding step.

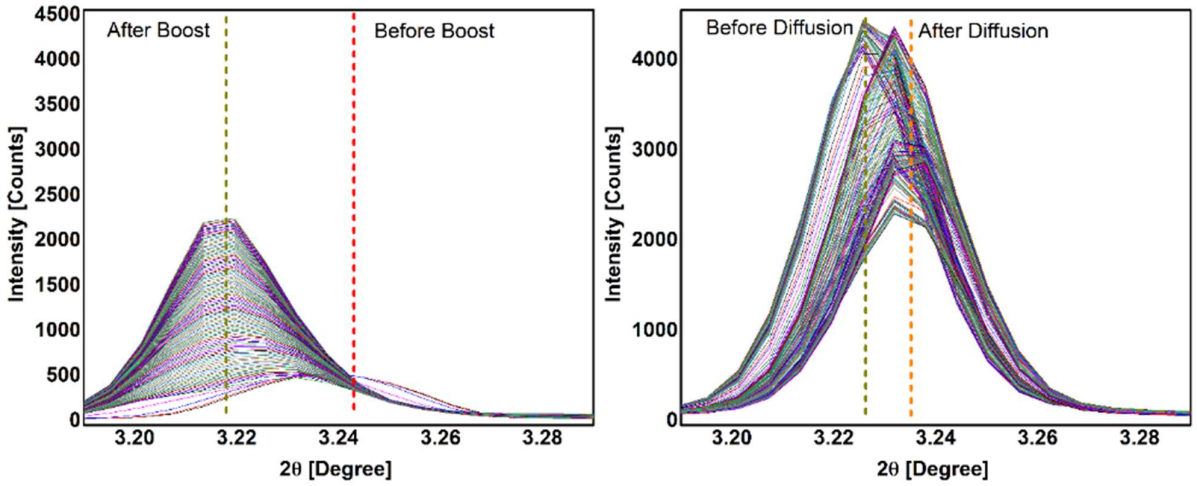

Figure 10-14: Austenite γ {111} peak shifting during third boost and diffusion step. Dashed lines show the peak positions before and after corresponding step.

10.10 Effect of Boost Diffusion Cycles on Peak Positions, FWHM and Lattice Parameters

Change of FWHM and peak positions of γ {111} austenite peak is given in Figure 10-15. During both experiments, a peak shift to the lower angles was systematically observed. Although the duration of the second boost step of sample 4BD is reduced to half compared to sample 3BD, the final peak positions are comparable. Moreover, except for the first boost step, the final peak positions after each boost step were almost the same, but the initial states vary depending on the diffusion step before each boost step.

The change of FWHM for all boost steps is also similar to the ones observed in previous sections. FWHM values increase when shifting starts and decrease slowly until the end of each step.

Similar to previous investigations, peak shifts were observed during the boost and diffusion steps of both experiments. These peak shifts are again directly related to carbon absorption and diffusion via the lattice parameter evolution.

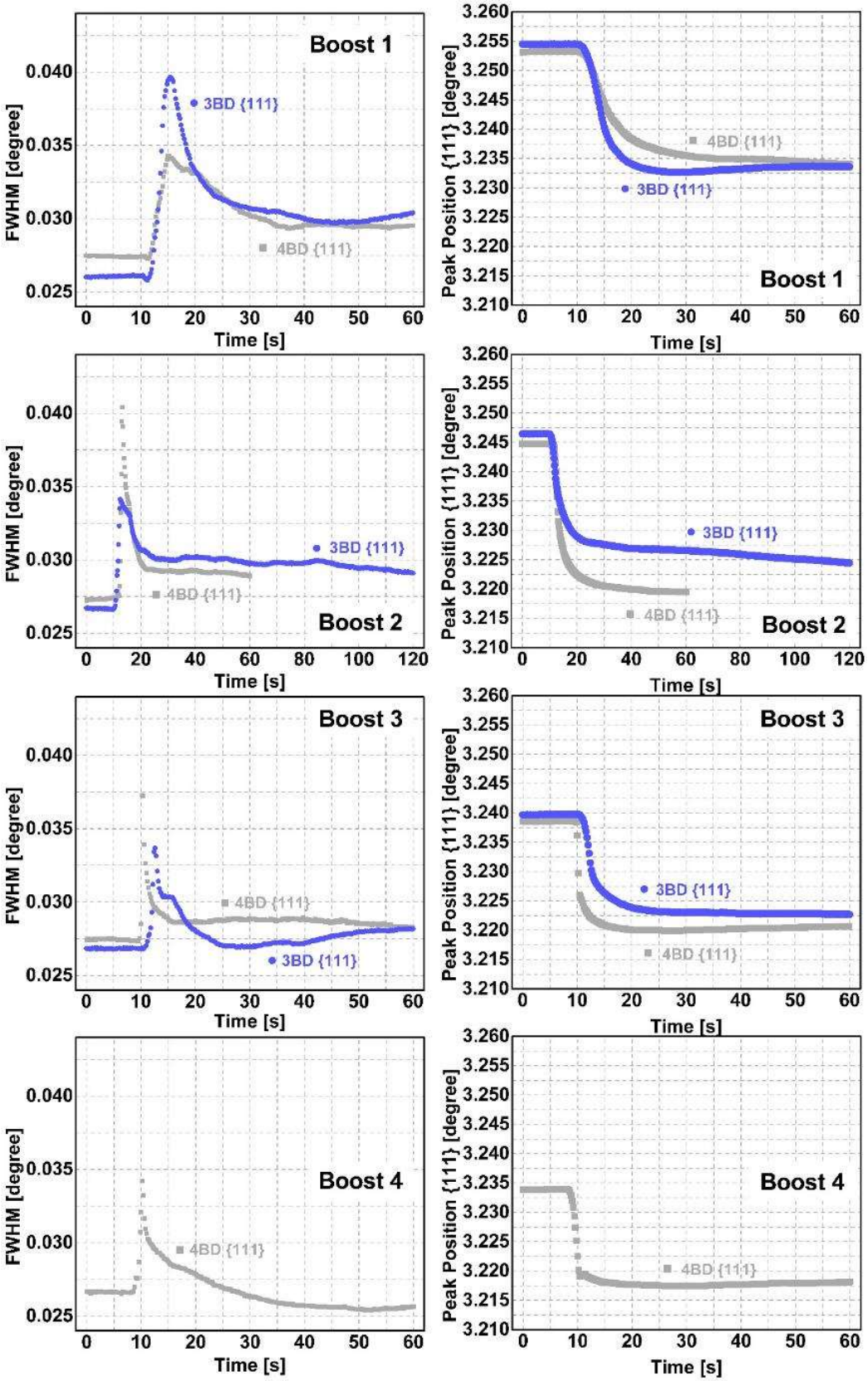

Figure 10-15: Change of FWHM and peak positions of γ {111} austenite peak with time for the boost step of two different samples carburized at 940 °C with different boost-diffusion cycles. Average error margin for FWHM is $3.3 \cdot 10^{-4}$ degree.

Integrated diffraction frames were analyzed, and the lattice parameter changes were found using the same procedure as previously presented. Figure 10-16 shows the change of lattice parameter of austenite during the boost and diffusion steps of two samples carburized with different parameters.

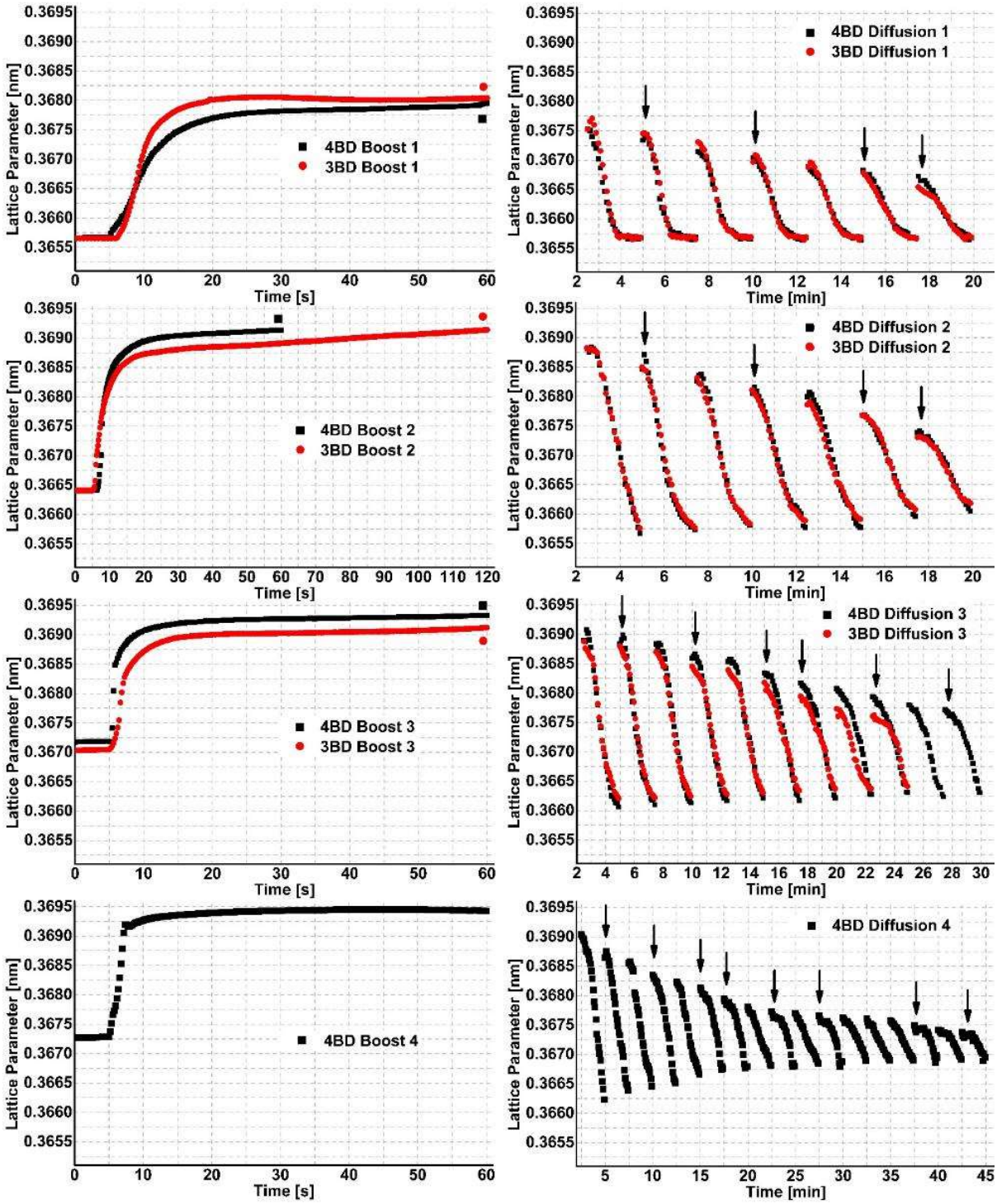

Figure 10-16: Evolution of the lattice parameter of austenite for 4BD and 3BD samples carburized at 940 °C. Black arrows in diffusion graphs show further investigated scans for the change of carbon content determination presented in Figure 5-36. Average error bars scale is $\pm$ 5.10^{-5} and it is smaller than symbols.

Lattice parameters are very close for both samples, especially for the first two boost-diffusion cycles. In the third boost step and the following diffusion step, the lattice parameter of 4BD is slightly higher than the lattice parameter of the 3BD sample.

10.11 Generation of Thermal Stresses During Quenching

Demonstration of this by using theoretical values of the yield strength and thermal stresses can be seen in Figure 10-17. In the figure, the evolution of stresses along with the yield stress of the material can be seen. When the thermal stresses exceed the yield stress, further increase towards the tensile direction can be observed as marked with a dashed red line.

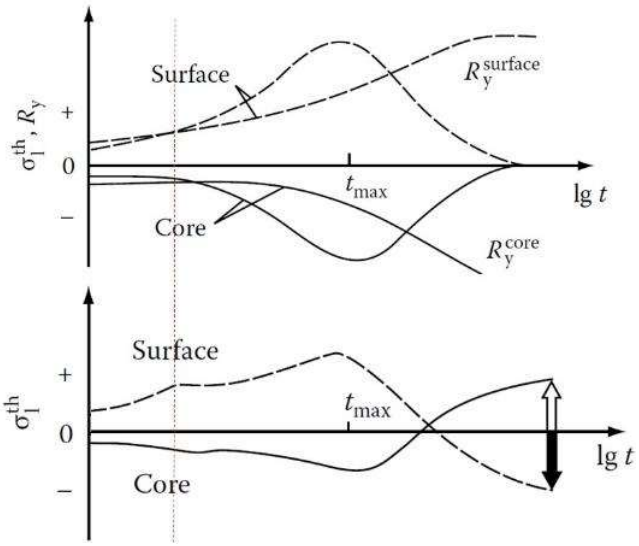

Figure 10-17: Generation of thermal stresses during quenching. R values are yield stresses [147]